Chemical and Catalytic Reactor Modeling

ACS SYMPOSIUM SERIES **237**

Chemical and Catalytic Reactor Modeling

Milorad P. Duduković, EDITOR
Washington University

Patrick L. Mills, EDITOR
Monsanto Company

Based on a symposium
sponsored by the Division of
Industrial and Engineering Chemistry
at the 185th Meeting
of the American Chemical Society,
Seattle, Washington,
March 20–25, 1983

American Chemical Society, Washington, D.C. 1984

ACS Symposium Series

M. Joan Comstock, *Series Editor*

Advisory Board

FOREWORD

The ACS SYMPOSIUM SERIES was founded in 1974 to provide
a medium for publishing symposia quickly in book form. The
format of the Series parallels that of the continuing ADVANCES
IN CHEMISTRY SERIES except that in order to save time the
papers are not typeset but are reproduced as they are sub-
mitted by the authors in camera-ready form. Papers are re-
viewed under the supervision of the Editors with the assistance
of the Series Advisory Board and are selected to maintain the
integrity of the symposia; however, verbatim reproductions of
previously published papers are not accepted. Both reviews
and reports of research are acceptable since symposia may
embrace both types of presentation.

PREFACE

THE CHEMICAL AND CATALYTIC REACTOR modeling topics included in this 21-chapter volume are illustrative of the current research emphasis from academic and industrial points of view. Most chapters present new research results and the others provide brief and timely user-oriented tutorials.

The book is divided into five sections. Each section corresponds to a particular reactor classification. The classifications covered here are trickle-bed reactors, slurry system and stirred tank reactors, novel reactors, packed-bed and tubular reactors, and catalyst deactivation.

The diverse topics covered in this volume, as well as the individual styles adopted by the authors who represent five countries, prevented us from achieving a completely uniform notation throughout. We hope that the readers will enjoy the various styles and that the technical merit of the chapters will far outweigh the lack of an impeccably uniform format. Many novel ideas are expressed in this volume and our desire is to bring these to the attention of a larger audience through publication in the ACS Symposium Series.

We are indebted to the authors for their contributions and to the staff of the ACS Books Department for their assistance and cooperation in making this volume possible.

M. P. DUDUKOVIĆ
Washington University
St. Louis, Missouri

P. L. MILLS
Monsanto Company
St. Louis, Missouri

August 1983

Trickling and Pulsing Transition in Cocurrent Downflow Trickle-Bed Reactors with Special Reference to Large-Scale Columns

D. M. DIMENSTEIN, S. P. ZIMMERMAN, and K. M. NG

Chemical Engineering Department, University of Massachusetts, Amherst, MA 01003

A model is presented to predict flow transition be-
tween trickling and pulsing flow in cocurrent down-
flow trickle-bed reactors. Effects of gas and liq-
uid flow rates, particle size, and pressure on the
transition are studied. Comparison of theory with
published transition data from pilot-scale reactors
shows good agreement. Since the analysis is inde-
pendent of reactor size, calculations are extended
to include large-scale columns; some interesting
observations concerning flow transition and liquid
holdup are obtained.

In the last two decades extensive research has been performed to
study the dynamics of trickle-bed reactors. Despite all these
efforts, it is generally agreed that the understanding is still
incomplete. In particular, the complex hydrodynamics inside the
bed has been identified as one of the major technical constraints
that needs to be resolved before trickle-bed reactors can be de-
signed in a reliable manner.
    Previous hydrodynamic studies of trickle-beds are primarily
experimental work involving pilot scale columns, for instance,
constructing flow regime maps, and correlating pressure drop and
liquid holdup data (1-5). Although these contributions have pro-
vided much insight, there is a lot of uncertainty in applying
these data for industrial applications.
    This difficulty arises because the size and operating con-
ditions of a large-scale reactor normally differ significantly
from that of a pilot-scale column. Commercial hydrodesulfuriza-
tion reactors are of size up to 20 by 30 ft. and may be operated
at up to 70 atmospheres and 400°C. In contrast, pilot-scale
hydrodynamic data are obtained from columns of a few inches, or
less, in diameter and several feet in height, at near atmospheric
pressure and room temperature.
    In order to bridge this gap, it is highly desirable to study

the flow phenomena on a more theoretical basis. Specifically,
models are needed to account for the effects of various factors
such as temperature, pressure, size and shape of catalyst parti-
cles, reactor dimensions, etc. on the hydrodynamics of the bed.
     In this paper, a model for predicting trickling-pulsing tran-
sition, as proposed by Ng (6), is extended to include large-size
columns. Preliminary calculations of pressure drop and holdup as
a function of bed height indicate several interesting features
associated with large-scale reactors.

Transition From Trickling to Pulsing Flow

     Consider a catalyst column consisting of randomly packed,
spherical particles of a uniform size, d_g, with cocurrent gas-
liquid downflow. Under trickling flow conditions, a liquid film
flows on the surface of the particles. The void space inside the
bed is made up of small constrictions and relatively larger pore
chambers. For such a constriction connected with a pore chamber
above it, the interstitial gas velocity at the constriction, u_g,
is greater than that at the pore chamber, u_g'. Based on continu-
ity considerations,

$$u_g = \left(\frac{d'}{d}\right)^2 u_g' \tag{1}$$

where d and d' are the diameter of the channel for gas flow at the
constriction and the pore chamber, respectively.
     Using Bernoulli's concept, the pressure at the constriction,
p, and the pressure at the pore chamber, p', are related by

$$p' - p = \frac{1}{2} \rho_g (u_g^2 - u_g'^2) \tag{2}$$

Due to the lower pressure at the constriction, the liquid film
tends to collapse there to form a liquid pulse. However, this is
counteracted by the capillary effect. Indeed, a pressure balance
through the liquid film yields

$$p' - p = \frac{4\sigma}{d_g} - \rho_1 g \, d_g/2 \tag{3}$$

Equations (1) to (3) would give u_g at which pulsing will take
place. Furthermore, realizing that $(d/d') \tilde{\ } 0.4$, we get

$$u_g = \sqrt{\frac{2}{\rho_g}\left(\frac{4\sigma}{d_g} - \rho_1 g \, d_g/2\right)} \tag{4}$$

Hence, the corresponding superficial flow rate of gas, G, is given by

$$G = \varepsilon u_g (1-\alpha)\rho_g \tag{5}$$

Here, ε is the porosity of the bed, α is the fraction of the cross-sectional area of void space occupied by liquid. At this point, a theoretical prediction of α is not available, but it can be estimated based on a correlation suggested by Wijffels et al. (7), which indicates that α increases with increasing superficial mass flow rate of liquid, L.

Comparison of Theory with Experimental Results

Figure 1 shows the comparison of theory for the trickling-pulsing transition with experimental results from pilot scale columns for air-water systems. Since most experimental studies did not mention the pressure inside the column, a value of 1.5 atm has been assumed. The agreement with the data of Weekman and Myers (1) is excellent and a good agreement with that of Chou et al. (8) is attained up to moderate gas flow rates. The theory would appear to be in poor agreement with Sato et al.; however, in Sato's paper, porosity was not mentioned. Experimental data (8) and theoretical calculations (6) indicate that the transition curve is sensitive to porosity. For lack of information, we have assumed a porosity value of 0.4, which may be different from the actual experimental value.

Figure 2 shows the influence of particle size on flow transition. It is interesting to note that the 4mm and 6mm transition curves intersect each other. This phenomenon can be explained by considering the effect of particle size on the interstitial gas velocity needed to induce pulsing and the liquid holdup of the bed.

As the particle size decreases, the liquid holdup increases. Thus it would be expected that a lower gas rate would be required to induce pulsing, as is observed in the case of the 2mm particles. However, with a decrease in particle size, the surface tension effect increases, which holds the films more securely in place. A higher gas flow rate is then required to cause the liquid films to collapse and induce slug formation. Therefore, the curves for the 4mm and 6mm particles intersect due to a balance in the effects of particle size upon the surface tension and liquid holdup.

Figure 3 shows the influence of pressure on flow transition. As the pressure increases the gas density increases. Since the transition to pulsing flow depends on the interstitial velocity, it is expected that higher gas mass flow rates are required to achieve flow transition.

Pressure and Holdup Profiles in Large-Scale Reactors

The relationship between pressure drop and gas and liquid flow rates is illustrated in Figure 4 for a column 9 m in height.
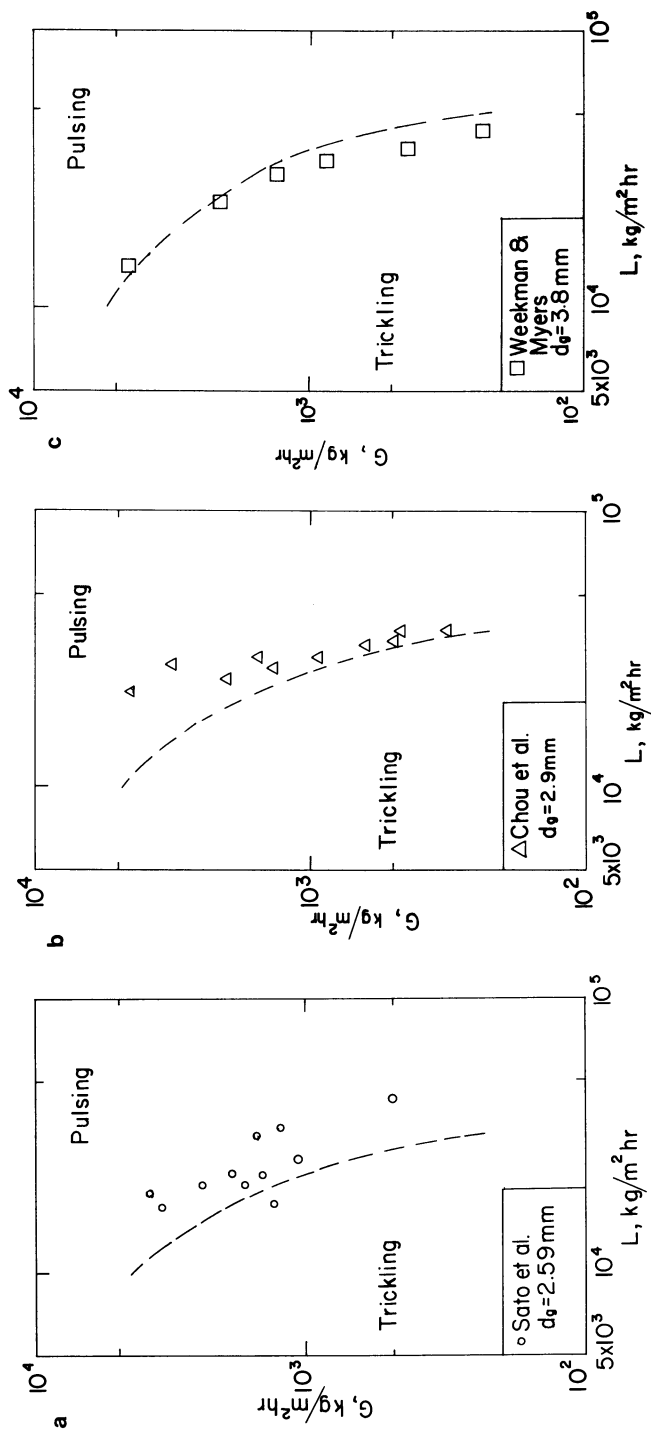
Figure 1. (a,b,c). Comparison of theory with published trickling-pulsing transition data from pilot-scale columns.
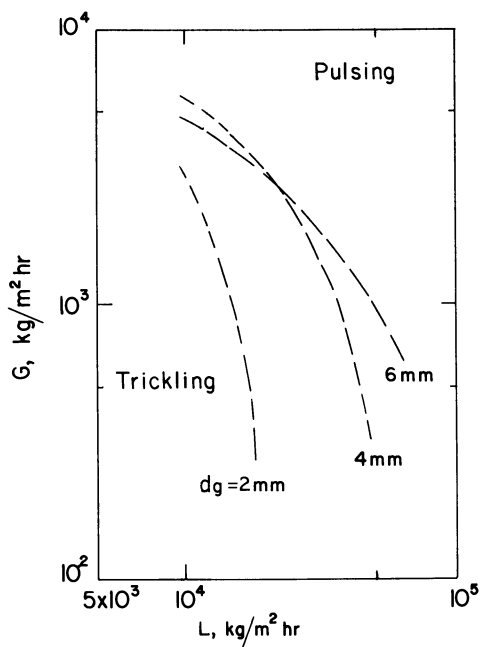
Figure 2.   Effect of particle size on trickling–pulsing
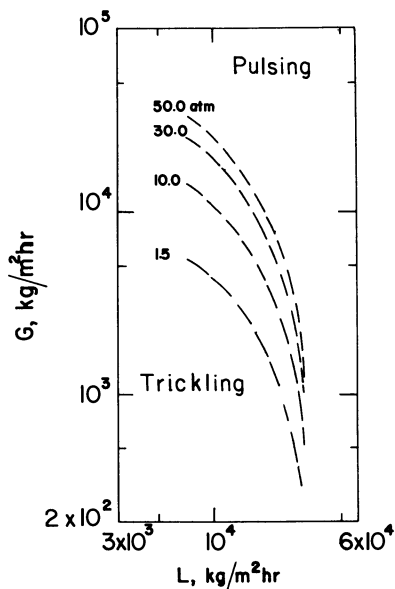transition.

Figure 3.　Effect of pressure on trickling-pulsing transition.
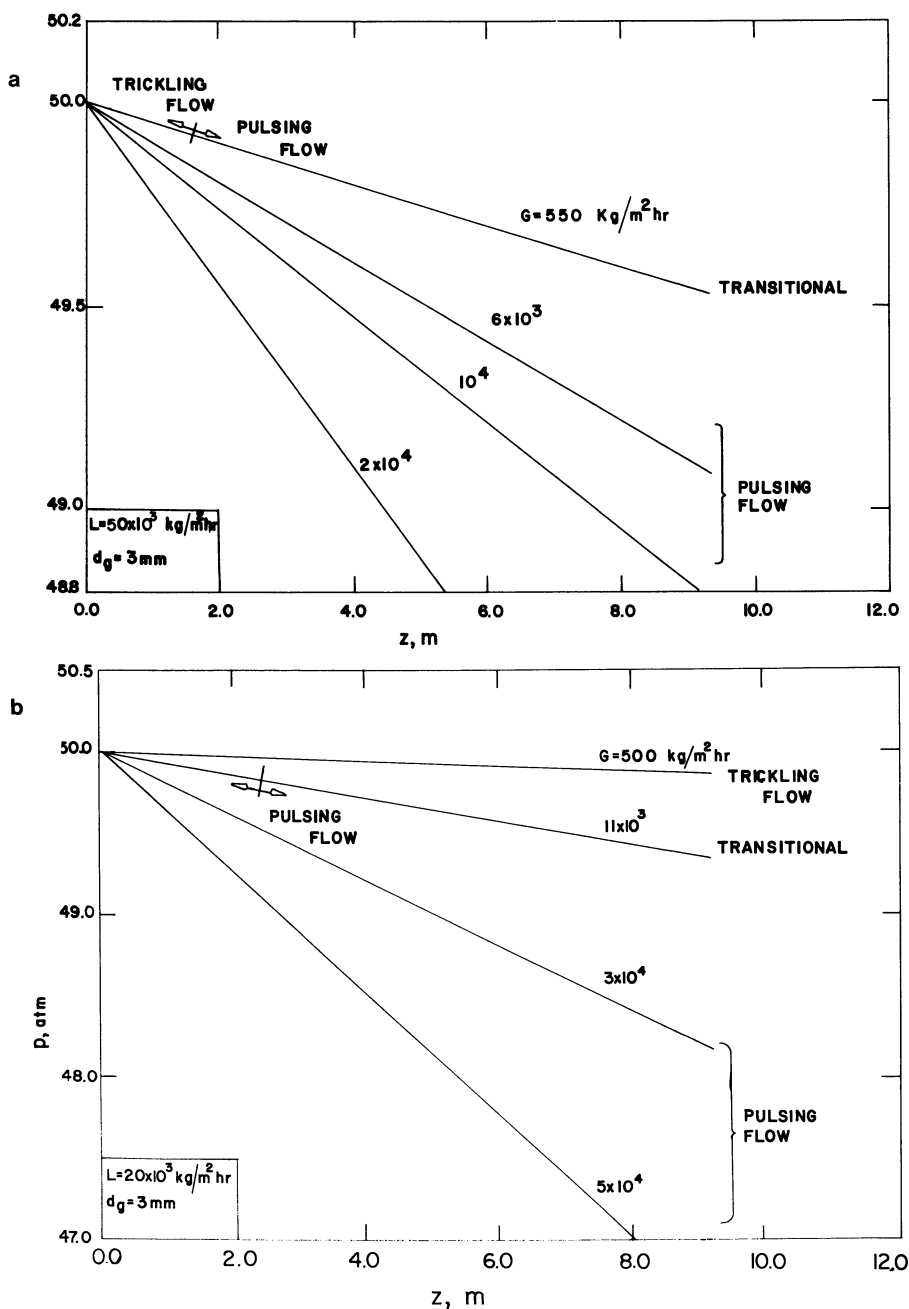
Figure 4 (a,b). Effect of gas flow rate on pressure pro-
file for a large-scale column.

These curves show the pressure profile in a trickle bed reactor for varying gas flow rates, and liquid flow rates of 5×10^4 kg/m^2 hr and 2×10^4 kg/m^2 hr respectively. The data are based on a correlation proposed by Sato et al. (2). Another correlation considered was that presented by Specchia and Baldi (9); however, the applicability of this relationship is somewhat in doubt. For a given gas flow rate of 10^4 kg/m^2 hr, the two-phase pressure drop predicted by the Specchia and Baldi correlation is considerably less than that calculated for one phase flow by the well developed Ergun equation. This seems unreasonable considering the energy dissipation associated with two-phase interactions. For the correlation presented by Sato et al., the two-phase pressure drop is a function of the Lockhart-Martinelli parameter, χ, which is the square root of the ratio of the single-phase pressure drop of liquid to that of the gas.

$$\sqrt{\frac{\Delta P_{1g}}{\Delta P_1}} = 1.30 + 1.85\chi^{-0.85}; \quad \chi = \sqrt{\frac{\Delta P_1}{\Delta P_g}} \qquad (6)$$

The single phase pressure drops are calculated using the correlation of Tallmadge (10).

$$150 + 4.2\,Re^{5/6} = \frac{\Delta P}{\Delta L}\frac{d_g^2\,\varepsilon^3}{\mu U\,(1-\varepsilon)^2}; \quad Re = \frac{d_g U\rho}{\mu\,(1-\varepsilon)} \qquad (7)$$

A wall effect correction factor employed by Sato was neglected due to the small particle to bed diameter ratio characteristic of commercial reactors.

For a given liquid flow rate the pressure gradient increases with increasing gas flow. This is expected due to the increased energy loss associated with the increased gas-liquid interactions.

It is interesting to note that for some liquid and gas flow rates two different flow regimes can be present in different regions of the trickle bed. This point is indicated in Figure 4. In the upper portion of the bed, trickling flow occurs, but when the gas velocity has increased enough, it tends to blow away liquid held up between the packing particles and pulsing flow is observed. This transition criterion is given in Equation (5).

The axial position of the transition point is highly sensitive to gas flow rates and for a 9 m column will occur in only a small range of values. It is important to mention that the model used in this paper assumes fully developed flow. This might not be the case in an industrial size reactor and an entrance effect might well be observed which is not predicted here.

The liquid holdup for different regions of the bed are shown for different inlet pressures in Figure 5. The values for liquid holdup were calculated using Sato's correlation.

$$\beta = 0.4 \left[\frac{6(1-\epsilon)}{d_g} \right]^{1/3} \chi^{0.22} \qquad (8)$$

It should be noted that the liquid holdup is a time averaged value. In practice, for flows in the pulsing regime at a given column depth, the holdup will vary with time due to the alternating passage of liquid and gas rich slugs.

For a 9 m column with high inlet pressure, the holdup is approximately constant throughout the entire bed. For the 4 m column with low inlet pressure, characteristic of lab or pilot scale reactors, there is a dramatic drop in the holdup as one moves down the bed. This can be explained by examining the relative difference in pressure between the top and bottom of the bed for the two cases.

As the fluids travel down the bed, the energy losses decrease the pressure. As the pressure is dropped, the gas expands. The expansion results in a decrease in liquid holdup. However, the relative pressure drop for the commercial size bed at a depth of 3.8 m is 1.9% of the initial value while for the laboratory column at the same depth this value is 73%. The gas in the low pressure bed consequently expands five fold from 200cc/g to 1000 cc/g, at a pressure of 4 atm, while the high pressure bed gas specific volume remains nearly constant at 23.8cc/g for a pressure of 35 atm. It is this large expansion which is responsible for the appreciable drop in liquid holdup for the small reactor.

It is apparent that for commercial reactors operating at moderate to high pressures, the total liquid holdup will be a constant value for a given G, L, and pressure. This concept is demonstrated in Figure 6 where lines of constant liquid holdup, are indicated on the flow map. This type of graph might be of use in designing industrial size trickle-bed reactors since it readily shows the holdup for a given set of operating conditions.

Conclusions

In this paper correlations presented by Sato et al. for liquid holdup and pressure drop in trickle bed reactors were used to examine the characteristics of large-scale columns. The trickling-pulsing transition relationship given by Ng was also employed to determine the flow regime present. Some interesting phenomena were observed, specifically:

1) Increasing the packing size shifts the transition curve to higher flow rates (Figure 2). There is a limiting value of particle size above which the location of the transition to pulsing flow for low liquid flow rates begins to shift back down to lower gas flow rates. This is in qualitative agreement with Sato's data (3).

2) Increasing the inlet pressure to the reactor shifts
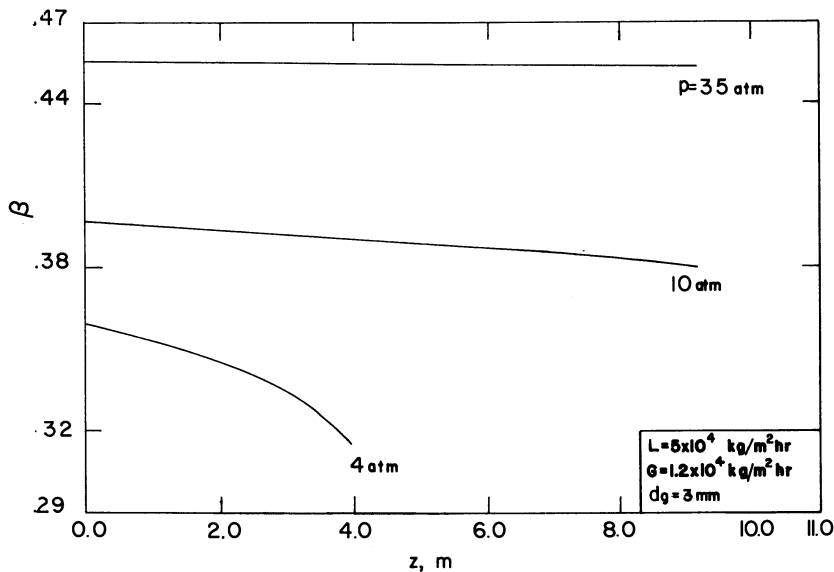
Figure 5. Effect of varying inlet pressure on liquid hold-up as a function of axial position in a trickle bed.
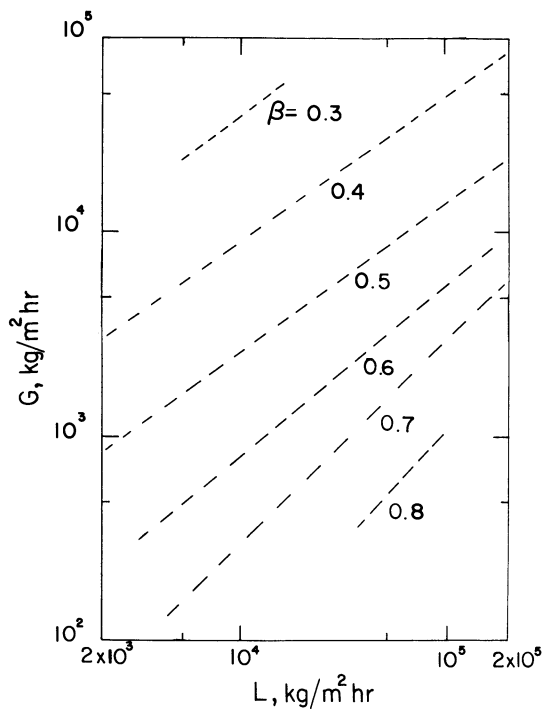
Figure 6. Liquid holdup for various gas and liquid flow rates in a high pressure reactor.

the trickling-pulsing transition curve to higher
gas and liquid flow rates. However, for high liquid
flow rates this shift is not so dramatic (Figure 3).
3) It is possible to have more than one flow regime
present in the reactor(Figure 4). The axial location
of the transition is highly dependent of gas flow rate.
4) The average total liquid holdup in a trickle bed
reactor decreases with increasing bed depth in a low
pressure laboratory or pilot scale column. However,
for commercial use where there is a moderate to high
pressure input, the holdup is essentially constant
(Figure 5).
5) The constant holdup in large reactors has led to
the formulation of a graph (Figure 6) which shows the
holdup for a given set of liquid and gas flow rates.
The fundamental understanding of factors contributing to
pressure drop and holdup in a trickle bed reactor is incomplete.
More work on the hydrodynamics associated with pulsing and
trickling flow is in progress.

Acknowledgments

Legend of Symbols

d	=	diameter of pore constriction available to gas flow
d_g	=	diameter of packing
d'	=	diameter of pore chamber available to gas flow
G	=	superficial mass flow rate of gas
g	=	acceleration due to gravity
L	=	superficial mass flow rate of liquid
p	=	pressure at pore constriction
p'	=	pressure at pore chamber
Re	=	Reynolds number
U	=	superficial velocity
u_g	=	interstitial gas velocity at pore constriction
u'_g	=	interstitial gas velocity at pore chamber

Greek Letters

α	=	fraction of cross-sectional area of void space occupied by liquid
β	=	liquid holdup
ΔL	=	length
ΔP_g	=	gas phase pressure drop
ΔP_l	=	liquid phase pressure drop
ΔP_{lg}	=	two phase pressure drop
ϵ	=	porosity

μ =   viscosity
χ =   interaction parameter (Equation 6)
ρ =   density
σ =   surface tension

Subscripts

g   =   gas
1   =   liquid

Literature Cited

1. Weekman, V.W. Jr.; Myers, J.E. AIChE J. 1964, 10, 951.
2. Sato, Y.; Hirose, T.; Takahashi, F.; Toda, M. J. Chem. Eng.
    Japan 1973, 6, 147.
3. Sato, Y.; Hirose, T.; Takahashi, F.; Toda, M.; Hashiguchi, Y.
    J. Chem. Eng. Japan 1973, 6, 315.
4. Charpentier, J.C.; Favier, M. AIChE J. 1971, 21, 1213.
5. Talmor, E. AIChE J. 1977, 23, 868.
6. Ng, K.M. "A Model for Flow Regime Transitions in Cocurrent
    Down-Flow Trickle-Bed Reactors" submitted to Ind. Eng. Chem.
    Fundam. 1983.
7. Wijffels, J.B.; Verloop, J.; Zuiderweg, F. ACS Monograph Ser.,
    No. 133, 1974; p. 151.
8. Chou, T.S.; Worley, F.L.; Luss, D. Ind. Eng. Chem. Proc. Des.
    Dev. 1977, 16, 424.
9. Specchia, V.; Baldi, G. Chem. Eng. Sci. 1977, 32, 515.
10. Tallmadge, J.A. AIChE J. 1970, 16, 1092.

Influence of the Reactional System on the Irrigation Rate in Trickle-Bed Reactors

P. RUIZ, M. CRINE[1], A. GERMAIN, and G. L'HOMME

Laboratoire de génie chimique et de chimie industrielle, Groupe de Chimie Appliquée, Université de Liège, Rue A. Stévart, 2, B-4000, Liège, Belgique

When designing a trickle-bed reactor, it is essential to know how the catalyst irrigation rate varies with the operating conditions. We previously developed a theoretical model based on percolation theory, relating irrigation rate to a hydrodynamic parameter characterizing the effective particle wettability, i.e., the one prevailing with the reactional system. In this paper, we present an experimental determination of the variations of this parameter with some characteristic variables of a specific reactional system: the hydrogenation of maleic acid into succinic acid on a Pd/Al_2O_3 supported catalyst. The data interpretation shows how temperature and concentrations may affect the catalyst irrigation rate, evidencing the importance of carrying out hydrodynamic experiments under chemical operation.

Catalytic fixed bed reactors with concurrent downflow of gas and liquid reactants are widely spread in the refining as well as in the chemical industry (1). They are generally operated in the trickling flow regime i.e. with the gas as the continuous phase and with the liquid trickling on the fixed bed of catalyst. It is well known that, in such trickle bed reactors, the performances strongly depend on :
- transfers of reactants at the gas-liquid interface,
- transfers of reactants at the liquid-solid interface,
- gas-liquid interfacial area,
- liquid-solid interfacial areas,
- specific activity of the catalytic system, including pore diffusion limitations.
- hydrodynamics. (see for example ref.2).

In addition, strong interactions between these physical and chemical phenomena make the prediction of performances very difficult. This does not guarantee that the separate study

---

[1]Research associate, F.N.R.S.

of each step of the reaction pathway is sufficient to completely
understand the behaviour of the reactor.
    A pure phenomenological model of such an intricate process,
taking into account all possible reaction steps, is therefore
a powerful tool for the scale up and the prediction of perfor-
mances of trickle-bed reactors. Such a model (3) has proved
to be able to correctly reproduce experimental data using only
two adjustable parameters.   It has been checked in several
cases (hydrogenation of alphamethylstyrene (3), hydrogenation
of 2-butanone (4), hydrorefining (5)), with more or less vola-
tile liquid reactants and it appeared to be also useful to
calculate a posteriori the extent of the different types of
wetted catalyst area and their different effectiveness factor.
 Of course, the fitting of the data can give rise to some com-
pensation effects and the accuracy of the determination of
the wetted areas (related to the topological description of
the liquid flow on the catalyst) is limited by the knowledge
of all the physico-chemical properties (vapour pressure, visco-
sities etc....) and of the correlated parameters (mass trans-
fer coefficient etc...) involved in the model.
Using a non-volatile liquid reactant would of course conside-
rably limit the number of possible reaction steps and, in the
fitting of the model, this would eliminate possible cross corre-
lations between the values which the model enable to calcu-
late.
    With this in mind, we test a trickle bed reactor using
the hydrogenation in aqueous solution of maleic acid into suc-
cinic acid in the presence of a supported palladium catalyst.
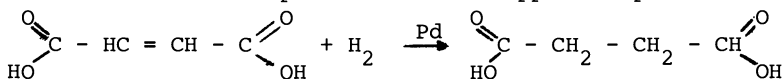
In the whole range of our experimental conditions, maleic acid
has no measurable volatility and we hoped so to obtain more
accurate information on the wetting efficiency as well as to
check the model in a much more constrained situation.   Moreover
the direct comparison of this reaction with the very similar
hydrogenation of alphamethylstyrene (the volatility of the
reactant excepted) which we experienced previously, could direc-
tly put into sight the role of dry or badly irrigated catalyst
particles.

E X P E R I M E N T A L   S E C T I O N

PRELIMINARY KINETIC STUDY

Reactional system

We first conducted a preliminary kinetic study in order to deter-
mine the intrinsic and particle scale apparent reaction rates.
A powder catalyst was used to determine the intrinsic reaction
rate while cylindrical particles were used both for the parti-

cle scale apparent reaction rate determination and for the
trickle-bed experiments. Typical properties of these catalysts
are listed in Table I.

TABLE I. Physical properties of the catalyst

Bulk form	Powder	Cylinder
Mean particle diameter, 10^{-4} m	2.5	-
Bulk dimensions, 10^{-3} m		
height	-	3.52
diameter	-	3.24
Carrier	γ -alumina	γ -alumina
Palladium content, %	0.5	0.5
Palladium dispersion, %	20	37
Total surface, m^2/kg	$5.9 \ 10^4$	$102 \ 10^5$
Particle apparent density kg/m^3	$2.44 \ 10^3$	$1.74 \ 10^3$
Particle porosity, %	35.2	53.7

In all our experiments, the selectivity of the reaction
was very good. The only by-product, fumaric acid, was
produced in very small amounts. High purity reactants were
used : 99% maleic acid (Fluka AG), 99.99% hydrogen and 99.8%
nitrogen (Air Liquide). Water used as solvent was distilled
in our laboratories. The only materials used in the experimental
apparatus were stainless steel, glass and PTFE in order to
avoid corrosion effects. Many metallic salts are indeed poisons
for the catalyst. Further details on the experimental operating
conditions and procedures are given elsewhere (6).

Intrinsic and particle scale apparent rate equations

The intrinsic reaction rate has been measured in a discon-
tinuous slurry stirred tank reactor and in a continuous micro-
trickle bed reactor (6). This last one is represented in Figure 1.
Both methods lead to rather similar expressions for the intrin-
sic rate equation r(mol/kg Pd. s)

$$r = 2.58 \times 10^{-1} \ \exp \ (\frac{39090}{R} \ \cdot \ (\frac{1}{300} - \frac{1}{T})) \cdot C_{AM}^{0.08} \cdot P_H^{0.6} \qquad (1)$$

The particle scale apparent reaction rate has been deter-
mined in a discontinuous Carberry type reactor and in a conti-
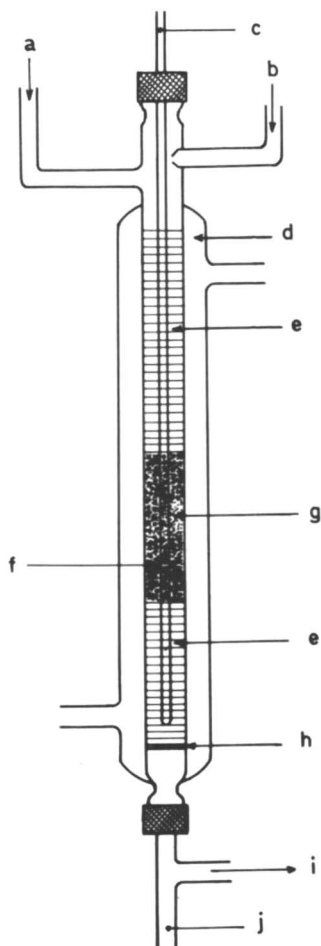nuous micro-trickle bed reactor in which catalyst particles

Figure 1. Microtrickle bed reactor. Key: a, gas inlet; b, liquid inlet; c, thermocouple; d, jacket; e, glass beads; f, catalyst; h, porous bed support; i, gas outlet; j, liquid outlet.

are diluted by inert glass beads (1.5×10^{-4} m diameter). Both techniques lead to similar results represented by the following equation :

$$r_a = 2.44 \times 10^{-2} \exp\left(\frac{24030}{R} \cdot \left(\frac{1}{300} - \frac{1}{T}\right)\right) \cdot C_{AM}^{0.06} \cdot P_{H}^{0.6} \qquad (2)$$

r_a is the particle scale apparent reaction rate (mole/kg Pd. s).

The main difference between parameter estimates based on continuous (micro-trickle bed reactor) and discontinuous (stirred tank reactor) experiments is the preexponential factor which is somewhat smaller for continuous operation. The parameter values reported in Eq. 1 and 2 correspond to continuous operations. This problem is analyzed elsewhere in more detail (6).

THE TRICKLE BED EXPERIMENTS

Experimental set-up

A simplified diagram of the experimental set-up is presented in Figures 2 and 3. The reactor consists in a jacketed glass column 0.45 m long and 4.10^{-2} m in diameter. Hydrogen and aqueous solutions of maleic acid are fed at the top of the reactor. The liquid is initially distributed by means of four small 1/16" pipes. An inert bed, realized with inert alumina pellets, ensured preheating, liquid saturation and an uniform distribution of both fluids. The reactor is provided with an axial thermocouple well. A sliding thermocouple can be moved along the bed axis allowing to measure the axial temperature profile and to check the isothermal operation of the reactor.

All experiments were done in preflooded beds. Throughout each run, liquid and gas flow rates, as well as temperature and liquid composition were kept constant. Liquid samples for analysis were collected at the inlet and outlet of the reactor. The range of operating conditions is given in Table II.

TABLE II. Range of operating conditions in trickle-bed experiments

Maleic acid concentration	20 to 220 mol/m³
Hydrogen partial pressure	1.4 bar
Liquid superficial velocity	0.064 to 2.0 kg/m².s
Gas superficial velocity	1.10^{-4} to 6.10^{-4} kg/m².s
Temperature	285 to 332 K

For all the runs, the conversion is very low (about 5 to 10%) so that the reactor may be considered as differential. Stationary
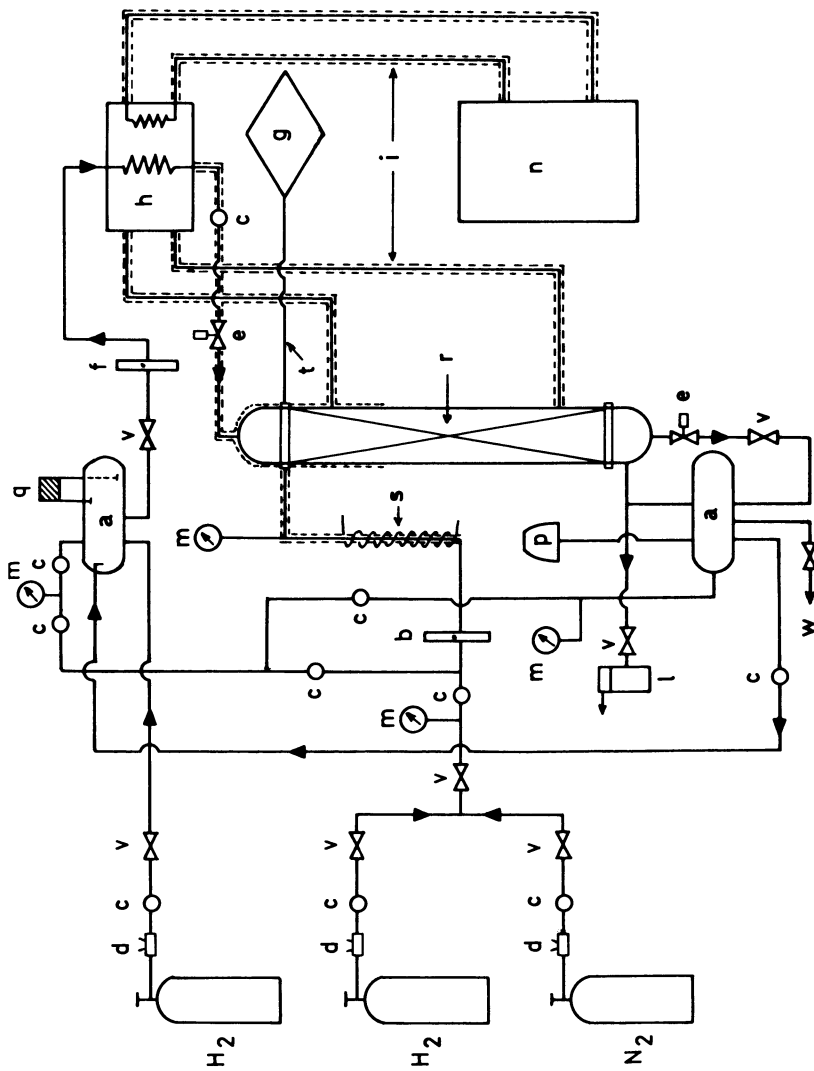
Figure 2. Experimental setup of trickle-bed reactor. Key: a, reactant vessel; b, gas rotameter; r, trickle-bed reactor; c, shut off valve; v, regulating valve; d, regulator; e, sample valve; m, pressure gauge; f, liquid rotameter; g, temperature recorder; h, thermostat; i, tubing insulation; l, gas outlet bubbler; q, level control; n, cryostat; p, vacuum pump; t, thermocouple; s, gas preheater; w, purge.
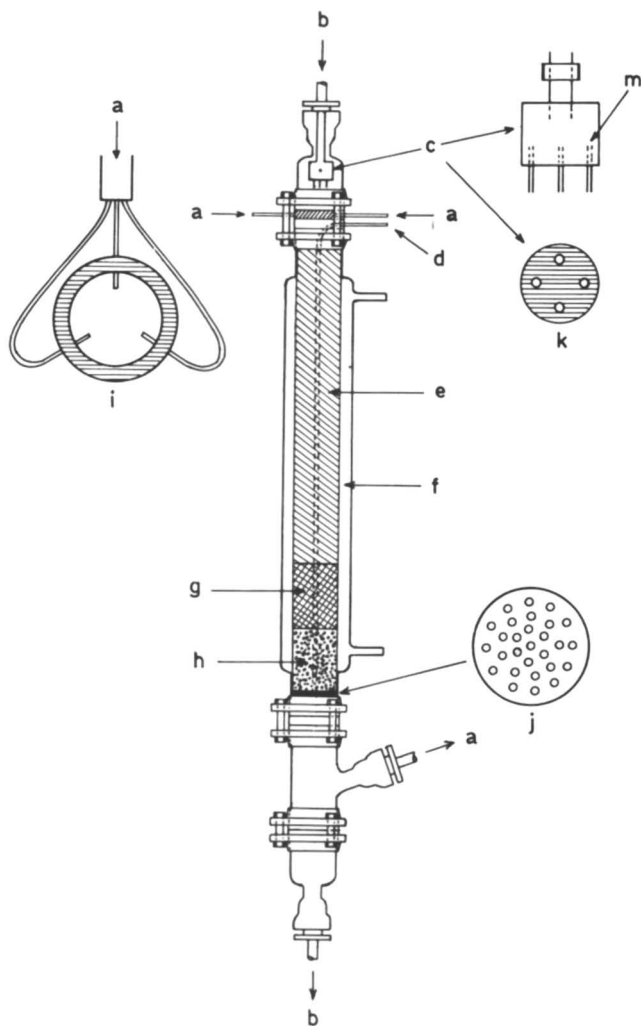
Figure 3.   Trickle-bed reactor. Key: A, gas; b, liquid; c, liquid
distributor; d, thermocouple; e, alumina particles; f, jacket;
g, catalyst; h, glass beads; i, gas distributor; j, packing
supporting plate; K; distributor plate.

state was reached after one hour. Reproductibility of experi-
ments was rather difficult to obtain due to variations in the
catalyst activity. An experimental scatter of about 20% has
been obtained. Most of the experiments were done in three
different beds. The data presented here are averaged values
of results obtained in these three beds. More details on expe-
rimental procedure are given elsewhere.(6).

Experimental results

      According to the experimental results the reactor perfor-
mances are not affected by the gas flow rate, suggesting the
absence of influence of this gas flow rate on the liquid-solid
interfacial area and the external mass transfer coefficient.
      The observed reaction rates are presented in Figure 4,
as a function of liquid flow rate and temperature, at the highest
concentration of maleic acid (220 moles/m^3). The temperature
varies between 284 and 328 K and the liquid flow rate between
0.05 and 2 kg/m^2.s. According to Figure 4, the reaction rate
increases first with the liquid velocity and then reaches a
maximum. When the liquid flow rate is increased above this
value, the reaction rate remains roughly constant or decreases
very slowly. The maximum of the reaction rate and its position,
increase with temperature.
      The reaction rates obtained in trickle-bed reactor are
smaller than those observed with the particle scale apparent
reaction rate experiments (see the preliminary kinetic study).
 The activation energy is rather low (13$\pm$4 kJ/mol), indicating
the existence of substantial pore diffusion and/or external
mass transfer limitations.
      The influence of the concentration of maleic acid has been
studied by varying the concentration between 20 and 200 mol/m^3
and keeping constant the temperature at 308 K. The results
are presented in Figure 5. This influence is important. It
should be explained by modifications of the fluid flow hydro-
dynamics. As pointed out above, the particle scale apparent
reaction rate is indeed nearly independent of the maleic acid
concentration.

T H E O R E T I C A L   S E C T I O N

DESCRIPTION OF THE GAS-LIQUID FLOW

The performance of a trickle-bed reactor may be markedly af-
fected by fluid flow hydrodynamics. That is the reason why an ac-
curate prediction or simulation of the performance of such
a reactor involves a detailed description of the fluid flow
hydrodynamics as well as of the various mass and/or heat trans-
port resistances between gas, liquid and solid.

	C_{AM} (mol/m^3)	Temp. (°C)	P_{H_2} (bar)	$G.10^{+4}$ (Kg/m^2.s)
+	215.4	55.0	1.4	4
o	215.4	35.0	1.4	4
●	215.4	12.5	1.4	4

Figure 4.   Bed scale apparent reaction rate against the
liquid   superficial   velocity   at   different   temperatures
($-$: model; +, o, ● : experiments).

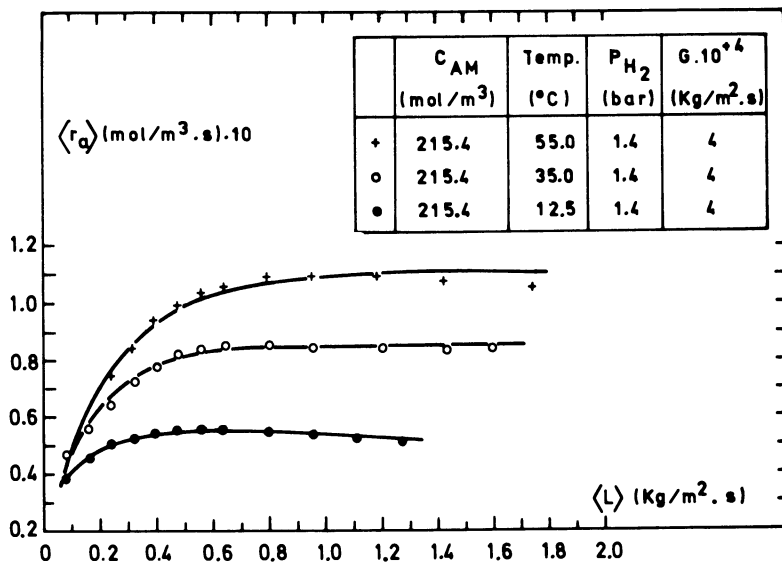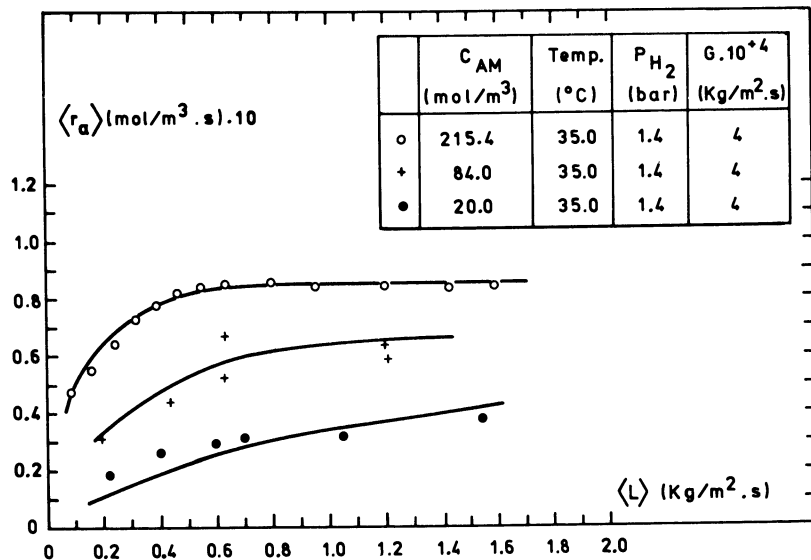|	C_{AM} (mol/m^3)	Temp. (°C)	P_{H_2} (bar)	$G.10^{+4}$ (Kg/m^2.s)
o	215.4	35.0	1.4	4
+	84.0	35.0	1.4	4
●	20.0	35.0	1.4	4

Figure 5.   Bed scale apparent reaction rate against the
liquid superficial velocity with different acid concentra-
tions ($-$: model; +, o, ● : experiments).

Actually, fluid flows through a packed bed may be analyzed at various levels, each one leading to completely different observations.   If one observes the bed as a whole (Figure 6) it seems reasonable to consider the medium as a continuum, owing to the small scale at which occur the elementary trans-port processess (e.g. the mass transfer between the trickling film and the catalyst particles).
In such a case, the mass balances may be described by equations of continuum media.   However, if one looks the bed closer e.g. at the particle scale as represented by the close-up of Figure 6, the representation of the flow process is comple-tely different. The liquid is distributed between different channels according to the local geometrical features of the packing. For example, the number of channels entering and leaving the cell represented in the close-up depends on these local geometrical features and varies randomly from point to point. The clustering of these channels generates various flow structures at the bed scale between which the liquid velocities are randomly distributed.

PERCOLATION MODEL OF THE FLUID FLOW

The flow process analyzed above is usually called a perco-lation process.   The main concepts of the percolation theory have been presented by Broadbent et al (7), Frish et al (8) and Kirkpatrick (9). For an exhaustive analysis of the theore-tical developments concerning percolation, the reader is refe-red to these reviews. The stochastic distribution of veloci-ties between the liquid flow structures has been derived else-where using the percolation concepts (10). The main features of this approach are recalled hereafter in order to clarify its application to the determination of the bed scale apparent reaction rate in trickle-bed reactors.

To analyze a percolation process, one can represent the scattering medium (i.e. the packed bed) by a lattice as depic-ted in Figure 7.   The sites of the lattice correspond to the contact points between the particles whereas the bonds cor-respond to the pores connecting two neighbour contact points. The walls of these pores are delimited by the external surface of the particles.   The percolation process is simulated by randomly distributing blocked and unblocked bonds within the lattice.   The clustering of the unblocked bonds generates the flow structures (11). The local liquid flow density is represented by a density of connection through the bonds. Let us assume this latter one takes the discrete values 1, 2, ...∞ , for the bonds belonging to the flow structures (irrigated zones) and 0 for the other ones (non irrigated zones).
The stochastic density distribution may be computed by maximi-zing the configurational entropy of the process investigated.
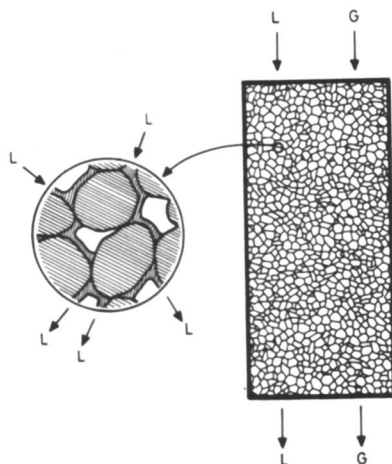
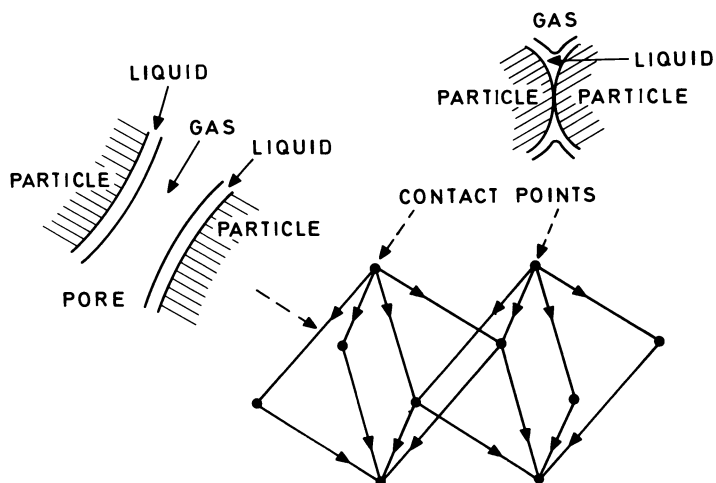Figure 6. Global and local observation levels of a packed bed. (13).

Figure 7. Lattice representation of a packed bed. (13).

Further details concerning this procedure are reported in
another paper (10). The solution is given by :

$$\alpha_i = \exp (a + bi) \qquad i = 0,1,2,\ldots, \qquad (3)$$

where

$$\exp a = \frac{1}{<i> + 1} \qquad (4)$$

and

$$\exp b = \frac{<i>}{<i> + 1} \qquad (5)$$

α_i represents the fraction of bonds with a density of connec-
tion equal to i. $<i>$ is the averaged value of i for the whole
lattice. The corresponding flow densities or liquid superfi-
cial velocities L_i are proportional to i, i.e. :

$$L_i = i\, L_m \qquad i = 0,1,2,\ldots, \qquad (6)$$

and

$$<L> = <i>\, L_m \qquad (7)$$

$<L>$ represents the bed scale averaged value of the liquid
velocity whereas L_m represents the minimum wetting velocity
in an isolated channel. This velocity corresponds to the
more stable flow configuration of this channel. It is conse-
quently closely related to the different sources of energe-
tical dissipation due to the creation of this channel (surface
energy, viscous drag,..). Actually, this parameter characte-
rizes the effective wettability of the packing, i.e., the
wettability under the actual operating conditions. This pro-
blem will be analyzed later in more detail.

DETERMINATION OF THE BED SCALE APPARENT REACTION RATE

In the preceeding section, we have shown how fluid flows
through a packed bed may be observed at various levels, leading
to completely different interpretations. Actually, when model-
ling any kinetic process, it is always necessary to consider
at least two observation levels in a trickle bed reactor :
the bed scale and the particle scale. The bed scale corres-
ponds to the whole bed or to a volume containing a large number
of particles. That is the level at which we want to derive
a model for the investigated process. However, this process
is generally ruled by gas-liquid-solid interactions occurring
at the particle scale.

The change of scale or volume averaging between those two
levels is ruled by the percolation process, i.e., by the velo-
city distribution defined by Eq.3. If ϕ is an extension quan-
tity, its bed scale averaged value $<\phi>$ is given by :

$$<\phi> = \sum_{i=o}^{\infty} \phi(L_i) . \alpha_i \qquad (8)$$

To describe the investigated process and to determine the
related quantity at the particle scale we have to adopt a
representation of the transport cell which is associated to

each bond in the lattice defined by the percolation process
(see Figure 7).   This cell is assumed to be exactly the same
at any position within the bed.   The randomnes of the process
is indeed accounted for by the percolation process.
    The following developments will be restricted to laminar
liquid flow with very low gas-liquid interactions; that is
the flow regime prevailing with the operating conditions adop-
ted in the experimental work.   Application of Eq.8, with some
simplifications, will be presented for the modelling of the
different processes controlling the apparent reaction rate
at the bed scale.

Particle scale modelling
========================
    The local transport cell is represented by a straight
pore with an inclination to the vertical characterized by
angle θ (see Figure 8).   The curvatures of gas-liquid and
liquid-solid interfaces are assumed to be negligible.   The
model also assumes that the laminar liquid flow is motivated
only by gravity.
    The apparent reaction rate r_a at the level of one pore
-i.e. of one particle-results from mass exchange between the
liquid flow and the porous structure of the catalyst particle
as depicted in the close-up of Figure 8.   The complexity of
the mass balance equations depends strongly on the number
of steps limiting the mass transfer processes as well as on
the complexity of the expression of r_a.   With the investigated
experimental system, the limiting reactant is hydrogen in
liquid phase. Maleic acid is indeed a non volatile substance
so that reaction occurs only on the irrigated zones of the
catalyst. Furthermore, the apparent reactional order for maleic
acid is very close to zero and the product $D_L.C_L$ - where D_L
represents the liquid molecular diffusivity and C_L the bulk
liquid concentration - is definitely smaller for hydrogen
than for maleic acid.   In such a condition, a single mass
balance equation has to be written for hydrogen as follows:

$$k_{LS}.a.f_w.(C_{H,L} - C_{H,S}) = r_a(C_{H,S}, T).(1 - \varepsilon).\rho_s \qquad (9)$$

$C_{H,L}$ and $C_{H,S}$ represent the dissolved hydrogen concentrations
at the gas-liquid (saturation) and liquid-solid interfaces,
respectively.   The analytical expression of t h e   p a r t i c l e
scale apparent reaction rate r_a as a function of $C_{H,S}$ has
been obtained and presented in the experimental section.
The unknown parameters are k_{LS} - the mass transfer coefficient
across the liquid film - and f_w - the local irrigation rate
i.e. the fraction of external solid surface covered by flowing
liquid.
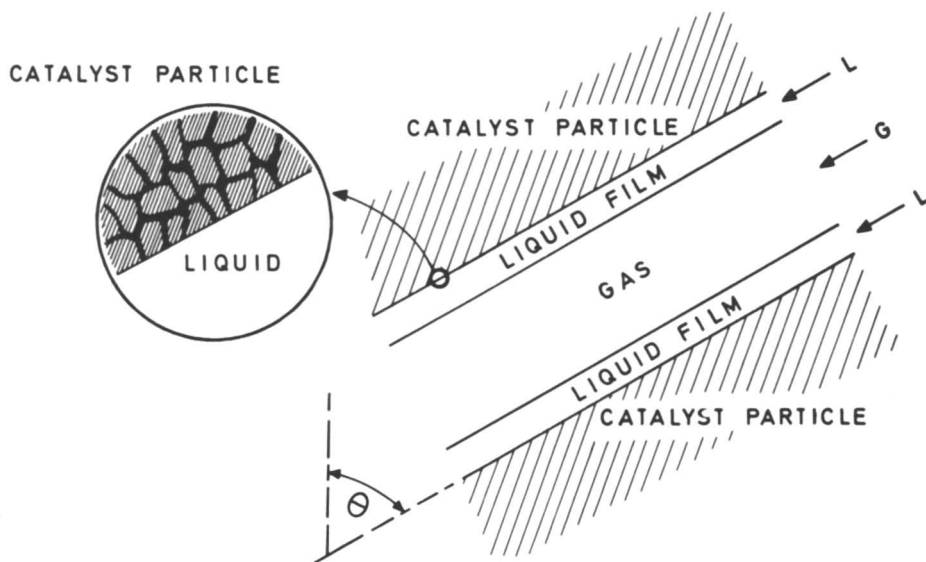
Figure 8. Modelling of gas-liquid flow in a local transport cell. (13).

These two quantities may be described on the basis of the pore flow model presented above.

f_w is assumed to equal unity when the pore is irrigated (no gas-solid interface) and zero in the absence of liquid.

$$f_w = 1 \quad \text{for } L_i \neq 0 \tag{10a}$$
$$ = 0 \quad \text{for } L_i = 0 \tag{10b}$$

k_{LS} may be determined assuming a fully developed laminar flow and adopting the assumptions of the stagnant film theory (3):

$$k_{LS} = D_L \cdot \left(\frac{\cos^2 \theta}{24}\right)^{1/3} \cdot a^{1/3} \cdot \left(\frac{\mu_L}{\rho_L^2 g}\right)^{1/3} \cdot Sc_L^{1/3} \cdot L_i^{-1/3} \tag{11}$$

The angle θ may be estimated assuming a random distribution of the local pore inclination (3).
This gives :
$$\cos \theta = \frac{2}{\pi} \tag{12}$$

Eqs. 9, 10, 11 and 12 allow to express, at the particle scale, r_a as a function of the bulk concentration $C_{H,L}$ (in equilibrium with P_H) and L_i.

Bed scale modelling

Using Eq. 8 and the implicit expression of r_a given by Eqs. 9,10, 11 and 12, it is theoretically possible to obtain a bed scale averaged value r_a.
However, this way would lead to a rather cumbersome numerical procedure involving the solution of the above mentionned equations for each specific value of L_i.
In order to keep the model in a more tractable form, we adopted the following simplifying assumption:an uniform liquid velocity $<L>$ is assumed in all the irrigated pores. $<L^*>$ may be determined as follows :
$$<L^*> = \frac{<L>}{<f_w>} \tag{13}$$

The brackets mean that bed scale averaged values are considered. $<f_w>$ is obtained by introducing Eqs. 10a and 10b into Eq. 8.
$$<f_w> = \sum_{i=1}^{\infty} \alpha_i = 1 - \alpha_0 \tag{14}$$

The value of α_0 is explicited by Eqs. 3 and 4.
Finally, one obtains :
$$<f_w> = \frac{<L>}{<L>+ L_m} \tag{15}$$

$\langle f_w \rangle$ is an increasing function of $\langle L \rangle$, reaching asymptotically unity for very large values of $\langle L \rangle$. Clearly $\langle f_w \rangle$ decreases when increasing L_m. The apparent log-slope of $\langle f_w \rangle$ versus $\langle L \rangle$ equals $1 - \langle f_w \rangle$. That means this slope ranges between 1 for a very small irrigation rate (linearity) and 0 for a nearly complete irrigation (asymptotic value).

The approximate averaged value $\langle k_{LS}^* \rangle$ is readily obtained replacing L_i by $\langle L \rangle$ in Eq.11.

$$\langle k_{LS} \rangle^* = D_L \cdot \left(\frac{\cos^2 \theta}{24}\right)^{1/3} \cdot a^{1/3} \cdot \left(\frac{\mu_L}{\rho_L^2 g}\right)^{-1/3} \cdot Sc_L^{1/3} \langle L \rangle^{*-1/3} \qquad (16)$$

The mass balance equation for the set of irrigated pores is then similar to Eq.9.

$$\langle k_{LS} \rangle^* a \, (C_{H,L} - C_{H,S}) = \langle r_a \rangle^* (1-\varepsilon) \cdot \rho_s \qquad (17)$$

Finally, the bed scale apparent reaction rate $\langle r_a \rangle$ in all the pores (irrigated and non irrigated) is given by :

$$\langle r_a \rangle = \langle f_w \rangle \langle r_a \rangle^* \qquad (18)$$

In the absence of external mass transfer limitation, $\langle r_a \rangle^*$ is independent of $\langle L \rangle$ so that $\langle r_a \rangle$ is proportional to $\langle f_w \rangle$. Consequently, the shapes of the curves $\langle r_a \rangle$ vs. $\langle L \rangle$ and $\langle f_w \rangle$ vs. $\langle L \rangle$ are identical. On the contrary, in the regime of external mass transfer limitation, $\langle r_a \rangle$ is proportional to $\langle f_w \rangle^{4/3} \cdot \langle L \rangle^{-1/3}$. That means that the apparent log-slope of $\langle r_a \rangle$ vs. $\langle L \rangle$ equals $1 - \frac{4}{3} \langle f_w \rangle$. Actually this slope ranges between 1 for a very small irrigation and -1/3 for a nearly complete irrigation. In practice, the curve is very flat near the maximum (for $\langle f_w \rangle = 0.75$ i.e. $\langle L \rangle = 3 L_m$) and the maximum region is very broad.

PHYSICAL MEANING OF THE PARAMETER L_m

As pointed out above, the minimum wetting velocity L_m corresponds the more stable flow configuration of an isolated rivulet i.e. the configuration realizing the minimum of energy dissipations. Consequently, this parameter must be a function of fluid properties characterizing the various sources of energy dissipation (μ_L, σ_L). Such dependences are obviously interesting in order to establish a reliable model for the design or the scale-up of trickle-bed reactors. A first attempt in this way, was proposed in a previous work (3). Two sources of energy dissipations were considered :
-     the viscous drag which corresponds to energy dissipations in the bulk of the liquid; it is a function of the liquid viscosity;

-     the surface energy which corresponds to the energy dissipated by the creation of the gas-liquid and liquid-solid

interfaces; it is related to the surface properties of the three phases.

Adopting the assumptions of the laminar pore flow model described above, it is possible to compute these two sources of dissipation and minimize the total dissipation. This leads to the following relation :

$$L_m = 1.51 \ (\frac{\mu_L \ \rho_L}{g})^{1/5} \ . \ a \ . \ E_s^{3/5} \qquad (19)$$

where E_s represents the surface energy per unit of solid area. E_s depends on the particle wettabilitiy (characterized by a contact angle or by an energy of adhesion between the solid and the liquid) but also on the dynamic surface tension i.e. the one prevailing under operation. This one is very sensitive to any heterogeneity in the film due e.g. to mass and/or heat transfers across the liquid film. That is the main reason why the hydrodynamics in a trickle-bed reactor may vary with the chemical system adopted and with the operating conditions. By fitting the model of the apparent reaction rate on the data reported in the experimental section, we will see how the parameter E_s (or L_m) varies with the operating conditions.

COMPARISON WITH EXPERIMENTS

In order to fit the proposed model of the bed scale apparent reaction rate on the experimental results, we considered two parameters. The first one is the surface energy E_s, as mentionned above. The second one is γ , a catalyst activity factor. This latter one accounts for variations in catalyst activity observed in micro trickle-bed (in which the particle scale apparent reaction rate was determined) and trickle-bed experiments (see the experimental section). The catalyst is indeed very sensitive to very small amounts of poisons and it is nearly impossible to adopt exactly the same experimental procedure and to obtain the same reactant purity in both installations. Actually, even in the same installation, activity fluctuations of about $\pm$ 20% were observed. Larger differences should be observed between the two different installations.

The results of the fitting are presented in Figures 4 and 5 in terms of the bed scale apparent reaction rate r_a against the liquid superficial velocity. L .

In Figure 4, we reproduced data obtained at three different temperatures and the same concentration of maleic acid (see the experimental section). Clearly the agreement between experiments and theory is quite satisfying.

The parameters estimates are given in Table III. The range of the activity factor γ corresponds to the activity fluctua-

tions of about 20% reported above. The mean value of this
parameter equals roughly 0.4. This value seems to be rather
logical in consideration with the remarks pointed out above.
The parameter E_s as well as L_m increase markedly with the
temperature. This dependence will be analyzed later on.

TABLE III. Estimated parameters corresponding to Figure 4

γ (-)	E_s (10^5 kg/s²)	L_m (kg/m²s)	Maleic acid conc. (mol/m³)	Temperature (K)
0.5	0.006	0.052	220	12.5
0.43	0.028	0.13	220	35.0
0.34	0.067	0.22	220	55.0

In Figure 5, we reproduced data obtained at a same temperature
and three different maleic acid concentrations. Once again,
the agreement between experiments and theory is satisfying.
The parameter estimates are given in Table IV. The range
of fluctuation of the activity parameter γ is nearly the same
as the one reported in Table III. It is worth noting that
the variations of trickle-bed performance with the acid concen-
tration cannot be explained by variations of the particle
scale apparent reaction rate. The reactional order is indeed
very small as pointed out in the experimental section. These
variations must consequently be explained in terms of hydro-
dynamics variations i.e. E_s or L_m variations. Table IV shows
clearly that these parameters increase markedly when decreasing
the acid concentration.

TABLE IV. Estimated parameters corresponding to Figure 5

(-)	E_s (10^5 kg/s²)	L_m (kg/m²s)	Maleic acid conc. (mol/m³)	Temperature (K)
0.43	0.028	0.13	220	308
0.37	0.125	0.31	80	308
0.50	1.67	1.51	20	308

The variations of E_s may be analyzed in terms of the physical meaning of this parameter. The surface energy is a function of the particle wettability. Actually, in the case of alumina porous particle in contact with aqueous solutions, this wettability is very good so that its contribution to E_s is very small. E_s is also a function of the dynamic surface tension and, consequently, of the composition heterogeneities within the liquid film. These heterogeneities increase when increasing the mass transfer through the film, e.g., by increasing the temperature. This may explain the temperature dependence of E_s. E_s is not only a function of the composition heterogeneities but also of the sensitivity of the surface tension with respect to these heterogeneities, e.g., the concentration gradients across the film. Usually, with aqueous solution of organic substances, this sensitivity – i.e. the derivative of the surface tension with respect to the concentration – increases when decreasing the concentration of organic substance (12). This may explain the concentration dependence of E_s. Obviously, these conclusions are essentially qualitative. Further experiments would be required in order to explain more quantitatively the variations of E_s. Nevertheless, the experiments and the theoretical model reported in this paper, show undoubtly that the operating conditions and the chemical system investigated may influence the catalyst irrigation rate and, in turn, all the hydrodynamic and transport processes occurring in a trickle-bed reactor.

The variations of the bed scale apparent reaction rate may be interpreted in terms of a contacting efficiency η_C and an external efficiency η_E (representing the external mass transfer limitaitons). η_C is given by

$$\eta_C = <f_w>\qquad\qquad(20)$$

and η_E by

$$\eta_E = \frac{<r_a(C_{H,S},T)>}{<r_a(C_{H,L},T)>}\qquad\qquad(21)$$

Obviously, the bed scale apparent reaction rate $<r_a>$ is proportional to the product $\eta_C \cdot \eta_E$. Typical variations of these quantities against the liquid superficial velocity $<L>$ are depicted in Figure 9. For the example reported in this figure ($L_m = 0.22$ kg/m^2.s i.e. $E_s = 6.7 \times 10^{-7}$ kg/s^2), the contacting efficiency η_C varies between 20% and 90% whereas the external efficiency η_E varies between 80% and 60%.

For the largest liquid velocities, η_C and η_E exhibit rather similar log-slope versus $<L>$, but of opposite sign, so that the product $\eta_C \cdot \eta_E$ and consequently $<r_a>$ are nearly independent of the liquid velocity. This explain the very broad maximum region observed in Figures 4 and 5.   Actually the shape of the curve $\eta_C \cdot \eta_E$ may be strongly modified by varia-
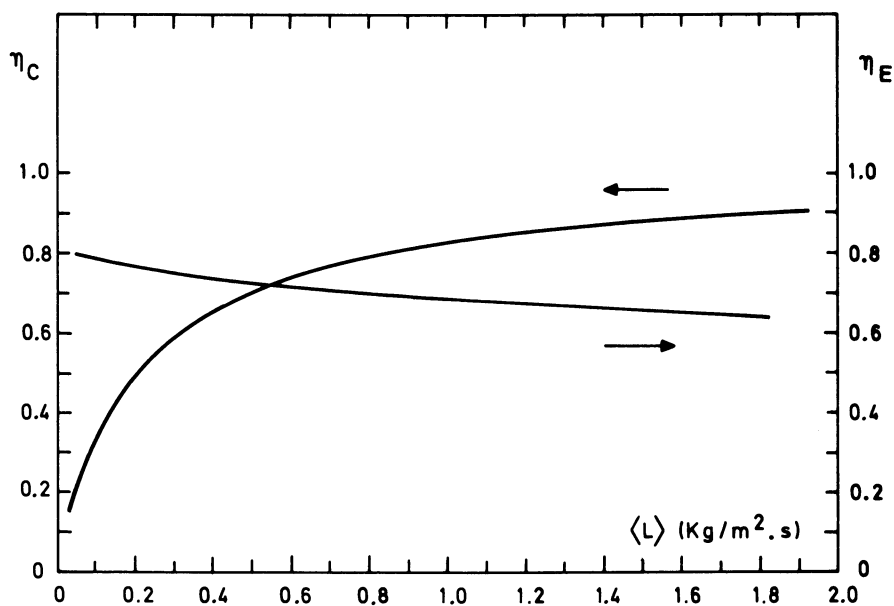
Figure 9. Typical variations of η_C et η_E versus the liquid superficial velocity (L_m = 0.22 kg/m^2 sec i.e. E_S = 6.7 x 10^{-7} kg/sec^2).

tions of the wetting parameter E_s and the transport properties
(i.e. k_{LS})

Legend of Symbols

a	specific geometric area of the packing (m^{-1})
a,b	parameters defined by Eqs 4 and 5 (-)
c_L	bulk liquid concentration (mol/m^3)
c_S^L	liquid concentration at the liquid-solid interface (mol/m^3)
D_L	liquid molecular diffusivity (m^2/s)
E_s	surface energy per unit of solid area (kg/s^2)
f_w	catalyst irrigation rate (-)
g	acceleration due to gravity (m/s^2)
i	local density of connection through one bond of the lattice (-)
k_{LS}	mass transfer coefficient across the liquid film (m/s)
L	volume averaged liquid superficial velocity $(kg/m^2.s)$
L_i	local liquid superficial velocity in one channel of the packing $(kg/m^2.s)$
L_m	minimum wetting velocity in an isolated channel $(kg/m^2.s)$
P_{H_2}	hydrogen partial pressure (bar)
r	intrinsic reaction rate (mol/kg Pd.s)
r_a	apparent reaction rate (mol/kg Pd.s)
R	universal gas constant (J/mol.K)
Sc_L	Schmidt number of the liquid phase (-)
T	temperature (K)

Greek letters

α_i	fraction of bonds with a density of connection equal to i (-)
ε	bed void fraction (-)
η_C	contacting efficiency (-)
η_E	external efficiency (-)
θ	mean inclination of pore to vertical (rad)
μ_L	liquid viscosity (kg/m.s)
ρ_L	liquid density (kg/m^3)
ρ_s	amount of catalyst per unit of reactor volume (kg/m^3)
ϕ	general transport on hydrodynamic quantity
γ	catalyst activity factor (-)

Subscripts

AM	variable related to maleic acid
H	variable related to hydrogen
i	variable defined in channel i
< >	averaged variable in set of channels

Superscript

| * | approximate averaged variable in set of irrigated channels |

Literature Cited

1. Germain, A., L'Homme, G. and Lefèbvre, A., in G. L'Homme (Ed), "Chemical Engineering of Gas-Liquid-Solid Catalyst Reactions", Ed. Cebedoc, Liège, 1979, Chap. 5, 134-171.
2. Shah, Y.T., Gas-Liquid-Solid Reactor Design, Mc Graw-Hill, New York, 1979, Chap. 4, 105-148.
3. Crine, M., Doctorat en Sciences Appliquées, Université de Liège, 1978.
4. Germain, A., Crine, M., Marchot, P. and L'Homme, G., "Chem. Reaction Eng. - Houston", Adv. in Chem. Ser. n° 65, 1978, 411.
5. Crine, M., Marchot, P. and L'Homme, G., Chem. Eng. Sci., 1980, 35, 51.
6. Ruiz, P., Doctorat en Sciences Appliquées, Université de Liège, 1982.
7. Broadbent, S.R. and Hammersley, J.M., Proc. Camb. Phil. Soc., 1957, 53, 629.
8. Frisch, H.L. and Hammersley, J.M., J. Soc. Ind. Appl. Math., 1973, 11, 894.
9. Kirkpatrick, S., Rev. Mod. Phys., 1973, 45, 574.
10. Crine, M. and Marchot, P., Entropie, 1981, 102, 28.
11. Crine, M. and Marchot, P., Entropie, 1981, 102, 37.
12. Meissner H.P. and Michaels A.S., Ind. Eng. Chem., 1949, 41, 2782.
13. Crine, M. and L'Homme, G. "Chem. Reaction Eng. -Boston", Adv. in Chem. Ser, n°196, 1982, 407

A Comparison of Current Models for Isothermal Trickle-Bed Reactors

Application to a Model Reaction System

P. L. MILLS

Corporate Research Laboratory, Monsanto Company, St. Louis, MO 63167

M. P. DUDUKOVIĆ

Chemical Reaction Engineering Laboratory, Washington University, St. Louis, MO 63130

Trickle-bed reactors are packed-beds of catalyst
which utilize cocurrent downflow of gas and liquid
reactants. This paper summarizes the various re-
action studies which have been performed to
support development of appropriate reactor models
for this reactor type, and gives a critical review
of these models. Prediction of the integral
trickle-bed reactor performance for a first-order,
gaseous reactant limiting reaction is attempted.
Conversion predicted by various models are com-
pared to experimental results obtained in a
laboratory-scale trickle-bed reactor using the
hydrogenation of α-methylstyrene in organic sol-
vents as a test reaction. It is shown that cer-
tain key items, such as i) extent of liquid-solid
wetting, ii) presence or absence of stagnant
versus actively flowing liquid films on the
catalyst surface, and iii) magnitude of mass
transport resistances, can all have a significant
effect on the predicted reactor behavior. The in-
ability of current correlations to predict mass
transfer coefficients is demonstrated.

Reactions between gases and liquids that are catalyzed by either
homogeneous organometallic complexes or heterogeneous catalysts
provide the basis for a significant portion of the products
manufactured in both chemical and petroleum processing. Reactor
types used to carry out these reactions include mechanically
agitated autoclaves, bubble columns, gas-lift reactors, packed-
bed reactors, or three-phase fluidized-bed reactors (1-3).
Heterogeneous catalyzed reactions are carried out using the
catalyst in a powdered form for slurry operation or a tableted
form for packed-bed operation (1). The problems associated
with filtration, regeneration, and recycle of spent powdered
catalysts, including the higher installed costs of slurry-type
reactor systems, to name a few (2), suggests that packed-bed

trickle-flow reactors offer several advantages over slurry
operation. However, the design and scale-up of trickle-bed
reactors is more difficult than slurry reactors which seems to
be a disadvantage (2). Accurate prediction of trickle-bed re-
actor performance requires reliable methods for estimation of
such items as intrinsic reaction kinetics, liquid-gas flow
distribution, liquid-solid contacting effectiveness, inter-
phase and intraphase heat and mass transfer, texture of liquid
films, and thermodynamic parameters. While methods for
measurement and interpretation of intrinsic reaction kinetics
for heterogeneous gas-liquid systems is fairly well understood
(1,4), little progress has been made toward solution of fun-
damental problems related to trickle-bed design and scale-up.
A consensus of opinion from recent symposia on multiphase
reactors (5) supports this conclusion.

Summary of Previous Reaction Studies and Models

The above issues associated with prediction of trickle-bed
reactor performance has motivated a number of researchers over
the past two decades to perform laboratory-scale studies using
a particular model-reaction system. These are listed in
Table I. Although a more detailed summary is given elsewhere
(29), a general conclusion seems to be that both incomplete
catalyst wetting and mass transfer limitations are significant
factors which affect trickle-bed reactor performance.
      Several forms of incomplete catalyst wetting were visually
observed and reported in previous studies. These observations
include: i) dry areas on a portion of the catalyst surface
with either stagnant liquid or actively flowing liquid present
on the remaining surface (7-10), ii) no dry area is present on
the catalyst surface, instead, the catalyst surface is covered
by a combination of stagnant liquid films and actively flowing
liquid (7,11-13), and iii) the entire catalyst surface and
internal catalyst pores may be completely dry as a result of
liquid reactant evaporation at reactor conditions (9,14-15)
Some of the remaining studies did not necessarily observe in-
complete catalyst wetting, but included this concept either
directly as an adjustable parameter in the model to fit the
observed conversion versus liquid mass velocity data,(7,9,13,
16-18),or indirectly via use of a correlation for liquid-solid
contacting established for non-porous absorber column packings
(11,19-20).
      Observed transport limitations in the studies given in
Table I depend upon the magnitude of the intrinsic reaction
rate. Petroleum hydrodesulfurization (19-21), certain types
of petroleum hydrogenations (22), or chemical decomposition
reactions (11) are liquid-limiting and proceed slowly enough
that only internal particle diffusion or combined pore diffusion
and liquid-to-solid resistances are controlling. Chemical

Table I.   Previous Reaction Studies in Trickle-Bed Reactors

Investigator	Reaction System
Hartman and Coughlin (7)	Oxidation of sulfur dioxide on activated carbon
Satterfield and Way (39)	Isomerization of cyclopropane to propylene on silica-alumina
Germain, Lefebvre and L'Homme (10)	Hydrogenation of α-methylstyrene to cumene in 0.5% and 1% Pd-on-alumina
Henry and Gilbert (21)	Petroleum hydrocracking, hydro-denitrogenation, hydrodesulfurization, and hydrogenation
Sedriks and Kenney (9)	Hydrogenation of crotonaldehyde on 0.5% Pd-on-alumina
Satterfield and Ozel (8)	Hydrogenation of benzene to cyclohexane on 2% Pt
Montagna and Shah (19)	Hydrodesulfurization of 36% and 53% reduced Kuwait crude
Goto and Smith (27)	Oxidation of formic acid on CuO – ZnO
Koros (11)	Hydrogen perioxide decomposition on activated carbon
Levec and Smith (28)	Oxidation of acetic acid on ferric oxide
Jawad (26)	Hydrogenation of α-methylstyrene to cumene on Pd catalyst
Hanika et al (25)	Hydrogenation of cyclohexene to cyclohexane using 3% Pd and 5% Pt-on-carbon catalysts
Enright and Chuang (40)	Deuterium exchange between hydrogen and water using 0.2% Pd-on-carbon
Hanika et al (15)	Hydrogenation of 1,5 cyclo-octadiene in cyclooctane using 38% Ni-on-kieselguhr
Morita and Smith (16)	Hydrogenation of α-methylstyrene to cumene using 0.5% and 2.5% Pd-on-alumina
Germain et al (12)	Hydrogenation of 2-butanone using Ru-on alumina
Mejstŕikova (24)	Hydrogenation of nitrobenzene on 1% Pd
Hanika et al (14)	Hydrogenation of cyclohexene to cyclo-hexene on 5% Pd-on-carbon
Somers, Shah, and Paraskos (22)	Hydrogenation of diolefins
Biskis and Smith (23)	Hydrogenation of α-methylstyrene to cumene on 0.5% Pd-on-alumina
Mata and Smith (13)	Oxidation of sulfur dioxide on activated carbon
Herskowitz, Carbonell and Smith (17)	Hydrogenation of α-methylstyrene to cumene using Pd-on-alumina
Turek and Lange (18)	Hydrogenation of α-methylstyrene to cumene using Pd-on-alumina
Montagna, Shah, and Paraskos (20)	Hydrodesulfurization of 22% and 36% reduced Kuwait crude

hydrogenations at low to moderate pressures (8-10,14-18, 23-26) or oxidations (7,13,27 28)   are usually gaseous reactant limiting and involve more active catalysts so that both internal and external transport processes or the latter ones only are controlling.

A summary of reactor models used by various authors to interpret trickle-bed reactor data mainly from liquid-limiting petroleum hydrodesulfurization reactions (19-21) is given in Table I of reference (37). These models are based upon: i) plug-flow of the liquid-phase, ii) the apparent rate of reaction is controlled by either internal diffusion or intrinsic kinetics, iii) the reactor operates isothermally, and iv) the intrinsic reaction rate is first-order with respect to the non-volatile liquid-limiting reactant. Model 4 in this table accounts for both incomplete external and internal catalyst wetting by introduction of the effectiveness factor η_{TB} developed especially for this situation (37).

A few reactor models have recently been proposed (30-31) for prediction of integral trickle-bed reactor performance when the gaseous reactant is limiting. Common features or assumptions include: i) gas-to-liquid and liquid-to-solid external mass transfer resistances are present, ii) internal particle diffusion resistance is present, iii) catalyst particles are completely externally and internally wetted, iv) gas solubility can be described by Henry's law, v) isothermal operation, vi) the axial-dispersion model can be used to describe deviations from plug-flow, and vii) the intrinsic reaction kinetics exhibit first-order behavior. A few others have used similar assumptions except were developed for non-linear kinetics (27-28). Only in a couple of instances (7,13, 29) was incomplete external catalyst wetting accounted for. Crine and co-workers (32-33) have developed a trickle-bed reactor model based upon percolation theory which more closely approximates the physiochemical processes on a particle and reactor-scale than previous models. Details which explain the model development have not been given by these authors so it has not gained wide applicability.

Objectives

The above discussion on previous experimental studies in trickle-bed reactors suggests that both liquid-solid contacting and mass transfer limitations play a role in affecting trickle-bed reactor performance. Except for a few isolated cases, the reactor models proposed in the literature for gaseous reactant limiting reactions have not incorporated particle-scale incomplete contacting as part of their development. For cases where it was used, this parameter served as an adjustable constant to match the observed conversion versus liquid mass velocity data so that the true predictive ability of the model

was not really tested. Additionally, it has not been clearly
established whether or not mass transfer coefficients deter-
mined from dissolution or gas absorption experiments under
non-reacting conditions give reliable values for porous
catalysts under reaction conditions. Some related questions
such as whether inactively wetted pellet surfaces under iso-
thermal conditions are covered by a thin,stagnant,liquid film
versus being completely dry in direct contact with the gas
(17) also have not been answered.

The present investigation has the overall objective of
testing the predictive ability for a trickle-bed reactor model
in which the gaseous reactant is limiting. First, a model is
presented which contains particle-scale incomplete contacting
as one of the key parameters. Second, model predictions for
various limiting cases are compared to experimental results
obtained in a laboratory scale trickle-bed reactor using
independently measured model parameters and available literature
mass transfer correlations.

Trickle-Bed Reactor Model for Gas Limiting Reactions

For purposes of developing a model for trickle-beds that
correspond to the test reaction given later, a single,
irreversible heterogeneous catalyzed reaction of the following
form is assumed to occur:

$$A(g) + bB(\ell) \rightarrow xX(\ell) \tag{1}$$

The mass balances which are given below assume that
i) liquid reactants are nonvolatile, ii) gas and liquid are
in cocurrent flow, iii) deviations of the gas and liquid flow
pattern from plug-flow are negligible, iv) solubility of the
gaseous reactant in the liquid can be described by Henry's law,
v) external mass transport and intraparticle diffusion effects
may be present, vi) the catalyst surface contains a fraction
η_{CE} which is contacted by actively flowing liquid, while the
remaining fraction $1 - \eta_{CE}$ is covered either by a stagnant
liquid or is in direct contact with the gas, vii) external con-
tacting efficiency η_{CE}, gas and liquid holdups, and gas and
liquid flow rates are constant over the active catalyst bed. A
key point to be emphasized here is that the catalyst surface is
assumed to contain both actively wetted and inactively wetted
(or dry) regions which are subject to finite mass transfer
resistances having unequal values. Besides this, a constant
gas-phase concentration of the gaseous (limiting) reactant is
assumed since this was implemented experimentally. Based upon
these assumptions, the following dimensionless mass balance
equations are obtained:

$$-\frac{du_{A\ell}}{d\xi} + St_{g\ell,A}\,(u_{Ag}-u_{A\ell}) - St_{\ell-aws,A}\,(u_{A\ell}-u_{A\ell,aws}) = 0 \quad (2)$$

$$-\frac{du_{B\ell}}{d\xi} - \eta_{CE}\,\eta\,r\,Da_o\,u_{A\ell,iws} - (1 - \eta_{CE})\cdot$$

$$\eta\,r\,Da_o\,u_{A\ell,iws} = 0 \quad (3)$$

$$St_{\ell-aws,A}\,(u_{A\ell}-u_{A\ell,aws}) = \eta_{CE}\,\eta\,Da_o u_{A\ell,aws} \quad (4)$$

$$St_{g-iws,A}\,(u_{Ag}-u_{A\ell,iws}) = (1 - \eta_{CE})\,\eta\,Da_o u_{A\ell,iws} \quad (5)$$

The boundary conditions at the reactor inlet $\xi = 0$ are:

$$\xi = 0 \cdot \begin{cases} u_{A\ell} = u_{A\ell,i} & (6a) \\[2ex] u_{B\ell} = u_{B\ell,i} = 1 & (6b) \end{cases}$$

Setting $u_{A\ell,i} = 0$ corresponds to a liquid feed which is innocent of dissolved gaseous reactant, while setting $u_{A\ell,i} = 1$ corresponds to a liquid feed which exists in equilibrium with the gas at the feed temperature, pressure, and composition. Definitions for the dimensionless variables which appear in Equations 2 - 6 are given in the nomenclature.

The solution of Equations 2 - 6 gives the following expressions for the dimensionless dissolved gas concentration $u_{A\ell}$ and liquid reactant conversion X_B as a function of the dimensionless axial coordinate ξ and model parameters:

$$u_{A\ell}(\xi) = \frac{1 - (1-\lambda\,u_{A\ell,i})\,\exp\,(-St_{g\ell,A}\,\lambda\,\xi)}{\lambda} \quad (7)$$

$$X_B(\xi) = \frac{b\,C^*_{A\ell,i}}{C_{B\ell,i}}\,Da_o \left\{ (1-\eta_{CE})\,\frac{\xi}{\dfrac{1}{\eta} + \dfrac{\Lambda^2}{\tilde{Bi}_d}} + \right.$$

$$\left. \frac{\eta_{CE}}{\lambda\,(\dfrac{1}{\eta} + \dfrac{\Lambda^2}{\tilde{Bi}_w})} \left[\frac{u_{A\ell,i}\,\lambda - 1}{St_{g\ell,A}\,\lambda}(1-e^{-St_{g\ell,A}\,\lambda\,\xi}) + \xi \right] \right\} \quad (8)$$

The parameter λ contains the Damkoehler number, Da_o, the Stanton number for gas-to-liquid transfer, $St_{g\ell,A}$, the external contact-

ing efficiency, η_{CE}, the effectiveness factor for a totally
wetted pellet, η, Aris' modified modulus, Λ, and Biot number
for actively flowing liquid-to-solid mass transfer, $\tilde{Bi}_w$. It is
given by

$$\lambda = 1 + \frac{Da_o}{St_{g\ell,A}} \frac{\eta_{CE}}{\frac{1}{\eta} + \frac{\Lambda^2}{\tilde{Bi}_w}} \tag{9}$$

An additional parameter which appears in the above expression
for $X_B(\xi)$ is the Biot number for stagnant liquid-to-solid mass
transfer, Bi_d.

Since dissolved gas concentrations in the liquid phase are
more difficult to measure experimentally than the liquid re-
actant concentration, Equation 8 evaluated at the reactor
exit $\xi = 1$ represents the key equation for practical appli-
cations involving this model. Nevertheless, the resulting
expression still contains a significant number of parameters,
most of which cannot be calculated from first principles. This
gives the model a complex form and makes it difficult to use
with certainty for predictive purposes. Reaction rate para-
meters can be determined in a slurry and basket-type reactor
with completely wetted catalyst particles of the same kind that
are used in trickle flow operation so that Da_o, η, and Λ^2 can be
calculated for trickle-bed operation. This leaves four para-
meters (η_{CE}, $St_{g\ell}$, $\tilde{Bi}_w$, $\tilde{Bi}_d$) to be determined from the available
contacting efficiency and mass transfer correlations. It was
shown that the model in this form does not have good predictive
ability (29,34).

A simpler model form can be obtained if the dissolved
gaseous reactant concentration in the bulk liquid is assumed
to be constant. Setting $du_{A\ell}/d\xi = 0$ in Equation 2 leads to
the following expression for the conversion of liquid reactant
B at the reactor exit, where $\xi = 1$:

$$X_{B,e} = \frac{b\, C^*_{A\ell,i}}{C_{B\ell,i}} Da_o \left(\eta_{CE} \frac{1}{\frac{1}{\eta} + \frac{\Lambda^2}{\tilde{Bi}_{wo}}} + (1-\eta_{CE}) \frac{1}{\frac{1}{\eta} + \frac{\Lambda^2}{\tilde{Bi}_d}} \right) \tag{10}$$

The Biot number $\tilde{Bi}_{wo}$ in this case is defined as $(V_p/S_{ex})k_s/D_e$
where $1/k_s$ represents an overall mass transfer resistance which
consists of the liquid side gas-to-liquid and liquid-to-solid
mass transfer resistances in series as given below:

$$\frac{1}{k_s a_{\ell s}} = \frac{1}{k_{g\ell} a_{g\ell}} + \frac{1}{k_{\ell s} a_{\ell-aws}}$$ (11)

The term $a_{\ell-aws}$ represents the ratio of the actively wetted external catalyst area per unit volume of reactor, while $a_{g\ell}$ represents the gas-to-liquid mass transfer interfacial area per unit volume of reactor.

If one has intrinsic and apparent reaction kinetics available, then Equation 10 may be viewed as a three-parameter model (η_{CE}, $\widetilde{Bi}_{wo}$, Bi_d) for prediction of isothermal trickle-bed reactor performance. However, Bi_{wo} depends on two mass transfer coefficients and a priori model parameter evaluation is no simpler than before.

A number of limiting cases can now be considered. If catalyst particles are assumed to be completely wetted by actively flowing liquid, then $\eta_{CE} = 1$ so that one obtains a single parameter model where $\widetilde{Bi}_{wo}$ is the only parameter:

$$X_{B,e} = \frac{b\, C^*_{A\ell,i}}{C_{B\ell,i}} Da_o \frac{1}{\dfrac{1}{\eta} + \dfrac{\Lambda^2}{\widetilde{Bi}_{wo}}}$$ (12)

If external mass transfer resistances are dominant ($1/\eta \ll \Lambda^2/\widetilde{Bi}_{wo}$):

$$X_{B,e} = \frac{b\, C^*_{A\ell,i}}{C_{B\ell,i}} St_{g\ell s}$$ (13)

The limiting step may be either gas-liquid mass transfer:

$$X_{B,e} = \frac{b\, C^*_{A\ell,i}}{C_{B\ell,i}} St_{g\ell,A}$$ (13a)

or liquid-solid mass transfer:

$$X_{B,e} = \frac{b\, C^*_{A\ell,i}}{C_{B\ell,i}} St_{\ell s}$$ (13b)

At the other extreme, one can assume that external mass transfer resistances are negligible ($1/\eta \gg \Lambda^2/\widetilde{Bi}_{wo}$) and that trickle-bed performance can be predicted based on basket reactor studies:

$$X_{B,e} = \frac{b\ C^*_{A\ell,i}}{C_{B\ell,i}}\ \eta\ Da_o \tag{14}$$

All of these models given by Equations 13-14 are single para-meter models and are limiting cases of Equation 12.

A two-parameter model is obtained if wetting is incomplete ($\eta_{CE} < 1$), but the inactively wetted surface is assumed to have negligible mass transfer resistance ($Bi_d \to \infty$). This latter condition was used by Mata and Smith ($\underline{13}$) and physically corresponds to the inactively wetted area being dry, or to the presence of stagnant liquid film which is at equilibrium with the gaseous reactant. The expression for the conversion given by Equation 10 reduces to:

$$X_{B,e} = \frac{b\ C^*_{A\ell}}{C_{B\ell,i}}\ Da_o \left[\eta_{CE}\ \frac{1}{\dfrac{1}{\eta} + \dfrac{\Lambda^2}{\widetilde{Bi}_{wo}}} + \eta\ (1-\eta_{CE}) \right] \tag{15}$$

Equations 10 - 15 are used in a later section to predict the performance of an isothermal trickle-bed reactor using measured values of all the model parameters except the mass transfer coefficients (and hence Biot numbers). The correlations of Goto and Smith ($\underline{35}$) and Turek and Lange ($\underline{18}$) were used to obtain values of $k_{g\ell}a_{g\ell}$, while the correlation of Dwivedi and Upadhyay ($\underline{36}$) was used to obtain values of $k_{\ell s}$. For ease of reference, these are given below as Equations 16-18:

$$\frac{k_{g\ell}a_{g\ell}}{D_m} = \alpha_L\ \left(\frac{G_\ell}{\mu_\ell}\right)^{n_L}\ Sc_\ell^{1/2} \quad \text{(Goto and Smith ($\underline{35}$))} \tag{16}$$

$$\frac{k_{g\ell}a_{g\ell}}{D_m} = 16.8\ Ga_\ell^{-0.22}\ Re_\ell^{1/4}\ Sc_\ell^{1/2} \quad \text{(Turek and Lange ($\underline{18}$))} \tag{17}$$

$$\varepsilon_B J_D = \begin{cases} 1.1068\ Re_\ell'^{-0.72} & , \quad Re_\ell' < 10 \\[2mm] 0.4548\ Re_\ell'^{-0.4069} & , \quad Re_\ell' > 10 \end{cases} \tag{18}$$

$$\text{(Dwivedi and Upadhyay ($\underline{36}$))}$$

It is worth noting that the correlation of Goto and Smith, Equation 16, was developed for oxygen gas-liquid mass

transfer in water, while the Turek and Lange correlation,
Equation 17 , was developed for hydrogen gas-liquid mass
transfer in α-methylstyrene-cumene liquid mixtures. A com-
parison between their respective predictions is available (18).
For the Goto and Smith correlation, values of α_L and n_L were
chosen to be 7.8 and 0.39 corresponding to their 0.0541
cm CuO·ZnO catalyst particles.

Application of Model to Prediction of Reactor Performance

The lumped parameter model given in the preceding section can be
applied to predict trickle-bed reactor performance for a system
which is gaseous reactant limiting and exhibits first-order
behavior. When used directly to predict conversion without
further simplification, the model requires an a-priori knowledge
of the intrinsic rate constant, k_v, the catalyst effectiveness
factor for a totally wetted pellet, η, gas solubility in the
liquid, $C_{A\ell}^*$, external liquid-solid contacting efficiency, η_{CE},
mass transfer coefficients k_s and $k_{g\ell s}$, liquid superficial
velocity, $u_{s\ell}$, and various catalyst and reactor bed character-
istics. Previous trickle-bed reactor studies quoted earlier
in Table I cannot provide a rigorous test of the model since
some key model parameters such as external contacting efficiency
η_{CE} or the intrinsic rate constant k_v were not determined in
independent experiments,but used as parameters to match the
experimental conversion versus liquid flow-rate data. In the
recent study of El-Hisnawi (29), however, most of the key para-
meters listed above which are needed to test the model pre-
dictions were measured via independent experiments. These have
been described (34) so that the details have been omitted here
for brevity. A brief description is given below.
     The first portion of El-Hisnawi's study (29) consisted of
determining both the intrinsic and apparent reaction kinetics
for the hydrogenation of α-methylstyrene to cumene using
cyclohexane, hexane, toluene, and 2-propanol as reaction
solvents in slurry and basket reactor runs. Measurements were
performed using both 0.5% and 2.5% Pd-on-alumina catalysts
specially prepared by Engelhard as 0.13 cm x 0.56 cm extrudates.
Both the intrinsic and apparent kinetics exhibited zero-order
dependence with respect to α-methylstyrene and first-order
dependence with respect to hydrogen over the temperature range
from 15°C to 30°C. Effectiveness factors for 0.5% Pd catalyst
were between 0.05 - 0.083 when cyclohexane was used as the
solvent, while values between 0.172 - 0.212 were obtained when
hexane was used as the solvent.
     The second portion of El-Hisnawi's study consisted of
evaluating liquid-solid contacting efficiency and liquid holdup
using impulse response tracer experiments. Experiments were
performed using the same catalyst packing and solvents employed

in the kinetic study to examine the effect of liquid physical properties. The contacting efficiency was evaluated from the square-root of the ratios of effective diffusivities in two-phase flow to those obtained in single-phase liquid flow using the variance of their impulse responses following the work of Baldi (38):

$$\eta_{CE} = \sqrt{\frac{(D_{eo})_{app}}{(D_{eo})_{\ell f}}} \qquad (19)$$

A more detailed explanation about the use of tracer methods to evaluate contacting efficiency, the relationships needed to interpret tracer response data, the experimental methodology, and various results are given by Mills and Dudukovic (41). It suffices to say here that the following correlations based upon Reynolds and Galileo numbers were determined by El-Hisnawi to represent the available data on small porous packings in the trickle-flow regime:

$$\eta_{CE} = 1.617 \; Re_{\ell}^{0.146} \; Ga_{\ell}^{-0.0711} \qquad (20)$$

$$\omega_D = 2.021 \; Re_{\ell}^{0.344} \; Ga_{\ell}^{-0.197} \qquad (21)$$

Equations (20) and (21) match the available data with an average error better than 7% and are valid within the following ranges of parameters: $0.161 \leq Re_{\ell} \leq 31.9$, $18.5 \leq \sigma_{\ell}$ (dynes/cm) ≤ 73.0, $0.656 \leq \rho_{\ell}$ (grs/cc) ≤ 1.0, $0.316 \leq \mu_{\ell}$ (cp) ≤ 2.18, $0.0718 \leq d_p$ (cm) $= 6 \; V_p/S_{ex} \leq 0.408$, and $1.06 \times 10^4 \leq Ga_{\ell} \leq 7.23 \times 10^5$.

The final portion of El-Hisnawi's study consisted of performing the α-methylstyrene hydrogenation under isothermal conditions using either cyclohexane or hexane solvent in trickle-flow. The liquid phase was saturated with the gaseous reactant (hydrogen) before being admitted to the reactor, thereby representing a so-called "equilibrium" feed. Pure hydrogen was used as the gas phase and maintained at a sufficiently high flow rate that further increases did not affect the measured α-methylstyrene conversion. This conversion was obtained as a function of liquid superficial velocity for both the 0.5% Pd and 2.5% Pd catalyst.

Table II gives an example of the fixed parameters used in calculating the model-predicted values of conversion for the α-methylstyrene-hexane solvent system and 0.5% Pd catalyst. These, along with the experimental conversion versus liquid superficial velocity data, were input to a computer program for data reduction. Similar data files were developed for each series of experiments and reduced in a similar fashion.

Table II. Summary of Fixed Parameters Used in Calculating
           the Model-Predicted Values of Conversion for a
                            Typical Run

SERIES	: TBR45 – TBR54	
SOLVENT	: HEXANE	
PALLADIUM CONTENT	: 0.5%	
PARTICLE DIAMETER	: 0.1748	cm
EQUIVALENT SPHERICAL DIAMETER	: 0.2857	cm
PARTICLE VOLUME/EXTERNAL SURFACE AREA	: 0.0291	cm
CATALYST SHELL VOLUME/EXTERNAL SURFACE AREA	: 0.00482	cm
PARTICLE POROSITY	: 0.5990	
PARTICLE DENSITY	: 1.1890	g/cm^3
BED POROSITY	: 0.4330	
ACTIVE CATALYST BED DEPTH	: 22.225	cm
LIQUID VISCOSITY	: 0.309	cp
LIQUID DENSITY	: 0.659	g/cm^3
SOLUTE MOLECULAR DIFFUSIVITY	: 0.132E-03	cm^2/s
SOLUTE SOLUBILITY	: 0.596E-05	mol/cm^3
EFFECTIVENESS FACTOR	: 0.194E+00	mol/cm^3
INTRINSIC RATE CONSTANT	: 7.4900	s^{-1}
INLET ALPHAMETHYLSTYRENE CONCENTRATION	: 0.132E-02	mol/cm^3
SOLUTE EFFECTIVE DIFFUSIVITY	: 0.397E-04	cm^2/s
EXTERNAL STATIC HOLDUP	: 0.0204	
LIQUID-SOLID CONTACTING CORRELATION CONSTANTS (1)	: 0.865, 0.232	
ENHANCEMENT FACTOR (LIQUID-SOLID)	: 1.00	
ENHANCEMENT FACTOR (GAS-LIQUID)	: 1.00	
AVERAGE HYDROGEN PRESSURE IN REACTOR	: 1.023	atm

Note 1: $\eta_{CE} = 0.865 \ (10 \ G_\ell)^{0.232}$

Results and Discussion

Comparisons between various model predictions and experimental values of α-methylstyrene conversion as a function of liquid space time are given in Figure 1 for 2.5% Pd-on-alumina catalyst. Predicted results for hexane solvent are shown by solid lines, while those for cyclohexane solvent are denoted by dashed lines. The case of negligible external calculated mass transfer limitations corresponds to the basket reactor and results in lines 1 calculated from Equation 14 which greatly overpredicts the conversion. This result may be viewed as an upper bound on the trickle-bed reactor conversion so that the comparison to actual experimental conversion indicates the relative degree of mass transfer limitations. The assumption of complete contacting (η_{CE} = 1) and estimation of mass transfer coefficients for Equation 12 from available correlations (16-18) results in the conclusion that the process should be entirely gas-liquid mass transfer controlled. Thus, there is no detectable difference between predictions of Equation 12, based on estimated mass transfer coefficients from Equations 16-18, and Equation 13a, which assumes gas-liquid mass transfer control. This is so because gas-liquid resistance is predicted to be dominant. This underpredicts conversion severely as shown by lines 2 in Figure 1. The case of complete contacting (η_{CE} = 1) with liquid-solid resistance controlling, given by Equation 13b, underpredicts the conversion also but less severely than the previous case as shown by lines 3. Again, kinetic resistance is negligible compared to the liquid-solid resistance.
   The case of incomplete contacting with finite gas-liquid-solid resistance on the actively wetted surface but negligible mass transfer resistance on the inactively wetted surface ($\widetilde{Bi}_d \rightarrow \infty$) is given by Equation 15 and lines 4 in Figure 1. This equation underpredicts the conversion for $L/u_{s\ell}$ < 240 seconds, but overpredicts the conversion for greater values. Since increasing $L/u_{s\ell}$ corresponds to decreasing liquid-solid contacting for both solvents (c.f., Figure 2), overprediction of conversion suggests that the inactively wetted surface must indeed be covered with a liquid film, and that a finite mass transfer resistance must be present. Underpredictions of conversion at small $L/u_{s\ell}$ corresponding to high liquid mass velocity where external contacting is nearly complete suggests that the available correlations for prediction of mass transfer coefficients in trickle-beds are inadequate. The recent study of Turek and Lange (18) showed that mass transfer coefficients in trickle-beds are enhanced by the presence of reaction which is also supported by the results obtained in this study.
   Since the available correlations for prediction of mass transfer coefficients in trickle-beds do not lead to accurate
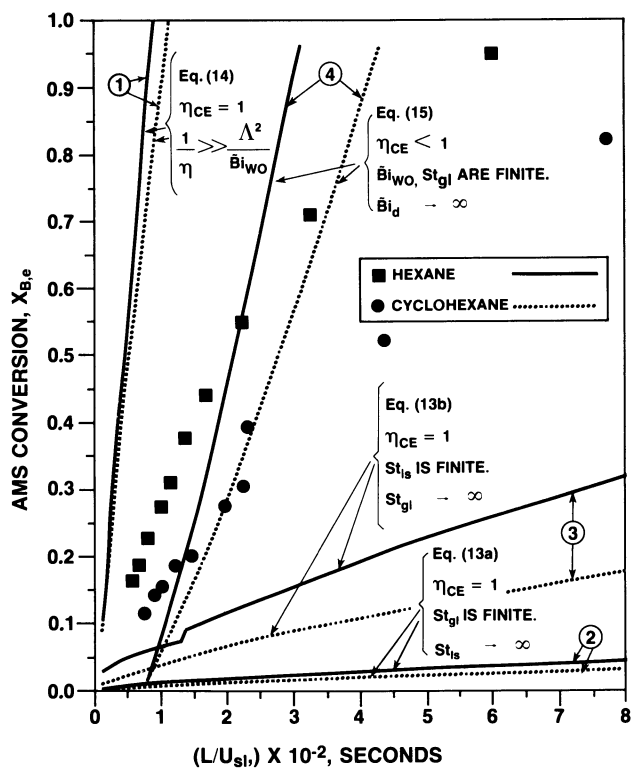
Figure 1. Comparison between experimental and model-
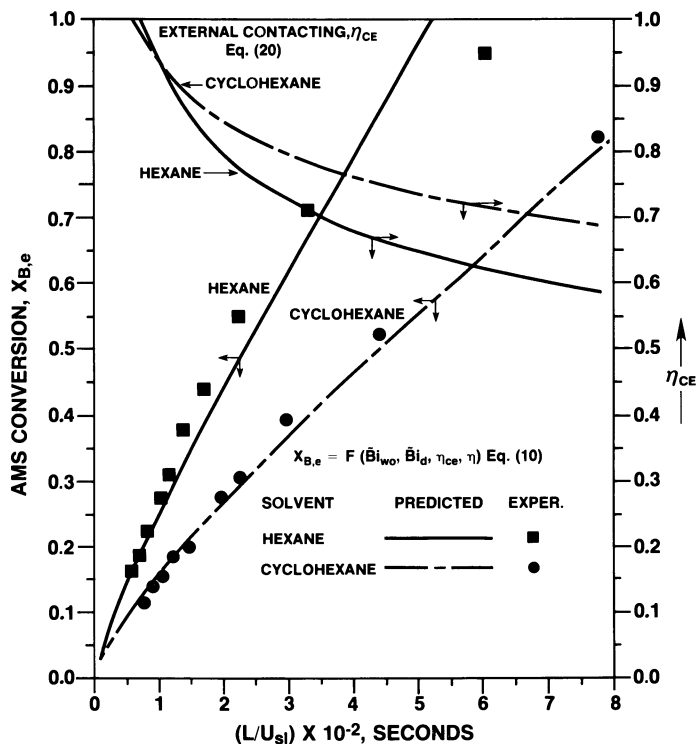predicted conversion based on available correlations.

Figure 2. Comparison between experimental and model-predicted conversions for 2.5% Pd catalyst using the modified mass transfer coefficient correlations.

model predictions, these correlations were modified in an attempt to fit the data. The strategy adopted here was to use trickle-bed data obtained in both hexane and cyclohexane solvents for the most active catalyst (2.5% Pd-on-alumina) to estimate parameters in assumed correlating equations for k_s and $k_{g\ell s}$. Next, the predictive ability of these correlations was tested using trickle-bed data obtained for the same two solvents but on the less active 0.5% Pd catalyst for comparison. The particular correlating equations for k_s and $k_{g\ell s}$ used in this work are given below:

$$\frac{k_s D_p}{D_m} = 9.72 \ Re_{\ell}'^{0.274} \ Sc_{\ell}^{0.395} \tag{22}$$

$$\frac{k_{g\ell s} D_p}{D_m} = 2850 \ H_{es} \tag{23}$$

The form of Equation 22 for the overall gas-liquid-actively wetted coefficient k_s is consistent with the expected Reynolds and Schmidt number dependence for flowing gases and liquid films in packed beds (12). Equation 23 for the stagnant liquid-to-solid coefficient $k_{g\ell s}$ may be viewed as some measure of the ratio of diffusivity to mean film thickness $(D_m/H_{es}/D_p)$.

The parameters in the correlations were obtained using nonlinear parameter estimation software and by minimizing the sum of the relative errors between experimental and predicted conversions for the 2.5% Pd catalyst. A comparison between predicted and experimental values of conversion for both solvents is given in Figure 2. The agreement between the two is seen to be satisfactory except for hexane at the highest conversion where deviations of the liquid-phase from plug flow may influence the result.

Figure 3 shows the results obtained when the above correlations developed using the more active 2.5% Pd catalyst are applied to data obtained on the less active 0.5% Pd catalyst. It can be seen that the agreement between the model predictions and experimental values is of lesser quality than the previous case. The deviations are especially noticeable with increasing $L/u_{s\ell}$ or decreasing external contacting efficiency since the predicted lines cross each other at an intermediate value which is opposite to the data. On a positive note, the predictions are more accurate than those that would be obtained using the literature correlations as shown earlier in Figure 1. Further work is needed to determine the underlying reason for this behavior, however.
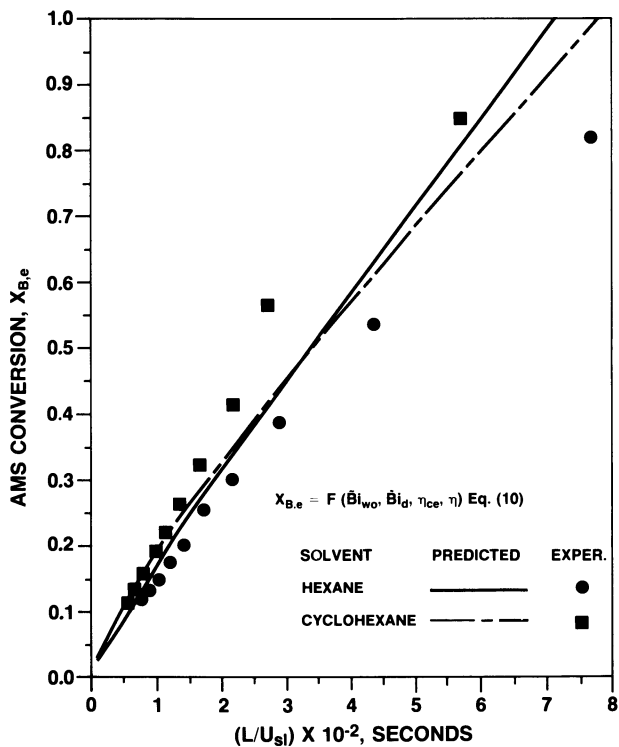
Figure 3. Comparison between experimental and predicted conversion for 0.5% Pd catalyst.

Conclusions

A review of previous reaction studies used to support the development of trickle-bed reactor models is presented. This review suggests that these previous models have neglected the effect of incomplete liquid-solid contacting even though it was experimentally observed in a number of cases. For the few cases where it was included, it was used as an adjustable parameter to match the measured conversion versus liquid mass velocity data to the model.

A model for isothermal trickle-bed reactors which includes the effect of incomplete external liquid-solid contacting is given. This model describes trickle-bed reactor performance for first-order, gaseous reactant limiting rate forms and has been applied to interpret trickle-bed reactor data obtained from a model reaction study. When used in the predictive mode with independently measured values of the effectiveness factor, external liquid-solid contacting efficiency, and other physio-chemical parameters, it was shown that current mass transfer correlations for trickle-beds lead to poor results. A modified form of the correlations shows better predictive ability when matched to the data, but further investigation is needed to obtain greater accuracy and to determine the reliability and generality of the suggested forms.

Legend of Symbols

$a_{g\ell}$ = gas-liquid interfacial area, per unit reactor value, cm^{-1}

$a_{\ell\text{-aws}}$ = liquid-to-actively wetted solid interfacial area per unit reactor volume,

$$\eta_{CE} \left(\frac{S_{ex}}{V_p}\right) (1-\varepsilon_B), \ cm^{-1}$$

$a_{\ell\text{-iws}}$ = liquid-to-inactively wetted solid interfacial area, per unit reactor volume,

$$(1-\eta_{CE}) \ (\frac{S_{ex}}{V_p}) \ (1-\varepsilon_B), \ cm^{-1}$$

$a_{\ell s}$ = overall gas to actively-wetted solid area per unit reactor volume, cm^{-1}

A   = denotes gaseous reactant A first appearing in Equation 1.

b   = stoichiometric coefficient for liquid reactant B first appearing in Equation 1.

B	=	denotes liquid reactant B first appearing in Equation 1.
$\tilde{Bi}_d$	=	Biot number for gas-solid mass transfer at the inactively wetted catalyst surface based on catalyst particle volume,

$$\frac{k_{g\ell s}}{D_e} \frac{V_p}{S_{ex}} \quad \text{or} \quad \frac{k_{\ell - iws}}{D_e} \frac{V_p}{S_{ex}}, \text{ dimensionless}$$

$\tilde{Bi}_w$	=	Biot number for liquid-solid mass transfer at the actively wetted catalyst surface based on catalyst particle volume,

$$\frac{k_{\ell s}}{D_e} \frac{V_p}{S_{ex}}, \text{ dimensionless.}$$

$\tilde{Bi}_{wo}$	=	Overall Biot number for gas through liquid-to-solid mass transfer at the actively wetted catalyst surface based on catalyst particle volume,

$$\frac{k_s}{D_e} \frac{V_p}{S_{ex}}, \text{ dimensionless.}$$

C_{Ag}	=	concentration of gaseous reactant A in the gas phase at position z in the reactor, mole cm^{-3}.
$C_{Ag,i}$	=	concentration of gaseous reactant A in the gas phase at the reactor inlet z = 0, mole cm^{-3}.
$C_{A\ell}$	=	concentration of dissolved gaseous reactant A in the liquid phase at position z in the reactor, mole cm^{-3}.
$C_{A\ell,i}$	=	concentration of dissolved gaseous reactant A in in the liquid phase at the reactor inlet z = 0, mole cm^{-3}.
$C_{A\ell,i}^*$	=	equilibrium concentration of dissolved gaseous reactant A in the liquid phase at the reactor inlet z = 0, $C_{Ag,i}/H_A$, mole cm^{-3}.
$C_{A\ell,aws}$	=	concentration of dissolved gaseous reactant A in the liquid phase on the actively wetted catalyst surface, mole cm^{-3}.
$C_{A\ell,iws}$	=	concentration of dissolved gaseous reactant A in the liquid phase on the inactively wetted catalyst surface, mole cm^{-3}.
$C_{B\ell}$	=	concentration of liquid reactant B in the liquid phase at position z in the reactor, mole cm^{-3}.
$C_{B\ell,i}$	=	concentration of liquid reactant B in the liquid phase at the reactor inlet z = 0, mole cm^{-3}.
Da_o	=	Damkoehler number first appearing in Equation 3 $k_v (1-\varepsilon_B) L/u_{s\ell}$, dimensionless.

d_p = catalyst particle diameter, cm.

D_p = particle diameter based on equivalent external surface area of a sphere, $0.564 \sqrt{S_{ex}}$, cm.

D_e = effective diffusivity of the solute in liquid-filled catalyst pores, cm^2, s^{-1}.

D_m = molecular diffusivity of the solute in the liquid phase, $cm^2 \ s^{-1}$.

$(D_{eo})_{\ell f}$ = effective diffusivity of the tracer obtained in liquid-full operation, $cm^2 \ s^{-1}$.

$(D_{eo})_{app}$ = effective diffusivity of the tracer obtained in trickle-flow or two-phase operation, $cm^2 \ s^{-1}$.

Ga_ℓ = Gallileo number of the liquid phase, $d_p^3 \ g\rho_\ell^2/\mu_\ell^2$, dimensionless.

G_ℓ = liquid mass velocity appearing in Equation 16, gms $cm^{-2} \ s^{-1}$.

H_A = Henry's law constant, cm^3 liquid/cm^3 gas.

H_{es} = external static liquid holdup appearing in Equation 23, dimensionless.

J_D = dimensionless mass transfer j-factor, $k_{\ell s} \ Sc_\ell^{2/3}/u_{s\ell}$.

k_v = first-order reaction rate constant, cm^3 liquid/cm^3 catalyst – s.

$k_{\ell-aws,A}$ = liquid-to-actively wetted solid mass transfer coefficient for dissolved gaseous reactant A, cm s^{-1}.

$k_{\ell-iws,A}$ = liquid-to-inactively wetted solid mass transfer coefficient for dissolved gaseous reactant A, cm s^{-1}.

$k_{g\ell}a_{g\ell}$ = gas-to-liquid volumetric mass transfer coefficient appearing in Equation 11, cm^{-1}.

k_s = combined gas-to-actively wetted solid mass transfer coefficient appearing in Equation 12, cm s^{-1}.

$k_{\ell s}$ = liquid-to-solid mass transfer coefficient appearing in Equation 12, cm s^{-1}.

L = length of active catalyst reactor bed, cm.

Re_ℓ = Reynolds' number based on particle diameter, $d_p \ u_{s\ell} \ \rho_\ell/\mu_\ell$, dimensionless.

Re_ℓ' = Reynolds' number based on equivalent sphere diameter, $D_p \ u_{s\ell} \ \rho_\ell/\mu_\ell$, dimensionless.

r = concentration ratio, b $C_{A\ell,i}^*/C_{B\ell,i}$.

Sc_ℓ = Schmidt number of the liquid phase, $\mu_\ell/\rho_\ell \ D_m$, dimensionless.

S_{ex} = external particle particle surface area, cm^2.

$St_{g\ell,A}$ = Stanton number for gas-to-liquid transport of gaseous reactant A, $k_{g\ell}a_{g\ell} \ L/u_{s\ell}$, dimensionless.

$St_{g\ell s}$ = Stanton number for overall gas-to-solid transport for reactant A, $k_s \ a_{\ell s} \ L/u_{s\ell}$.

$St_{\ell s}$ = Stanton number for liquid-solid transport of A, $k_{\ell s} \ a_{\ell-aws} \ L/u_{s\ell}$.

$St_{\ell-aws,A}$ = Stanton number for liquid-to-actively wetted solid transport of dissolved gaseous reactant A, $k_{\ell-aws} a_{\ell-aws} L/u_{s\ell}$, dimensionless.

$St_{g-iws,A}$ = Stanton number for gas-through-liquid-to-inactively wetted solid transport for dissolved gaseous reactant A, $k_{\ell-iws,A} a_{\ell-iws} L/u_{s\ell}$ or $k_{g\ell s} a_{\ell-iws} L/u_{s\ell}$, dimensionless.

$u_{s\ell}$ = superficial liquid velocity, cm s^{-1}.

u_{Ag} = dimensionless gas concentration, $C_{Ag}/C_{Ag,i}$.

$u_{A\ell}$ = dimensionless concentration of dissolved gaseous reactant A in the liquid, $C_{A\ell}/C^*_{A\ell,i} = C_{A\ell}/(C_{Ag,i}/H_A)$.

$u_{A\ell,aws}$ = $C_{A\ell,aws}/C^*_{A\ell,i}$.

$u_{A\ell,iws}$ = $C_{A\ell,iws}/C^*_{A\ell,i}$.

$u_{B\ell}$ = dimensionless liquid concentration, $C_{B\ell}/C_{B\ell,i}$.

V_p = catalyst pellet volume, cm^3.

X_B = conversion of reactant B at position ξ, $(C_{B\ell,i} - C_B)/C_{B\ell,i}$.

$X_{B,e}$ = conversion of reactant B at the reactor exit.

Greek Symbols

ε_B = bed porosity.

η = catalyst effectiveness factor for a totally wetted pellet.

η_{CE} = external contacting efficiency.

Λ = modified modulus based on particle volume,

$$\frac{V_p}{S_{ex}} \sqrt{\frac{k_v}{D_e}}$$

λ = parameter defined by Equation 9.

μ_ℓ = liquid viscosity, gm cm^{-1} s^{-1}.

ξ = axial coordinate, z/L, dimensionless.

ρ_ℓ = liquid density, gm cm^{-3}.

ω_D = dynamic saturation, H_D/ε_B.

Acknowledgments

Literature Cited

1. Ramachandran, P. A.; Chaudhari, R. V. "Three-Phase Catalytic Reactors", Gordon and Breach Science Publishers, Ltd.: London, 1983; Chapter 12.

2. Germain, A. H.; L'Homme, G. A. "Chemical Engineering of Gas-Liquid-Solid Catalyzed Reactions, L'Homme, G. A., Ed.; CEBEDOC: Liege, 1978.

3. Van Landeghem, H. Chem. Eng. Sci., 1980, 35, 1912-1949.
4. Roberts, G. W., "Catalysis in Organic Synthesis", Rylander,
    P. N., and Greenfield, H., Eds., Academic Press, New York,
    1976; pgs. 1-47.
5. "NATO Advanced Study Institute on Multiphase Reactors",
    Vimeiro, Portugal, August 18-30, 1980.
6. Turek, F.; Chakrabartic, R. K.; Lange, R.; Geike, R.;
    Flock, W. Chem. Eng. Sci., 1983, 38(2), 275-283.
7. Hartman, M.; Coughlin, R. W. Chem. Eng. Sci., 1972, 27,
    867-881.
8. Satterfield, C. N.; Ozel, F. AIChE J,, 1973, 19(6),
    1259-1261.
9. Sedricks, W.; Kenney, C. N. Chem. Eng. Sci., 1973, 28,
    559-569.
10. Germain, A. H.; Lefebvre, A. G.; L'Homme, G. A., Adv.
    Chem. Series, 1974, 133, 164-179.
11. Koros, R. M., paper presented at the 4th International
    Symposium on Chemical Reaction Engineering, Heidelberg,
    West Germany, 1976.
12. Germain, A.; Crine, M.; Marchot, P.; L'Homme, G. A. Adv.
    Chem. Ser. Symp. Ser., 1978, 65, 411-424.
13. Mata, A. R.; Smith, J. M. Chem. Eng. J., 1981, 22,
    229-235.
14. Hanika, J.; Sporka, K.; Ulbrichová, Z.; Novák, J.; Pyzicka,
    V. Coll. Czechoslov. Chem. Commun., 1974, 39, 210-215.
15. Hanika, J.; Vosecký, V.; Ruzicka, V. Chem. Eng. J., 1981,
    21, 108-114.
16. Morita, S.; Smith, J. M. Ind. Eng. Chem. Fundam., 1978,
    17(2), 113-119.
17. Herskowitz, M.; Carbonell, R. G.; Smith, J. M. AIChE J.
    1979, 25(2), 272-283.
18. Turek, F.; Lange, R. Chem. Eng. Sci., 1981, 36, 569-579.
19. Montagna, A. A.; Shah, Y. T. Ind. Eng. Chem. Process Des.
    Dev., 1975, 14(4), 479-483.
20. Montagna, A. A.; Shah, Y. T.; Paraskos, J. A. Ind. Eng.
    Chem. Proc. Des. Dev., 1977, 16(1), 152-155.
21. Henry, H. C.; Gilbert, J. B. Ind. Eng. Chem. Proc. Des.
    Develop., 1973, 12(3), 328-334.
22. Somers, A.; Shah, Y. T.; Paraskos, J. Chem. Eng. Sci.,
    1976, 31, 759-765.
23. Biskis, E. G.; Smith, J. M. AIChE J., 1963, 9(5),
    677-680.
24. Mejstrikova, M. Coll. Czechoslov. Chem. Commun., 1974,
    39, 210-215.
25. Hanika, J.; Sporka, K.; Ruzicka, V.; Krausova, J.
    Chem. Eng. Commun., 1975, 2, 19-25.
26. Jawad, A., Ph.D. Thesis, University of Birmingham, England,
    1974.
27. Goto, S.; Smith, J. M. AIChE J., 1975, 21, 714-718.

28. Levec, J.; Smith, J. M. AIChE J., 1976, 22, 159–168.
29. El-Hisnawi, A. A. D.Sc. Thesis, Washington University, St. Louis, Missouri, 1981.
30. Goto, S.; Smith, J. M. AIChE J., 1978, 24(2), 286–293.
31. Goto, S.; Smith, J. M. AIChE J., 1978, 24(2), 294–302.
32. Crine, M.; Marchot, P.; L'Homme, G. A. Chem. Eng. Sci., 1980, 35, 51–57.
33. Crine, M.; Marchot, P.; L'Homme, G. A. American Institute of Chemical Engineers Meeting, San Francisco, California, 1979.
34. El-Hisnawi, A. A.; Duduković, M. P.; Mills, P. L. ACS Symposium Series, 1982, 196, 421–440.
35. Goto, S.; Smith, J. M. AIChE J., 1975, 21(4), 706–713.
36. Dwivedi, P. N.; Upadhyay, S. N. Ind. Eng. Chem. Proc. Des. Dev., 1977, 16, 157.
37. Duduković, M. P.; Mills, P. L. ACS Symposium Series, 1978, 65, 387–399.
38. Baldi, G., "NATO Advanced Study Institute on Multiphase Chemical Reactors", Vimeiro, Portugal, August 18–30, 1980.
39. Satterfield, C. N.; Way, P. N. AIChE J., 1972, 18(2), 305–311.
40. Enright, J. J.; Chuang, T. T. Can. J. Chem. Eng., 1978, 56, 236–250.
41. Mills, P. L.; Duduković, M. P. AIChE J., 1981, 27(6), 843–904.

Stability of Trickle-Bed Reactors

C. H. BARKELEW and B. S. GAMBHIR

Shell Development Company, Houston, TX 77001

Trickle-bed reactors, in which gas and liquid flow co-currently downwards through a bed of catalyst particles, are commonly used for hydrogenation of various hydrocarbons. These reactors can develop local exotherms in which undesirably high temperatures occur. In this paper a rule for prevention of these hot spots is developed. Its form has been derived from theory and its two parameters have been estimated from real process data. Its use assures safe operation of adiabatic trickle-bed reactors.

Trickle-bed reactors, which are widely used for hydrogenation of refinery hydrocarbon streams, are known to be prone to development of irregular flow patterns. In extreme cases, these irregularities can lead to large variability of the extent of reaction, with temperatures rising hundreds of degrees above normal, sintering the catalyst into massive clumps. This usually destroys the catalyst, but more seriously, it can lead to structural damage of the reactor vessel, with attendant personnel hazards. Safety requires that reactors be operated in such a way that they are free of hot spots at all times. Although many process operators have learned by experience how to run their units safely, there has as yet been no analytical treatment of the subject which gives them firm guidelines.

A Model Of A Trickle Bed

A suitable model of a trickle bed, with which its stability can be analyzed, can be devised by assuming that there are

irregularities in packing density and in the flows of the
phases, with characteristic dimensions on the order of a few
tens of particle diameters. Observations on laboratory models
of trickle-bed reactors confirm this, and furthermore indicate
that irregularities, once formed, tend to persist for a
substantial fraction of the bed height.

We start by considering the steady state in a cylindrical
irregularity, extending downward into the bed from near its
upper surface. Outside the disturbed region, the reaction can
be described by the usual heat and material balance equations
for a reactor in plug flow,

$$CF\frac{dT}{dl} = k_s Hf(x) \exp (-E/RT) \tag{1}$$

$$F\frac{dx}{dl} = k_s f(x) \exp (-E/RT) \tag{2}$$

The symbols are defined under "Nomenclature", below.

The units of these quantities are irrelevant, so long as
they are mutually consistent.

Equations (1) and (2) can be combined into a single
dimensionless equation,

$$\frac{d\tau}{dz} = SD \exp (\tau) \tag{3}$$

Equation (3) includes the approximation:

$$\exp(-E/RT) \approx \exp(-E/RT_o) \exp[E(T-T_o)/RT_o^2] \tag{4}$$

and is strictly valid only for the known zero-order kinetics of
hydrotreating.

The solution of Equation (3) is

$$SDz = 1 - \exp (-\tau) \tag{5}$$

Within the cylindrical disturbed region, the temperature
and composition vary with lateral position. For our purposes,
this variation can be adequately described by adding another
term to Equation (3), putting it into the form:

$$\frac{\partial \psi}{\partial z} = SD^* \exp (\psi) + \frac{L^2}{P^*} \nabla_r^2 \psi \tag{6}$$

Stability of the Model

The behavior of systems described by Equation (6) is well-
known. It was first analyzed by Frank-Kamenetskii (1) in the
1940's in a study of the theory of thermal explosions. He was
interested in the transient behavior of a fixed volume of
reactant, which is also describable by Equation (6), with z

interpreted as time. He showed that there is or is not a
steady state, according to the value of a dimensionless number
which includes the quantities we have called SD^* and P^*, and
which is proportional to the square of the diameter of the
cylindrical region. In our notation, his criterion is

$$SD^*P^*R^2/L^2 \;(\leqslant) 2 \; \exp \;(-\tau) \qquad\qquad (7)$$

The dimensionless ratio Fd/κ, where d is the particle
diameter, is known to be correlated with particle Reynolds
number, solid conductivity, void fraction, and particle shape
(2). It is a complicated but weak function of these
quantities, which approaches a constant value of about 10 for
large Reynolds numbers and low solid conductivity. This
limiting value can be used for our purpose, leading to, $P^* = 10$
L/d.

Write $SD^* = G \cdot SD$, defining G as the disturbance ratio.
Then combination of Equations (5) and (7), using the limiting
value of P^*, gives

$$GR^2[\exp \; (\tau) - 1]/Ld < 1/5 \qquad\qquad (8)$$

This can be interpreted as the condition that the
temperature within the disturbed region will not diverge
exponentially from that in the normal region of the bed. G, R,
L and d are fixed parameters for a given reactor configuration
and flow rate, hence Equation (8) can be interpreted as a
stability criterion which simply states that the normal-bed
temperature rise must not exceed some limiting value, otherwise
hot spots will develop.

Development Of A Stability Criterion

We now turn to devising a procedure for estimating the maximum
allowable temperature rise. Equation (8) is not useful in a
quantitative sense because the parameters G and R cannot be
measured or estimated. However, it is possible to deduce from
elementary considerations how they might vary with reaction
conditions.

G is the ratio of the dimensionless number SD in the
disturbed region to its value in the normally-operating part of
the bed. SD contains the activation energy, heat of reaction,
inlet temperature and bed height, all of which have fixed
constant values in all regions of the bed. It also contains
the possibly variable quantities C, k_s and F. C is the average
heat capacity of the fluid, and depends on the local phase
ratio. k_s is the specific rate constant, and depends on the
local catalyst density and the phase holdup. F is the local
average linear velocity, which can vary from point to point for
a variety of reasons.

The phase flow varies from the top to the bottom of the bed, primarily because volatile components vaporize with rising temperature. We expect the linear velocity of the gas phase to increase relative to that of the liquid, and furthermore we expect increasing velocity to smooth out those fluctuations in G which are dependent on phase ratio. There is a part of G which should not depend on gas velocity, namely that which is attributed to fluctuations in packing density. This qualitative reasoning leads us to suspect that the quantity G depends on the gas flow rate like $A + B/f(F)$, where f is some increasing function of gas flow.

R, the radius of the disturbed cylindrical region, is likely to be proportional to the particle diameter. We also suspect that it may not be a constant over the bed, but may vary with height. In particular it may vary in such a way that the effective value of R^2 to use in Equation (8) is like L^n, where L is the total bed height and n is a small positive number. This assumes that the disturbed region grows as the fluids move downward. Putting all this into Equation (8), we find that something like

$$\exp(\tau) - 1 < \frac{K_1}{L^{n-1}d\left(1 + \dfrac{K_2}{f(F)}\right)} \tag{9}$$

ought to correlate with freedom from hot spots, if we can find appropriate values for the K's and can specify a form for f.

We have tried a number of forms for f, in the procedure to be described below, and concluded that ρF^2 at the reactor outlet is the form we prefer to use. This is the kinetic energy density of the gas, commonly used to correlate drag, and it seems reasonable that it is a reasonable way for velocity to affect local fluctuations of phase ratio. In the absence of more data, we cannot be more precise about f, except to say that ρF^2 works. We do take note of the fact that the form does not extrapolate neatly to zero gas velocity. This is not a significant limitation.

Some interesting conclusions can be drawn from the form of Equation (9). The K's can be determined only by comparison with data; they cannot, to our knowledge, be predicted from first principles or existing correlations. The assumed value of 10 for the particle Peclet number is completely absorbed into K_1, making that an uncritical assumption.

If the development of hot spots were independent of gas flow, then Equation (9) could be transformed to

$$\log[\exp(\tau) - 1] < \log K_3 - (n-1)\log L \tag{10}$$

with K_3 a different constant. A straight line on a plot of log [exp (τ) - 1] vs. log L would separate reactors that develop hot spots from those which do not.

If the cross section of the disturbed region were to vary linearly with length, then all the tendency toward unstable behavior would be caused by flow variability. Equation (9) could then be written:

$$\frac{1}{\exp (\tau) - 1} > \frac{1}{K_1} + \frac{K_2}{K_1} \cdot \frac{1}{\rho F^2} \qquad (11)$$

and a straight line on a plot of $1/[\exp (\tau) - 1]$ vs $1/(\rho F^2)$ would separate safe and unsafe operation. The limiting cases, Equations (10) and (11), will be considered later.

Determination of Parameters From Process Data

We have collected operating data over a period of 15 years from four separate trickle-bed hydrotreater reactors. These four have operated with a number of different catalyst loadings, have processed a variety of feedstocks, and have operated over a wide range of average temperatures and pressures. Physical descriptions of the four reactors are given in Table I.

Table I. Physical Descriptions of Reactors

Reactor	Diameter (ft)	Range of Bed Height (ft)	Catalyst Diameter (in.)
1	11	13-22	1/16
2	11	30-48	1/16
3	13.5	32.5	1/16
4	13.5	40.5	1/16

During the period of observation, six separate incidents occurred in which hot spots started to develop. The conditions that led to these incidents are summarized in Table II. The outlet vapors include components originally in the liquid feed, vaporized during passage through the bed. The amounts of these components were estimated using correlated equilibrium ratios.

A set of operating conditions known to be safe, from the same four reactors, is given in Table III.

The data of Tables II and III can be compared with the stability criterion Equation (9) by making plots of the sort suggested by Equations (10) and (11). The intermediate data

Table II. Conditions Leading to Hot Spots

Case No.	Reactor No.	Bed Height (ft)	Inlet Temp. (°F)	Temp. Rise (°F)	Pressure (psia)	Feed Liquid Flow (lb/hrX10^{-4})	Outlet Vapor Flow (lb/hrX10^{-4})	Superficial Vapor Velocity (ft/hr)	Feed Gas Mol. Wt.
1	2	48	480	35	1295	8.8	1.36	144	5.3
2	1	22	575	60	1565	10.2	2.79	133	5.3
3	2	48	620	40	1615	16.0	2.30	61	5.3
4	1	15	627	68	1600	16.4	3.70	86	5.3
5	3	32.5	680	40	1200	22.9	2.40	79	13.0
6	4	40.5	643	40	900	32.8	1.30	61	23.0

Table III. Operating Conditions Known to Be Safe

Case No.	Reactor No.	Bed Height (ft)	Inlet Temp. (°F)	Temp. Rise (°F)	Pressure (psia)	Feed Liquid Flow (lb/hrX10^{-4})	Outlet Vapor Flow (lb/hrX10^{-4})	Superficial Vapor Velocity (ft/hr)	Feed Gas Mol. Wt.
7	1	22	500	7	1295	8.8	1.37	151	5.3
8	2	48	535	9	1565	10.2	1.52	115	5.3
9	1	22	643	57	1615	16.0	4.50	94	5.3
10	1	13	620	50	1550	17.2	4.43	126	5.3
11	2	30	610	30	1550	17.2	2.92	97	5.3
12	3	32.5	660	50	1200	31.6	2.92	140	7.4
13	4	40.5	600	15	900	32.8	.41	58	5.8

for these plots are listed in Table IV. An activation energy
of 27 kcal/mole (3) was used for calculating the values in the
third column.

Figure 1 is the plot suggested by Equation (10), which
assumes that flow rate does not affect the disturbance ratio
G. Clearly, the map does not separate into "safe" and "unsafe"
regions, although if points 9 and 12 could be lowered and
points 5 and 6 raised, it might do so. Inspection of Table IV
shows that 9 and 12 have relatively high values of ρF^2, and
that 5 and 6 have relatively low values. This suggests that
the form of Equation (11), which allows for the effect of flow
on G but also assumes that R^2 is proportional to L, be tried.

Figure 2 is the map suggested by Equation (11). The
separation is almost clean, with point 13 being the sole "safe"
condition that falls into the "unsafe" zone. Case 13 has an
unusually low vapor flow rate, and thus the discrepancy
suggests that flow is weighted too heavily by Equation (11).
This form does correct the deficiencies of Equation (10),
however.

If the dashed line on Figure 1, with slope = -1, were
accepted as an approximate border, the exponent, n, would be
2. In Figure 2, this exponent is 1 by hypothesis. Since these
two figures are for opposite kinds of limits, there is a
suggestion that an intermediate exponent, say 1.5, should be
considered. Similarly, the discrepancies of Figure 1 indicate
that the dependence of G on flow ought to be greater than what
was assumed in drawing that figure. The single discrepancy on
Figure 2 suggests that its assumed flow dependence is too
large. Again, something in between is suggested, say
$G = [1 + (K_4/\rho F^2)]^{1/2}$.

Together, these transform Equation (9) to:

$$\exp(\tau) - 1 < \frac{K_1}{L^{\frac{1}{2}} d \left(1 + \frac{K_4}{\rho F^2}\right)^{\frac{1}{2}}} \tag{12}$$

or equivalently:

$$\frac{1}{L[\exp(\tau) - 1]^2} > K_5 + \frac{K_6}{\rho F^2} \tag{13}$$

This says that a plot of $1/[L(\exp(\tau) - 1)^2]$ vs. $1/\rho F^2$ should
be separable into safe and unsafe regions by a straight line.
Figure 3 is such a plot, with values of the ordinate taken from
the last column of Table III. The dashed line is represented
by

$$\frac{10^3}{L[\exp(\tau) - 1]^2} = 1 + \frac{3 \times 10^5}{\rho F^2} \tag{14}$$

Table IV.   Intermediate Data of Plots

Case No.	log L	E/RT_o^2	τ	$\log[\exp(\tau)-1]$	$1/[\exp(\tau)-1]$	$(10^5)/\rho_F^2$ ft hr^2/lb	$(10^3)/L[\exp(\tau)-1]^2$ ft^{-1}
1	3.87	.0277	.969	.492	.611	4.85	7.79
2	3.09	.0228	1.370	1.077	.341	2.55	5.27
3	3.87	.0210	.839	.273	.761	6.62	12.07
4	2.71	.0207	1.408	1.127	.324	2.98	7.00
5	3.48	.0188	.753	.116	.890	7.49	24.4
6	3.70	.0200	.800	.203	.816	18.2	16.4
7	3.09	.0265	.186	-1.588	4.89	4.59	1094.
8	3.87	.0247	.222	-1.392	4.02	5.43	337.
9	3.09	.0201	1.146	.763	.466	2.24	9.87
10	2.56	.0210	1.049	.617	.539	1.70	22.4
11	3.40	.0214	.641	-.107	1.113	3.34	41.3
12	3.48	.0195	.975	.502	.605	3.46	11.3
13	3.70	.0218	.327	-.951	2.59	59.2	165
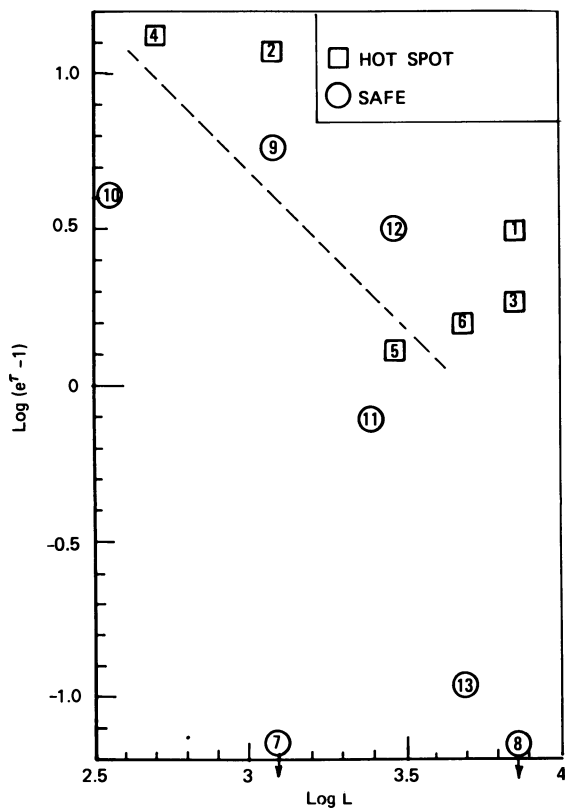
Figure 1.   Stability Map with no Flow Effect.
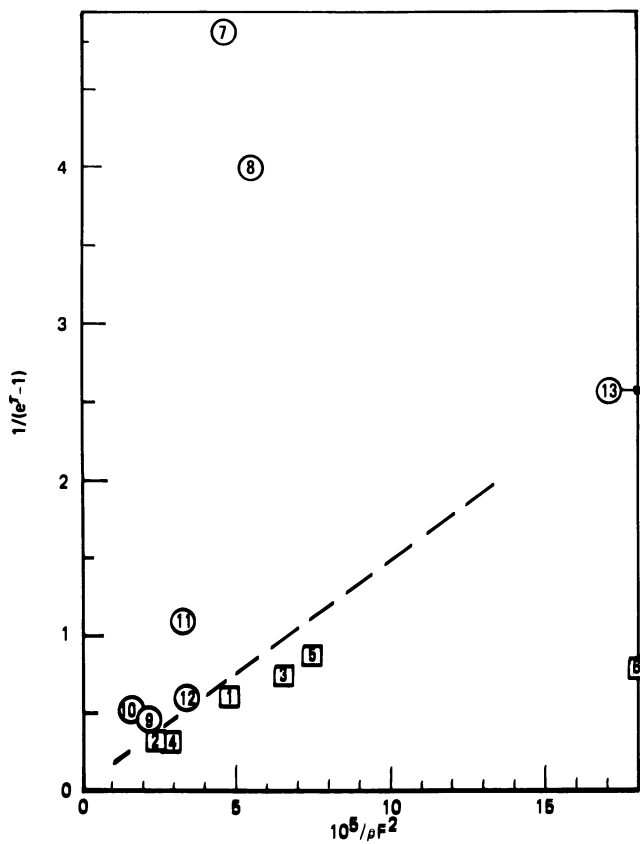
Figure 2.   Stability Map with Dominating Flow Effect.
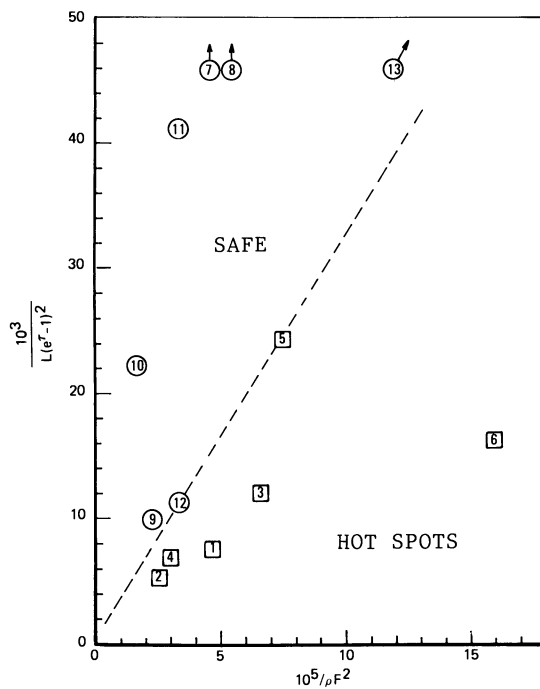
Figure 3. Recommended Stability Criterion.

Two of the points, 5 and 12, are close to the line, and point 13 is slightly on the wrong side, but these discrepancies are minor and within the uncertainty of the data. Further refinement is possible but hardly warranted with the limited data. One might be tempted to draw the separating line of Figure 3 with a slightly steeper slope, passing closer to points 2 and 4. However, this must not be done in such a way that the line intersects the horizontal axis at a positive value. Unphysical, imaginary values of temperature would be indicated if it were to do so.

Equation (14) is equivalent to

$$\tau < \tau^* \equiv \log \left[1 + \left(\frac{10^3}{L \left(1 + \frac{3 \times 10^5}{\rho F^2} \right)} \right)^{1/2} \right] \quad (15)$$

which is our suggested stability criterion for trickle beds with catalyst particles 1/16" in diameter. Operation of a reactor with a temperature rise a few degrees less than that suggested by Equation (15) should be free of hot spots.

Table V compares observed temperature rises for each of the cases with the maximum allowable value calculated from Equation (15).

Table V. Comparison of Observed Temperature Rises for Each Case

Case	Hot Spot	Observed ΔT	Maximum Safe ΔT
1	Yes	35	28
2	Yes	60	41
3	Yes	40	33
4	Yes	68	62
5	Yes	40	40
6	Yes	40	26
7	No	7	38
8	No	9	30
9	No	57	61
10	No	50	72
11	No	30	47
12	No	50	50
13	No	15	15

The criterion is in satisfactory correspondence with the data.

Characteristic Features Of the Stability Criterion

Dimensions The numerical constants in Equation (15) are dimensional, with length in feet, mass in pounds, and time in hours. This unfortunate bit of untidiness does not detract from the utility of Equation (15), however. A proper dimensional analysis must wait until we have a better physical understanding of the mechanics of trickle flow. Presumably the characteristic length needed to make "10^3" dimensionless would be the diameter of a disturbance that spontaneously forms in the upper part of the bed. The characteristic drag force for "3×10^5" would presumably involve liquid-solid capillary effects.

Effects of Particle Size The dependence of these two parameters on the dimension of the catalyst particles can be inferred from elementary reasoning. Equation (9) indicates directly that "10^3" should be inversely proportional to the square of d. This involved the assumption that both the size of the disturbances and the effective conductivity are proportional to d. On the other hand, the drag constant ought to be relatively insensitive to d. This can be deduced by supposing that the force acting to break up accumulated pockets of excess reactivity is proportional to ρF^2 and acts over the circumference of the pocket, making the total disruptive force proportional to particle diameter. The amount of material in the pocket is proportional to the cross section, and hence to d^2, but the resistance to breakup is proportional to the solid surface per unit volume, or to $1/d$. The net is again proportional to d, making the balance between disruptive and cohesive forces, and hence the parameter "3×10^5," independent of diameter. Although this analysis indicates how the criterion could be used for different particle sizes, some degree of caution is advisable until data with other particles become available.

Effects of Reaction Parameters An unusual feature of Equation (15) is that it does not appear to involve the heat of reaction and heat capacity. This is because they were algebraically eliminated by combining the Frank-Kamenetskii relation, Equation (7), with the adiabatic relation, Equation (3). Both are important in determining stability, of course, and this importance can be demonstrated by eliminating τ between Equation (15) and (3). This gives an equally valid but less useful stability criterion:

$$ SD < 1 \Bigg/ \left[1 + \left(\frac{L \left(1 + \frac{3 \times 10^5}{\rho F^2} \right)}{10^3} \right)^{1/2} \right] \tag{16} $$

Estimation of Unknown Parameters   Approximate values of R and G
can be estimated from the numerical constants of Equation(15)
and (8). We have

$$G = \left(1 + \frac{3 \times 10^5}{\rho F^2}\right)^{1/2} \tag{17}$$

and

$$R^2 = \frac{Ld}{5\sqrt{\dfrac{10^3}{L}}} \tag{18}$$

Excluding the two low-velocity cases, G varies from 2.5 for
case 10 to 4.8 for case 5. The largest G is 13, for case 13.
   The disturbance diameters, from Equation (18), range from
1" for case 10 to 2 1/2" for cases 1, 3 and 8. These estimates
of R are rather sensitive to the way the line is drawn in
Figure 3, since they are proportional to the intercept on the
vertical axis. They should be considered as very crude
estimates.

Effect of Inlet Temperature   If Equation (15) is written as

$$\Delta T^* = \frac{RT_o^2}{E} \log \left[1 + \left(\frac{10^3}{L\left(1 + \frac{3 \times 10^5}{\rho F^2}\right)}\right)^{1/2}\right] \tag{19}$$

a curious feature appears. The stability seems to be enhanced
as the inlet temperature increases, contrary to intuition.
This is a direct consequence of using the Arrhenius rate
expression. The relative change in rate per degree of
temperature increase becomes smaller as the average temperature
rises. The feature is less puzzling if it is considered as an
effect of declining catalyst activity. As the catalyst
gradually ages, the inlet temperature must be increased to
maintain conversion. The less-active catalyst has a lower
temperature dependence of rate, as well as a lower rate. This
results in an increasing tolerance to disturbances.

Temperature Fluctuations   The above physical description of a
trickle-bed reactor does not include the assumption that the
temperature in the "normal" region is uniform in a cross
section. In an adiabatic reactor, all fluctuations grow in
amplitude and size, even the infinitesimal ones. A mottled
temperature structure cannot be avoided, and a set of
temperature sensors at a given height will not necessarily be
consistent. A band of temperature readings will always occur.
   A rough estimate of the width of this band can be found
from the steady-state solution of Equation (6). The

temperature profile within a positive fluctation is given by the solution of

$$\nabla_r^2 \; \psi = - \frac{GSDPR^2}{L^2} \; \exp \; (\psi) \tag{20}$$

with $\psi = \tau$ at $r = 1$,
which is

$$\psi_o - \psi = 2 \; \log \; \left(1 + \exp \; (\psi_o) \; r^2 \; \frac{GSDPR^2}{8L^2}\right) \tag{21}$$

The boundary condition is

$$\psi_o - \tau = 2 \; \log \; \left(1 + \exp \; (\psi_o) \; \frac{GSDPR^2}{8L^2}\right) \tag{22}$$

or

$$\exp \; (\psi_o - \tau) = \left(1 + \exp \; (\psi_o - \tau) \; \frac{GSDPR^2}{8L^2 \exp \; (-\tau)}\right)^2 \tag{23}$$

a quadratic equation in $\exp \; (\psi_o - \tau)$.

If a disturbance is on the verge of developing into a hot spot, the parameter group $(GSDPR^2)/[L^2 \exp \; (-\tau)]$ is near its critical value of 2, at which point the quadratic equation is

$$\exp \; (\psi_o - \tau) = \left(1 + \frac{\exp \; (\psi_o - \tau)}{4}\right)^2 \tag{24}$$

whose solution is $\exp \; (\psi_o - \tau) = 4$. The magnitude of the temperature fluctuation is thus $(RT_o^2)/E \log 4$, about 60°F for typical conditions from Table I. Negative fluctuations are never very large, so this corresponds roughly to the maximum possible safe width of the temperature band.

Operators will often watch the readings from an array of thermocouples in a reactor, as an indication of imminent hot spot formation. The historical danger point for the reactors of Table I has been a band of 35°F. It is interesting to note that the average positive temperature fluctuation within a disturbance, from the integral of Equation (21), is about 30°F.

Effects of Assumptions

The stability criterion Equation (15) has two different meanings. First, it is an interpolation procedure, guided by theoretical considerations, for predicting the future behavior of a group of reactors from historical observations on those same reactors. As such it cannot be particularly sensitive to

assumptions made in developing the theory. The second
interpretation of Equation (15) is that it can be used for
other reactions, with different kinetic parameters, for
example. In this sense, it is an extrapolation procedure, and
may be sensitive to assumptions made about the model.

We have made simple tests of the effects of three of the
assumptions. They are a) that the reactor is in plug flow, b)
that the activation energy to be used with the process data is
27 kcal/mole, and c) that the reaction is of zero order. Each
of these is discussed briefly below.

Plug Flow With a significant amount of axial dispersion,
Equation (3), describing the normal bed temperature profile,
must be modified to account for this dispersion. The effect
of this modification is that the ultimate vertical asymptote in
temperature is moved forward in the extended bed. Dispersion
enhances the tendency of a reactor to run away. However, with
the type of dispersion that occurs in a trickle bed, by
variations in velocity from point to point, the profile retains
its vertical asymptote. The solution of Equation (3) plus
dispersion is almost identical with Equation (5), but with a
different value of SD. Since SD drops out in the ultimate
stability criterion, axial dispersion cannot be of any
particular significance in the development of local hot
spots. It affects the global stability of the normal part of
the reactor, but it has little influence on the way
disturbances grow, relative to the normal regions.

Activation Energy Although the assumed activation energy of 27
kcal/mole is based on measurement, and is probably about right,
its use could conceivably be questioned because the catalysts
may have been different. It has been reassuring to find that
our conclusions are not sensitive to this assumed value.

To assess the effect of the assumption, we have repeated
the entire data-fitting procedure for two other values of E,
13.5 and 18 K cal/mole. For the lower value, the procedure
does not work. The model in effect says that if the activation
energy were that low, the observed hot spots could not have
occurred. For E = 18, however, a criterion equivalent to
Equation (15) can be derived in the same way as before. We
give the result, without details.

$$\tau < \tau^* \equiv \log \left[1 + \left[\frac{10^3}{L\left(16 + \frac{5.4 \times 10^5}{\rho F^2}\right)} \right]^{1/2} \right] \tag{25}$$

The comparison equivalent to Table IV is equally good;
however, the estimates of R and G are changed. R doubles, and
G decreases slightly. Physically, this can be interpreted as

saying that if sensitivity to temperature fluctuations is decreased, the disturbances must be bigger to account for the observed hot spots.

The effect of assuming a particular activation energy is thus insignificant for the interpolative aspect of Equation (15). For extrapolation to other reactions, however, there will be an error in the estimated critical temperature rise which is proportional to and opposite in direction to the error in the assumed activation energy of hydrotreating.

Reaction Order   The assumption that the reaction is of zero order is reasonable for a stability analysis because of its conservatism. Extension of Equation (15) to other systems, however, may require consideration of other kinetics.

We show how this can be done for a first-order reaction. For other orders, the procedure is equivalent, and with about the same degree of complexity.

The condition for stability of a disturbed region is that a solution exist for the system of equations:

$$\nabla_r^2 \psi = - \frac{GSDPR^2}{L^2} \exp (\psi) \, x$$

$$\psi = \tau \text{ at } r = 1$$

$$\nabla_r^2 x = \frac{GDPR^2}{L^2} \exp (\psi) \, x \tag{26}$$

$$x = x_o \text{ at } r = 1$$

The notation is the same as before, with ψ representing the variable dimensionless temperature within the disturbance, x representing composition variable. The reaction is first order and the Peclet numbers for heat and mass transfer are assumed to be equal. x_o represents the composition in the normal region, equal to $1 - (\tau/S)$ with τ and S defined as before.

The differential equations of (26) can be combined to give

$$\nabla_r^2 \psi + S \nabla_r^2 x = 0 \tag{27}$$

from which it follows that

$$\psi + Sx = S \tag{28}$$

if cylindrical symmetry holds within the disturbance. Combination of Equation (28) with the first equation of (24)

gives

$$\nabla^2 \psi = \frac{GSDPR^2}{L^2} \exp (\psi) \left(1 - \frac{\psi}{S}\right) \qquad (29)$$

A characteristic of runaway reactions is that they start with the dimensionless temperature, ψ, close to unity. S is typically 15 to 20 or higher. Hence, $(\psi/S) \ll 1$, and $1 - (\psi/S) \approx \exp(-\psi/S)$, to a sufficient degree of approximation. Then,

$$\nabla^2 \psi = \frac{GSDPR^2}{L^2} \exp [\psi (1 - 1/S)]$$

or

$$\nabla^2 \psi [1 - (1/S)] = \frac{GSDPR^2 (1 - 1/S)}{L^2} \cdot \exp [\psi (1 - 1/S)] \qquad (30)$$

with $\psi (1 - 1/S) = \tau (1 - 1/S)$ at $r = 1$.

Equation (30) is identical in form with the steady state of Equation (6), hence it has exactly the same condition for stability,

$$\frac{GSDPR^2 (1 - 1/S)}{L^2 \exp [-\tau (1 - 1/S)]} < 2 \qquad (31)$$

For a first-order adiabatic reaction in the normal zone, with plug flow,

$$\frac{d\tau}{dz} = SD \exp (\tau) x \qquad (32)$$

and

$$x = 1 - \tau/S \qquad (33)$$

Together these give

$$\frac{d\tau}{dz} = SDe^\tau (1 - \tau/S) \qquad (34)$$

whose solution is

$$SD = Se^{-S} [Ei(S) - Ei (S - \tau)] \qquad (35)$$

where $Ei(-)$ is the Exponential Integral Function. For large S, and $\tau \ll S$,

$$Ei(S) \approx \exp (S)/S$$

$$Ei(S-\tau) \approx \exp (S-\tau)/(S-\tau)$$

which together give

$$SD \approx 1 - \exp\ (-\tau)/(1 - \tau/S)$$

$$\approx 1 - \exp\ [-\tau\ (1 - 1/S)] \qquad (36)$$

Substitution of Equation (36) into (31) gives

$$\frac{GPR^2\ (1 - 1/S)}{L^2} \left(\exp\ [\tau\ (1 - 1/S)] - 1\right) < 2 \qquad (37)$$

This is of exactly the same form as the stability criterion for a zero-order reaction, except that G and τ are both multiplied by the factor [1 - (1/S)], which is not greatly different from unity.

   The ultimate form of the criterion by which the stability of an adiabatic first-order reaction can be judged is identical with Equation (19) except that $RT_o{}^2$ /E is replaced by $RT_o{}^2$ /E[1-(1/S)]. In this respect, a first-order reaction behaves like a zero-order reaction with a slightly-lower activation energy.

   With these comments, we may confidently conclude that none of the assumptions used in deriving our model for hot spot development has a significant effect on the stability conditions deduced from that model.

Some Ideas That Did Not Work

During the course of the development described above, we tried a number of alternative models, none of which led to a satisfactory correspondence between theory and observations. These are listed below, with brief comments.

   Liquid-phase flow does not correlate in any way with hot spot development. All our attempts to find such a correlation led only to random scatter. This is consistent with the hypothesis that there is a minimum flow necessary to distribute the liquid over the cross section of the reactor, and that above the minimum the effect is only one of holdup. All the observed data appear to be above this minimum.

   Functions of gas flow other than ρF^2 do not correlate the data. In particular, we tried to write G as a function of ρ F and F, separately, and to use inlet flows. We found no way of devising a separable map like Figure 3 with these relations.

   Attempts to solve Equation (6) numerically, using the existing "software" of high-powered computers, are useless. Solutions can be readily obtained, assuming a variety of initial conditions and disturbance patterns, but they cannot be fitted into the patterns of Tables II and III, without the introduction of "fudge factors." The essence of our development is that it is necessary to introduce such factors, like the parameters n, K^1, and K^2 of Equation (9), to explain the

observations, for instance, the apparent inverse correlation of
allowable temperature rise and bed height. The computers
confirm this, but give no deeper insight into the nature of the
phenomena.

Concluding Comments

We have used a rather crude description of two-phase flow
through packing, invoking imprecise notions like "regions of
disturbance," solving boundary-value problems with no definable
boundary, using extremely simplified descriptions of the
reactions that take place, and yet from this we have devised
what appears to be an accurate rule for predicting the onset of
runaway exotherms in trickle beds, given by Equation (15). It
is not that uncertainties and assumptions have disappeared or
have been hidden, but rather that they have been directed into
estimates of quantities whose values are unimportant in
defining stability limits. The important quantities are
strongly related to direct measurement and only weakly to
uncertain inferences. The stability rule is intended to apply
to all exothermic reactions in trickle-bed reactors, in
particular to hydrogenation of petroleum fractions, the primary
data source.

Nomenclature

A,B	Adjustable constants
C	Heat capacity
γ	E/RT_0^2
α	Particle diameter
D	kV/F
E	Activation energy
f	Symbol for function
F	gas velocity at the reactor outlet, ft/hr
G	Disturbance ratio, SD^*/SD
H	Heat of reaction
k	Specific rate constant at inlet $= k_s$ exp $(-E/RT)$
k_s	Specific rate constant
K_i	$i = 1,2, \ldots$ Adjustable constants
κ	Effective thermal conductivity
1	Length or height variable
L	Bed height, ft
n	Exponent in relation of R^2 to L
P	Peclet number Fd/κ
P^*	FL/κ
r	Radial variable
R	Radius of disturbance, gas constant
ρ	Gas density, lb/ft^3
S	$EH/RT_0^2 C$
SD^*	SD in disturbed region

T	Temperature
T_o	Inlet temperature
ΔT_*	Temperature rise
ΔT	Maximum safe temperature rise
τ_*	$\gamma \Delta T$
τ	Critical value of τ
V	Bed volume
x	Conversion or composition variable
z	Fraction of height, 1/L
ψ	Symbol for τ in a disturbance
ψ_o	Peak value of ψ

Literature Cited

1. Frank-Kamenetskii, D. A., "Diffusion and Heat Transfer in Chemical Kinetics;" Plenum Press, 1969.
2. Beek, J., "Design of Packed Catalytic Reactors;" Advances in Chemical Engineering, Vol. 3, p. 231, Academic Press, 1962.
3. Beuther, H., and B. K. Schmid, "Reaction Mechanisms and Rates in Residue Hydrodesulphurization;" Proc. 6th World Petroleum Congress, Section III, 1964, p. 297.

Gas Absorption with Complex Chemical Reactions

A General Computational Scheme for Rate Calculations

P. A. RAMACHANDRAN

Department of Chemical Engineering, Washington University, St. Louis, MO 63130

A general computational scheme using orthogonal col-
location on finite elements has been developed for
calculation of rates of mass transfer accompanied by
single or multistep reactions. The method can be
used to predict enhancement in absorption or desorp-
tion rates for a wide class of industrially impor-
tant situations.

Gas absorption accompanied by a single step or multistep reactions
is encountered in many industrial processes (Astarita (1),
Danckwerts (2), Savage (3)). A number of specific complex reaction
schemes such as two-step, consecutive, etc., have been analyzed in
the literature (see Shah (4) for a summary of the major works in
this area. In some cases, some of the reactants or products are
also volatile and a number of papers analyze this problem (see for
instance, Shah and Sharma (5)). Finally a class of industrial
problems involves simultaneous absorption of two or more gases
which react in the liquid (Ramachandran and Sharma (6).
    A general computational analysis which is applicable to any
reaction scheme is useful as it permits direct calculation of the
absorption or desorption rates once the kinetics of the various
reactions and the physico-chemical parameters are specified. Such
a computational package is also useful for developing a general
program for design of industrial absorbers or desorbers. Compu-
tational aspects of multistep instantaneous reactions have been
analyzed by Bhattacharya and Ramachandran (7). A general formula-
tion and computational procedure for reactions with finite rates
does not appear to have been presented and this paper is directed
towards this objective.

Generalized Model Equations

Consider M species denoted as A_1, A_2, A_i, A_M participating in NR
independent reactions represented as:

$$\sum_{j=1}^{M} \nu_{ij} A_j = 0 \qquad \text{with i = 1 to NR} \qquad (1)$$

where ν_{ij} is the stoichiometric coefficient of the jth species in
the ith reaction (which is taken as positive or negative depend-
ing on whether the particular species is a product or a reactant,
respectively). For generality, all the species will be considered
as volatile in the model equations. In actual practice, some of
the species will be non-volatile and this case can easily be
treated as a particular case of this general analysis by taking
the corresponding gas-film mass transfer coefficients as zero.
    Let r_i be the net rate of the ith reaction at a position x in
the diffusion film (defined such that $\nu_{ij} r_i$ represents the quan-
tity of jth species produced per unit time per unit volume by that
reaction). Then the mass balance equation for the jth species
can be formulated based on the film theory as:

$$D_j \frac{d^2 A_j}{d x^2} = \sum_{i=1}^{NR} \nu_{ij} r_i \qquad \text{with j = 1 to M} \qquad (2)$$

The corresponding equation in dimensionless form is:

$$\frac{d^2 a_j}{d y^2} = \sum_{i=1}^{NR} \frac{\nu_{ij}}{s_j} \Omega_i \qquad \text{with j = 1 to M} \qquad (3)$$

$$\Omega_i = \frac{r_i \delta^2}{D_{ref} A_{ref}} \qquad (4)$$

where Ω_i is the dimensionless rate of the ith reaction, A_{ref} is
any suitable chosen concentration used to non-dimensionalize the
concentrations, and D_{ref} is the diffusivity of a chosen species to
normalize D_j.
    The boundary condition at x = 0 for the jth species is:

$$H_j k_{gj} (A_j^* - A_{js}) = - D_j \left(\frac{dA_j}{dx}\right)_{x = 0} \qquad (5)$$

where A^* is the equilibrium solubility corresponding to the gas

phase concentration of the jth species. The formulation reduces
to the no-flux condition at the interface for species that are
essentially non-volatile by simply setting k_{gj} equal to zero.
Equation 5 can be expressed in dimensionless form as:

$$\gamma_j \, (a_j^* - a_{js}) + \left(\frac{da_j}{dy}\right)_{y=0} = 0 \tag{6}$$

where

$$\gamma_j = H_j \, k_{gj} \, \delta/D_j \tag{7}$$

The second boundary condition is:

$$a_j = a_{jo} \qquad \text{at} \quad y = 1 \tag{8}$$

where a_{jo} are the prescribed dimensionless bulk concentrations.
It may be noted here that if the reactions are assumed to be
sufficiently fast to occur to an appreciable extent in the dif-
fusion film, then the various species can be assumed to be in
chemical equilibrium in the bulk. Thus only (M - NR) bulk
concentrations can be fixed independently for fast reactions.
The dimensionless rate of absorption of a gaseous species
(or desorption of a volatile species) is given as:

$$I_{o,j} = \frac{R_{A,j}}{k_L A_{ref}} = -\left(\frac{da_j}{dy}\right)_{y=o} = \gamma_j (a_j^* - a_{js}) \tag{9}$$

The quantity $I_{o,j}$ also represents the enhancement in rate of
absorption due to chemical reaction. The net rate of consumption
of a non-volatile species in the film is given as

$$D_j \left(\frac{dA_j}{dx}\right)_{x=\delta}$$

Spline Collocation Formulation

In this section, we shall develop the solution procedure based on
the method of orthogonal collocation on finite elements. Carey
and Finlayson (8) have discussed the general details. In this
method, the gas-liquid film is divided arbitrarily into two
regions, 0 to λ and λ to 1, and the collocation method is applied
separately to each of these regions. The method is also known as
spline collocation and λ is called the spline point. The con-
centration profiles in the region 0 to λ are generally steeper
than in the region λ to 1 and hence we shall use for simplicity
only one interior point in the region λ to 1. This point will be

located in the center of this region for convenience. The pro-
gram can be easily modified to include additional points in this
region.
    The following set of equations are then obtained for each of
the species j.
1. Boundary condition at y = 0

$$(A_{11} - \lambda \gamma_j) \; a_j(1) + A_{1N} \; a_j(N) + \lambda \gamma_j \; a_j^* + \sum_{k=2}^{N-1} A_{1k} \; a_j(k) = 0 \quad (10)$$

2. Zero residual at the interior points in the region 0 to λ

$$B_{k1} \; a_j(1) + \sum_{\ell=2}^{N-1} B_{k\ell} \; a_j(\ell) + B_{kN} \; a_j(N) - \lambda^2 \sum_{i=1}^{NR} \frac{\nu_{ij}}{s_j} \; \Omega_i(k) = 0$$

$$\text{with } k = 2 \text{ to } N-1 \quad (11)$$

3. Continuity of flux at y = λ

$$A_{N1} a_j(1) + \sum_{k=2}^{N-2} A_{Nk} a_j(k) + A_{NN} a_j(N) + \frac{\lambda}{1-\lambda}[3a_j(N) - 4a_j(N+1) + a_{jo}] = 0$$
$$(12)$$

4. Zero residual at the interior point in the region λ to 1

$$4 \; a_j(N) - 8 \; a_j(N+1) + 4 \; a_{jo} - (1-\lambda)^2 \sum_{i=1}^{NR} \frac{\nu_{ij}}{s_j} \; \Omega_i(N+1) = 0 \quad (13)$$

    For each species, N+1 equations as defined by Equations 10
to 13 results and the total number of equations to be solved is
M(N+1). (The equations for the various species are coupled
through Ω.) The use of the rank of the stoichiometric matrix to
reduce the dimensionality of the problem [Amundson (9)] may not
be of great advantage here because the interfacial concentrations,
Aj(y=0), are unknown for most of the species.
    A program XSOLVE available on file in Washington University
Chemical Reaction Engineering Laboratory was used to solve the
set of algebraic equations. This program utilizes the Marquardt's
algorithm (10) and combines the best attributes of the steepest
descent method and the Gauss-Newton method. For the cases
examined in this paper, convergence was obtained within 100 iter-
ations for arbitrary starting values. The CPU time to solve 18
equations (N=5, M=3, NR=2) was approximately 6s in double-
precision mode on DEC-20 computer. A rational choice of the
starting values and use of single-precision arithmetic would
reduce the computational time considerably.
    The flux of a diffusing species, j, across the gas-liquid

interface can be obtained from the converged concentration pro-
files as:

$$I_{o,j} = \frac{-1}{\lambda} \left[A_{11} \, a_j(1) + \sum_{k=2}^{N-1} A_{1k} \, a_j(k) + A_{1N} \, a_j(N) \right] \tag{14}$$

Choice of Spline Point

The choice of spline point, λ, is important in order to achieve
the maximum possible accuracy for a given number of collocation
points. As suggested by Carey and Finlayson (8), the magnitude
of mean square residual can be used as a guide to the location
of an optimum value of λ. This quantity defined as

$$\epsilon_j^2 = \int_o^1 \left[\frac{d^2 a_j}{dy^2} - \sum_{i=1}^{NR} \frac{\nu_{ij}}{s_j} \Omega_i \right]^2 dy \tag{15}$$

can be readily calculated, once a converged solution is obtained
for a given λ. It is convenient to calculate the mean square
residuals separately for the two regions

$$\epsilon_{1,j}^2 = \int_o^1 \left[\frac{d^2 a_j}{dz^2} - \lambda^2 \sum_{i=1}^{NR} \frac{\nu_{ij}}{s_j} \Omega_i \right]^2 dz \tag{16}$$

where $z = y/\lambda$
and

$$\epsilon_{2,j}^2 = \int_o^1 \left[\frac{d^2 a_j}{dz_1^2} - (1-\lambda)^2 \sum_{i=1}^{NR} \frac{\nu_{ij}}{s_j} \Omega_i \right]^2 dz_1 \tag{17}$$

where $z_1 = \frac{y-\lambda}{1-\lambda}$
     These residuals can be calculated by fitting a polynomial to
the converged solution and then evaluating the integrals by
Simpson's rule or Gaussian quadrature. The number of quadrature
points to be used should be of the order of 3N in the region 0
to λ.
     Once a converged solution for a given λ is obtained, a new
set of solutions can be obtained by perturbing the value of λ in
either direction. Finally, an optimum of λ can be determined
which minimizes the value of the mean square residual error.

Illustrative Examples

In this section, we shall present some illustrative results
obtained from the program.
1. Pseudo-first order reactions
     The results for a pseudo-first order reaction with γ_1 = 1000
and $\dfrac{k\delta^2}{D_1}$ = 100, is shown in Figure 1. It is seen that a low order
collocation with four total points in the region 0 to λ is suffi-
cient to reasonably match the analytical solution. The effect of
choice of λ is also shown in this Figure. A choice of λ = 0.2 is
inferior and the mean square residual for this case is also
larger. The enhancement factor calculated for this case was
9.854 which is within 0.5% the exact value.
2. Second order reaction with depletion of liquid reactant
     Results for a second order reaction of this type

$$A_1 + A_2 \rightarrow \text{products}$$
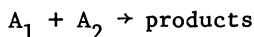
are shown in Figure 2. Here A_2 is chosen as a nonvolatile liquid
phase reactant. Parameters for Figure 2 were $k_1 A_{20} \delta^2/D_1$ = 300,
A_{20}/A_1^* = 3, γ_1 = 1000. The concentration profiles predicted for
λ = 0.4 and 0.5 were almost identical for this case. This implies
that the solution is not strongly sensitive to λ within an
appropriate range. The enhancement factor calculated for this
case was 3.912 while the approximate analytical solution based on
Hikita – Asai (11) method yields a value of 3.948.
3. Two-step reaction
     Concentration profiles generated for a two-step reaction of
this type

$$A_1 + A_2 \rightarrow A_3 \qquad , \qquad \text{rate} = k_1 A_1 A_2$$

$$A_2 + A_3 \rightarrow \text{product} \qquad , \qquad \text{rate} = k_2 A_2 A_3$$
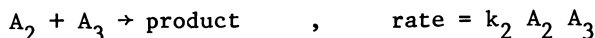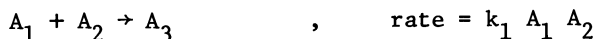
as shown in Figure 3 for $k_1 A_{20} \delta^2/D_1$ = 300, A_{20}/A_1^* = 3,
A_{30}/A_1^* = 0, k_1/k_2 = 1. This problem was first analyzed numer-
ically by Brian and Beaverstock (12). Approximate analytical
solution to this problem is also available (Ramachandran (13)).
Figure 3 has been mainly presented to test the method for multi-
step reaction scheme and hence detailed comparison of the
accuracy of the solution and the influence of the number of
collocation points was not done for this case.

Conclusions

The computational scheme presented here can be used for any reac-
tion scheme with only a user-supplied subroutine for the kinetic
rate form for the various reactions and the physico-chemical
parameters of the system. It can also be used as 'rate
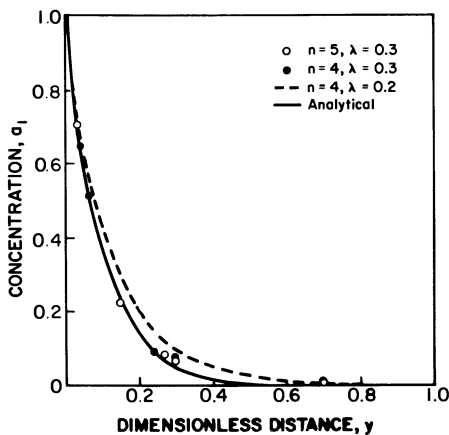
Figure 1. Concentration profiles generated by spline collocation for absorption with a pseudo-first order reaction, $k \, \delta^2/D_1 = 100$, $\gamma_1 = 1000$.
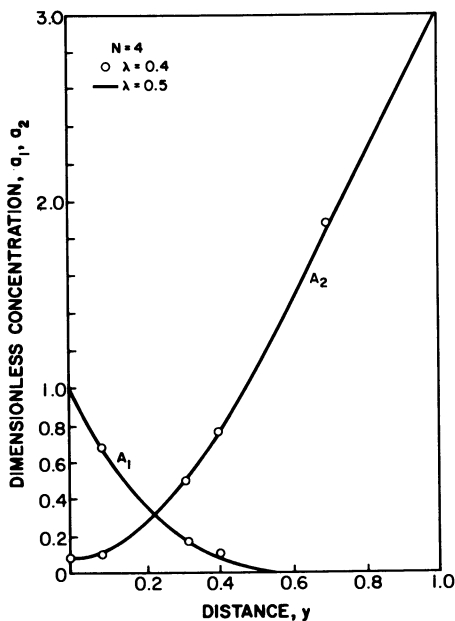
Figure 2. Concentration profiles generated by spline collocation for absorption with a second order reaction, $k_1 \, A_{20} \, \delta^2/D_1 = 300$, $A_{20}/A_{1g} = 3$, $\gamma = 1000$.
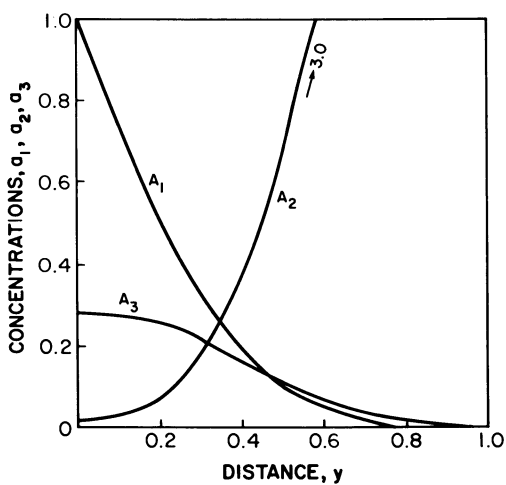
Figure 3. Concentration profiles generated by spline collocation for an absorption with two-step reaction. Parameters are same as in figure 2 with $k_1/k_2 = 1$, $N = 4$, $\lambda = 0.5$.

calculation subroutine' in the design of absorbers such as packed
and plate columns.

Notation

a_j	dimensionless concentration of species A_j at any point in liquid film, A_j/A_{ref}
a_j^*	dimensionless liquid phase concentration of species A_j in equilibrium with the bulk gas
$a_j(k)$	dimensionless concentration of species j at the kth collocation point
$a_j(N+1)$	concentration of species j at the single interior point in λ to 1
a_{js}	dimensionless concentration of A_j at interface (y=0)
a_{jo}	dimensionless concentration of A_j in the bulk liquid
A_j	species A_j or its concentration
A_j^*	liquid phase concentration of species A_j in equilibrium with bulk gas
A_{jg}	concentration of A_j in bulk gas
A_{js}, A_{jo}	concentration of A_j at interface and in the bulk liquid respectively
A_{ref}	a chosen reference concentration used for normalization
A_{ij}	collocation matrix for first derivative in Equations 10 to 14
B_{ij}	collocation matrix for second derivative in Equations 10 to 13
D_j	liquid phase diffusivity for species j
D_{ref}	a chosen diffusivity used for normalization
H_j	Henry's law constant for species j defined as A_{jg}/A_j^*
$I_{o,j}$	dimensionless rate of absorption for j^{th} species (Equation 9)
k	pseudo first-order reaction rate constant
k_L	liquid phase mass transfer coefficient of reference species (A_{ref})
k_{gj}	gas film mass transfer coefficient of species j based on concentration driving force
k_1, k_2	second-order reaction rate constants
M	total number of species taking part in all the reactions
N	total number of collocation points in the region 0 to λ
NR	number of independent reactions
r_i	local rate of ith reaction per unit volume
$R_{A,j}$	rate of absorption of jth species per unit interfacial area
s_j	diffusivity ratio, D_j/D_{ref}
x	distance into the liquid film measured from interface
y	dimensionless distance variable, x/δ

Greek Symbols

γ_j dimensionless group $H_j \, k_{gj} \, \delta/D_{ref}$

δ film thickness

ν_{ij} stoichiometric coefficient of the jth species in the ith reaction

λ position of the spline point which divides the film into two regions

Ω_i dimensionless rate of ith reaction, $r_i \, \delta^2/D_{ref} \, A_{ref}$

ε_j^2 mean square residual for species j

$\varepsilon_{1,j}^2$ mean square residual in 0 to λ for species j

$\varepsilon_{2,j}^2$ mean square residual in λ to 1 for species j

Literature Cited

1. Astarita, G. "Mass Transfer with Chemical Reaction";
    Elsevier: Amsterdam, 1967.
2. Danckwerts, P. V. "Gas-Liquid Reactions"; McGraw-Hill:
    New York, New York, 1970.
3. Savage, D. W. "Recent Developments in Separation Science",
    Vol. VII, N. N. Li, Ed; CRC Press Boca Raton, Florida, 1982.
4. Shah, Y. T. "Gas-Liquid-Solid Reactor Design"; McGraw-Hill:
    New York, New York, 1978.
5. Shah, Y. T.; Sharma, M. M. Trans. Instn. Chem. Engrs. 1976,
    1, 54.
6. Ramachandran, P. A.; Sharma, M. M. Trans. Instn Chem. Engrs.
    1971, 49, 253.
7. Bhattacharya, A.; Ramachandran, P. A. "Mass Transfer
    Accompanied by Multistep Instantaneous Reversible Reactions:
    A Generalized Analysis". 1983. Submitted for publication.
8. Carey, G. F.; Finlayson, B. A. Chem. Eng. Sci. 1975, 30, 587.
9. Amundson, N. R. "Mathematical Methods in Chemical Engineer-
    ing, Vol. I: Matrices"; Prentice-Hall Publishing Company,
    1966.
10. Marquardt, D. W. Journal of the Society for Industrial and
    Applied Mathematics 1963, 2, 11.
11. Hikita, H.; Asai, S. Kagaku Kogaku 1963, 27, 823.
12. Brian, P. L. T.; Beaverstock, M. C. Chem. Eng. Sci. 1965,
    20, 47.
13. Ramachandran, P. A. Chem. Eng. Sci. 1972, 27, 1807.

Modeling of Gas–Liquid Continuous-Stirred Tank Reactors (CSTRs)

A. A. SHAIKH and A. VARMA

Department of Chemical Engineering, University of Notre Dame, Notre Dame, IN 46556

Some specific aspects in the modeling of gas–liquid
continuous-stirred tank reactors are considered. The
influence of volatility of the liquid reactant on the
enhancement of gas absorption is analyzed for irrever-
sible second-order reactions. The impact of liquid
evaporation on the behavior of a nonadiabatic gas-
liquid CSTR where steady-state multiplicity occurs is
also examined.

Previous analyses of the effect of chemical reaction on the rate
of gas absorption have almost exclusively used film- or penetra-
tion-theory models (1–3) which assume the liquid reactant to be
non-volatile. In some industrial applications (4), however,
the liquid is volatile and evaporation of the liquid may there-
fore have important implications.
      In a previous work (5), the film theory was used to analyze
special cases of gas absorption with an irreversible second-
order reaction for the case involving a volatile liquid reactant.
Specifically, fast and instantaneous reactions were considered.
Assessment of the relative importance of liquid reactant volati-
lity from a local (i.e., enhancement) and a global (i.e., reac-
tor behavior) viewpoint, however, necessitates consideration of
this problem without limitation on the reaction regime.
      In the first part of this paper, we therefore generalize the
analysis of the above-mentioned reaction system. An approximate
reaction factor expression is derived without restriction on the
reaction regime, and the accuracy of this factor is tested by
comparison with numerical solutions of the film-theory model.
The relative importance of volatility of the liquid reactant
with respect to the enhancement of gas absorption is analyzed by
using this reaction factor.
      The second part of this paper is devoted to assessing the
influence of liquid evaporation on the steady-state behavior of
gas–liquid CSTRs. The reaction factor expression developed in
the first part is utilized for this purpose.

Enhancement of Gas Absorption

For the irreversible second-order reaction:

$$A_{(g \to \ell)} + \nu B_{(\ell)} \to P_{(\ell)}$$
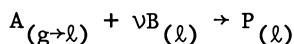
the film-theory model can be cast in dimensionless form as follows:

$$\frac{d^2 a}{d\zeta^2} = M^2 ab \tag{1}$$

$$\frac{d^2 b}{d\zeta^2} = \nu M^2 ab \tag{2}$$

$$\zeta = 0: \quad a = 1 \quad ; \quad \frac{db}{d\zeta} = \gamma' b \tag{3}$$

$$\zeta = 1: \quad \frac{da}{d\zeta} = [M^2(\alpha'-1) + \beta'] a \quad ; \quad b = 1 \tag{4}$$

and the reaction factor is defined by:

$$E_A^* = - \left. \frac{da}{d\zeta} \right|_{\zeta=0} \tag{5}$$

Note that volatility of the liquid reactant is accounted for by the parameter γ' which reflects the magnitude of the equilibrium distribution coefficient relative to that of the liquid-side mass transfer coefficient.

Approximate Solution. Assuming a linear concentration profile for reactant B in the liquid-side film (5):

$$b = b_i + (1-b_i)\zeta \quad , \quad \zeta \epsilon [0,1] \tag{6}$$

an approximate solution of the preceding model is (6):

$$E_A^* = M\sqrt{b_i} \; (\psi_1 + \psi_2 \sqrt{b_i} \; a_\ell) \tag{7}$$

$$b_i = \frac{E_i - E_A^* - a_\ell}{(1+\gamma')(E_i-1)} \tag{8}$$

$$a_\ell = \frac{M\psi_3}{[M^2(\alpha'-1) + \beta'] \sqrt{b_i} + M \sqrt{b_i} \; \psi_4} \tag{9}$$

where ψ_j, j = 1 → 4, are parameters defined below:

$$\psi_1 = (I^\ell_{-1/3} \, I^i_{-2/3} - I^\ell_{1/3} \, I^i_{2/3})/D$$

$$\psi_2 = -\left(\frac{\pi}{\sqrt{3}} \, M'_i \, D\right)^{-1}$$

$$\psi_3 = \left(\frac{\pi}{\sqrt{3}} \, M'_\ell \, D\right)^{-1}$$

$$\psi_4 = (I^i_{-1/3} \, I^\ell_{-2/3} - I^i_{1/3} \, I^\ell_{2/3})/D \qquad\qquad (10)$$

$$D \equiv I^i_{-1/3} \, I^\ell_{1/3} - I^i_{1/3} \, I^\ell_{-1/3}$$

$$I^i_\mu \equiv I_\mu \, (M'_i) \equiv I_\mu \left[\frac{2}{3} \, M \, \sqrt{b_i} \; \frac{b_i}{(1-b_i)} \right]$$

$$I^\ell_\mu \equiv I_\mu \, (M'_\ell) \equiv I_\mu \left[\frac{2}{3} \, \frac{M}{(1-b_i)} \right]$$

where $\mu = \pm\, 1/3,\ \pm\, 2/3$.

   Note that expression 7 for the reaction factor is <u>implicit</u> in nature. However, for relatively high values of the Hatta number: a_ℓ, ψ_2 and $\psi_3 \to 0$, while ψ_1 and $\psi_4 \to 1$; thus the reaction factor becomes <u>explicit</u> in this limit.

<u>Approximate vs. Numerical Solution.</u> The accuracy of the approximate reaction factor expression has been tested over wide ranges of parameter values by comparison with numerical solutions of the film-theory model. The methods of orthogonal collocation and orthogonal collocation on finite elements (7,8) were used to obtain the numerical solutions (details are given by Shaikh and Varma (6)). Comparisons indicate that deviations in the approximate factor are within few percents (< 5%). It should be mentioned that for relatively high values of Hatta number (M >20), the asymptotic form of Equation 7 was used in those comparisons.

<u>Volatile vs. Non-Volatile Liquid Case.</u> The effect of the parameter γ' on the reaction factor is shown in Figure 1, where the reaction factor of the corresponding non-volatile case (i.e., when $\gamma' = 0$), is also shown. It is clear that the volatile nature

of the liquid reactant is detrimental to the enhancement of gas
absorption. Figures 2a and 2b reveal the influence of the para-
meter rq on enhancement, as well as the relative effect of vola-
tility of the liquid reactant. Note that while volatility can
be markedly detrimental to enhancement, its effect is not sig-
nificant in the slow- and instantaneous-reaction regimes. The
regions of influence of liquid reactant volatility are shown more
clearly in Figure 3.

Steady-State Reactor Behavior

The occurrence of steady-state multiplicity in gas-liquid CSTRs
has been demonstrated in experimental (9) and theoretical inves-
tigations (cf., 10). The irreversible second-order reaction
system, in particular, has been treated extensively in several
theoretical studies (10-15). These studies are however based on
neglecting energy and material losses which result from evapora-
tion of the liquid.
     In this section we develop a model to simulate the behavior
of a nonadiabatic gas-liquid CSTR taking into account volatility
of the liquid reactant. The model is then tested for its capa-
bility to predict some experimental results.

Reactor Model. The following assumptions are made in the de-
velopment of the model:
1.   The physical and thermal properties of the gas and liquid,
     interfacial area and liquid holdup, physical mass transfer
     coefficients, diffusion coefficients, and volumetric flow
     rate of the liquid are independent of temperature and con-
     version.
2.   The liquid feed is free of any dissolved gaseous reactant.
     The gas feed contains species A and other inert species.
3.   The gas and liquid are at the same temperature inside the
     reactor. The gas effluent is saturated with vapor of spe-
     cies B, and passes through an ideal condenser. The conden-
     sate is returned continously to the reactor.
4.   The total pressure is independent of position and tempera-
     ture.
5.   Phase equilibria of the gaseous reactant follows Henry's
     law, and that of the liquid reactant follows Raoult's law.
6.   The gas-side mass-transfer resistance and volatility of the
     liquid product are both negligible.
7.   The ideal gas law and Arrhenius' law hold.

     The steady-state reactant conversions, x_A and x_B, and dimen-
sionless reactor temperature, θ, are thus given by (see (16) for
details):

$$x_A(1-y_{Af}x_A) - D_g E_A^*(1-y_B)(1-x_A) \exp\left[\delta(1+\theta)^{-1}\right] = 0 \qquad (11)$$
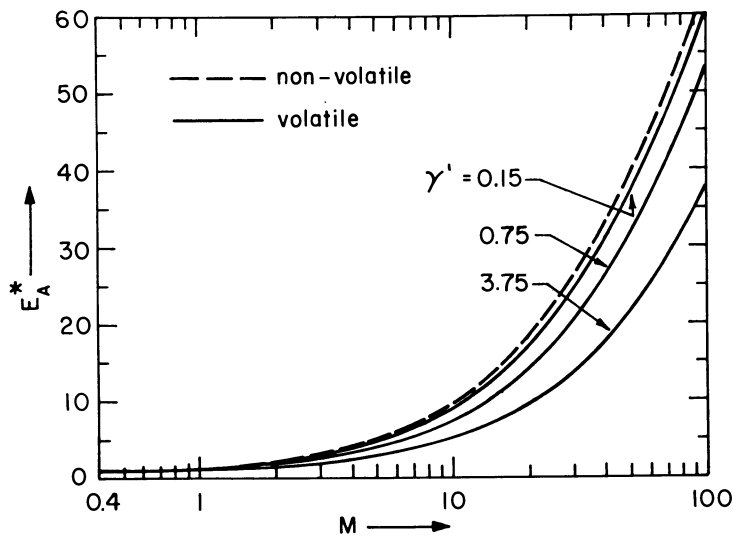
Figure 1.   Effect of liquid volatility on the reaction factor; rq = 100, α' = 50, and β' = 0.01 (6).
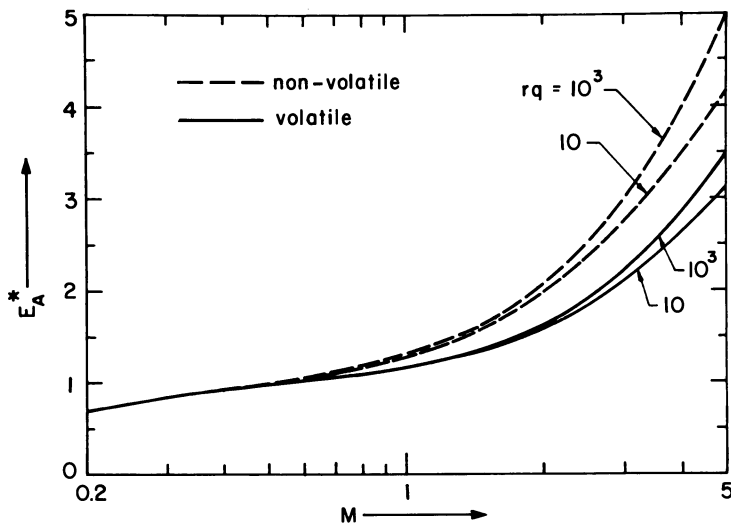
Figure 2a.   Effect of the group (rq) on the reaction factor; α' = 50, β' = 0.01, and γ' = 1.5 (6).

Figure 2b. Effect of the group (rq) on the reaction factor; $\alpha' = 50$, $\beta' = 0.01$, and $\gamma' = 1.5$ (6).
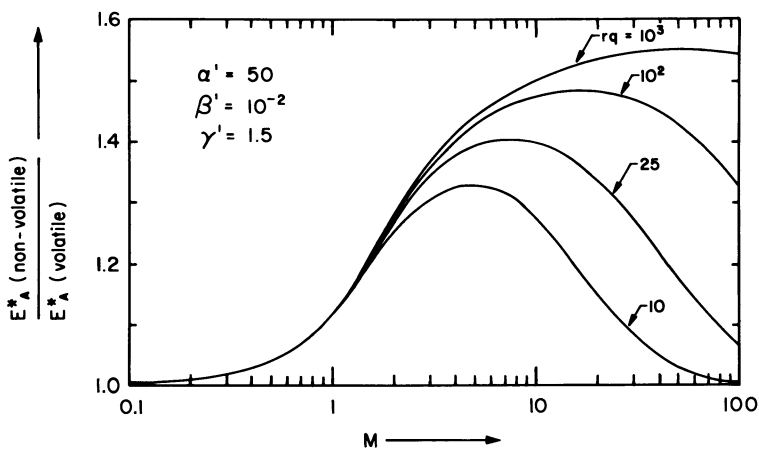
Figure 3. Effect of Hatta number and the group (rq) on the ratio of reaction factors for volatile and non-volatile liquid (6).

$$q_f(x_B + \nu a_{\ell f}) \quad - \quad \nu Q x_A \quad = \quad 0 \tag{12}$$

$$- \left[Q^{-1} + R(1 - y_{Af} x_A) \right] \theta \quad + \quad BD_g E_A^* \ (1 - y_B) \ (1 - x_A)$$

$$(1 - y_{Af} x_A)^{-1} \quad \exp \left[\delta (1 + \theta)^{-1} \right] + (R + \nu \tilde{y}_B) \ y_{Af} x_A$$

$$+ \ R(\theta_r - 1) \ - \ \nu \tilde{y}_B \ - \ p q_f a_{\ell f} \ - \ \beta(\theta - \theta_c) = 0 \tag{13}$$

where y_B is mole fraction of the liquid vapor and $\tilde{y}_B = y_B(1 - y_B)^{-1}$.
Note that now E_A^* is given by Equation 7. It is also worth men-
tioning that Equations 11-13 reduce to the corresponding expres-
sions presented earlier (10) when $y_{Af} \ll 1$, $y_B = 0$, and $\theta_r = 1$.

Equations 11 and 13 can be combined to yield a <u>single</u> non-
linear equation for the reactor temperature that can be solved
numerically. It can also be shown (16) that the steady-state
temperature is bounded by:

$$\frac{\beta \theta_c + R(\theta_r - 1) - \nu \tilde{y}_B}{\alpha + \beta} \ \leq \ \theta \ \leq \ \frac{B + R y_{Af} + \beta \theta_c + R(\theta_r - 1)}{\alpha + \beta - R y_{Af}} \tag{14}$$

<u>Model vs. Experimental Results</u>. The model described by the pre-
ceding equations was used to simulate the behavior of an ex-
perimental gas-liquid CSTR (chlorination of n-decane (9)), and
its predictions were compared to those of a model in which the
liquid volatility is neglected. The physicochemical parameters
used in the simulation are given elsewhere (10, 16), and the
computational procedure adopted to solve for θ is also reported
elsewhere (16).

Figure 4 shows the temperature-liquid residence time pre-
dictions of the two models and the experimental results of Ding
et al. (9); note that the empty squares represent unstable
steady states. It is clear that the two models give identical
predictions of the lower-temperature branch, whereas predictions
of the higher-temperature branch are markedly different in each
case. This branch is predicted rather well by the model which
accounts for evaporation, while the other model gives signifi-
cantly higher values. The extinction value of τ_ℓ predicted by
the volatile liquid model is also very close to the experimental
value, whereas the other model predicts a relatively much lower
value. We also found that two additional high-temperature
branches (not shown in Figure 4) are predicted by the non-vola-
tile liquid model.

These differences in predictions between the two models can
be explained by examining Figure 5, where $y_B - \tau_\ell$ predictions of
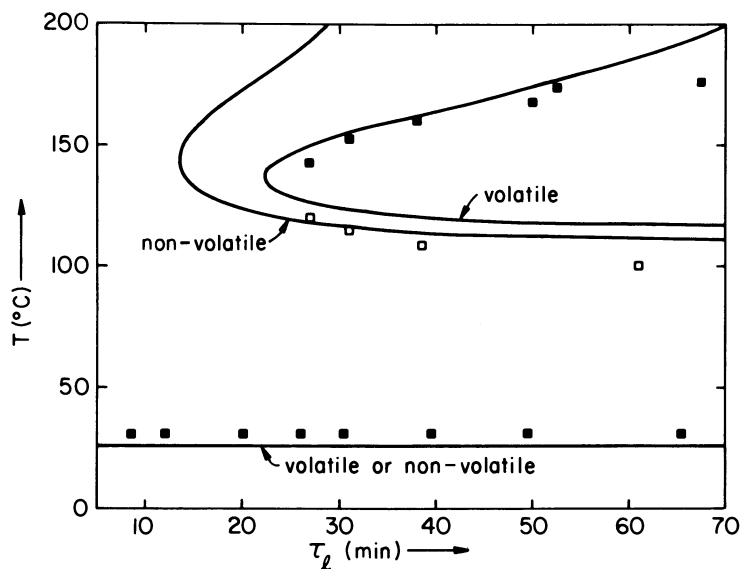
Figure 4. Model predictions of reactor steady-state temperature with experimental results.
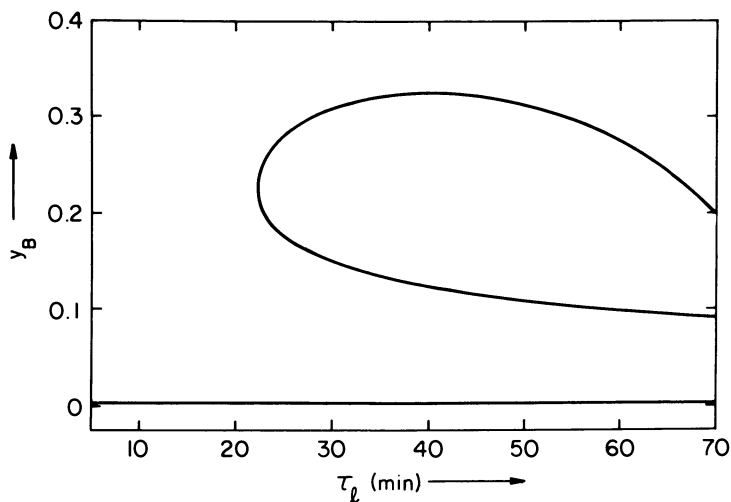
Figure 5. Effect of liquid residence time on mole fraction of vapor of the liquid reactant.

the model which accounts for evaporation are shown. It can be observed that y_B values corresponding to the lower-temperature branch are virtually zero, and as a result the two models should yield identical predictions. On the other hand, evaporation of the liquid is significant ($y_B \sim 20\text{-}30\%$) at the higher-temperature branch. Consequently, the use of a model in which evaporation is neglected can lead to erroneous results regarding the number and regions of multiple steady states.

Concluding Remarks

It is demonstrated that volatility of the liquid reactant has a detrimental effect on the enhancement of gas absorption. It is also shown that failing to account for effects due to liquid evaporation in the modeling of gas-liquid CSTRs can lead to significantly different predictions of the number and region of multiple steady states.

It is important to recognize that results of this study are based on models which involve several assumptions. The validity of some of these assumptions may be questionable under certain circumstances. However, gas-liquid reaction systems involve complex interacting events, which are difficult to describe precisely. There is also a paucity of experimental data on the behavior of gas-liquid reactors. In view of all this, we believe that studies of this type can be valuable qualitatively for the purpose of model discrimination.

Legend of Symbols

A	liquid phase concentration of gas
a	A/A_i
$a_{\ell f}$	$A_\ell / B_{\ell f}$
$\underline{a}$	interfacial area per unit reactor volume
B	liquid phase concentration of liquid
B	$(-\Delta H_S - \Delta H_R)\, A_{gf} / \rho_\ell C_{p\ell} T_{\ell f}$
b	B/B_ℓ
C_p	molar heat capacity
D_A, D_B	diffusion coefficients
D_g	$k_\ell^o \underline{a} V_R H_o / F_{gf}$

E_i $(1+rq)$

F volumetric flow rate

H_o Henry's law coefficient

$\Delta H_{R,S,V}$ heat of reaction, solution, or vaporization

I_μ the modified Bessel function of the first kind

K_B equilibrium constant for liquid

k reaction rate constant

k_g^o gas-side mass-transfer coefficient

k_ℓ^o liquid-side mass-transfer coefficient

M Hatta number, $\sqrt{kD_A B_\ell}/k_\ell^o$

p $(-\Delta H_R)\, F_\ell A_{gf}/F_{gf}\rho_\ell\, C_{p\ell} T_{\ell f}$

p_B partial pressure of species B

Q F_{gf}/F_ℓ

q B_ℓ/A_i

q_f $B_{\ell f}/A_{gf}$

R $\rho_{gf} C_{pg}/\rho_\ell C_{p\ell}$

R_g universal gas constant

r $D_B/\nu D_A$

S reactor cooling area

T, T_c temperature, cooling medium temperature

U heat transfer coefficient

V_R reactor volume

v $(-\Delta H_V)\rho_{gf}/\rho_\ell\, C_{p\ell}\, T_{\ell f}$

x conversion

y mole fraction

z distance in liquid from interface

Greek Letters

α $(Q^{-1}+R)$

α' $\varepsilon_\ell k_\ell^o / \underline{a} D_A$

β $US/F_{gf} \rho_\ell C_{p\ell}$

β' $\varepsilon_\ell / \underline{a} k_\ell^o \tau_\ell$

γ' $(D_A k_g^o K_B / D_B k_\ell^o) \ (1 - p_{Bg}/p_{Bi})$

δ $(-\Delta H_S)/R_g \ T_{\ell f}$

δ' thickness of liquid-side film

ε_ℓ liquid holdup

ζ z/δ'

θ $(T/T_{\ell f}) - 1$

ϑ_r $T_{gf}/T_{\ell f}$

ν stoichiometric coefficient

ρ molar density

τ_ℓ residence time of liquid

Subscripts

f   feed

g   gas phase

i   gas-liquid interface

ℓ liquid phase

Literature Cited

1. Astarita, G. "Mass Transfer with Chemical Reaction";
    Elsevier: Amsterdam, 1967.
2. Danckwerts, P. V. "Gas-Liquid Reactions"; McGraw-Hill:
    New York, 1970.

3. Charpentier, J.-C. in "Advances in Chemical Engineering"; Drew, T. B.; Cokelet, G. R.; Hoopes, Jr., J. W.; Vermeulen, T., Eds., Academic Press: New York, 1981; Vol. 11, p. 1.
4. Shah, Y. T.; Sharma, M. M. Trans Instn. Chem. Engrs. 1976, 54, 1.
5. Pangarkar, V. G. Chem. Eng. Sci. 1974, 29, 877.
6. Shaikh, A. A.; Varma, A. Chem. Eng. Sci. (submitted for publication).
7. Villadsen, J.; Michelsen, M. L. "Solution of Differential Equation Models by Polynomial Approximation"; Prentice-Hall: Englewood Cliffs, New Jersey, 1978.
8. Finlayson, B. A. "Nonlinear Analysis in Chemical Engineering"; McGraw-Hill: New York, 1980.
9. Ding, J. S. Y.; Sharma, S.; Luss, D. Ind. Eng. Chem. Fundam. 1974, 13, 76.
10. Huang, D. T.-J.; Varma, A. AIChE J. 1981, 27, 481.
11. Hoffman, L. A.; Sharma, S.; Luss, D. AIChE J. 1975, 21, 318.
12. Raghuram, S.; Shah, Y. T. Chem. Eng. J. 1977, 13, 81.
13. Raghuram, S.; Shah, Y. T.; Tierney, J. W. Chem. Eng. J. 1979, 17, 63.
14. Huang, D. T.-J.; Varma, A. Chem. Eng. J. 1981, 21, 47.
15. Singh, C. P. P.; Shah, Y. T.; Carr, N. L. Chem. Eng. J. 1982, 23, 101.
16. Shaikh, A. A.; Varma, A. Chem. Eng. Sci. (submitted for publication).

The Effect of Gas and Liquid Velocities and Solid Size on Solid Suspension in a Three-Phase Bubble Column Reactor

BARRY W. BRIAN and PAUL N. DYER

Air Products and Chemicals, Inc., Allentown, PA 18105

In the design of upflow, three phase bubble column reactors, it is important that the catalyst remains well distributed throughout the bed, or reactor space time yields will suffer. The solid concentration profiles of 2.5, 50 and 100 μm silica and iron oxide particles in water and organic solutions were measured in a 12.7 cm ID bubble column to determine what conditions gave satisfactory solids suspension. These results were compared against the theoretical mean solid settling velocity and the sedimentation diffusion models. Discrepancies between the data and models are discussed. The implications for the design of the reactors for the slurry phase Fischer-Tropsch synthesis are reviewed.

Three phase, upflow, bubble column reactors are used in the process industry because of their simplicity and good liquid mixing characteristics, without the need for mechanical agitation. While current applications include hydrogenation and fermentation, slurry bubble columns have recently been the subject of renewed study for use in two areas of hetergeneous catalysis, SRC coal liquefaction and the Fischer-Tropsch reaction to produce hydrocarbons from synthesis gas.

An important aspect of the design of three phase bubble columns is the variation of catalyst distribution along the reactor height, and its effect on reactor performance. Many factors influence the degree of catalyst distribution, including gas velocity, liquid velocity, solid particle size, phase densities, slurry viscosity, and, to a lesser extent, column diameter, solid shape and chemical affinity between the solid and liquid phases.

Three phase bubble column reactors are of interest for Fischer-Tropsch synthesis because of their following characteristics:

(a) a high heat axial dispersion and isothermicity,
(b) excellent control of the reaction exotherm, leading to lower
yields of CH_4,
(c) the ability to accept CO rich syngas and produce higher mole-
cular weight products, without the coking or plugging that is
inherent with other reactor types.

As part of the work undertaken by APCI under contract to the
DOE, to develop a slurry phase Fischer-Tropsch process to produce
selectively transportation fuels, a study of the hydrodynamics
of three phase bubble column reactors was begun using cold flow
modelling techniques (1). Part of this study includes the
measurement of solid concentration profiles over a range of inde-
pendent column operating values.

Roy, et al (2) empirically determined the gas velocity
needed to completely suspend a given amount of solid in a 5 cm id
x 1.52 m Lucite column using coal and quartz slurried in water,
alcohol, or oil. The degree of suspension was found to depend
on physical properties as well as gas holdup, volume fraction,
bubble diameter, and the contact angle between the solid and
liquid.

Cova (3) measured the solid concentration profiles of a
Raney nickel catalyst with an average diameter of 15.7 µm in a
4.6 cm id reactor, using water and acetone as the liquids. He
developed a sedimentation diffusion model, assuming solid and
liquid dispersion coefficients were equal, and slurry settling
velocities were independent of solid concentration. The model
was then applied to data for Raney nickel in 6.35 and 44.7 cm
id bubble columns, in both cocurrent and countercurrent flow.

Imafuku, et al (4) measured the solid concentration profiles
of several solids in 5, 10 and 20 cm columns, in water and
aqueous glycerine. The solid particles ranged from 64 to 180 µm
in diameter, and included glass spheres, iron silicate and copper
powders. They measured solid dispersion coefficients, confirming
Cova's assumption of equal liquid and solid dispersion coeffi-
cients, and developed an empirical correlation between the ob-
served terminal settling velocity in a three phase system, and
the calculated terminal settling velocity of a single particle
in a stagnant liquid.

Kato, et al (5) measured solid concentration profiles, solid
dispersion coefficients and terminal settling velocities for
glass spheres in water, using 6.6, 12.2 and 21.4 cm bubble
columns. They developed a dimensionless, empirical correlation
for the solid dispersion coefficients which agreed with their
observed values to within ±20%.

Sivasubramanian, et al (6) and Moujaes, et al (7) measured
solid concentration profiles of sand in water and ethanol/water,
using 12.7 and 30.5 cm bubble columns. They developed a solids
accumulation model, which correlated successfully with an actual
30.5 cm solvent refined coal dissolver.

The work described in this paper extends the understanding of solid concentration profiles in three phase bubble column reactors, with emphasis on the Fischer-Tropsch synthesis, by:
1) utilizing C_9-C_{11} hydrocarbon liquid as the slurry base,
2) using solids similar to Fischer-Tropsch bulk and supported catalysts, and
3) modelling operating conditions typical of slurry phase Fischer-Tropsch reactors, including the use of internal heat transfer elements and a variation in gas distributor plate.

The limitations of the sedimentation-diffusion model for describing solid dispersion in these systems are discussed.

Theoretical

Solid concentration profiles are produced from a balance of gravitational with buoyancy and kinetic energy transfer forces. For a single particle in a stagnant liquid, the settling velocity, V_P, is given by (8):

$$V_P = \left(\frac{4}{3} \frac{g\ d_S}{f} \left(\frac{\rho_S - \rho_L}{\rho_L} \right) \right)^{\frac{1}{2}}$$ (1)

where f, the Fanning friction for spheres, is a function of Reynolds number,

$$f = \begin{cases} 24/Re & Re < 1 & (2a) \\ 18.5\ Re^{3/5} & 1 < Re < 1000 & (2b) \\ 0.44 & 1000 < Re < 20{,}000 & (2c) \end{cases}$$

For a slurry system with no gas phase, a single particle sees the properties of the slurry, not the liquid. Also, because the particles make up a sizable fraction of the total volume, the liquid can no longer be considered stagnant, but moves upward to displace the volume of falling solid by

$$V_L = \frac{\epsilon_S V_{ST}}{\epsilon_L} = \frac{W_S \rho_L V_{ST}}{W_L \rho_S}$$ (3)

where

$$V_L = V_{SU}/(1 - \epsilon_G)$$ (4)

For d_S 50 m, equations 1, 2a and 3 give the following expression for the particle settling velocity in a slurry:

$$V_{ST,\ CALC} = g\ d_S^2\ (\rho_S - \rho_{SL})/(18\ \mu_{SL}\ (1 + W_S \rho_L/W_L \rho_S))$$ (5)

Introducing the third, gaseous phase to the reactor changes the environment considerably. A large amount of mixing is introduced by the gas bubbles, carrying slurry in their wakes (9). This high degree of mixing has successfully been modeled by a one dimensional diffusion mechanism, i.e. diffusion superimposed on the superficial slurry flow, for both the liquid (10-11) and the solid phases (4-5), in both the continuous (positive slurry velocity) and batch (zero slurry velocity) operating modes.

From Cova (3) and Kato (5) for continuous flow of both gas and slurry:

$$C_2 = \left[C_H / (V_L - V_{ST}) \right] \left(V_L - V_{ST} \ \exp \ \left[(V_L - V_{ST})(Z_2 - L)/E_{ZS} \right] \right) \qquad (6)$$

For batch operation with $V_L = 0$,

$$C_2 = C_1 \ \exp \ \frac{-V_{ST}}{E_{ZS}} \ (Z_2 - Z_1) \qquad (7)$$

The value of the solid dispersion coefficient, E_{ZS}, may be calculated from the experimental data as follows, with the assumption that E_{ZS} is independent of V_L.

The steady state concentrations from an identical batch and continuous run are measured at two or more points. Equation 7 can be rewritten as

$$\frac{\ln C_2 / C_1}{Z_1 - Z_2} = \frac{\Delta \ln C}{\Delta Z} = \frac{+V_{ST}}{E_{ZS}} \qquad (8)$$

A plot of ln C vs. Z for the batch run, therefore, yields a straight line with a slope of $-V_{ST}/E_{ZS}$. Equation 6 can be rewritten as;

$$V_L / E_{ZS} = (V_{ST} / E_{ZS}) \ \exp \ (D(Z_2 - L)) - (C_2 / C_H) D \qquad (9)$$

where

$$D = (V_{ST} / E_{ZS} - V_L / E_{ZS}) \qquad (10)$$

The three upper slurry samples taken for each solid concentration profile, along with equation 9, provided three independent equations, from which two parameters, V_L / E_{ZS}, a least squares technique was used to estimate the two parameters. Since V_L is known, experimental values for E_{ZS} and V_{ST} were then independently determined.

Experimental

Apparatus. Experiments were conducted in a 12.7 cm id x 1.52 m
Plexiglass and 30.5 cm id x 475 cm borosilicate glass column (1)
(see Figure 1). Four ports to sample the solid concentration
were mounted at approximately 9, 38, 76 and 114 cm above the per-
forated plate distributor in the 12.7 cm column, and 2, 15, 302,
and 453 cm in the 30.5 cm column.

Table I shows the size ranges and concentrations of the
slurries of silica and iron oxide in isoparaffin and water, that
were utilized in the tests. From the stirred, baffled reservoir
tank, which was approximately the same volume as the columns,
slurry was pumped with a diaphragm pump, using a tranquilizer to
even out the flow, into the bottom of the 12.7 cm column, and
above the distributor for the 30.5 cm column. In the 12.7 cm
column, therefore, slurry passed with the gas through the distri-
butor plate for V_L >0. At the top of the column, the slurry was
separated from the gas, and returned by gravity to either the
reservoir tank, or to a calibrated volume used for slurry flow
measurement.

Nitrogen or air was metered with a rotameter in the 12.7 cm
column, and with a differential pressure cell in the 30.5 cm
column, and entered the columns beneath the distributor plate.

With the highest slurry loadings, a small gas sidestream was
also used in the slurry feed to facilitate pumping from the reser-
voir to the column.

For the 12.7 cm column, the gas and slurry distributor was
1.25 mm thick, with a 10% to 13% open area of 0.9 mm holes. The
30.5 cm column used different 0.3% open area, distributor plates,
with 0.9, 3.2 and 12.7 mm diameter holes. The gas traveled with
the slurry, separated at the column top, and passed through a
demister pad, liquid trap, and rotameter before being vented.
All metal parts were grounded to prevent electric arcing during
experiments with the non-conducting hydrocarbon liquid.

Experimental Procedure. Gas flow was initially fed to a column
approximately 2/3 full of slurry. After the gas flow rate was
set, the slurry flow was started and adjusted using the calibrated
volume. Flow rates were held constant during the runs, which
lasted 45 to 75 minutes for the 12.7 cm column, and 180 minutes
for the 30.5 cm column. At the end of this time, slurry samples
were taken, starting at the top of the column and working down,
so as not to disturb upstream conditions. All slurry ports were
purged before taking a sample, and stopcocks were turned quickly
to full open and full closed to prevent settling of slurry within
the sample line.

Hydrocarbon slurries were analyzed by filtration on a tared
micropore polymer funnel, using a pentane wash. Water based
slurries were analyzed by oven evaporation. Control tests using
slurries of known weight percent gave an absolute accuracy within
0.1% for both methods.
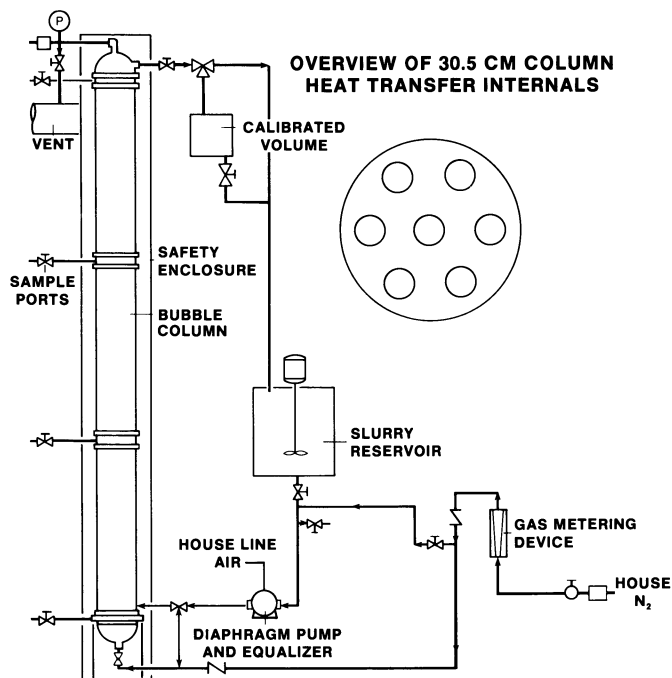
Figure 1.   12.7 and 30.5 cm column schematic.

Table I.   Range of Operating Conditions
Slurry medium	:Isoparaffin, water
Superficial gas velocity	:1.5-16.4 cm/sec
Superficial liquid velocity	:0.0-3.0 cm/sec
Solid (density)	:Silicon oxide (2.6), iron oxide (5.2 g/cm^3)
Solid size	:1-5, 45-53, 90-106 μm
Solid concentration	:0, 10, 20, 30 wt%
Column diameter	:12.7, 30.5 cm

Additional 30.5 cm Column Variables

Heat transfer internals	:None, plain
Distributor hole size	:0.9, 3.2, 12.7 mm

The range of operating conditions for the 276 experimental
runs in the 12.7 cm column and 20 experimental runs to date in the
30.5 cm column are shown in Table I. Relevant physical properties
of the liquids are listed in Table II., and compared with esti-
mated data for the slurry phase Fischer-Tropsch pilot plant
reactor at Rheinpreussen (12). Solid densities were obtained from
the literature (13). As received, the isoparaffin (14) sample
was saturated with water. However, this ppm level of water was
soon removed during the initial experiments by the dry nitrogen
gas. Additional isoparaffin was added when required to maintain
the solid concentration weight percent. All water based runs
used humidified air.

Results

Effect of Particle Size on Solid Concentration Profiles. Figures
2 (a and b) and 3 (a and b) show the dominant effect that particle
size has on the suspension of solids in a three phase bubble
column, without mechanical agitation. Examples in each figure
were chosen to represent as closely as possible identical opera-
ting conditions. While a known solid weight fraction was charged
to the total system, the resulting distribution of solid between
reservoir and column made it difficult to match average solid
weight fractions in the column precisely. In each figure, there-
fore, it is the profile slope, and not the actual weight fraction
values, which determine how well the solid is suspended.
    In every case, as expected by theory, larger particle sizes
produced greater solid concentration slopes. In the 30.5 cm
column, no effect from the heat transfer internals on solid con-
centration profiles was observed for any of the three size ranges
studied.

Table II. Physical Properties of Liquids

Liquid	Temp. °C	Surface Tension N/m	Viscosity Kg/m·s	Density g/cm³	Gas Diffusivity cm²/s	Specific Heat J/g °K	Thermal Conductivity W/m °K
Water	20	72.7×10^{-3}	1.00×10^{-3}	1.00	2.5×10^{-5} (O_2)	4.187	0.477
Isoparaffin	20	22×10^{-3}	1.20×10^{-3}	0.73	1.2×10^{-5} (O_2)*	2.09	0.17
Rheinpreussen-type paraffinic oil*	260	11×10^{-3}	0.33×10^{-3}	0.67	8×10^{-5} (CO)	2.93	0.13

*Estimated
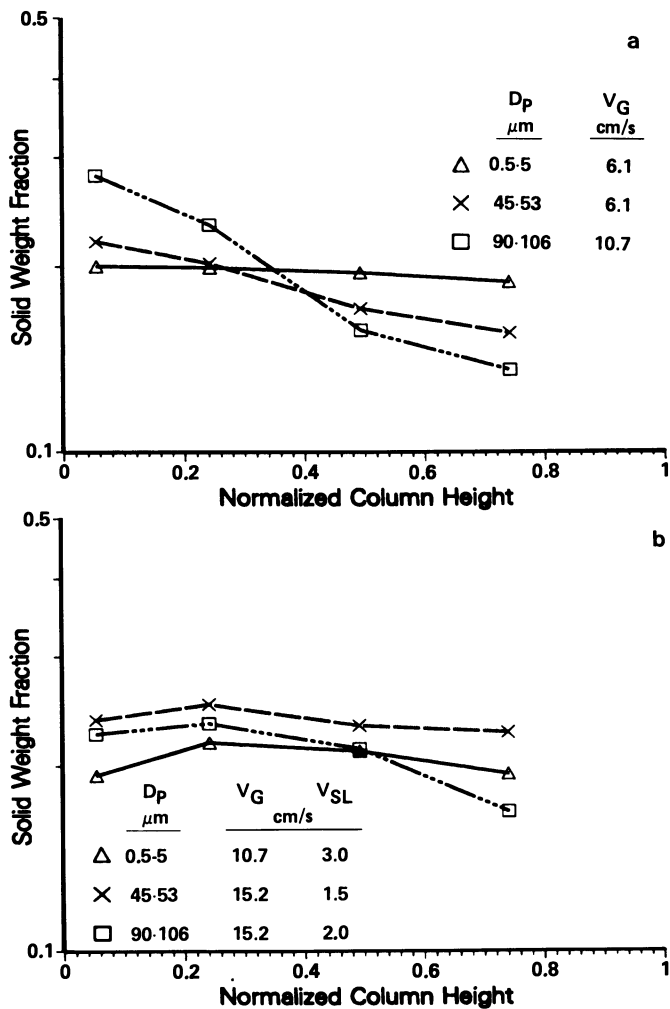
Figure 2. Particle size effect on solid profiles, iso-
paraffin, iron oxide, N_2. (a) Batch system, zero liquid
velocity. (b) Continuous system, positive liquid velocity.
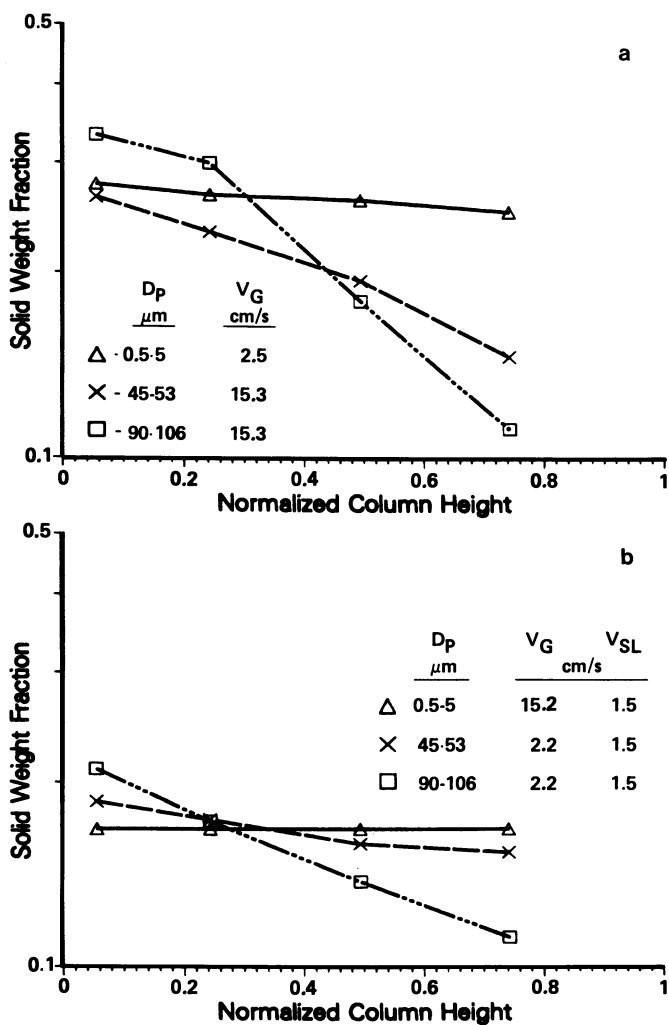
Figure 3. Particle size effect on solid profiles, iso-paraffin, silicon oxide, N_2. (a) Batch system, zero liquid velocity. (b) Continuous system, positive liquid velocity.

Effect of Slurry Velocity on Solid Concentration Profiles.
Figures 2a and 2b show axial solid concentration profiles for the
iron oxide system in batch and continuous mode, respectively.
Figures 3a and 3b show the same information for the silicon oxide
system. For both systems, concentration profiles were much more
uniform in continuous mode than in batch mode. This is to be
expected from equation 6, because of the dependence shown on the
difference between the solids settling velocity and the upward
slurry velocity.

Solid/Liquid Interaction Effects. Figures 4a and 4b show the
effect of different solid/liquid pairs on solid concentration
profiles. In 4a and 4b, the steepest profiles were observed for
the silicon oxide/isoparaffin and iron oxide/water systems. The
other solid/liquid pairs, silicon oxide/water and iron oxide/
isoparaffin, gave much less pronounced concentration profiles, and
in fact, for the continuous runs, were essentially horizontal.

Discussion

Solids Settling Velocity. Solids settling velocities, $V_{ST_{OBS}}$,
were calculated from 84 experimental runs on the 12.7 cm column.
Figure 5 plots the observed solid settling velocity ($V_{ST_{OBS}}$) as
determined from equations 8 and 9 against the theoretically
derived solid settling velocity obtained from equation 5, for all
four combinations of solid/liquid pairs. A considerable spread
of values is observed. This is because a small change in solid
weight fraction can cause a wide change in calculated solids
settling velocity when solid profiles are nearly horizontal. In
spite of this spread, qualitative differences are evident in com-
paring the silicon oxide and iron oxide results in Figure 5.
While there appears to be some agreement between the observed and
theoretical iron oxide solids settling velocities, the observed
silicon oxide values appear to be several times greater than
expected. This difference in behavior of the silicon oxide and
iron oxide slurries cannot be accounted for by density effects.
Since the ratio of the density of iron oxide and silica is ~2.14,
the predicted V_{ST} for an iron oxide would be ~3.8 times greater
than for silica. Further work is needed to determine the critical
characteristics of a solid that are important in governing its
settling velocity.

Solid Dispersion Coefficients. Solid dispersion coefficients,
E_{ZS}, were calculated from the same 84 experimental runs as the
solid settling velocity results. Many of the solid concentration
profiles for the 0.5–5 μm size particles were uniform to within
0.2 weight percent. As uniform profiles suggest an infinite
dispersion coefficient, scatter for the smallest size particles
was too large to be included in the analysis. For the iron oxide
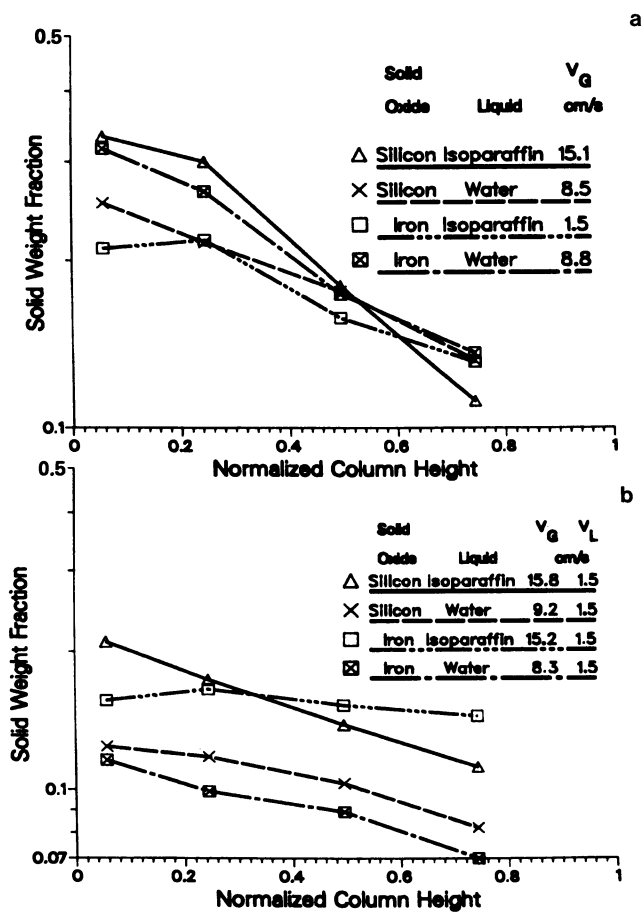
Figure 4. Particle type and liquid effect on 90–115 μm
solid profiles. (a) Batch system. (b) Continuous system.
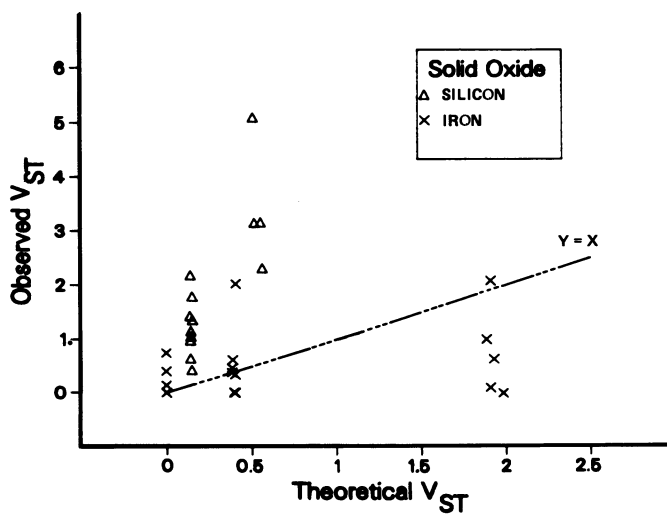
Figure 5. Solids settling velocity, observed vs. theoretical, isoparaffin system.

system, the values were in the same range as predicted by Kato, et al (5),

$$P_e = \frac{13 \; F_r}{1 + 8 \; F_r^{0.85}}$$

(11)

although a scatter of ±100% was still too large for quantitative analysis. The silicon oxide/isoparaffin system gave better agreement with the Kato correlation, and in Figure 6, they are graphically compared. Although there is still scatter in this plot, the results seem to conform to Kato's empirical analysis, confirming the assumption of equal liquid and solid dispersion coefficients for this system.

Effect of Solid Concentration Profiles on Reactor Performance.
If a three phase bubble column is operated in a regime without significant diffusional limitations, and with high liquid axial dispersion and complete solid suspension, the effects of a non-uniform solid catalyst profile are expected to be minimal for the reactor space time yield, although product selectivity may be affected in the case of the Fischer-Tropsch synthesis. However, if the reactor is operated in a regime with a significant diffusional resistance, as is likely in an ultimate commercial design, any nonuniformity in the solid catalyst suspension profile will become more important, because of the effect of local solid loading in gas to liquid mass transfer. In tests of a 14.7 wt% slurry of reduced Fe_2O_3 catalyst, utilizing a stirred reactor with 1.4:1 CO/H_2 at 3.2 MPa, significant gas to liquid mass transfer resistance was observed at T >250°C in the range 800-1600 rpm (1, 15). Therefore, it is anticipated that nonuniformity in solid suspension will be an important consideration in the performance of a Fischer-Tropsch bubble column reactor, and this will be the subject of further work.

If the catalyst is not completely suspended, reactor space time yields could be adversely affected even without significant diffusional limitations. The sedimentation diffusion model predicts a straight line when the log of the solid weight fraction is plotted against column height. At the onset of solid settling, however, both V_{ST} and E_{ZS} will decrease, leading to a more negative gradient (equations 6 and 8). This can be seen in Figure 7, where the solid weight fraction at the lowest port is more than twice the value extrapolated from the upper three ports. Figure 7 shows that this effect occurs both with and without heat transfer internals. The effect is also independent of the gas distributor hole size. For >90 μm particle size, the maximum average solid concentration that can be suspended appears to be a practical constraint to the loading of a silicon oxide supported catalyst, and is ~20 wt% for this height reactor.
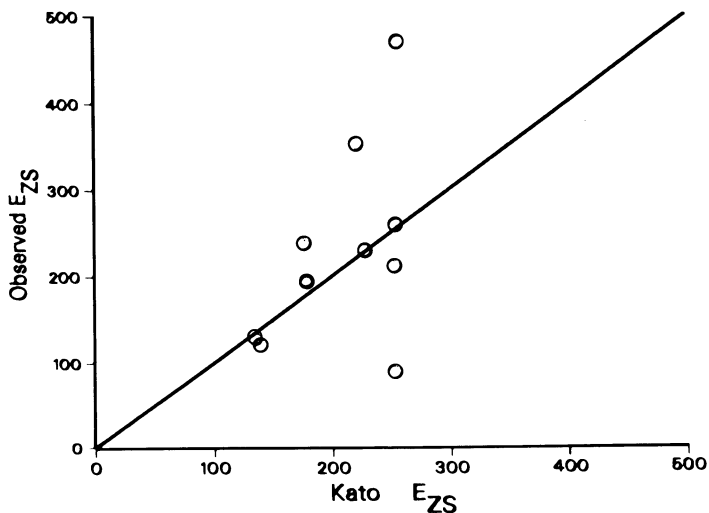
Figure 6.   Solid dispersion coefficient, literature comparison, silicon oxide, isoparaffin system.
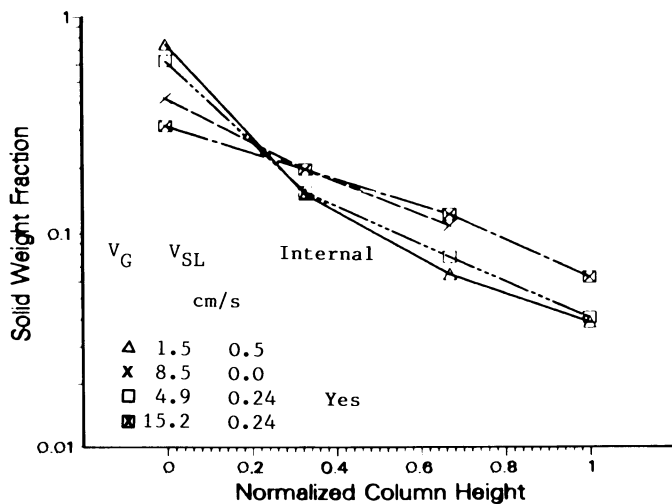
Figure 7.   Maximum solid loading, 12" cold flow simulator, isoparaffin, 90-115 μm silicon oxide, N_2.

Conclusions

1. The sedimentation diffusion model, when applied to the iron oxide system, gave solid settling velocities in agreement with theory. Solid dispersion coefficients were in the range predicted by the Kato correlation, but showed considerable experimental scatter.

2. The sedimentation diffusion model, when applied to the silicon oxide system, gave solid settling velocities several times higher than predicted by theory. Solid dispersion coefficients, however, did mostly agree with the Kato correlation.

3. Non-agglomerating catalyst particles $\lesssim 60$ μm should be suitable for bubble column batch operation, as no unsuspended solids were observed for either solid system studied.

4. Silicon oxide concentration profiles were unaffected by the presence of plain tube heat transfer internals.

Acknowledgments

Legend of Symbols

A	constant, g/cm^3
B	constant, g/cm^3
C	concentration, g/cm^3
D	constant
d	diameter, cm
E_Z	dispersion coefficient in the Z-direction, cm^2/s
f	Fanning friction factor
Fr	$V_G/\sqrt{g\ d_C}$ Froude number
g	gravitational acceleration constant, cm/s^2
L	column length, cm
n	mass flux relative to stationary coordinates in a gravitational field, $g/cm^2 s$
Pe	$V_G\ d_C/E_Z$ Peclet number
Rep	$V_p d_S \rho_L/\mu_L$ Particle Reynolds number based on liquid properties
Re_{SL}	$V_{ST} d_S \rho_{SL}/\mu_{SL}$ Particle Reynolds number based on slurry properties
t	time, s
V	velocity, cm/s
W	weight fraction
Z	distance above distributor, cm

Δ   finite difference
ε   volume fraction, holdup
ρ   density, g/cm^3
μ   viscosity, $g/cm \cdot s$

Subscripts

C   column
CALC   calculated
F   feed
G   gas
H   top of column
L   liquid
OBS   observed
P   particle
S   solid
SL   slurry
ST   particle in slurry
SU   superficial liquid (velocity)
ZL   in Z-direction of liquid
ZS   in Z-direction of solid
1   at a position in the column, higher than point 2
2   at a position in the column, lower than point 1

Literature Cited

1. Dyer, P. N.; Pierantozzi, R.; Brian, B. W.; Bauer, J. V.
    Quarterly Technical Progress Reports 1-8, US DOE PC/30021,
    1980-82.
2. Roy, N. K.; Guha, D. K.; Rao, M. N. Chem. Eng. Sci., 1964,
    19, 215.
3. Cova, D. R. Ind. and Eng. Chem. Proc. Des. and Dev., 1966,
    5, 20.
4. Imafuku, K.; Wang, T.-Y.; Koide, K.; Kubota, H. Chem. Eng. of
    Japan, 1968, 1, 153.
5. Kato, Y.; Nishiwaki, A.; Fukuda, T.; Tanaka, S. Chem. Eng. of
    Japan, 1972, 5, 112.
6. Sivasubramania, R.; Ying, D. H. S.; Givens, E. N. Proc. 16th
    Intersociety Energy Conv. Eng. Conf., 1981, 1, 1092.
7. Moujaes, S.; Ying, D. H. S.; Sivasubramania, R. Proc. IECEC
    '82, 17th Intersociety Energy Conv. Eng. Conf., August 1982.
    Los Angelos.
8. Bird, R. B.; Stewart, W. E.; Lightfoot, E. N. "Transport
    Phenomena"; 1960; Wiley & Sons Inc.; 190.
9. Levenspiel, O. "Chemical Reaction Engineering"; 1972; Wiley &
    Sons Inc.; 310.
10. Khang, S.-J.; Kothari, S. P. Chem. Eng. Sci., 1980, 35, 2201.
11. Ohki, Y.; Inoue, H. Chem. Eng. Sci., 1970, 25, 1.
12. Kölbel, H.; Ralek, M. Catal. Rev. - Sci. Eng., 1980, 21, 2,
    225.

13. Weast, R. C. "CRC Handbook of Chemistry and Physics"; 53rd
    Edition; 1972, B-99.
14. Soltrol 100, Phillips Petroleum Co., Special Products Divi-
    sion, Drawer "O", Borger, TX 79007.
15. Bauer, J. V.; Brian, B. W.; Butter, S. A.; Dyer, P. N.;
    Parsons, R. L.; Pierantozzi, R. 17th Mid. Atlantic Regional
    Mtg., ACS, White Haven, PA, 6-8 April 1982.
16. Reid, R. C.; Sherwood, T. K. "The Properties of Gases and
    Liquid: Their Estimation and Correlation", 2nd Edition;
    Mc-Graw-Hill, 1966.

Bubble Behavior in a Slurry Bubble Column Reactor Model

D. N. SMITH, W. FUCHS, R. J. LYNN, and D. H. SMITH

U.S. Department of Energy, Pittsburgh Energy Technology Center, Pittsburgh, PA 15236

M. HESS

Hess Technical Services, 2389 Mill Grove Road, Pittsburgh, PA 15241

Local axial and radial gas-phase characteristic measurements were made at steady-state conditions in a 0.108-m-i.d. slurry bubble column apparatus with a two-point electrical conductivity probe. The gas, solid, and liquid phases used in this study were nitrogen, glass beads, and either water, silicone oil, ethylene glycol, or aqueous ethanol, respectively. Two densities of solids were used (2420 or 3990 kg/m^3) and three narrow particle size fractions having particle sizes of 48.5 μm, 96.5 μm, and 194 μm. Engineering parameters obtained from the gas-phase measurements include bubble area per unit volume of column and bubble diameter distribution.

Bubble column reactors are quite commonly employed in the petrochemical industries for many oxidation and hydrogenation reactions (1). This type of reactor is ideal for reactions occurring in the slow reaction regime in which relatively low energy input is required to minimize the effect of mass transfer resistance. Nevertheless, attention has been drawn to the importance of gas absorption resistance of Fischer-Tropsch reactions occurring in three-phase slurry bubble column reactors (2-6).

Gas absorption is a function of the gas and liquid mass transfer coefficients, the interfacial area, and the enhancement due to chemical reaction. The gas-liquid interfacial area is related to the Sauter mean bubble diameter and the gas holdup fraction. The gas holdup fraction has been reported to vary with radial position (7-11) for column internal diameters up to 0.6 m. Koide et al. (12), however, found that the radial distribution of gas holdup was nearly constant for a column diameter of 5.5 m. Axial distribution of average gas holdup has been reported by Ueyama et al. (10). The average gas holdup

increased with an increase in axial position, i.e., distance
above the gas distributor. Other investigations (7, 11)
reported no obvious change in gas holdup with axial position.
        Radial distributions of bubble diameters in a bubble column
have been reported for column diameters up to 5.5 m (12). In
all cases, the bubble size increased from the wall to the center
of the column. The axial distribution of bubble diameters in
bubble columns has only been reported by a few investigators
(7, 10). Rigby et al. (7) observed that the average bubble
length increased with axial position, whereas Ueyama et al. (10)
did not observe a significant change in bubble diameter with
axial position.
        As indicated previously, to obtain meaningful estimates of
gas absorption rates, the gas-liquid interfacial area must be
known locally. The present work is concerned with the effect of
gas-liquid interfacial area on the performance of a slurry
bubble column reactor.

Experimental

A schematic diagram of the bubble column apparatus is shown in
Figure 1. The bubble column is a transparent plastic cylinder
having an inside diameter of 10.8 cm and a length of 194 cm. A
multiple-orifice plate (76 x 0.1-cm triangular pitch) located at
the bottom of the column is used to introduce the slurry and gas
phases. Several ports are located along the axis of the column
to allow insertion of the probe as well as slurry sampling tubes
and differential pressure gauges.
        A depiction of a twin-electrode conductivity probe inserted
into the slurry bubble column is given in Figure 2. The con-
ductivity probe circuit and related data acquisition system are
shown in Figure 3. A detailed description of the conductivity
probe and data collection system has been given previously (13).
A few design improvements were made with the twin electrodes to
allow the probe to function properly in a slurry environment.
These improvements are shown in Figure 2.
        Radial distributions of gas-phase characteristics were
measured from the wall to the center of the column in 1/4-inch
increments. For gas-liquid flows, steady-state operation was
achieved in 10 minutes, whereas for gas-liquid-solid flows,
measurements were not performed until one hour after flow con-
ditions were established. At the end of each run, average gas
holdup was measured by quick closure of the feed stream valve.
The sampling rate for the conductivity probes was 0.5
millisecond per point, and the total sample time for each local
measurement was 60 seconds. These sampling conditions are com-
parable to those of another investigator of gas-phase
characteristics in bubble columns (11).
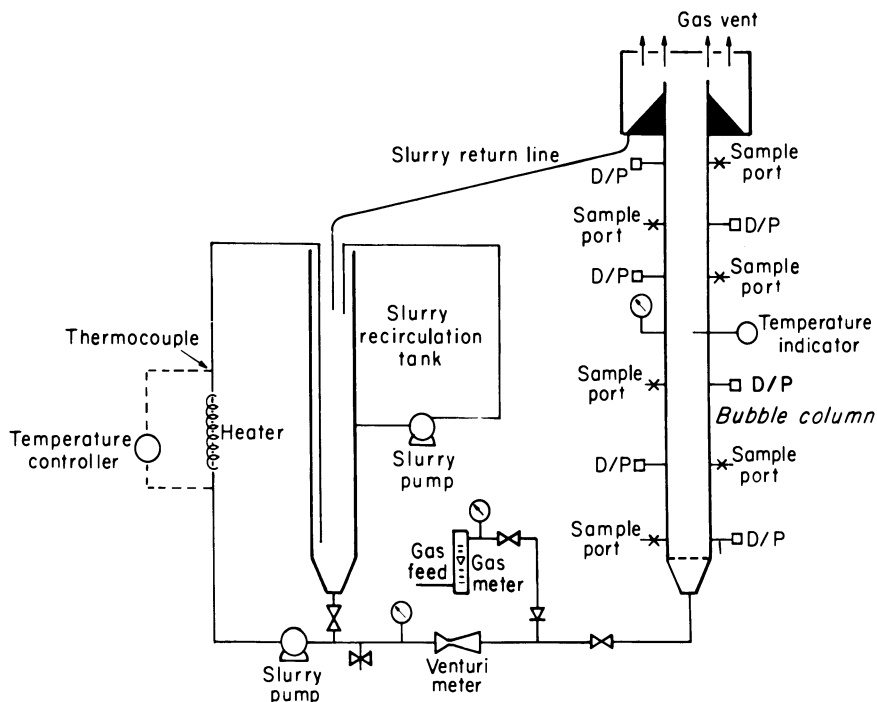
Figure 1.   Schematic diagram of 10.8 cm internal
diameter slurry bubble column apparatus.
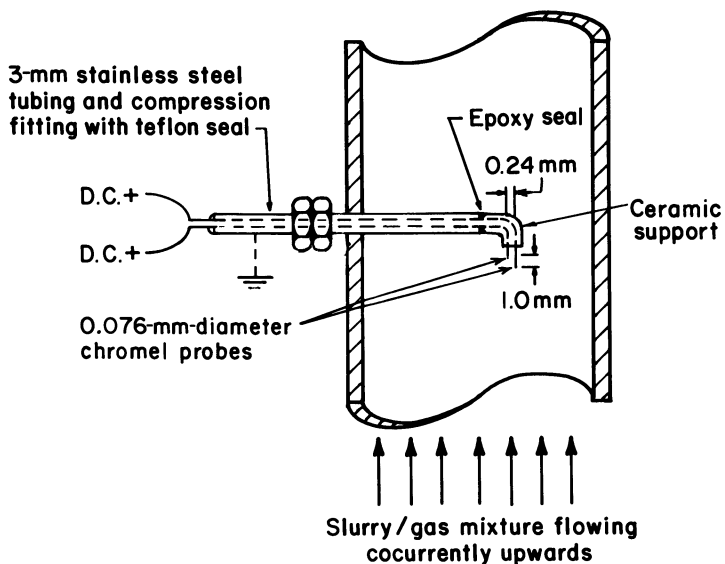
Figure 2.   Probe configuration for conductivity
measurements.
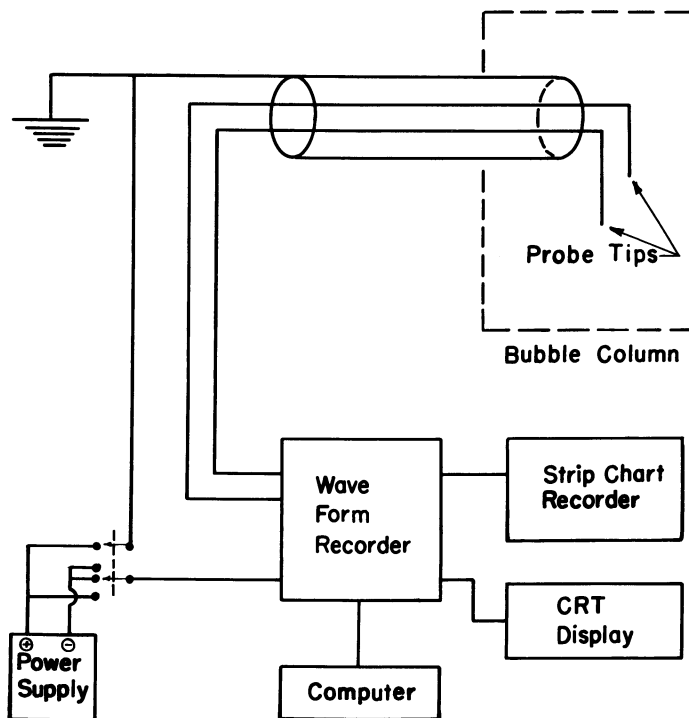
Figure 3.   Electrical conductivity probe circuit and
data acquisition system.

Calibration of Conductivity Probes

The comparison of probe signal response with a motion picture (1 frame per 8 milliseconds) was performed in a two-dimensional chamber into which single nitrogen bubbles were injected into a stagnant liquid phase. The orifice diameter of the injector varied from 0.53 mm to 1.6 mm, and the chord length of the bubble passing through the electrodes varied from less than 1 mm to 5 mm. The bubble velocity obtained by the motion picture was within 10 percent of the velocity obtained by the conductivity probes. The chord length of each bubble was photographed from two angles (front view and side view), and the motion picture was synchronized by the trigger light mechanism provided by the waveform recorder of the conductivity probe signal response. Within the precision of the motion picture, the bubble lengths measured by both methods were in agreement.

Interpretation of Probe Measurements

The interpretation of local gas holdup, bubble chord length, and bubble velocity from the probe response has been discussed previously (13). As indicated earlier, the measured bubble length is not equal to the bubble diameter but rather is associated with the probability of a single bubble striking the probe over the projected area of the bubble and with the shape of the bubble. The relationship between measured chord length and bubble size has been discussed previously (14, 15). The more recent approach to interpret bubble length has been adopted in this analysis. Local bubble diameter distributions have been assumed to be described with the log-normal function (15, 16).

$$F(d_b) = \frac{1}{\sigma \, d_b \sqrt{2\pi}} \exp\left[\frac{-1}{2\sigma^2} (\ln(d_b) - \mu)^2\right] \qquad (1)$$

Employing the probabilistic model developed by Tsutsui and Miyauchi (14), the following expression is derived for the local frequency distribution of bubble length (17).

$$Z = \frac{\lambda \int_\lambda^\infty f(x) \, dx}{\int_0^\infty \lambda \int_\lambda^\infty f(x) \, dx \, d\lambda} \qquad (2)$$

The inner-integral of Equation (2) was numerically integrated using a four-point Gaussian quadrature. The mean bubble length was calculated from the first moment of the frequency distribution function given in Equation (2).

$$\bar{\lambda} = \int_0^\infty \lambda \, Z \, d\lambda \qquad (3)$$

The variance of the measured bubble lengths was calculated from the second moment and first moment as given in the following equation.

$$\beta = \int_0^\infty \lambda^2 Z \, d\lambda - \bar{\lambda}^2 \qquad (4)$$

For a given value of σ and μ in the log-normal distribution function, the mean and variance of the distribution function were computed and compared with the mean and variance of the measured bubble lengths. A regula falsi technique was used to minimize the difference between observed and calculated mean and variance. The values of σ and μ that minimized the difference between observed and calculated mean and variance were then employed in Equation (1) to describe the local bubble diameter distribution. The Sauter mean bubble diameter was evaluated from the second and third moments of Equation (4).

$$d_{vs} = \exp\left[\mu + 2.5\,\sigma^2\right] \qquad (5)$$

Gas Holdup

The local gas holdup was calculated from the ratio of the time the probe was immersed in the bubble to the total sample time.

$$\epsilon_g = T_g / T_s \qquad (6)$$

In addition to the local gas holdup measurements, average gas holdup measurements were made by detecting the difference in height of the three-phase dispersion and liquid-solid suspension. A systematic study of average gas holdup as a function of gas velocity was performed for several gas-liquid and gas-liquid-solid systems. Four liquids -- water, aqueous ethanol (95 percent ethanol), silicone oil, and ethylene glycol -- were used in this study. The gas and solid phases were nitrogen and glass beads. Physical properties of the liquid and solids are given in Table 1.

The relationship of average gas holdup with superficial gas velocity is shown in Figure 4. Clearly the gas holdup increases with an increase in gas velocity and a decrease in surface tension of the liquid. A correlation similar to that developed by Hughmark (18) and later applied to three-phase bubble columns by Smith and Ruether (19) is obtained for all experimental data.

$$\bar{\epsilon}_g = \left[2.25 + (33.9 / \bar{U}_g)(\rho_{SL}\sigma_L / 72)^{0.31}\mu_{SL}^{0.016}\right]^{-1} \qquad (7)$$

The slurry viscosity is assumed to be a function of liquid viscosity and solids void fraction in the slurry. A correlation proposed by Barnea and Mizrahi (20) is used to estimate slurry viscosity.

$$\mu_{SL} = \mu_L \exp\left[\frac{5/3\,\phi_s}{(1-\phi_s)}\right] \qquad (8)$$

Table I. Experimental conditions for average gas holdup measurements. (Gas phase is nitrogen)

Liquid			Solid			Key
ρ_L gm/cm³	σ_L dyne/cm	μ_L cp	ρ_s gm/cm³	ϕ_s —	d_p μm	
1.0	71.5	0.83	—	—	—	◯
0.82	17.4	0.82	—	—	—	□
0.82	22.5	1.2	—	—	—	+
0.82	22.5	1.2	2.42	0.050	96.5	●
1.0	71.5	0.83	2.42	0.045	48.5	■
1.0	71.5	0.83	2.42	0.045	19.4	▲
1.0	71.5	0.83	2.42	0.045	96.5	X
1.0	71.5	0.89	3.99	0.028	96.5	△
1.1	47.0	17.1	—	—	—	◇
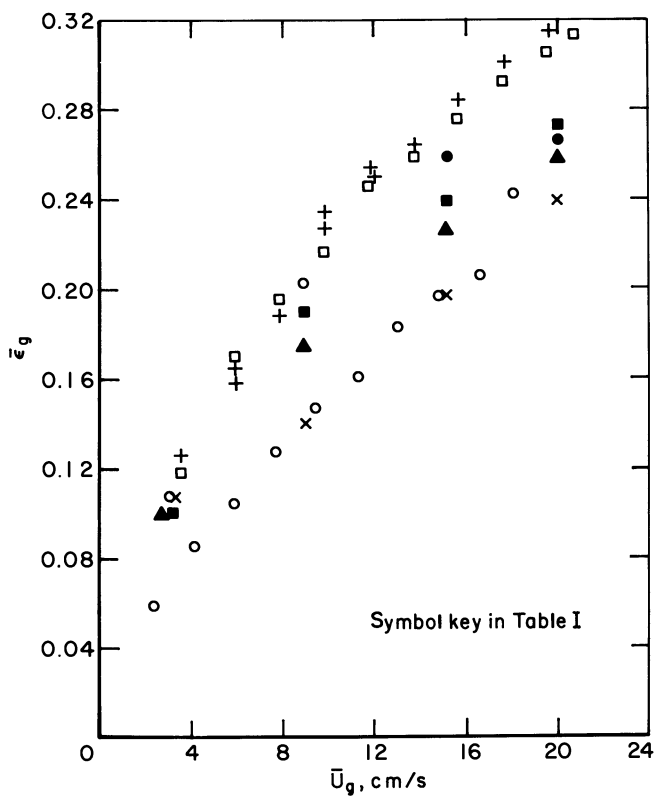
Figure 4.   Relationship of gas holdup fraction with
superficial gas velocity.

The average absolute relative error for estimated gas holdup is 7.8 percent when using Equation (7).

Local gas holdup has been measured as a function of radial and axial position for the flow conditions given in Table 2. The liquids used with the conductivity probe measurements were either water or aqueous ethanol (48 volume percent). For the three-phase flow measurements, the solid phase was narrow-sized glass beads.

Local gas holdup is well described as a function of radial position with a third-order polynominal equation.

$$\epsilon_g = a_1 + a_2 r^* + a_3 r^{*2} + a_4 r^{*3} \tag{9}$$

The empirical coefficients are obtained from least squares regression of the observed and calculated gas holdup. The average gas holdup at a given axial position is obtained from the first moment.

$$\bar{\epsilon}_g = \int_0^1 2 r^* \epsilon_g \, dr^* \tag{10}$$

The average gas holdup calculated from the difference between the heights of the gas-liquid dispersion and the clear liquid has been compared to the average holdup obtained from Equation (10). The average absolute relative error is less than 10 percent for all measurements.

Figure 5 shows the distribution of gas holdup with radial position for a nitrogen-water system. The gas holdup increases from the wall to the center of the column, with a maximum gas holdup at an r* between 0.1 and 0.2. Figure 6 shows the radial distribution of gas holdup for a nitrogen-aqueous ethanol system. Again the gas holdup increases from the wall to the center of the column, but the maximum gas holdup is now located at an r* between 0.35 and 0.45. A similar shape in radial distribution of gas holdup has been reported by Rigby et al. (7). Figure 7 shows the effect of solids on the radial profile of gas holdup. In general, the addition of 4 volume percent solids slightly decreases the gas holdup for the experimental conditions of this study.

Bubble Length and Bubble Diameter Distributions

For each local measurement of gas-phase characteristics, approximately one hundred to six hundred bubbles were measured. The fraction of bubbles rising vertically varied from 20 to 50 percent. Since analysis of bubble length and velocity can only be made for vertically rising bubbles, fifty to three hundred bubbles' lengths and velocities were obtained for each local position in the bubble column.

Table II. Experimental conditions for bubble measurements. (Gas phase is nitrogen, and solid density is 2.42 g/cm^3)

$\bar{U}_g$ cm/s	Z^* —	ρ_L gm/cm³	σ_L dyne/cm	μ_L cp	d_p μm	ϕ_s —	Key
3.1	0.931	1.0	72	0.93	—	—	○
3.1	0.564	1.0	72	0.93	—	—	□
3.1	0.223	1.0	72	0.93	—	—	+
8.9	0.931	1.0	72	0.89	—	—	●
8.9	0.564	1.0	72	0.89	—	—	■
8.9	0.223	1.0	72	0.89	—	—	▲
3.1	0.931	1.0	72	0.89	48.5	0.041	X
3.1	0.564	1.0	72	0.89	48.5	0.041	△
8.9	0.564	1.0	72.	0.89	48.5	0.041	◇
3.1	0.564	0.92	30	2.60	—	—	∅
3.1	0.223	0.92	30	2.60	—	—	⬚
3.1	0.931	0.92	30	2.60	—	—	⬚
3.1	0.564	0.92	30	2.60	48.5	0.041	⬚
3.1	0.931	0.92	30	2.60	48.5	0.041	■
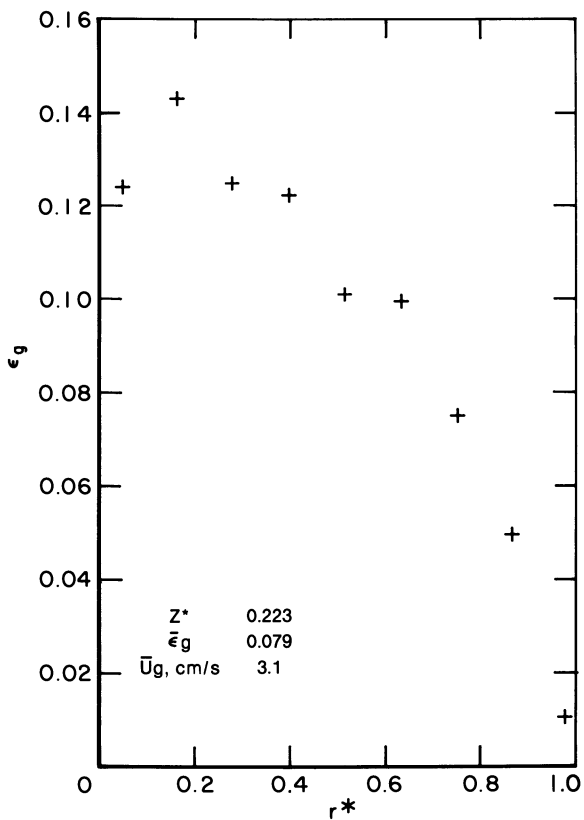
Figure 5. Gas holdup as a function of radial position for nitrogen-water system.
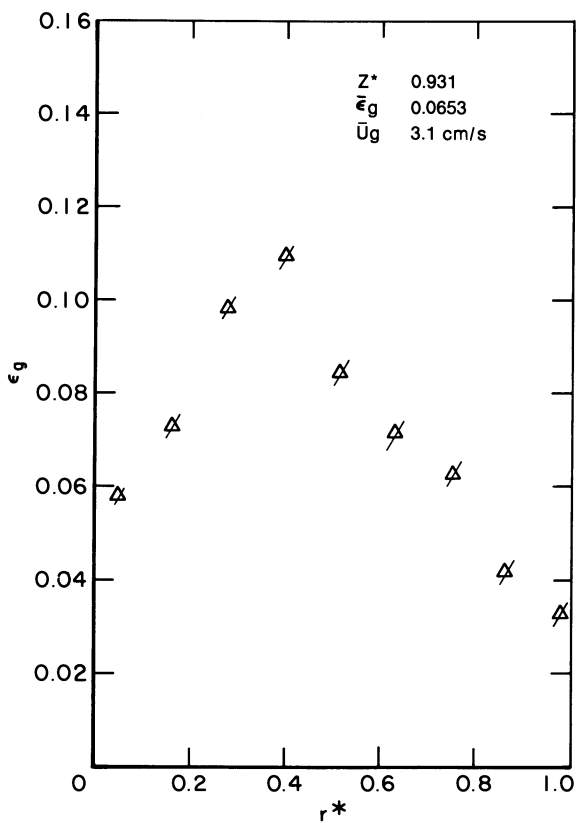
Figure 6. Gas holdup as a function of radial position for nitrogen-aqueous ethanol system.
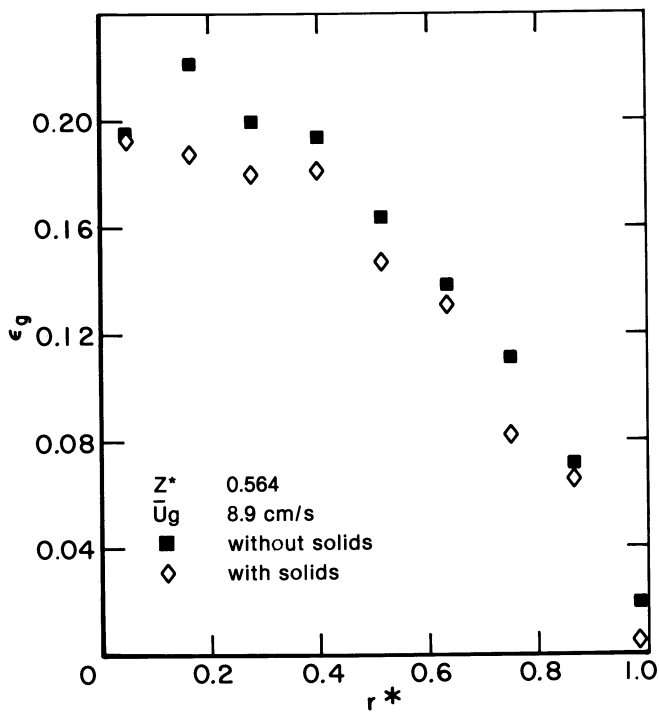
Figure 7. Comparison of radial distribution of gas holdup with and without solids in a nitrogen-water system.

An example of the cumulative bubble length distributions for three different axial positions is given in Figure 8 for a nitrogen-water system. The bubble length distributions for the top and bottom axial positions are remarkably similar. However, the bubble length distribution near the middle of the bubble column is notably different, indicating a statistically larger bubble size. This variation in bubble size characteristics was observed qualitatively. The bubbles were observed to be smaller near the bottom of the column and then to expand in size with increasing axial position. However, at the top of the column, the bubbles were noticeably smaller and more concentrated, which is somewhat similar to the fountain effect observed by Botton et al. (21). For the aqueous ethanol systems, the fountain effect was visually observed to be much smaller.

The Sauter mean bubble diameter was calculated from the measured bubble length distributions as described earlier. In agreement with other investigators (10, 22), the Sauter mean bubble diameter is a linear function of average bubble length. A linear regression of all experimental data gave the following expression.

$$d_{vs} = 1.46\, \bar{\lambda} - 0.00253 \tag{11}$$

The regression coefficient, r^2, was 0.985 for the use of the above equation to predict Sauter mean bubble size.

An important aspect in determining the average bubble size or average gas holdup is the ability to measure the entire range of bubble sizes that are present in a bubble column. An empirical correlation that describes the minimum unselected bubble diameter that can be measured with microprobes is given by Buchholz et al. (23).

$$d_{min} = 4\left(\Delta\, d_r\right) + d_n + i_c \tag{12}$$

Using this equation, the minimum bubble size that can be detected without bias is approximately 0.05 cm. This is in reasonably good agreement with the smallest bubble length of 0.03 cm measured with the conductivity probes of this investigation.

An example of the local Sauter mean bubble diameter as a function of radial position for nitrogen and aqueous ethanol (48 volume percent) is given in Figure 9. A slight increase in local bubble size is observed from the column wall to the center, and then the bubble size remains nearly constant for $0 < r* < 0.5$. In Figure 10, the effect of solids on the radial distribution of Sauter mean bubble diameter is given for nitrogen and aqueous ethanol (48 volume percent). A slight decrease in bubble size is observed with solids present.

Parameter	Symbol		
—	O	□	+
r^*, —	0.515	0.515	0.515
Z^*, —	0.931	0.564	0.223
$\bar{d}_{vs}$, cm	0.417	0.563	0.407
$\bar{U}_g$, cm/s	3.1	3.1	3.1
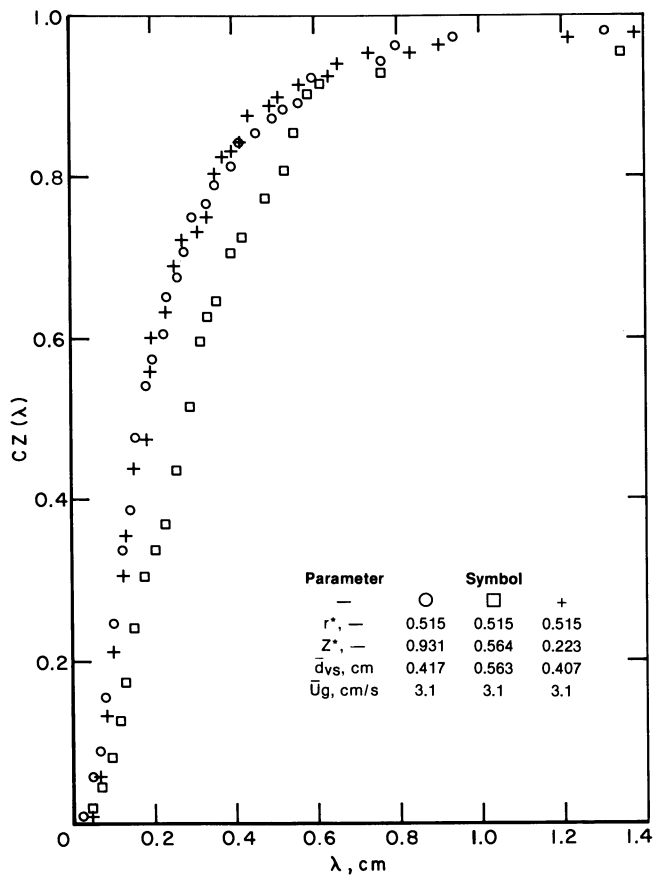
Figure 8.   Cumulative bubble length distribution as a function of axial position in a nitrogen-water system.
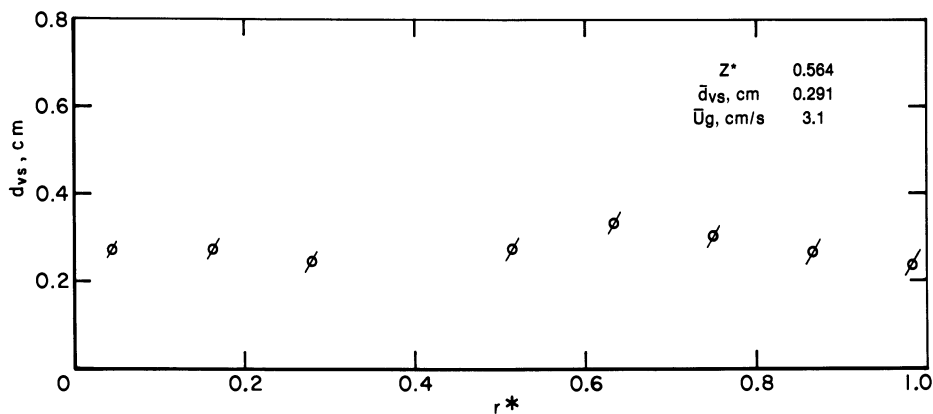
Figure 9.   Sauter mean bubble size as a function of
radial position in nitrogen-aqueous ethanol system.
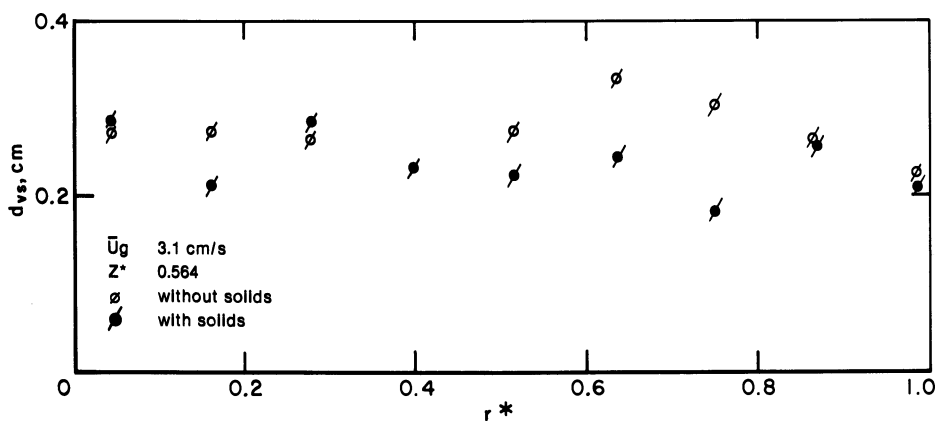
Figure 10.   Effect of solids on radial distribution of
Sauter mean bubble diameter in nitrogen-aqueous ethanol
system.

From this investigation, the average Sauter mean bubble size can be over 200 percent greater than the Sauter mean bubble size measured near the wall ($r* = 0.985$). In general, the average Sauter mean bubble size is larger than that measured near the wall with the exception of large bubble diameters (d_{vs} near the wall greater than 0.4 cm). This trend is similar to that found by Ueyama et al. (10) for an air-water system.

Gas Interfacial Area

The gas interfacial area per unit volume of column is related to the gas holdup and Sauter mean bubble size.

$$a = 6 \; \epsilon_g/d_{vs} \tag{13}$$

The radial distribution of interfacial area for a two-phase system is shown in Figure 11. As discussed earlier, the gas holdup fraction is a strong function of radial position, but the Sauter mean bubble size is a less pronounced function of radial position. Consequently, the radial distribution of interfacial area has a shape similar to the gas holdup radial profile. Therefore, the interfacial area is well described with a third order polynominal equation.

$$a = b_1 + b_2 r* + b_3 r*^2 + b_4 r*^3 \tag{14}$$

The first moment of the interfacial area is then used to obtain the average interfacial area for a given axial position.

$$\bar{a} = \int_0^1 2 \, r* a \, dr* \tag{15}$$

In Figure 12, the radial distribution of interfacial area is given for a three-phase system. Similar to Figure 11, the aqueous ethanol system has a larger interfacial area than the water system. The addition of 4 volume percent solids, however, causes only a slight increase of interfacial area.

The axial distribution of average interfacial area for two-phase systems is shown in Figure 13. For the nitrogen-aqueous ethanol system, the average interfacial area decreases slightly with increasing axial position. For the nitrogen-water system, the interfacial area decreases with increasing axial position near the bottom of the column. However, at some axial position between the middle and the top of the column, the interfacial area increases to nearly the same magnitude as that at the bottom of the column. This axial distribution profile for the nitrogen-water system is similar to the gas holdup profile.

A comparison of the interfacial area obtained with the conductivity probe measurements has been made with a correlation
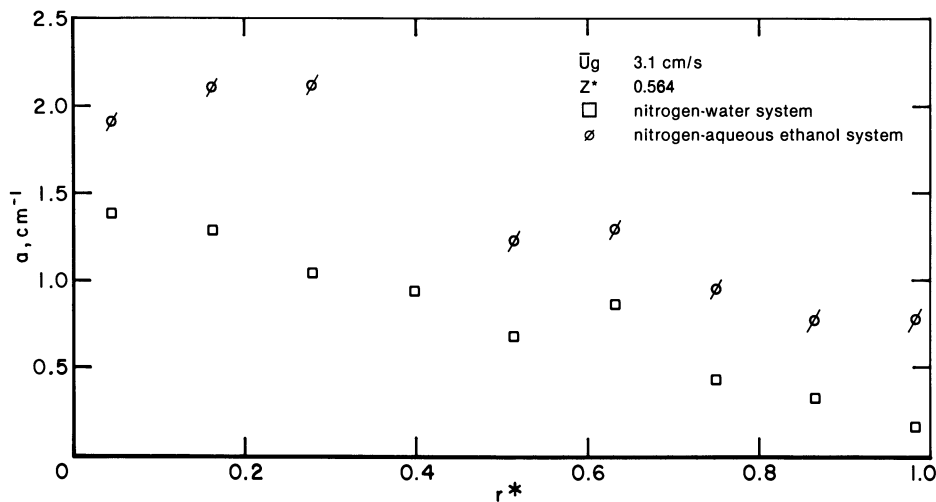
Figure 11.   Interfacial area as a function of radial position for a gas-liquid system.
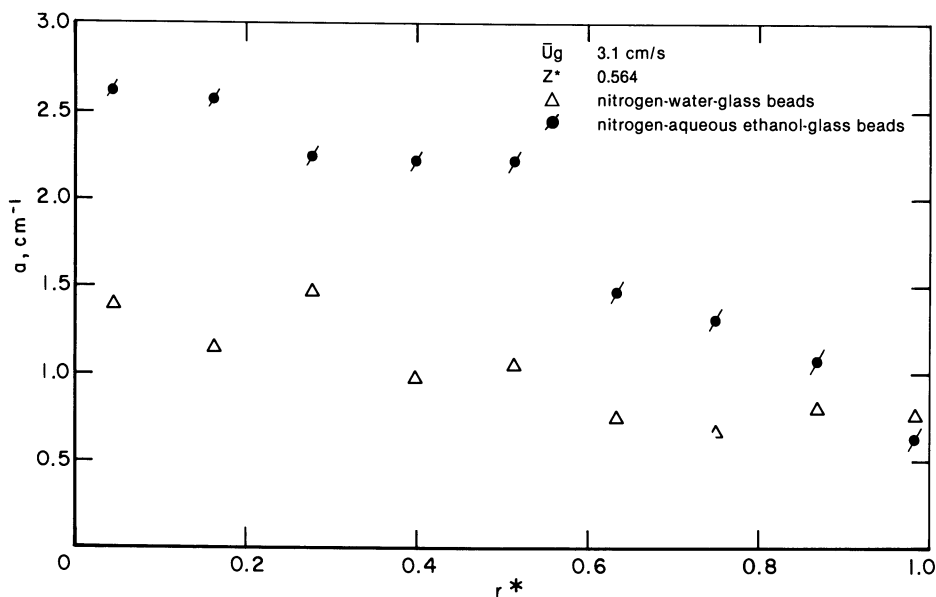
Figure 12.   Interfacial area as a function of radial position for a gas-liquid-solid system.
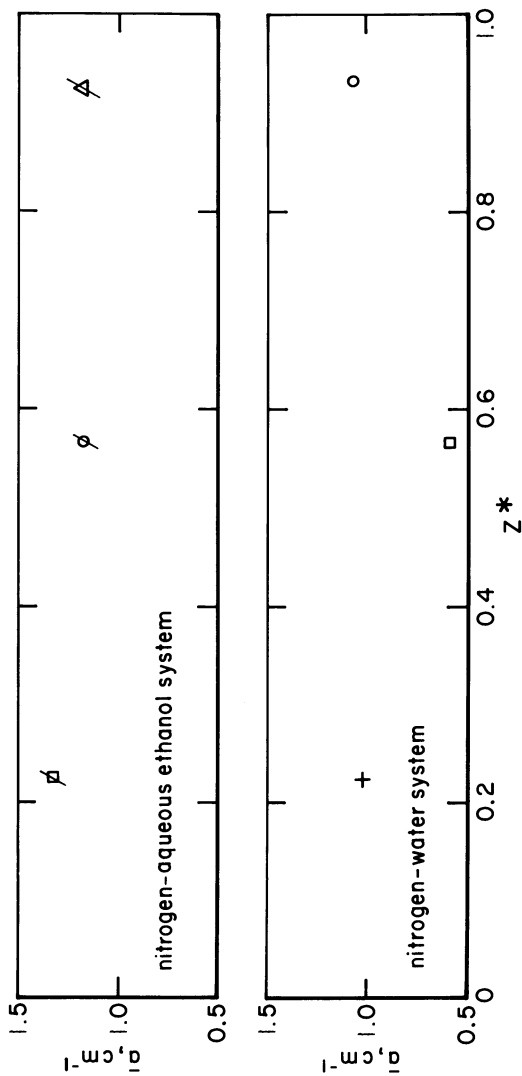
Figure 13. Interfacial area of gas-liquid dispersion as a function of axial position for superficial gas velocity of 3.1 cm/s.

proposed by Akita and Yoshida (16) for a nitrogen-water system. Good agreement is found between measured and predicted inter-facial areas at $Z^* = 0.564$ for the two gas velocities employed in this investigation. For the interfacial area measured near the top and bottom of the column, the correlation proposed by Akita and Yoshida (16) underpredicts the experimental observations.

Discussion

In the preceeding sections, development of the measurement technique and analysis of gas-phase characteristics in a slurry bubble column have been made along with some comparison of the experimental data with other correlations from the literature. Up to this point, analysis of gas-phase characteristics has included only single or binary liquid components. Recently, a large effect on gas holdup and bubble size has been observed for multicomponent liquid mixtures that contain small concentrations of surface-active species (24). In their study, mixtures of alcohols and water at alcohol concentrations less than 0.1 percent caused a dramatic increase in gas holdup (up to a factor of 2) and a decrease in bubble size (up to a factor of 4) com-pared to those observed for the water system. The authors think the effect is the result of- interaction between molecules of different species, leading to an enrichment of one species in the interface. Therefore, in multicomponent liquid mixtures, it is necessary to have knowledge of the presence of surface-active species as well as the physical properties of the fluid.

Conclusions

The conductivity probe technique has been applied successfully to gas-phase measurements in a slurry bubble column. The presence of solids does not appreciably change the gas-phase characteristics for a volume fraction of solids less than 5 percent. The radial distribution functions of gas holdup and interfacial area increase significantly from the wall to the center of the column. The average Sauter mean bubble diameter is greater than the Sauter mean bubble diameter measured near the wall.

For multicomponent liquid mixtures in a slurry bubble column, the gas-phase characteristics appear to be greatly altered if small concentrations (less than 0.1 percent) of a surface active species are present (24). The degree to which the gas-phase characteristics are changed appears to be related to the type and concentration of the surface-active component and the turbulence in the bubble column.

Acknowledgments

The authors are grateful to Charles Brodd for helpful suggestions on the design improvements of the conductivity probe and the careful calibration and testing of the conductivity probe.

Disclaimer

Reference in this report to any specific commercial product, process, or service is to facilitate understanding and does not necessarily imply its endorsement or favoring by the United States Department of Energy.

Nomenclature

a	=	Local gas interfacial area, cm^{-1}
$\bar{a}$	=	Average gas interfacial area, cm^{-1}
a_i	=	i^{th} coefficient in Equation (9)
b_i	=	i^{th} coefficient in Equation (14)
$CZ(\lambda)$	=	Cumulative bubble length distribution
D	=	Internal diameter of column, cm
d_b	=	Bubble diameter, cm
D_{min}	=	Minimum detectable bubble size, cm
d_n	=	Diameter of electrode for conductivity probe, cm
d_{vs}	=	Local Sauter mean bubble size, cm
$\bar{d}_{vs}$	=	Average Sauter mean bubble size, cm
$F(d_b)$	=	Log-normal bubble distribution function, cm^{-2}
$f(x)$	=	Distribution function in Equation (2)
g	=	Gravitational acceleration, cm/s^2
i_c	=	Insulation constant defined in Equation (12)
r^*	=	Dimensionless radial position
T_g	=	Time probe is immersed in gas-phase, s
T_s	=	Total sample time of probe measurement, s
Ug	=	Superficial gas velocity, cm/s
Z	=	Bubble length distribution
Z^*	=	Dimensionless axial position

Greek Symbols

β	=	Variance of bubble length distribution, cm^2
Δd_r	=	Radial distance between conductivity probe wires, cm
ε_g	=	Local gas holdup
$\bar{\varepsilon}_g$	=	Average gas holdup
λ	=	Bubble length, cm
$\bar{\lambda}$	=	Average bubble length, cm
μ	=	Natural log of geometric mean bubble diameter
μ_L	=	Liquid viscosity, cp

Greek Symbols, (Cont.)

μ_{SL} =   Slurry viscosity, cp
ρ_L =   Liquid density, g/cm^3
ρ_{SL} =   Slurry density, g/cm^3
σ^2 =   Variance of log-normal distribution, cm^2
σ_L =   Surface tension, dyne/cm
ϕ_s =   Volume fraction of solids in slurry

Literature Cited

1. Shah, Y.T., Kelkar, B.G., Godbole, S.P., and Deckwer, W.-D., AIChE J. 1982, 28, 353.

2. Calderbank, P.H., Evans, F., Farley, R., Jepsen, G., and Poll, A., Catalysis in Practice (London: Inst. Chem. Engrs.) 1963, 66.

3. Deckwer, W.D., Serpemen, Y., Ralek, M., and Schmidt, B., Chem. Eng. Sci. 1981, 36, 765.

4. Kölbel, H., and Ralek, M., Catal. Rev. - Sci. Eng.; 1980, 21, 225.

5. Kuo, J.C.W., Aditya, S.K., Bukur, D., and Gupte, K.M., Quarterly Progress Report DOE/PC/30022-1, January, 1981.

6. Satterfield, C.N., and Huff, G.A., Chem. Eng. Sci. 1980, 35, 195.

7. Rigby, G.R., Blockland, G.P. van, Park, W.H., and Capes, C.E., Chem. Eng. Sci., 1970, 25, 1729.

8. Kobayashi, K., Yoshihiro, I., and Kanegae, N., Bulletin of JSME 1970, 13, 1005.

9. Hills, J.H., Trans. Inst. Chem. Engrs. 1974, 52, 1.

10. Ueyama, K., Morooka, S., Koide, K., Kaji, H., and Miyauchi, T., Ind. Eng. Chem., Process Des. Dev. 1980, 19, 592.

11. Linneweber, K.-W., and Blass, E., Proceedings of Second World Congress of Chemical Engineering, 3, 1981, 50.

12. Koide, K., Morooka, S., Ueyama, K., Matsuura, A., Yamashita, F., Iwamoto, S., Kato, Y., Inoue, H., Shigeta, M., Suzuki, S., and Akehata, T., J. Chem. Eng. Japan 1979, 12, 98.

13. Fuchs, W., and Smith, D., Sixth Annual Symposium on Instrumentation and Control for Fossil Energy Processes, 1982, 233.

14. Tsutsui, T., and Miyauchi, T., Int. Chem. Eng. 1980, 20, 386.

15. Darton, R.C., and Harrison, D., I. Chem. Trans. Symposium Series, No. 38, 1, 1974, Paper Bl, The Inst. Chem. Engrs., London.

16. Akita, K., and Yoshida, F., Ind. Eng. Chem., Process Des. Dev. 1974, 13, 84.

17. Hess, M., U.S. DOE Final Report No. DE-AC22-82PC12320, 1982.

18. Hughmark, G.A., Ind. Eng. Chem., Process Des. Dev. 1967, 6, 218.

19. Smith, D.N., and Ruether, J.A., submitted to Chem. Eng. Sci. 1983.

20. Barnea, E., and Mizrahi, J., Chem. Eng. J. 1973, 5, 171.

21. Botton, R., Cosserat, D., and Charpentier, J.C., Chem. Eng. J. 1978, 16, 107.

22. Yamashita, F., Mori, Y., and Fujita, S., J. Chem. Eng. Japan 1979, 12, 5.

23. Buchholz, R., Zakrzewski, W., and Schugërl, K., Int. Chem. Eng. 1981, 21, 180.

24. Keitel, G., and Onken, U., Chem. Eng. Sci. 1982, 37, 1635.

A Two-Bubble Class Model for Churn Turbulent Bubble Column Slurry Reactor

S. JOSEPH and Y. T. SHAH

Chemical and Petroleum Engineering Department, University of Pittsburgh, Pittsburgh, PA 15261

A two-bubble-class model for the churn turbulent bubble column reactor is proposed. The model parameters include both small and large bubble holdups, liquid side mass transfer coefficients for small and large bubbles, and the small and large bubble diameters. All of these parameters, except the large bubble diameter, are either measured or estimated. The model is used to correlate and explain the experimental data of Schumpe et al. (7) for the absorption of CO_2 in NaOH. The model is believed to be more realistic than the conventional single-bubble-class model. It, however, requires independent measurements of large bubble diameters under a wide range of operating conditions. Further verification of the model requires additional experimental data at superficial gas velocities greater than 0.2 m/s and in large diameter columns. The data for slow reaction systems (e.g., absorption of CO_2 in Na_2CO_3) would also be desirable for the further critical evaluation of the model.

A bubble column is a contactor which involves the passage of a discontinuous gas phase in the form of bubbles, through a continuous phase, which can either be a liquid or a homogeneous slurry. The various flow regimes that can occur in a bubble column have been characterized by Shah et al. (1). The bubbly flow regime occurs for low superficial gas velocities (< 0.05 m/s), and is distinguished by bubbles of uniform size. At higher gas velocities, the homogeneous gas-in-liquid dispersion cannot be maintained and two bubble classes develop: large bubbles moving with high rise velocities in the presence of small dispersed bubbles. This has been classified as the heterogeneous or churn turbulent regime.

Bach and Pilhofer (2) have suggested that the churn turbulent regime is the most commonly encountered flow regime in the industrial bubble columns. Vermeer and Krishna (3) have concluded from their studies on a bubble column operating in the churn turbulent regime that gas transport in this regime occurred exclusively due to large bubbles. The bimodal distribution of bubble sizes in the churn turbulent regime has been reported by several investigators (3-6).

The churn turbulent regime has been modeled by a single class of bubbles moving in a plug flow manner (7). The concept of a mean gas phase residence time in this regime is somewhat meaningless. The two bubble classes behave differently as they move up the column. The large bubbles travel in a plug flow manner due to their high bubble rise velocities, while the small bubbles tend towards complete backmixing due to liquid circulations. Hence the mean residence time of the large bubbles is smaller than that of the small bubbles. A realistic model for the churn turbulent regime should thus consider the contribution of both bubble classes.

The application of the two bubble class model is important for reactions which are mass transfer controlled. The scale-up of a mass transfer controlled operation based on a fixed gas phase residence time assumes incorrect and higher actual gas velocities. Thus, when the flow regime changes from homogeneous to churn turbulent, an apparent drop in conversion could be encountered due to decreased mass transfer rates. Generally, the scale-up of a bubble column is accompanied by the change in flow regime and under this situation, the two bubble class model will give a more reliable scale-up than the conventional single bubble class model. In this paper, we first develop the two bubble class model for a bubble column reactor which carries out a simple rapid first order reaction in the liquid phase. The model is applied to the absorption of CO_2 in NaOH in the churn turbulent regime. The application of the model to a slurry reactor is also briefly discussed.

Development of Model

Consider a gas A which is being absorbed into a liquid solution containing a reactive species B. The reaction between dissolved A and B is given by

$$A + ZB \rightarrow \text{products} \tag{1}$$

For simplicity, we assume the concentration of B in the liquid phase to be in excess and the rate of reaction to be pseudo-first order with respect to A. Thus

$$r_A = k_1 C_{AL} \tag{2}$$

The reaction is in the fast reaction regime, if

$$Ha = \sqrt{k_1 \ D_A} \ / \ k_L > 3 \tag{3}$$

The following assumptions are made in the development of the model.

1. The large bubbles are assumed to travel in a plug flow manner.
2. The small bubbles are either partially or completely backmixed.
3. The variation in gas molar flow rate caused by absorption and reaction is negligible. When the gas phase reactant is diluted with an inert (as in this case), this is a reasonable assumption.
4. There are no axial variations in gas holdup.
5. The pressure varies linearly along the axis of the column and is given as

$$P = P_T \ [1 + \alpha \ (1-z)] \tag{4}$$

where

$$\alpha = \frac{\rho_L g \ L \ (1-\varepsilon_G)}{P_T}$$

6. The equilibrium liquid phase concentration of A is given by Henry's law for both small and large bubbles. Thus,

$$(c_{AL}^*)^S = \frac{P Y_{AG}^S}{H}, \quad (c_{AL}^*)^L = \frac{P Y_{AG}^L}{H} \tag{5}$$

7. There is no interaction between the two bubble classes.
8. The gas phase resistance is negligible.

The mass balance for A in large bubbles based on these assumptions is

$$-\frac{d}{dx} \ (U_G^L \ Y_{AG}^L \ \frac{P}{RT}) = (k_L a)^L \ ((c_{AL}^*)^L - C_{AL}) \ \phi \tag{6}$$

where ϕ is the enhancement factor due to chemical reaction and for Ha > 3, ϕ = Ha. The mass balance for A in small bubbles is

$$\frac{U_G^S}{RT} \ \{ \ P_0 \ Y_{AG,0}^S - P_1 \ Y_{AG,1}^S \} = L \ (k_L a)^S \ ((c_{AL}^*)^S - C_{AL}) \ \phi \tag{7}$$

If the small bubbles are assumed to be partially backmixed, then the following mass balance equation can be written,

$$\frac{1}{Pe}\frac{d^2 Y^S_{AG}}{dz^2} - \frac{d\, Y^S_{AG}}{dz} - \frac{L(k_L a)^S}{U^S_G}\frac{RT}{P}((C^*_{AL})^S - C_{AL})\,\phi = 0 \quad (8)$$

with the boundary conditions

at z = 0, $Y^S_{AG} = Y^S_{AG,0} + \frac{1}{Pe}\frac{d\, Y^S_{AG}}{dz}$

at z = 1, $\frac{d\, Y^S_{AG}}{dz} = 0$.

The solution of this equation is

$$Y^S_{AG} = A_1 \exp(m_1 z) + A_2 \exp(m_2 z) \qquad\qquad (9)$$

where

$$m_{1,2} \quad \frac{-1 \pm \sqrt{1 + 4\, St_G/Pe}}{2/Pe}$$

$$Pe = \frac{U^S_G\, L}{D^S_G\, \varepsilon^S_G}$$

$$St_G = a^S \sqrt{D_A k_1}\;\left(\frac{RT}{H}\right)\left(\frac{L}{U^S_G}\right)$$

$$A_2 = \frac{Y^S_{AG,0}}{1 + (m_2/Pe - m_2/m_1)\exp(m_2 - m_1) - m_2/Pe}$$

$$A_1 = -(A_2\, m_2/m_1)\exp(m_2 - m_1)$$

The concentration of A in the bulk liquid is zero and hence its liquid phase balance can be neglected.   The flux of A through large and small bubbles is given by

$$U_G^L = U_{br}^L \, \varepsilon_G^L$$

$$U_G^S = U_{br}^S \, \varepsilon_G^S$$

(10)

Equation 6 can be integrated to give

$$Y_{AG,1}^L = Y_{AG,0}^L \, (1 + \alpha) \, \exp \left\{ -L \, a^L \, \frac{RT \sqrt{D_A \, k_1}}{H \, U_{br}^L \, \varepsilon_G^L} \right\}$$

(11)

The mass balance for A in small bubbles, equation 7, can be simplified to give

$$Y_{AG,1}^S = \frac{C_1 \, Y_{AG,0}^S}{1 + C_2}$$

(12)

where

$$C_1 = \frac{U_{br}^S \, \varepsilon_G^S \, H}{L \, a^S \, RT \sqrt{D_A \, k_1}} \, \frac{P_0}{P_m}$$

and

$$C_2 = C_1 \, \frac{P_1}{P_0}$$

Note the solution given in both equations 11 and 12 do not depend on k_L, but on the intrinsic rate parameter k_1 and on "a" for large and small bubbles.

The gas phase conversion for A is calculated from the overall mass balance for the gas phase as,

$$U_{br}^S \, \varepsilon_G^S \, Y_{AG,1}^S + U_{br}^L \, \varepsilon_G^L \, Y_{AG,1}^L = U_G \, Y_{AG,1}$$

(13)

and

$$X_A = \frac{Y_{AG,0} - Y_{AG,1}}{Y_{AG,0}}$$

(14)

Hence, the gas phase conversion X_A for a pseudo-first order reaction in the churn turbulent regime can be calculated if the fractional gas holdups, rise velocities, and interfacial areas for the two bubble classes as well as the physico-chemical data are known.

154

CHEMICAL AND CATALYTIC REACTOR MODELING

The assumption of a plug flow model for the entire gas phase leads to the following expression for the gas phase conversion, (7)

$$Y_{AG,0}\, X_A - (1 - Y_{AG,0})\, \ln(1 - X_A) = St_G \tag{15}$$

where

$$St_G = a\, \sqrt{D_A\, k_1}\, \left(\frac{L}{U_{GO}}\right) \left(\frac{RT}{H}\right)$$

Model Parameter Estimations

The key parameters in this model are the fractional gas holdups due to the large and small bubbles, the bubble rise velocities, and the bubble diameters. The fractional gas holdup structure due to different size bubbles has been determined by a number of investigators (3,5) using the dynamic gas disengagement technique. This technique involves the measurement of the rate of drop in the dispersion height when the gas supply is instantly shut off (8). The following systems have been studied: air-water (9), air-Soltrol-130 (a mixture of C_9^+ isoparaffins) (9) and N_2 – Turpentine-5 (3). The reported fractional gas holdup due to small bubbles for these three systems could be correlated by the following expression, with a maximum deviation of ± 6.0%.

$$\epsilon_G^S = 1.156 \left(\frac{U_G\, \mu_L}{\sigma}\right)^{0.321} \tag{16}$$

The parity plot for the above equation for holdup is shown in Figure 1. While the validity of the above correlation for an electrolyte solution may be questionable due to its coalescence hindering property, at present, no conclusive data illustrating this effect, particularly for dilute NaOH solutions are available. Experiments were performed at different dispersion heights (L/D = 5.7, 8.0, 9.8) at the same superficial gas velocity and the deviation from the mean of the small bubble gas holdups was ±3.0%. Hence, it can be assumed that the gas holdup structure does not change substantially with the dispersion height.

In the present study, the model is applied to the absorption of CO_2 in a NaOH solution. The total gas holdup data in the churn turbulent regime ($U_G > 0.07$ m/s) for this system reported by Schumpe et al. (7) could be correlated by the expression

$$\epsilon_G = 0.668\, U_G^{0.518} \tag{17}$$

In Chemical and Catalytic Reactor Modeling; Dudukovi, M., el al.;
ACS Symposium Series; American Chemical Society: Washington, DC, 1984.

Both ε_G and ε_G^S for $CO_2/NaOH$ system obtained from the above correlations as a function of gas velocity are shown in Figure 2. ε_G^L can be obtained from the difference between these curves.

The liquid-side mass transfer coefficients $(k_L)^L$ and $(k_L)^S$ for large and small bubbles can be estimated from the correlation of Calderbank and Moo-Young (10). Table I gives the physico-chemical data used in this study. The interfacial areas a^S and a^L were calculated by the following equations

$$a^S = \frac{6\ \varepsilon_G^S}{d_b^S} \qquad \text{and} \qquad a^L = \frac{6\ \varepsilon_G^L}{d_b^L} \qquad (18)$$

The unknown parameters in the expressions for the interfacial areas are the small and large bubble diameters d_b^S and d_b^L. From visual observation, the small bubble diameter can be estimated to be 1 mm. As shown later, it is not, however, a very sensitive parameter, for the prediction of conversion.

Table I.   Physico-Chemical Data Used in this Study

$(k_L)^S = 0.0074\ \dfrac{cm}{sec}$

$(k_L)^L = 0.031\ \dfrac{cm}{sec}$

$k_1^* = \dfrac{RT}{H}\ \sqrt{k_1 D_A} = 0.11\ \dfrac{cm}{sec}$ (4)

Viscosity of liquid phase = 0.001 Pa.s
Surface tension   = 0.072 N/m

The bubble rise velocity of small bubbles in the system air-water has been calculated to be 0.2 m/s, independent of the superficial gas velocity (9). From a knowledge of the small bubble rise velocity and the gas holdups due to large and small bubbles, the bubble rise velocity of large bubbles can be calculated from the gas volume balance as,

$$U_G = U_{br}^L\ \varepsilon_G^L + U_{br}^S\ \varepsilon_G^S \qquad (19)$$

The large bubble rise velocities calculated from equation 19 are shown in Table II and they are significantly higher than the rise velocities of single bubbles of the same diameter.
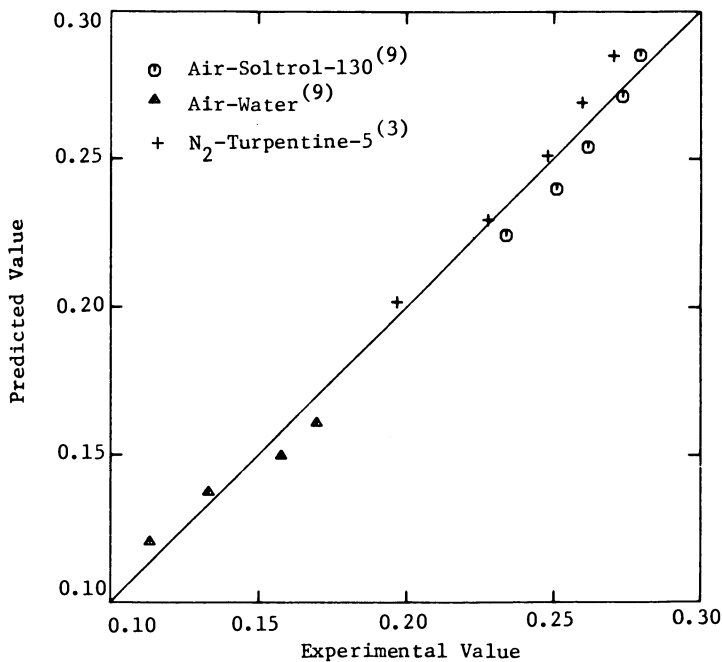
Figure 1. Parity Plot for Correlation of Small Bubble Holdup, ε_G^S.
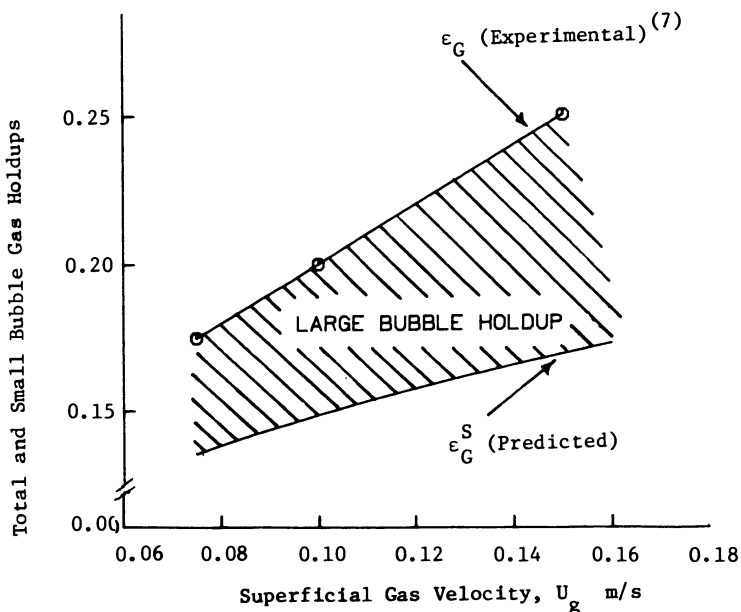
Figure 2. Total and Small Bubble Gas Holdups for CO_2-NaOH System.

Hills and Darton (11) measured the rise velocities of large bubbles in a dispersion of small bubbles and obtained rise velocities of the order of 1.0 m/s. Vermeer and Krishna (3) also measured large bubble rise velocities and obtained values up to 1.8 m/s. Thus, the large bubble rise velocities used in this study are typical of those prevalent in the churn turbulent regime.

The holdup of large bubbles is smaller than that of small bubbles. However, the flux of large bubbles is much larger compared to that of small bubbles as can be seen in Table II. The bubble rise velocity calculated from the correlation of Grace et al. (12) for a single bubble is much smaller than the large bubble rise velocities obtained in this study. Hence, the bubble swarm characteristics in the bubble column should be considered for predicting the large bubble rise velocities. Gal-or and Waslo (13) used a cell model to obtain an expression for the rise velocity of an ensemble of bubbles. Unfortunately, their treatment is limited to low Reynolds numbers. Marrucci (14) proposed a relation for the rise velocity of a swarm of spherical bubbles based on the cell model, which applies to slightly higher Reynolds numbers ($1 \ll Re < 300$). The large bubble rise velocities calculated from this relation were not significantly different from the single bubble rise velocities and were much lower than the bubble rise velocities shown in Table II. The assumption of spherical bubbles made by him is not completely valid for the churn turbulent regime in which large bubbles have an irregular, continuously changing shape, and these deviations from a spherical shape have a significant influence on the rise velocity of bubbles. An extension of the cell model to higher Reynolds numbers is thus required to obtain rise velocities of large bubbles under churn turbulent flow conditions.

Table II. Fluxes of Small and Large Bubbles and Large Bubble Rise Velocities

U_G	$U_{br}^S \, \varepsilon_G^S$	$U_{br}^L \, \varepsilon_G^L$	U_{br}^L
m/s	m/s	m/s	m/s
0.075	0.0271	0.0479	1.222
0.1	0.0297	0.0703	1.297
0.15	0.0338	0.1162	1.438

Analysis and Comparison with Experimental Data

The two bubble class model is applied here to the absorption of CO_2 in NaOH, which conforms to a fast pseudo-first order reaction under certain operating conditions (15). In the data reported by Schumpe et al. (7), CO_2 was absorbed during cocurrent flow in NaOH solution in a 0.102 m diameter bubble column. The gas phase consisted of approximately 10 vol % of CO_2 in N_2. The gas velocities ranged from 0.025 to 0.15 m/s. Since the churn turbulent regime prevailed for gas velocities greater than approximately 0.07 m/s, only the data in the range 0.07 m/s to 0.15 m/s were considered.

Figure 3 shows a comparison between the conversions predicted by the two bubble class model and the experimentally measured values of Schumpe et al. (7). In the theoretical calculations, the small bubble diameter was chosen to be 1 mm based on physical observations made by several investigators. As shown in Table III, the predicted conversions were, however, found to be relatively insensitive to the small bubble diameter. In these calculations, the small bubble diameter was varied from 1 mm to 3 mm and little effect on the conversions was observed.

Table III.   Effect of Small Bubble Diameter Value on Predicted Conversions for a Column Length of 2.36 m

Gas Velocity U_G, m/s	Fractional Conversion of A		
	d_b^S = 1 mm	d_b^S = 2 mm	d_b^S = 3 mm
0.075	0.905	0.900	0.896
0.10	0.865	0.861	0.858
0.15	0.744	0.741	0.738

The large bubble diameter is the most significant parameter in the proposed two bubble class model. Table IV shows the large bubble diameters that were used to predict the conversions. The large bubble diameters are approximately constant at the different dispersion heights (for the same superficial gas velocity) except at L = 0.41 m. This can be attributed to entrance effects due to the small dispersion height in which the bubbles do not achieve their stable equilibrium size. A slight increase in d_b^L with an increase in gas velocity may be caused by the possible increased coalescence at higher gas velocity.
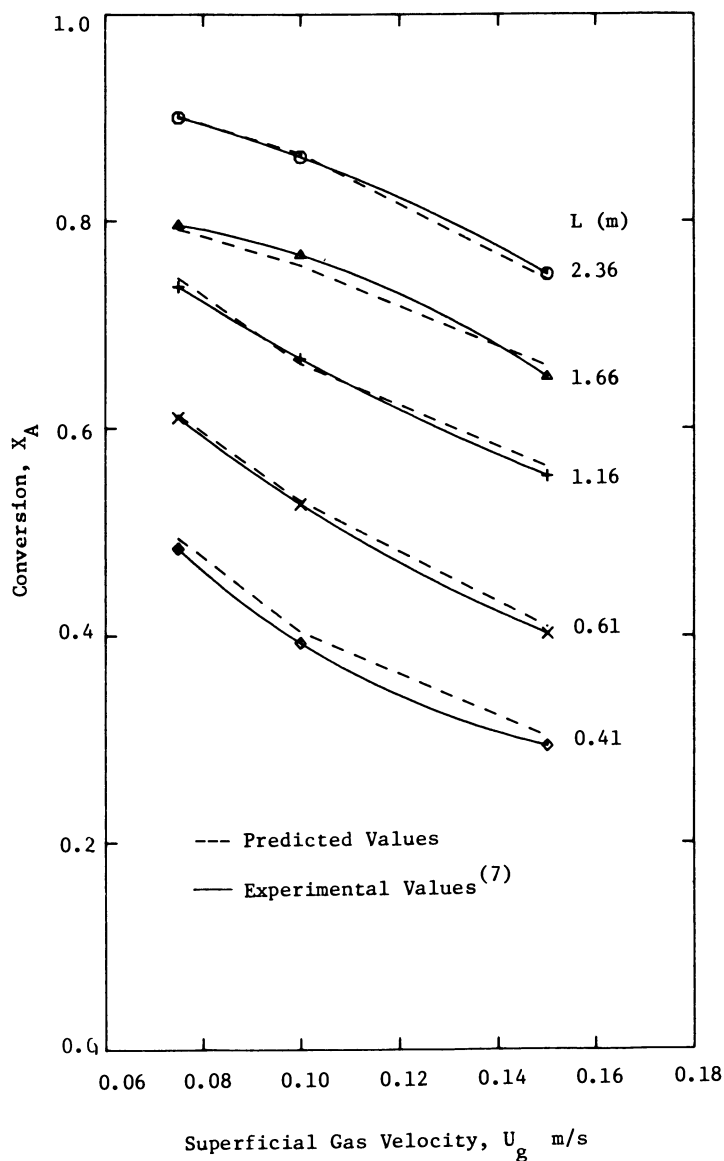
Figure 3. Comparison between conversions predicted by Two-Bubble-Class model and experimental values of Schumpe et al. (7).

Table IV. Large Bubble Diameter Used in the Two Bubble Class Model (d_b^S = 1 mm)

Length, m	2.36	1.66	1.16	0.66	0.41
Gas Velocity U_G, m/s			d_b^L, mm		
0.075	6.0	7.0	6.0	6.0	7.0
0.10	6.5	7.0	7.0	7.0	9.0
0.15	8.5	8.0	8.0	9.0	12.0

The effect of variation in the large bubble diameter on the conversion is shown in Figure 4. In order to determine the sensitivity of conversion to d_b^L, the latter parameter is changed from 10 mm to 20 mm and a large drop in conversion is encountered.

The two bubble class model was compared with the plug flow model outside the range of experimental gas velocities ($U_G >$ 0.15 m/s). The interfacial areas required for the plug flow model (equation 15) were extrapolated from the data of Schumpe et al. (7). A steadily increasing large bubble diameter was used for the two bubble class model. The typical results shown in Figure 5 indicates that the two bubble class model predicts a much sharper drop in conversion than the plug flow model. The maximum value of the large bubble diameter used at U_G = 0.5 m/s was 18 mm. Figure 5 also shows the predictions of the two bubble class model with a constant large bubble size of 10 mm. For this case, while the conversion did not drop as sharply with increased gas velocity, it was still lower than that for the plug flow model. Similar results were obtained for the other experimental conditions. It is, therefore, essential to obtain experimental data for gas velocities greater than 0.2 m/s for further verification of this model.

Discussion

From the results described above, it is seen that the two bubble class model predicts conversions that fit the experimental data. The predicted conversions were obtained with the assumption that the large bubble size varies somewhat with the gas velocity. Thus it is required to have a knowledge of the large bubble diameter (as a function of gas velocity) to properly evaluate the validity of this model.

It should be noted that while in reality, a bubble size distribution exists, a mass transfer model based on the entire bubble size distribution will contain a large number of
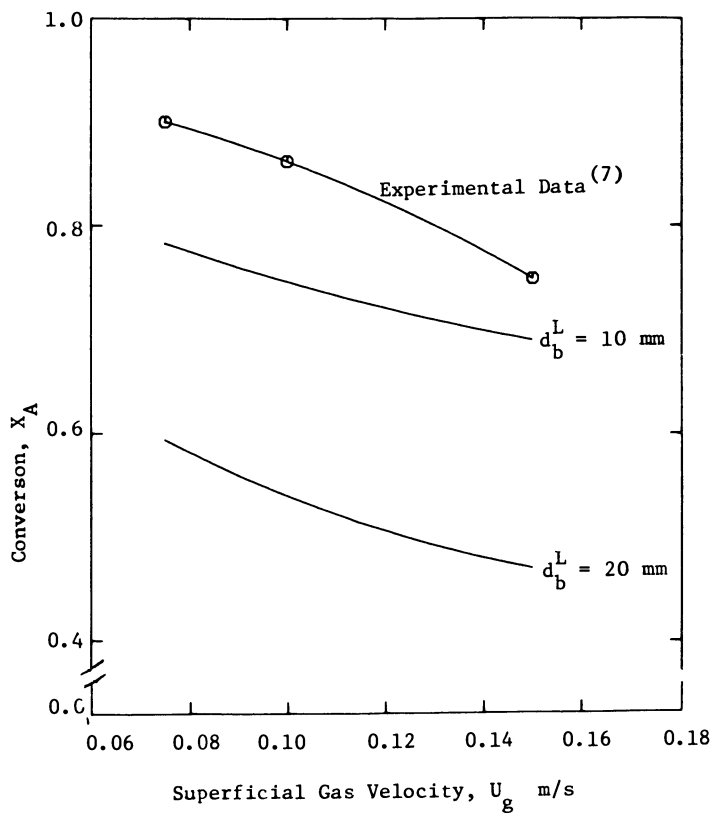
Figure 4.   Effect of large bubble diameter on predicted conversions for L = 2.36 m.
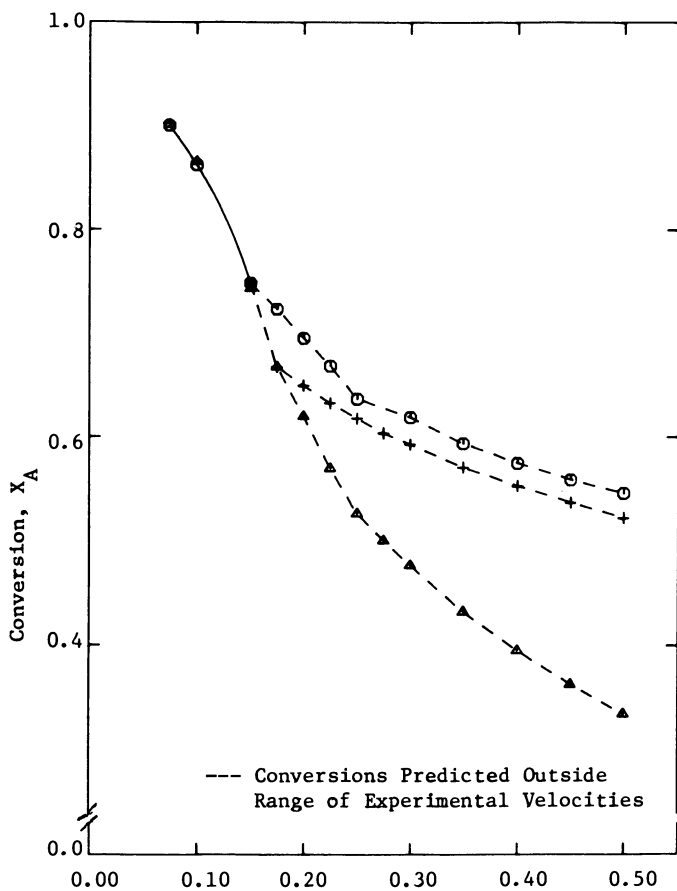
Figure 5. Comparison between Plug Flow model and Two-Bubble-Class model outside range of experimental velocities. (◐ - Plug Flow model, ▲ - Two-Bubble-Class model, varying d_b^L, + - Two-Bubble-Class model, d_b^L = 10 mm).

parameters which would be difficult to evaluate under a wide range of operating conditions. Such a model would, therefore, be of limited value for scale up purposes. Although the two bubble class model presented here is a lumped parameter model, the number of parameters in this model are not large and can be evaluated under a wide range of operating conditions.

The large bubble fractional throughput ($U_{br}^L \, \varepsilon_G^L$) is also a significant parameter in the two bubble class model. As can be seen from Figure 2, the gas holdup due to large bubbles increases with the superficial gas velocity. This also causes the fractional throughput of the large bubbles to increase. However, the increase in large bubble diameter has a more pronounced effect and this causes a decrease in conversion. This result needs to be checked by further experimental study. Consideration of partial backmixing of the small bubbles had no significance on the overall conversion, as is seen in Figure 6. This is due to the fact that for the present case, the conversion in the large bubbles mainly dictates the overall conversion. Figure 7 shows the relative conversions in large and small bubbles. While the conversion in the small bubbles remains constant, the conversion in the large bubbles decreases with an increase in gas velocity causing an overall drop in conversion. The two bubble class model thus has more applications in systems where the large bubble gas holdup is significant, e.g., highly viscous systems, like some fermentation media.

The fractional holdup due to the large bubbles is a function of the physical properties of the system. Thus in a system like N_2-Turpentine-5, Vermeer and Krishna (3) have reported large holdup values due to the large bubbles. This led them to conclude that all the gas was transported as large, fast rising bubbles while small bubbles were merely entrained by local liquid circulations. This is an extreme case in which only the large bubbles contribute to mass transfer. In the present study, the contribution of small bubbles to the overall mass transfer is small since the reaction is fast and the gas in the small bubbles gets almost completely converted. However, for slow reactions, like the absorption of CO_2 in Na_2CO_3, where the gas phase conversion in the small bubbles is low, the contribution of small bubbles to the overall mass transfer can become significant. In the present analysis, the enhancement factor ϕ is assumed to be constant for the large bubbles (i.e., the liquid side mass transfer coefficient predicted by Calderbank and Moo-Young's correlation is independent of bubble diameter for a bubble diameter > 2.5 mm). The liquid side mass transfer coefficient k_L is, however, a function of bubble size and increases with increasing bubble size (16). The presence of surfactants can also affect k_L. If surfactants concentrate at the gas-liquid interface, circumferential surface tension gradients caused by bubble
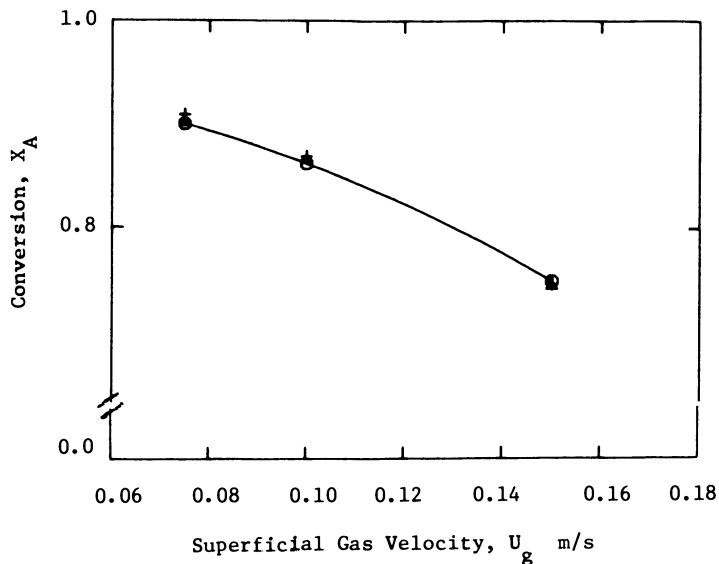
Figure 6. Effect of partial backmixing of the small bubbles on the overall conversion. (⊙ – experimental conversions, ▲ – complete backmixing of small bubbles + – partial backmixing of small bubbles).
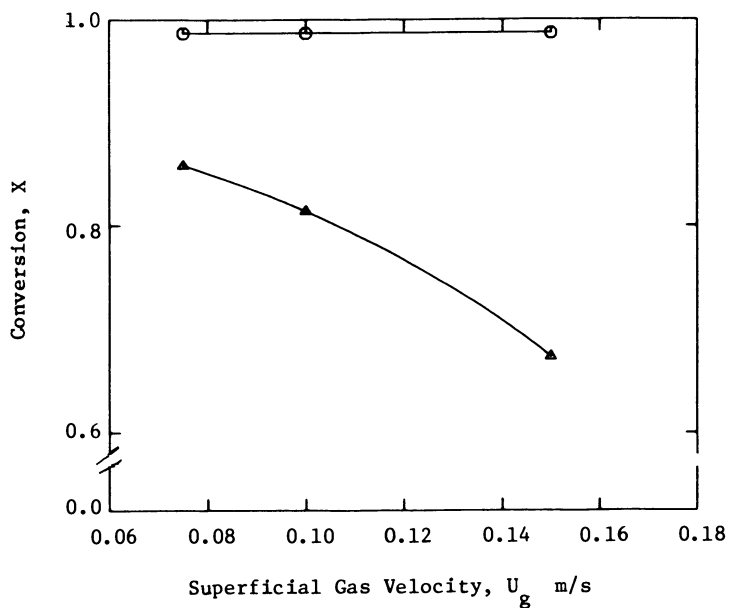
Figure 7. Conversions in large and small bubbles. (⊙ – conversion in small bubbles, ▲ – conversion in large bubbles).

motion retard circulation and vibration. Thus, the high liquid
side mass transfer coefficients obtained for large bubbles may
be reduced to those obtained for rigid spheres in the presence
of surfactants. It is, therefore, important that k_L for both
large and small bubbles be known for the particular gas-liquid
or gas-liquid-solid systems being considered. Furthermore,
Miller (16) has shown that the enhancement factor is dependent
on the bubble diameter and can become negligible for very large
bubble diameters. This implies that mass transfer for very
large bubbles may not occur in the fast reaction regime. In
the range of bubble sizes considered here (6.5 mm to 18 mm),
however, the enhancement factor may be assumed to remain
constant.

     Schumpe et al. (7) analyzed the mass transfer with
chemical reaction in the churn turbulent regime and concluded
that the reactor geometry must be chosen so as to ensure
operation in the homogeneous regime. This, however, means that
low gas velocities should be used. In slurry reactors, a
certain minimum gas velocity is needed for uniform dispersion
of the catalyst. The minimum gas velocity may be as high as
0.1 m/s (for particle sizes < 50 μm (17)) and this precludes
operation in the homogeneous regime. Thus, homogeneous flow
regimes may be rarely encountered in industrial-scale slurry
reactors. The reaction rate at the solid catalyst surface may
be high enough to be influenced by mass transfer. In these
situations, the two bubble class model should be used for scale
up considerations. Godbole (9) has used the two bubble class
model to study the Fischer-Tropsch synthesis in slurry
reactors.

Conclusions

The two bubble class model is more realistic than the single
class plug flow model for the churn turbulent regime. The two
bubble classes that develop in this regime and their separate
contributions to the overall mass transfer are considered in
this model. A knowledge of the large bubble diameter is
required for the application of this model. The model is
particularly useful for slurry reactors where the churn
turbulent regime cannot be avoided. Even with fast intrinsic
kinetics, conversions of the key gas reactant could be limited
to about 80% when the gas velocity is above 0.1 m/s. When the
scale-up of a bubble column is accompanied by a change in flow
regime, the two bubble class model will give a more reliable
scale-up than the single class plug flow model.

Acknowledgments

Legend of Symbols

a	gas-liquid interfacial area, m^{-1}
A	gas phase reactant in the reaction given by equation 1
B	liquid phase reactant in the reaction given by equation 1
C_{AL}	liquid phase concentration of A, $kgmole/m^3$
C_{AL}^{*}	equilibrium concentration of A in the liquid phase, $kgmole/m^3$
d_b	bubble size, mm
D	diameter of column, m
D_A	diffusivity of A, m^2/s
D_G	gas phase dispersion coefficient, m^2/s
g	acceleration due to gravity, ms^{-2}
H	Henry's constant, $Pa.m^3/kgmole$
Ha	Hatta number
k_1	first order reaction rate constant, s^{-1}
k_L	liquid side mass transfer coefficient, m/s
$k_L a$	volumetric liquid side mass transfer coefficient, s^{-1}
L	dispersion height, m
P	pressure at any point in the column, Pa
P_T	pressure at the top of the column, Pa
R	Gas constant, $Pa.m^3/kgmole.K$
St_G	gas phase Stanton number
T	temperature, K
U_{br}	bubble rise velocity, m/s
x	distance along reactor, m
X_A	conversion of gas phase reactant, A
Y_{AG}	mole fraction of A in the gas phase
z	dimensionless axial distance along reactor
Z	stoichiometric factor for reaction between A and B

Greek Letters

ε_G	gas holdup
μ_L	liquid phase viscosity, Pa.s
σ	surface tension, N/m
ϕ	enhancement factor due to chemical reaction
ρ_L	liquid phase density, kg/m^3

Subscripts

0	inlet of reactor
1	outlet of reactor
m	mean value

Superscripts

L   large bubbles
S   small bubbles

Literature Cited

1.   Shah, Y. T.; Kelkar, B. G.; Godbole, S. P.; Deckwer, W. D.
     AIChE J. 1982, 28, 353.
2.   Bach, H. F.; Pilhofer, T. Ger. Chem. Eng. 1978, 1, 270.
3.   Vermeer, D. J.; Krishna, R. Ind. Eng. Chem. Process Des.
     Dev. 1981, 20, 475.
4.   Schumpe, A. Dr. Thesis, Universitat Hannover, Hannover,
     1981.
5.   Godbole, S. P.; Honath, M. F.; Shah, Y. T. Chem. Eng.
     Commun. 1982, 16, 119.
6.   Kelkar, B. G.; Godbole, S. P.; Honath, M. F.; Shah, Y. T.;
     Carr, N. L.; Deckwer, W. D. AIChE J. 1983, 29, 361.
7.   Schumpe, A.; Serpemen, Y; Deckwer, W. D. Ger. Chem. Eng.
     1979, 2, 234.
8.   Sriram, K.; Mann, R. Chem. Eng. Sci. 1977, 32, 571.
9.   Godbole, S. P. Ph.D. Thesis, University of Pittsburgh,
     Pittsburgh, 1983.
10. Calderbank, P. H.; Moo-Young, M. Chem. Eng. Sci. 1961, 16,
     39.
11. Hills, J. H.; Darton, R. C. Trans. I ChemE 1976, 54, 258.
12. Grace, J. R.; Wairegi, T.; Nguygen, T. H. Trans. I ChemE
     1973, 51, 116.
13. Gal-or, B; Waslo, S. Chem. Eng. Sci. 1968, 23, 1431.
14. Marrucci, G. Ind. Eng. Chem. Fundam. 1965, 4, 224.
15. Danckwerts, P. V.; Sharma, M. M. The Chem. Engr. 1966, 46,
     CE 244.
16. Miller, D.N. AIChE J. 1983, 29, 312.
17. Brian, B.W.; Dyer, P.N. a paper to be published in ACS
     Symposium Series (1983).

Mathematical Modeling of Cross-Flow, Solid State Electrochemical Reactors

P. G. DEBENEDETTI and C. G. VAYENAS[1]—Department of Chemical Engineering, Massachusetts Institute of Technology, Cambridge, MA 02139

I. YENTEKAKIS—Department of Chemical Engineering, University of Patras, Patras, Greece

L. L. HEGEDUS—W. R. Grace & Co., Research Division, Columbia, MD 21044

There is increasing interest in solid-state electro-
catalytic reactors for a variety of potential appli-
cations (fuel cells, cogenerators of chemicals and
electricity, chemical reactors, and electrolyzers).
All of these applications demand high surface area
per unit reactor volume. Such a geometric require-
ment is best satisfied by cross flow monolithic
elements; this paper provides the first mathematical
analysis of solid-state electrocatalytic reactors
with such geometry.
     A two-dimensional mixing-cell model has been
constructed to simulate the distribution of temper-
ature, concentration and current density in cross-
flow monoliths. Preliminary model calculations
are presented here.

One of the emerging uses of solid-state electrocatalytic systems
is in fuel cells, to convert a significant portion of the Gibbs
free energy change of exothermic reactions into electricity rather
than heat. The thermodynamic efficiency of such power generating
schemes compares favorably with thermal power generation which is
limited by Carnot-type constraints.
     Solid-electrolyte fuel cells, operating on H_2 or CO as the
fuel, have been constructed and tested for years (1-2). Similar
devices have been used for steam electrolysis (3), for NO decom-
position (4), and for methane synthesis from CO and H_2 (5).
     Zirconia cells with Pt catalyst-electrodes can also be used
to convert ammonia to nitric oxide with simultaneous electrical
energy generation (6-7). Other industrially important oxidation
reactions have been recently proposed for solid-state electro-

[1]Current Address: Department of Chemical Engineering, University of Patras, Patras, Greece.

catalytic reactors, such as sulfur conversion to SO_2 or SO_3 ([8])
or ethylene epoxidation ([9]).

The practical usefulness of these electrochemical converters
is partly a function of their volume power densities. This para-
meter is composed of the oxygen ion transfer area per unit reactor
volume (cm^2/cm^3) multiplied by the power density per unit oxygen
ion transfer area (W/cm^2). Previous fuel cells ([1,10]) exhibited
volume power densities in the range of 300-400 W/ℓ; the fuel cell
configuration we describe here has the potential of further in-
creasing this number, primarily by increasing the oxygen ion
transfer area per unit reactor volume by about a factor of four
to five.

Cross-flow monoliths have been explored by Degnan and Wei
([11-12]) as cocurrent and countercurrent reactor-heat exchangers.
Four cross-flow monoliths in series were employed; the individual
blocks were analyzed by a one-dimensional approximation. They
found good agreement between theory and experiment.

Roy and Gidaspow ([13-14]) developed two-dimensional continuum
models to describe cross-flow monolithic heat exchangers and
catalytic reactors.

Despite the geometric similarities, the problem analyzed
here is fundamentally different from that of cross-flow heat ex-
changers or catalytic reactors in that the solid is not only used
as a heat-exchange medium or as a catalyst support but also as
the electrolyte across which oxygen ion transport occurs. This
introduces an integral electron conservation balance which re-
sults in an integro-differential problem.

The modelling of single-cell, solid-state electrocatlytic
reactors was recently discussed by Debenedetti and Vayenas ([15]);
this paper's objective is to develop an analysis for cross-flow
monolithic designs.

Reactor Configuration

A schematic diagram of a cross-flow monolith fuel cell reactor is
given in Figure 1. The reactor consists of two sets of channels
in the x and y direction, respectively.

Channels in the x direction serve for the oxidant flow.
Their surface is coated with a catalyst such as Pt or Ag which
facilitates the reduction of O_2 to O^{2-}. Since yttria-doped zir-
conia is a pure O^{2-} conductor, the oxygen ions migrate through
the solid electrolyte wall to channels y which serve for the fuel
flow.

Channels y are perpendicular to channels x and the two al-
ternate along the z axis of the monolith. The walls of channels
y are coated with a suitable metal or conductive metal oxide
catalyst which catalyzes the fuel's anodic oxidation.

The fuel can be either inorganic such as hydrogen, carbon
monoxide, ammonia, sulfur vapor, sulfur dioxide, or organic such as
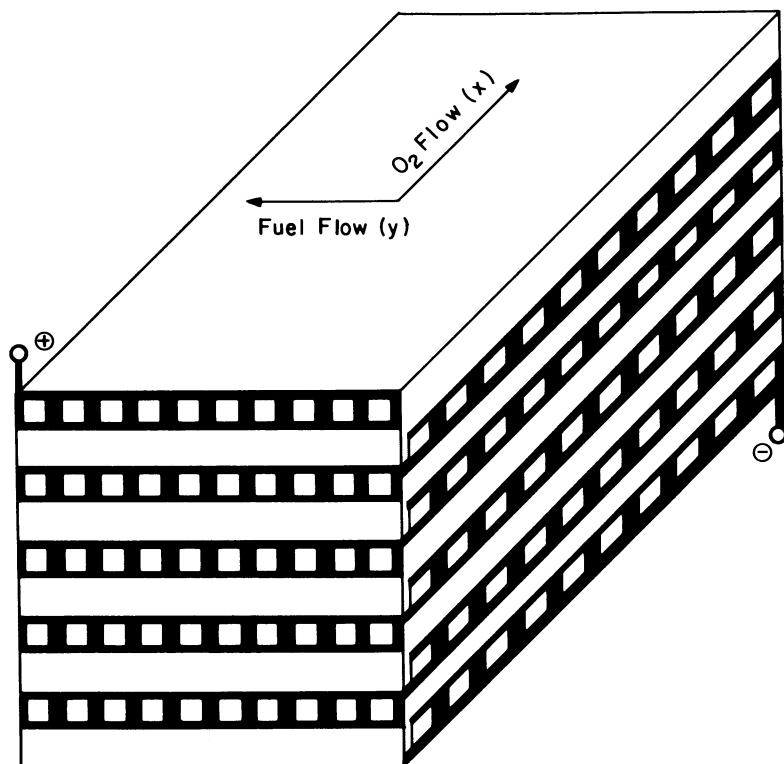
Figure 1. Schematic diagram of cross-flow monolith fuel cell; Z=5; series connection; 100 unit cells per battery. Dark areas indicate conductive metal film coating.

methane or methanol. Other fuels can of course also be used; de-
pending on the nature of the fuel and that of the desired partial
or complete oxidation product, one must use different catalyst-
electrode materials in channels y. Thus, one can use Pt for
ammonia conversion to NO (6) or for H_2 and CO combustion (2), Ag
for ethylene epoxidation (9), or complex base metal oxide systems
for H_2 and CO oxidation (10).

    One restriction regarding the nature of the catalyst coating
on the walls of channels x and y is that it must be electrically
conductive but also reasonably porous so that it allows the ac-
cess of fuel or O_2 molecules to the solid electrolyte-catalyst-
gas three-phase boundary.

    Porous and highly conductive Pt, Ag, and In_2O_3 films can be
deposited on zirconia (2,9,4,10).

    Although the present analysis is focused on the case of CO
oxidation to CO_2, the application of the model to other oxidation
reactions is quite straightforward.

    Considering the oxidation reaction

$$nA + O_2 \rightarrow nB \tag{1}$$

the following reactions take place at the cathode, i.e., x chan-
nels and anode, i.e., y channels, respectively:

$$O_2 + 4e^- \rightarrow 2O^{2-} \tag{2}$$

$$nA + 2O^{2-} \rightarrow nB + 4e^- \tag{3}$$

    Thus the net effect is the conversion of A into product B
and simultaneous electrical energy generation.

    Under low current density conditions, i.e., at very large
external loads, a large fraction of the Gibbs free energy change
of the above oxidation reaction is converted into electrical en-
ergy. At higher current densities, the cell voltage E drops from
its reversible value E_{rev}.

    In the absence of activation and concentration polarization,
the power output P = EI of the cell is maximized when the exter-
nal resistance R_{ex} equals the internal resistance of the cell.

    The thermodynamic cell efficiency η is ususally defined as
the dimensionless cell voltage

$$\eta = E/E_{th} = W/(-\Delta H^\circ) \tag{4}$$

where the thermoneutral voltage E_{th} is given by

$$E_{th} = n(-\Delta H^\circ)/4F \qquad (5)$$

and W is the electrical work produced per mole of fuel.
    Since, in general,

$$E = E_{rev} - \phi_{ohm} - \phi_{act} - \phi_{conc} \qquad (6)$$

and

$$E_{rev} = n(-\Delta G)/4F = n(-\Delta H+T\Delta S)/4F \qquad (7)$$

it follows that for low current densities, i.e., for low values of ϕ_{ohm}, ϕ_{act}, and ϕ_{conc}, the cell efficiency η can exceed unity for reactions with positive ΔS, such as NH_3 oxidation to NO, but will be less than one (about 0.75) for CO oxidation, even at vanishing current densities, due to the negative ΔS associated with this reaction.

Mathematical Model

The geometry of the reactor is shown in Figure 1. We assume that the top and bottom surfaces are insulated, so that there is no net heat flux in the z-direction and thus the problem becomes two-dimensional.
    There is of course no net mass flow in the z direction, except for that of the 0^{2-} ions inside the electrolyte which is accounted for in the electron balance equations.
    For modeling purposes, the reactor is considered to be composed of unit cells; one such unit cell is shown in Figure 2.
    There are K times L such unit cells in each unit battery and KLZ unit cells in the entire reactor. The unit cells are labeled 1,2 ... k ... K in the x direction (oxidant flow), 1,2 ... ℓ ... L in the y direction (fuel flow), and they are stacked along the z direction but not indexed due to the two-dimensional nature of the problem.
    The unit batteries, as shown in Figure 1, are connected in series. The model formulation can easily be extended to cover parallel unit battery configurations. However, all numerical runs were carried out for the series configuration.
    Within each unit cell, we assumed uniform solid temperature and uniform gas-phase composition and temperature for both streams. However, the (uniform) fuel and oxidant stream temperatures are of course, different from each other and from the solid temperature.
    The model describes mass and energy transport between neighboring cells, as well as the coupling between these and the elec-
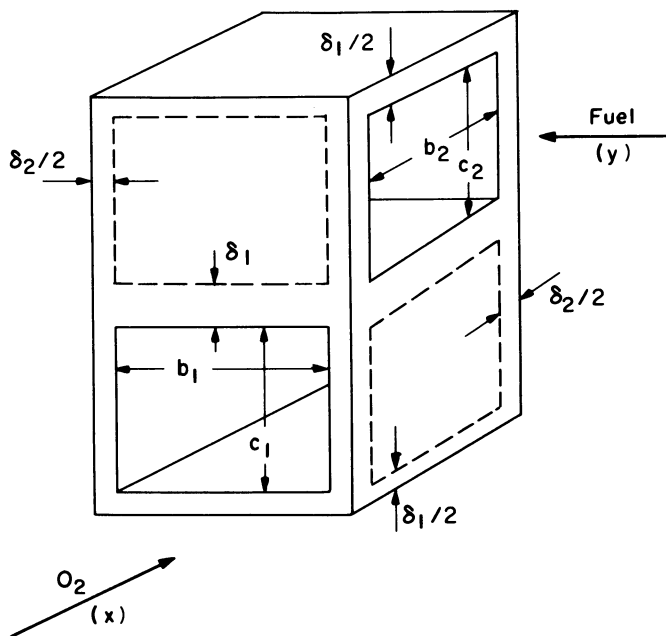
Figure 2.   Schematic diagram of a unit cell.

tric circuit equations, which can be viewed as "electron balance" equations. Kirchoff's first law completes the electrical description and introduces an integral balance into the mathematical model.

<u>Fuel Channel Mass Balance</u>. Since the current produced by an electrocatalytic reaction is related to the conversion of reactive species, we can express the local mass balances in terms of local current densities, using Faraday's law.

   Thus, for the fuel A in cell (k, ℓ) we obtain

$$i_{k, \ell} = \lambda N_A (\frac{4F}{n}) \frac{c_2}{b_1} (X_{A, k, \ell} - X_{A, k, \ell-1}) \tag{8}$$

Defining a dimensionless local current density as

$$\xi_{k, \ell} = \frac{i_{k, \ell}}{N_A (\frac{4F}{n}) \frac{c_2}{b_1}} \tag{9}$$

and substituting it into Equation 8, we obtain a dimensionless fuel conservation equation in the form of

$$\xi_{k, \ell} = \lambda (X_{A, k, \ell} - X_{A, k, \ell-1}) \tag{10}$$

where $\lambda=1$ for series connection of unit batteries with insulating plates between adjacent unit batteries (as shown in Figure 1) and $\lambda = 0.5$ for parallel connection of unit batteries.

   The choice of parallel or series connections, or their combinations, allows one to manipulate the internal resistance of the unit in order to maximize its power output for a desired value of external load.

   In principle, parallel connection doubles the effective oxygen ion transfer surface area when compared with series connection, since the entire geometric electrolyte surface is utilized for oxygen ion transfer. This is a consequence of the geometry of the cross-flow monolith configuration.

<u>Oxidant Channel Mass Balance</u>. Using the Faraday relationship as for the fuel, the consumption of oxygen in the oxygen channel of unit cell (k,ℓ) becomes

$$i_{k, \ell} = N_{O_2} (4F) \frac{c_1}{b_2} (X_{O_2, k, \ell} - X_{O_2, k-1, \ell}) \tag{11}$$

Substituting the dimensionless current density $\xi_{k, \ell}$ from

Equation 9, we obtain

$$\xi_{k,\ell} = N_1 \lambda (X_{O_2,k,\ell} - X_{O_2,k-1,\ell}) \tag{12}$$

where

$$N_1 = \frac{N_{O_2}}{N_A} \cdot n \cdot \frac{c_1 b_1}{c_2 b_2} \tag{13}$$

<u>Fuel Stream Energy Balance</u>. The following components contribute to the heat balance of the gas phase of the fuel channel in unit cell (k,ℓ):

$$b_2 c_2 N_A (1-X_{A,k,\ell-1}) C_{P,A} T_{F,k,\ell-1} +$$

$$b_2 c_2 N_A X_{A,k,\ell-1} C_{P,B} T_{F,k,\ell-1} +$$

$$b_2 c_2 N_D C_{P,D} T_{F,k,\ell-1} +$$

(convective enthalpy input from cell $(k,\ell-1)$)

$$\frac{\lambda i_{k,\ell}}{(\frac{4F}{n})} b_1 b_2 C_{P,B} T_{S,k,\ell} =$$

(enthalpy gain through product transfer from solid)

$$b_2 c_2 N_A (1-X_{A,k,\ell}) C_{P,A} T_{F,k,\ell} +$$

$$b_2 c_2 N_A X_{A,k,\ell} C_{P,B} T_{F,k,\ell} +$$

$$b_2 c_2 N_D C_{P,D} T_{F,k,\ell} +$$

(convective enthalpy loss to cell $(k, \ell+1)$)

$$\frac{\lambda i_{k,\ell}}{(\frac{4F}{n})} b_1 b_2 C_{P,A} T_{F,k,\ell} +$$

(enthalpy loss through reactant transfer to solid)

$$2 h_F (b_1+\delta_2)(b_2+c_2)(T_{F,k,\ell} - T_{S,k,\ell}) \tag{14}$$

(heat loss to solid through heat transfer)
We define dimensionless temperatures as

$$\theta_F = T_F/T_{F,in} \tag{15}$$

$$\theta_S = T_S/T_{F,in} \tag{16}$$

with which, after algebraic rearrangement, one obtains

$$\theta_{F,k,\ell} - \theta_{F,k,\ell-1} = \frac{(\theta_{S,k,\ell} - \theta_{F,k,\ell})[N_2 + N_{11}(X_{A,k,\ell} - X_{A,k,\ell-1})]}{1 + N_3 + (N_{11}-1)X_{A,k,\ell-1}} \tag{17}$$

where

$$N_2 = \frac{2h_F(b_1+\delta_2)(b_2+c_2)}{b_2 c_2 N_A C_{P,A}} \tag{18}$$

$$N_3 = N_D C_{P,D}/N_A C_{P,A} \tag{19}$$

$$N_{11} = C_{P,B}/C_{P,A} \tag{20}$$

<u>Oxidant Stream Energy Balance</u>. Similar terms were considered for the oxidant compartment of the gas phase of unit cell (k,ℓ), so it is not necessary to list them in detail.
    The resulting dimensionless oxidant stream energy balance is

$$\theta_{OX,k,\ell} - \theta_{OX,k-1,\ell} = \frac{N_4(\theta_{S,k,\ell} - \theta_{OX,k,\ell})}{1 + N_5 - X_{O_2,k-1,\ell}} \tag{21}$$

with

$$\theta_{OX} = T_{OX}/T_{F,in} \tag{22}$$

$$N_4 = \frac{2h_{OX}(b_2+\delta_2)(b_1+c_1)}{b_1 c_1 N_{O_2} C_{P,O_2}} \tag{23}$$

$$N_5 = N_{N_2} C_{P,N_2}/N_{O_2} C_{P,O_2} \tag{24}$$

<u>Solid Energy Balance</u>. The solid-phase energy balance is composed of terms related to thermal communication with the walls of neighboring unit cells, with the two gas-phase compartments of unit cell (k,ℓ), and of the electrical work produced. For clarity, we have elected to show these terms in detail.

$$\frac{k_s A_{S,F}(T_{S,k,\ell+1} - T_{S,k,\ell})}{(b_1+\delta_2)} +$$

$$\frac{k_s A_{S,F}(T_{S,k,\ell-1} - T_{S,k,\ell})}{(b_1+\delta_2)} +$$

$$\frac{k_s A_{S,OX}(T_{S,k+1,\ell} - T_{S,k,\ell})}{(b_2+\delta_2)} +$$

$$\frac{k_s A_{S,OX}(T_{S,k-1,\ell} - T_{S,k,\ell})}{(b_2+\delta_2)}$$

(conductive input from neighboring cells)

$$-2h_{OX}(b_2+\delta_2)(b_1+c_1)(T_{S,k,\ell} - T_{OX,k,\ell})$$

$$-2h_F(b_1+\delta_2)(b_2+c_2)(T_{S,k,\ell} - T_{F,k,\ell}) +$$

(heat transfer from solid to gas)

$$b_1 b_2 \lambda \frac{i_{k,\ell}}{4F} C_{P,O_2}(T_{OX,k,\ell} - T_{F,in}) +$$

$$b_1 b_2 \lambda \frac{i_{k,\ell}}{(\frac{4F}{n})} [C_{P,A}(T_{F,k,\ell} - T_{F,in}) + H_A^\circ]$$

$$- b_1 b_2 \lambda \frac{i_{k,\ell}}{(\frac{4F}{n})} [C_{P,B}(T_{S,k,\ell} - T_{F,in}) + H_B^\circ]$$

$$= \lambda i_{k,\ell} b_1 b_2 E \qquad\qquad (25)$$

(electrical work produced by unit cell)

where

$$A_{S,F} = \delta_1(b_2+\delta_2) + c_2\delta_2 \qquad\qquad (26)$$

$$A_{S,OX} = \delta_1(b_1+\delta_2) + c_1\delta_2 \qquad\qquad (27)$$

Introducing the above-defined dimensionless temperatures and recalling the definition of η from Equation 4, after appropriate algebraic manipulation we obtain

$$(\theta_{S,k,\ell+1} + \theta_{S,k,\ell-1} - 2\theta_{S,k,\ell}) +$$

$$N_6(\theta_{S,k+1,\ell} + \theta_{S,k-1,\ell} - 2\theta_{S,k,\ell})$$

$$-N_7(\theta_{S,k,\ell} - \theta_{OX,k,\ell}) - N_8(\theta_{S,k,\ell} - \theta_{F,k,\ell}) +$$

$$\lambda N_9 \xi_{k,\ell} [N_{10}(\theta_{OX,k,\ell}-1)+(\theta_{F,k,\ell}-1)-N_{11}(\theta_{S,k,\ell}-1) +$$

$$N_{12}(1-\eta)] = 0 \tag{28}$$

where

$$N_6 = (\frac{A_{S,OX}}{A_{S,F}})(\frac{b_1+\delta_2}{b_2+\delta_2}) \tag{29}$$

$$N_7 = \frac{2h_{OX}(b_2+\delta_2)(b_1+c_1)(b_1+\delta_2)}{k_S A_{S,F}} \tag{30}$$

$$N_8 = \frac{2h_F(b_1+\delta_2)^2(b_2+c_2)}{k_S A_{S,F}} \tag{31}$$

$$N_9 = \frac{b_2 c_2 (b_1+\delta_2) N_A C_{P,A}}{k_S A_{S,F}} \tag{32}$$

$$N_{10} = \frac{C_{P,O_2}}{n C_{P,A}} \tag{33}$$

$$N_{12} = \frac{(-\Delta H^\circ)}{C_{P,A} T_{F,in}} \tag{34}$$

Note that, despite the typically high operating temperatures of fuel cells, radiative heat transfer was neglected. Lee and Aris (16) have discussed such effects in parallel-channel monoliths. The importance of radiative transport depends on the emissivity of the surface; for the low (about 0.1) emissivity of Pt-coated catalyst-electrodes, their analysis suggests that radiative effects can be neglected.

Electron Balance Equations. In order to solve the system of dif-

ference equations (10,12,17,21,28), it is necessary to express the local current density $\xi_{k,1}$ and the dimensionless cell voltage η in terms of local solid temperatures and gaseous compositions.

It can be shown that for typical thicknesses of solid electrolyte (say, 100 μm) and porous metal catalyst film (say, 10μm), the major source of ohmic resistance (>99%) is the solid electrolyte. The consequence is that the actual dimensionless operating voltage η is constant along each channel and also constant for all channels electrically connected in parallel (as shown in Figure 1), i.e., constant within each unit battery. This observation significantly simplifies the development of the electron balance equations.

Considering an elementary unit cell (k,ℓ), and neglecting activation and concentration overpotential, one obtains from Equation 6

$$E_{k,\ell} = E_{rev,k,\ell} - b_1 b_2 \, i_{k,\ell} R_{k,\ell} \tag{35}$$

where the last term represents the ohmic overpotential ϕ_{ohm}.

In most high-temperature, solid-electrolyte fuel cells, the major source of overpotential is ohmic (1-2, 17).

Activation overpotential may become important with a number of electrocatalysts; however, as Debenedetti and Vayenas (15) have discussed, the actual current-voltage behavior of the unit at moderate and high current densities can be well approximated by subtracting the activation overpotential from E_{rev}. For CO oxidation over Pt, this correction is not necessary if the feed contains either 2-3 vol. % H_2 or H_2O (with small amounts of Cr_2O_3 in the catalyst in the latter case)(18).

Concentration overpotential arises due to external or internal mass transfer limitations. For typical cross-flow monoliths, Debenedetti (19) has shown that concentration overpotential is not important under conditions similar to those explored here. The analysis employed mass transfer coefficients for fully developed laminar flows in square ducts.

The unit cell resistance $R_{k,\ell}$ can be expressed in terms of the ionic resistivity of the solid electrolyte:

$$R_{k,\ell} = \rho_{k,\ell} \frac{\lambda \delta_1}{b_1 b_2} \tag{36}$$

We can also express E_{rev} in terms of fuel and oxygen conversions employing the Nernst relationship. With these, Equation 36, and

noting that $E_{k,\ell} = E$ for all k and ℓ as discussed,

$$E = E^{\circ}_{k,\ell} + \frac{nRT}{4F} \ell n (P_T^{1/n}) \frac{(1-X_{A,k,\ell})(1-X_{O_2,k,\ell})^{1/n}}{X_{A,k,\ell}}$$

$$- \rho_{k,\ell} i_{k,\ell} \lambda \delta_1 \qquad\qquad (37)$$

Note again that although all right-hand terms in Equation 37 are different for each unit cell, their sum (E) is invariant with unit cell conditions due to the high conductivity of the catalyst-electrode.

The electrolyte resistivity, $\rho_{k,\ell}$, depends exponentially on the local solid termperature:

$$\rho_{k,\ell} = \rho_o \exp \left[- \frac{E_{Act}}{RT_{F,in}} (1- \frac{1}{\theta_{S,k,\ell}}) \right] \qquad\qquad (38)$$

This can be substituted into Equation 37.

To obtain a second equation between E and $i_{k,\ell}$, it is necessary to specify the nature of the electrical connections between the unit batteries.

Series Connection of Unit Batteries. In this case every second plate in the monolith is not covered with a catalyst-electrode.

The total voltage of the monolith can be computed from Kirchhoff's first law:

$$ZE = \sum_{k=1}^{K} \sum_{\ell=1}^{L} b_1 b_2 i_{k,\ell} [(Z+1)R_e + R_{ex}] \qquad\qquad (39)$$

where Z is the number of unit batteries in the structure, R_e is the ohmic resistance of each connection between adjacent batteries, and R_{ex} is the external resistive load where the electrical power produced is dissipated.

Equations 37, 38, and 39 can be rearranged and expressed in dimensionless form as

$$\xi_{k,\ell} = [N_{13} + (N_{14}+N_{15} \ell n \frac{P_T^{1/n}(1-X_{A,k,\ell})(1-X_{O_2,k,\ell})^{1/n}}{X_{A,k,\ell}}) \theta_{s,k,\ell}$$

$$- N_{16} \sum_{k=1}^{K} \sum_{\ell=1}^{L} \xi_{k,\ell}] \exp [N_{17}(1-\frac{1}{\theta_{S,k,\ell}})] \qquad\qquad (40)$$

$$\eta = N_{18} \sum_{k=1}^{K} \sum_{\ell=1}^{L} \xi_{k,\ell} \qquad (41)$$

where

$$N_{13} = \frac{(-\Delta H^\circ)}{N_A (4F/n)^2 \rho_o} \left(\frac{b_1}{c_2 \delta_1 \lambda}\right) \qquad (42)$$

$$N_{14} = \frac{(\Delta S^\circ) T_{F,in}}{N_A (4F/n)^2 \rho_o} \left(\frac{b_1}{c_2 \delta_1 \lambda}\right) \qquad (43)$$

$$N_{15} = \frac{RT_{F,in}}{N_A (4F/n)^2 \rho_o} \left(\frac{b_1}{c_2 \delta_1 \lambda}\right) \qquad (44)$$

$$N_{16} = \frac{b_1 b_2 [(Z+1)R_e + R_{ex}]}{Z \delta_1 \rho_o \lambda} \qquad (45)$$

$$N_{17} = E_{act}/RT_{F,in} \qquad (46)$$

$$N_{18} = \frac{b_2 c_2 (4F/n)^2 N_A [(Z+1)R_e + R_{ex}]}{Z(-\Delta H^\circ)} \qquad (47)$$

It is interesting to note that $\xi_{k,\ell}$ in Equation 40 is in fact equivalent to a dimensionless rate; the right side of the equation shows how the local rate depends on the concentrations (expressed as fractional conversions) of the reactants. The double summation indicates that the reaction rate is not only a function of local properties but also of the global performance of the reactor. This represents a feedback mechanism to each unit cell.

Parallel Connection of Unit Batteries. In this case there are only two external connections of resistance R_e. For a total of Z unit batteries it can be shown that the electron balance equations (40) and (41) remain valid, but the dimensionless numbers N_{16} and N_{18} will change:

$$N_{16}(\text{parallel}) = \frac{b_1 b_2 (Z) (R_{ex} + 2R_e)}{\delta_1 \rho_o \lambda} \qquad (48)$$

$$N_{18}(\text{parallel}) = \frac{b_2 c_2 (\frac{4F}{n})^2 N_A (R_{ex} + 2R_e) Z}{(-\Delta H°)} \qquad (49)$$

Boundary Conditions. The boundary conditions of the problem
arise through the appropriate specification of cells at the geo-
metric boundaries of the cross-flow monolith body.
    From the standpoint of mass balances, this required the spec-
ification of inlet concentrations. For the energy balances of
the outer cell layers ($k = 1$ and K, and $\ell = 1$ and L), the speci-
fications included perfect thermal insulation at the outer unit
cell walls, to simulate adiabatic behavior.

Oxygen Ion Transfer Area per Unit Reactor Volume. As discussed
above, the prime attraction of the cross-flow monolith configura-
tion is its potentially high oxygen ion transfer area per unit re-
actor volume. From our unit cell (Figure 2), this volume-specific
area computes as

$$S = \frac{b_1 b_2}{\lambda(b_1 + \delta_2)(b_2 + \delta_1)(c_1 + c_2 + 2\delta_1)} \qquad (50)$$

    For 1mm x 1mm channels, with 100μm walls, we obtain (series
connection) $S = 3.76$ cm^2/cm^3. Within the limits of ceramics pro-
cessability, this number, in principle, can be significantly in-
creased.

Numerical Solution of the Equations

It should be noted that if a differential mass, energy and elec-
tron balance approach were followed to describe the reactor's be-
havior one would obtain a set of non-linear, partial, integro-
differential equations. However, since the reactor is simulated
by a two-dimensional array of mixing cells, a large number of al-
gebraic equations result in which there are no differentials and
in which double integrals are replaced by double summations.
    For a 10x10 array of unit cells, there is a total of 601 e-
quations: 200 mass balances (Equations 10 and 12), 300 energy
balances (Equations 17, 21, 28), 100 electron balances (Equation
40) and one voltage equation (41). The corresponding 601 un-
knowns are 200 local fuel and oxidant conversions, 300 local fuel,
oxidant and solid temperatures, 100 local current densities, and
the dimensionless operating voltage.
    In this paper we have not explored the "lumping" of unit cells
into clusters to reduce the number of equations required to model
a given structure. Work is in progress along these lines, how-

ever; such lumping, if successful, would permit the modeling of cross-flow structures of more realistic size than the ones explored here.

The solution is greatly simplified by realizing that of the 601 equations, only the 100 electron balances are non-linear.

Arbitrary initial values were given to the 100 $\xi_{k,\ell}$ variables. Then the mass balance equations (10 and 12) were solved directly for all oxygen conversions $X_{O_2,k,\ell}$ and fuel conversions $X_{A,k,\ell}$. Subsequently, the 300 linear energy balance equations (17), (21) and (28) were solved for $\theta_{F,k,\ell}$, $\theta_{Ox,k,\ell}$ and $\theta_{S,k,\ell}$ using a Gauss elimination subroutine with pivoting. Then the electron balance equations (40) were solved to obtain new values for $\xi_{k,\ell}$

and the iterative procedure was repeated until all $\xi_{k,\ell}$ matched their previous value within 10^{-3}. This usually required five to ten iterations.

Results and Discussion

The system's parameters can be divided into three groups: feed conditions (N_A, N_{O_2}, N_D, N_{N_2}, n, $T_{F,in}$, $T_{OX,in}$), reactor operating conditions (P_T, R_{ex}), and reactor design parameters (λ, b_1, b_2, c_1, c_2, δ_1, δ_2, R_e, K, L, Z).

Computed performance indicators included $\overline{X}_A$, $\overline{X}_{O_2}$, $T_{s,k,\ell}$, E, $i_{k,\ell}$, $\overline{i}$, η and the power density of the assembly.

No formal optimization of the parameters was attempted. Instead, individual feed, operating, and design parameters were perturbed around a standard set to assess their influence on the computed performance parameters.

For this reference set, the following quantities were chosen: $T_{F,in}=T_{O_2,in}=700$ K ; $N_A=N_{O_2}=25.9$ μmole /cm^2.s; $N_D=0$; $N_{N_2}=97.4$ μmole/cm^2.s ; $b_1=0.1$ cm ; $R_{ex}=90.6$ ohm; Z=10.

The parameters which were left unperturbed are listed in Table I, while the numerical values of various physical, chemical and thermodynamic properties, which entered the calculations, are shown in Table II.

The general behaviour of the system is illustrated in Figure 3 (solid temperature distribution) and Figure 4 (current density distribution). In Figures 3 and 4, $N_A=N_{O_2}=103$ μmole/cm^2.s; $N_D=N_{N_2}=0$; $b_1=0.33$ cm; $R_{ex}=90.6$ ohm ; Z=122.

Both the solid temperature and the current density surfaces are nearly symmetrical about the xy angle bisector, because equal fuel and (undiluted) oxygen flow rates were used. It can be seen

Table I.

Parameters Which Were Left Unperturbed
During the Computations

$n = 2$ (for CO oxidation)

$\delta_1 = \delta_2 = 10^{-2}$ cm

$R_e = 0.1$ ohm

$P_T = 1.0$ bar

$\dfrac{b_1}{b_2} = \dfrac{c_1}{c_2} = \dfrac{b_1}{b_1} = 1$ (so that when b_1 is perturbed, the
shape of the unit cell remains un-
changed)

$K = L = 10$

$\lambda = 1$ (series connection

$\dfrac{T_{OX,in}}{T_{F,in}} = 1$

Table II.

Numerical Values of System Properties
Used During the Computations

$\Delta H° = -283{,}000$ J/mole A

$\Delta S° = -86.83$ J/K mole A

$C_{p,A} = C_{p,B} = C_{p,O_2} = C_{p,N_2} = C_{p,D} = 32$ J/K mole

$k_s = 2.09$ J/smK

$h_F = h_{OX} = 253$ J/sm^{2}K (a)

$\rho = 4.17 \cdot 10^{-5} \exp(9700/T)$ ohm m

(a)   Lower values of the heat transfer coefficient helped
convergence without significantly affecting the numeri-
cal results.
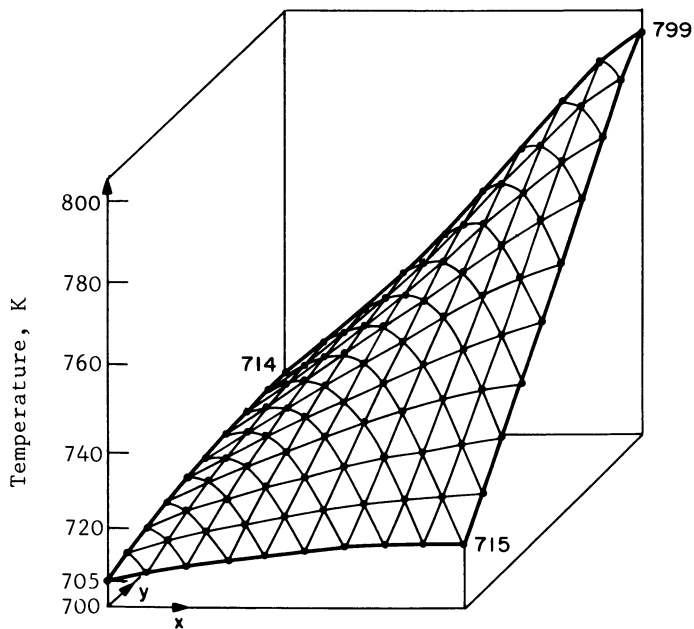
Figure 3.   Two-dimensional solid temperature profile in a
(3.3 cm x 3.3 cm) structure (see text for conditions).
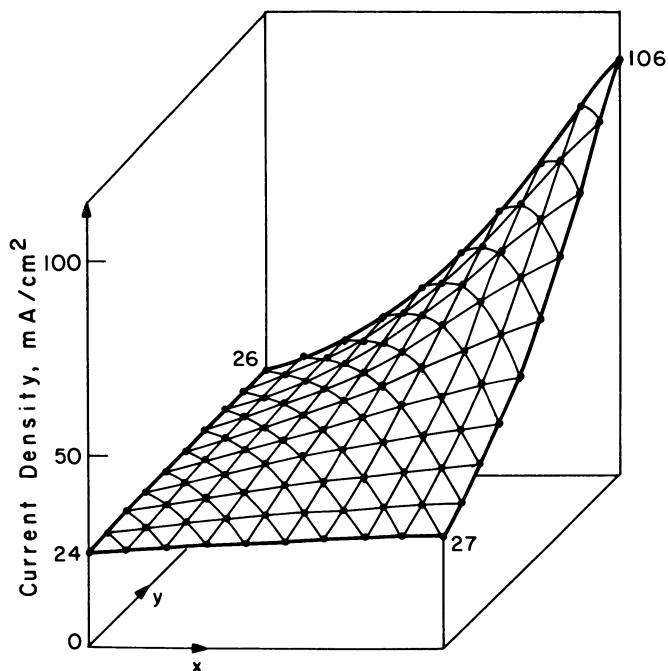
Figure 4.   Two dimensional current density profile in a
(3.3 cm x 3.3 cm) structure (see text for conditions).

that significant temperature gradients can develop within the monolith, accompanied by significant gradients in current density.

Unless fuel or oxygen starvation occurs inside the monolith, the minimum and maximum solid temperatures as well as current densities occur in the (1,1) and (K,L) unit cells, respectively.

Over the range of parameters examined, the fuel and oxidant temperatures were within 1 K of the solid temperature of the unit cell, indicating only minimal heat transfer resistance between gas and solid. This suggests that the model could be simplified to allow uniform and equal gas and solid temperatures within a unit cell; this would reduce the number of equations from 601 to 401 in a (10x10) structure, and also eliminate some of the difficulties in convergence which we have encountered for small temperature differences between gas and solid.

Effect of Inlet Temperatures. Figure 5 illustrates the effect of inlet fuel and air temperature on the maximum and minimum solid temperature ($N_A = N_{O_2} = 25.9$ mole/cm^2.s; $N_D = 0$; $N_{N_2} = 97.4$ mole/cm^2.s; $b_1 = 0.1$ cm; $R_{ex} = 90.6$ ohm; Z=10).

As the feed temperature increases, the nonisothermality of the reactor is accentuated, together with increasing temperature gradients in the structure.

Increasing the feed temperature from 557 K to 700 K caused a dramatic increase in fuel conversion (0.2% to 12.8%), mean current density (0.99 mA/cm^2 to 64.2 mA/cm^2), power density (0.03 W/1 to 140.3 W/1), cell voltage (.0089 V to .587 V) and efficiency (0.6% to 40.1%).

The dramatic increase of operating voltage (and cell efficiency) with temperature is due to the fact that the exponential decrease in electrolyte resistivity outweighs the corresponding decrease in E_{rev} (due to the negative ΔS) of this reaction system.

Similar results, not shown in Figure 5, were obtained with dilute fuel feed at constant space velocity ($N_A = 2.59$ µmole/cm^2.s; $N_D = 23.3$ µmole/cm^2.s; other parameters unperturbed). When the feed temperature was varied between 600 K and 700 K, fuel conversion increased from 6.8% to 98%; the mean current density from 3.41 mA/cm^2 to 50 mA/cm^2; power density from 0.4 W/1 to 85 W/1; cell voltage from .03 V to .5 V, and the efficiency from 2.1% to 34.2%.

While high-temperature fuel cells typically operate at close to 1300 K, the maximum temperature we have explored is only about 800 K. This is due to numerical convergence difficulties we have encountered at higher temperatures. Clearly, an improved numerical scheme is required to make computations at higher temperatures; work aimed at this purpose is in progress.

Effect of Gas Flow Rate. Figure 6 shows the effect of increasing the flow rates of the fuel (pure CO) and oxidant (pure O_2) on the
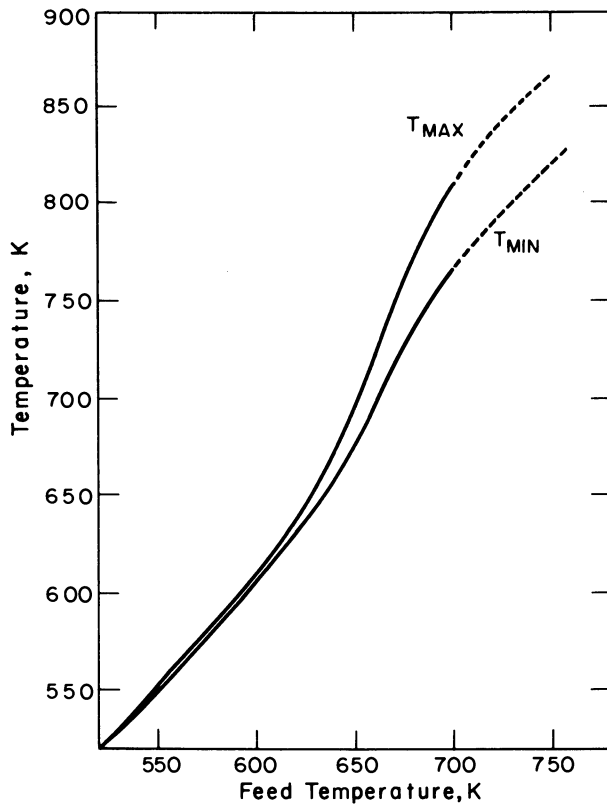
Figure 5. Effect of inlet fuel temperature on the maximum
and minimum solid temperature; see text for conditions.
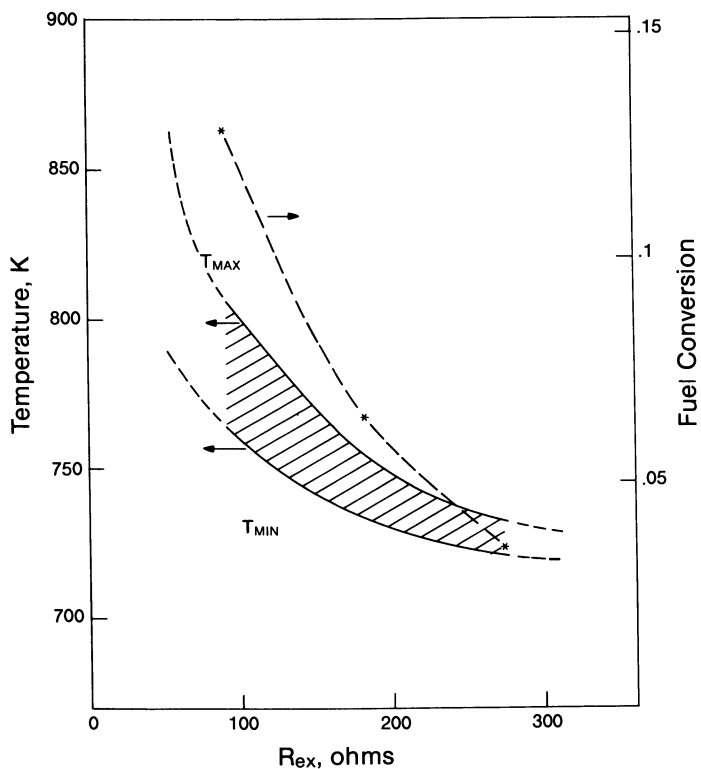
Figure 6.   Effect of fuel flow rate on maximum and minimum solid temperature; see text for conditions.

maximum and minimum temperatures in the monolith structure. As expected, increased space velocities make the reactor more iso-thermal.

The above mentioned set of standard conditions was perturbed in two successive high-flow runs ($N_A = N_{O_2} = 103$ μmole/cm^2.s; $N_A = N_{O_2} = 518$ μmole/cm^2.s). Increased space velocities also result in decreased fuel conversions (12.8% for standard run, 2.5% for in-termediate velocity, 0.3% for high velocity), current density (64.2 mA/cm^2; 50.7 mA/cm^2; 29.4 mA/cm^2), power density (140.28 W/1; 87.9 W/1; 29.4 W/1) and thermodynamic efficiency (40.1%; 31.7%; 18.4%), concomitant with the decreasing reactor tempera-ture.

Effect of External Resistance. Figure 7 shows that the external resistance has a pronounced effect on monolith temperature and on fuel conversion. For the feed conditions of these runs ($N_A = N_{O_2} = 25.9$ μmole/cm^2.s; $N_D = 0$; $N_{N_2} = 97.4$ μmole/cm^2.s; $T_{F,in} = T_{O_2,in} = 700$ K), the adiabatic temperature for complete conversion in a chemical reactor would be around 2400 K. The external resistance R_{ex} "freezes" the reactor, both by reducing the rate of the reac-tion and by allowing only a portion of the reaction enthalpy change ($-\Delta H°$) to be converted into heat.

Increasing the external load casues a decrease in power den-sity (140.3 W/1 for standard run; 72.33 W/1 for $R_{ex} = 182.3$ ohm; 32.98 W/1 for $R_{ex} = 274$ ohm) while the voltage goes through a max-imum (0.587 V, 0.594 V, 0.490 V). The latter is due to a balance between a decreasing current and an increasing load (Equation 41).

Concluding Remarks

Consideration of diffusional and kinetic limitations, when justi-fied by physical reality, may yield additional information on the behaviour of cross flow monolithic electrochemical reactors. A balance between added numerical complexity and a more complete description of electrode kinetics, should, of course, be kept in mind.

Our mathematical model, while it has not yet been directly compared with experiment, generally predicts reasonable trends for all computed performance indicators, and should lend itself as a useful design and optimization tool.
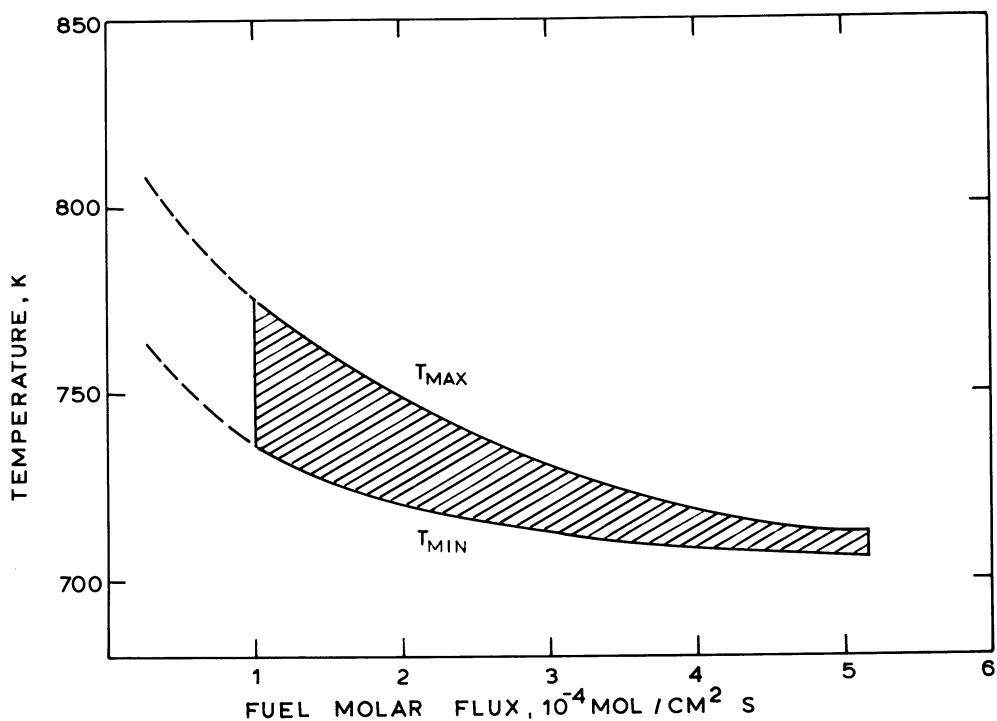
Figure 7.   Effect of external resistance R_{ex} on maximum and minimum solid temperature and on fuel conversion; see text for conditions.

Legend of Symbols

A = Fuel

B = Oxidation Product

b_1 = Unit cell dimension, see Figure 2

b_2 = Unit cell dimension, see Figure 2

c_1 = Unit cell dimension, see Figure 2

c_2 = Unit cell dimension, see Figure 2

C_p = Specific heat, J/mole·K

D = Diluent in fuel stream

E = Unit cell operating voltage, V

E_{rev} = Reversible Nernst voltage, V

$E°$ = Reversible Nernst voltage at unit activity of react-
ants and products, V

E_{th} = Thermoneutral voltage V

E_{act} = Activation energy for 0^{2-} conduction in solid elec-
trolyte, J/mole

F = Faraday constant, 96484 Cb/mole

h = Gas-solid heat transfer coefficient, $J/m^2 \cdot s \cdot K$

I = Current, A

$\bar{I}$ = Mean current density, A/m^2

$i_{k,\ell}$ = Current density of (k,ℓ) element, A/m^2

k = Solid thermal conductivity, J/s·m·K

K = # of unit cells in x direction

L = # of unit cells in y direction

$N_{j,j}$ = 1,...,18 = Dimensionless numbers defined in text

N_A = Feed fuel molar flux, $mole/m^2 \cdot s$

N_D = Fuel diluent molar flux, $mole/m^2 \cdot s$

N_{O_2} = Feed oxygen molar flux, $mole/m^2 \cdot s$

N_{N_2} = Nitrogen molar flux, $mole/m^2 \cdot s$

n = Stoichiometric coefficient in Equation (1)

P = Power output, W

P_T = Operating pressure, bar

R = Gas constant, 8.3105 J/mole·K

$R_{k,\ell}$ = Resistance of (k,ℓ) element, ohm

R_e = Resistance of electrical connection between unit bat-
teries, ohm

R_{ex} = External resistive load, ohm

S = Oxygen ion transfer area per unit reactor volume,
cm^2/cm^3

T = Temperature, K

$T_{F,in}$ = Fuel feed temperature, K

$T_{OX,in}$ = Oxidant feed temperature, K

T_F, T_{OX}, T_S = Fuel, oxidant and solid temperatures, K

W = Electrical work produced per mole of A,J

X_A = Fuel conversion

$\overline{X}_A$ = Mean exit fuel conversion

X_{O_2} = Oxygen conversion

$\overline{X}_{O_2}$ = Mean exit oxygen conversion

Z = No. of unit batteries in z-direction

Greek Symbols

δ_1 = Horizontal electrolyte wall thickness, m

δ_2 = Vertical electrolyte wall thickness, m

ΔG = Gibbs energy change of reaction (1), J/mole A

$\Delta H°$ = Standard Enthalpy change of reaction (1), J/mole A

$\Delta S°$ = Standard Entropy change of reaction (1), J/mole A·K

η = Cell efficiency, E/E_{TH}

θ = Dimensionless temperature, $T/T_{F,in}$

λ = 1 for series connection and = .5 for parallel connection of unit batteries

$\xi_{k,\ell}$ = Dimensionless current density

ρ = Electrolyte resistivity, ohm·m

ρ_o = Electrolyte resistivity at $T_{F,In}$, ohm·m

ϕ_{act} = Activation overpotential, V

ϕ_{conc} = Concentration overpotential, V

ϕ_{ohm} = Ohmic overpotential, V

Literature Cited

1. Archer, D.H.; Alles, J.J.; English, W.A.; Elikan, L.; Sverdrup, E.F.; Zahradnik, R.L.; in "Fuel Cell Systems"; R.F. Gould, ed.; ADVANCES IN CHEMISTRY SERIES No. 47, 1965, p. 332.
2. Etsell, T.H. and Flengas, S.N., J. Electrochem. Soc. 1971, 118 (12), 1890.
3. Weissbart, J., Smart, W.H., and Wydeven, T., Aerosp. Med. 1969, 40, 136.
4. Gur, T.M. and Huggins, R.A., J. Electrochem. Soc. 1979, 126(6), 1067.

5. Gur, T.M. and Huggins, R.A., Solid State Ionics 1981, 5, 563.
6. Vayenas, C.G. and Farr, R.D., Science 1980, 208, 593.
7. Sigal, C.T. and Vayenas, C.G., Solid State Ionics 1981, 5, 567.
8. Yang, Y., Debenedetti, P.G., Britt, H., Vayenas, C.G. and Evans, L.B., Proc. Intern. Symp. on Process Systems Engineering, Tokyo, 1982.
9. Stoukides, M. and Vayenas, C.G. in "Catalysis under Transient Conditions", A.T. Bell and L.L. Hegedus, Eds.; ACS SYMPOSIUM SERIES No. 178; 1982, p. 181.
10. Federmann, E.F., Isenberg, A.O., Summers, W.A., Vidt, E.J., and Feduska, W. DOE/ET/11305-T8, Feb. 25, 1981.
11. Degnan, T.F. and Wei, J., AIChE Journal 1979, 25(2), 338.
12. Degnan, T.F. and Wei, J., AIChE Journal 1980, 26(1), 60.
13. Roy, D. and Gidaspow, D., Chem. Eng. Science 1972, 27, 779.
14. Roy, D. and Gidaspow, D., Chem. Eng. Science 1974, 29, 2101.
15. Debenedetti, P.G., and Vayenas, C.G., Chem. Eng. Sci., accepted for publication, 1983.
16. Lee, S.T. and Aris, R., Chem. Eng. Science 1977, 32, 827.
17. Farr, R.D. and Vayenas, C.G., J. Electrochem. Soc. 1980, 127(7), 1478.
18. Archer, D.H.; Elikan, L.; Zahradnik, R.L., in "Hydrocarbon Fuel Cell Technology": B.S. Baker, ed.; Academic Press, New York, 1965.
19. Debenedetti, P.G., MS Thesis, Massachusetts Institute of Technology, 1981.

Modeling of Chemical Vapor Deposition Reactors for the Fabrication of Microelectronic Devices

KLAVS F. JENSEN

Department of Chemical Engineering and Materials Science, University of Minnesota, Minneapolis, MN 55455

The modelling of reactors for chemical vapor deposition (CVD) of thin solid films is reviewed. Both production and experimental reactor systems are considered. The discussion of production equipment centers on conventional horizontal, barrel, and tubular reactors while the treatment of experimental systems focuses on rotating disk and stagnation point flow reactors. The analogies between CVD and heterogeneous catalysis are pointed out and also illustrated through a modelling study of the multiple-wafer-in-tube low pressure CVD reactor. The reactor model is shown to be equivalent to a fixed bed reactor model. The deposition of polycrystalline Si from SiH_4 is considered as a specific example. The model predicts experimental observations and provides quantitative comparison with experimental data from reactor studies.

Chemical vapor deposition (CVD) is one of the fundamental processes in the microelectronics industry where it is used to deposit stable, thin solid films. The terms "chemical" and "vapor" derive from the fact that the solid film is deposited by chemical reactions of gaseous components. This distinguishes CVD from physical deposition processes such as sputtering and gives the process its flexibility. In the microelectronics industry CVD is used to grow a wide range of thin solid films which serve as dielectronics, conductors, passivation layers, dopant sources, and oxidation barriers. These films in turn form the basis for many different electronic devices including semiconductor memories, semiconductor lasers, light detectors, power transistors, and microprocessors. CVD is well established in the growth of the basic silicon derived electronic materials: polycrystalline Si, epitaxial (doped) Si, SiO_2, and Si_3N_4. In addition, the process is gaining importance in the formation of the next generation of materials based on III-V compounds (e.g. GaAs, InP, and AlGaAs) which currently find use in optoelectronic devices.

Chemical vapor deposition is not restricted to the microelec-
tronics industry. It is the key process in the fabrication of
optical fibers where it enables grading of the refractive index as
a function of the radial position in the fiber (1). In the manu-
facturing industry the technique provides coatings with special
properties such as high hardness, low friction, and high corrosion
resistance. Examples of CVD reactions and processes are given in
Table 1.

Table I. Typical Chemical Vapor Deposition Systems

System	Overall Reaction
Halide transport	$WF_6 + H_2 \rightarrow W$ $SiCl_4 + H_2 \rightarrow Si$
Organometallic CVD	$Al(C_4H_9)_3 + H_2 \rightarrow Al$ $Ga(CH_3)_3 + AsH_3 \rightarrow GaAs$
Low pressure CVD	$SiH_4 \rightarrow Si$ $SiH_4 + N_2O \rightarrow SiO_2$ $SiH_4 + NH_3 \rightarrow Si_3N_4$
Plasma enhanced CVD	$SiH_4 \rightarrow Si:H$ (amorphous) $SiH_4 + NH_3 \rightarrow Si_3N_4$
Photochemical vapor deposition	$SiH_4 + N_2O \xrightarrow{\frac{h\nu}{Hg}} SiO_2$ $SiH_4 + NH_3 \xrightarrow{\frac{h\nu}{Hg}} Si_3N_4$

The widespread use of CVD is due to its many advantages. (i)
Gaseous reactants are easier to handle and keep pure than are liq-
uids or melts. (ii) The substrate can be cleaned before deposi-
tion by a slight etch with a reactive gas. (iii) The film is
formed at temperatures well below its melting point, especially in
plasma or photo-enhanced CVD, where film temperatures typically
are a few hundred degrees. (iv) The growth of an epitaxial layer
on top of another single crystalline material with differing lat-
tice parameters (i.e. heteroepitaxy) can be realized by varying
the composition of the growing film so that the lattice parameters
change smoothly across the interface between the two materials.
(v) Similarly, donor/acceptor concentrations in the film may be
controlled by varying the gas phase composition. (vi) In contrast
to sputtering methods, CVD provides good step coverage, which is
particularly important since patterns are etched and subsequently
covered by new layers during the processing of a device.

To effectively exploit the above advantages it is necessary to have a detailed understanding of the chemical and physical rate mechanisms underlying CVD. These encompass mass transport in the gas phase by convection and diffusion, homogeneous as well as heterogeneous reactions, and heat transfer by both convection and radiation. The situation is further confounded by complex flow fields and boundary conditions. The formation of SiO_2 from $SiCl_4$ exemplifies the importance of knowing the role of each rate process. The heterogeneous reactions are necessary to grow thin Si films for bipolar devices, while homogeneous nucleation of SiO_2 is essential in the production of optical fibers.

There exists a considerable literature on CVD (2) but relatively few attempts have been made to combine chemical and physical rate processes to give a complete representation of the deposition process. Most CVD studies have focused on demonstrating the growth of a particular material or crystal structure. However, the combined analysis is necessary in order to design CVD reactors where it is possible to deposit thin films of constant thickness and uniformity across an entire wafer. This is particularly important in the realization of submicron feature sizes for Very Large Scale Integrated Circuits. The further development of devices based on III-V compounds also depends on CVD reactor design improvements since the composition and thus the electronic properties of these materials vary considerably with process conditions.

Chemical vapor deposition and heterogeneous catalysis share many kinetic and transport features, but CVD reactor design lags the corresponding catalytic reactor analysis both in level of sophistication and in scope. In the following we review the state of CVD reactor modelling and demonstrate how catalytic reactor design concepts may be applied to CVD processes. This is illustrated with an example where fixed bed reactor concepts are used to describe a commercial "multiple-wafers-in-tube" low pressure CVD reactor.

CVD Reactors

Figure 1 illustrates conventional CVD reactors. These reactors may be classified according to the wall temperature and the deposition pressure. The horizontal, pancake, and barrel reactors are usually cold-wall reactors where the wall temperatures are considerably cooler than the deposition surfaces. This is accomplished by heating the susceptor by external rf induction coils or quartz radiant heaters. The horizontal multiple-wafer-in-tube (or boat) reactor is a hot-wall reactor in which the wall temperature is the same as that of the deposition surface. Therefore, in this type of reactor, the deposition also occurs on the reactor walls which presents a potential problem since flakes from the wall deposit cause defects in the films grown on the wafers. This is avoided in the cold-wall reactors, but the large temperature gradients in those reactors may induce convection cells with associated problems in maintaining uniform film thickness and composition.
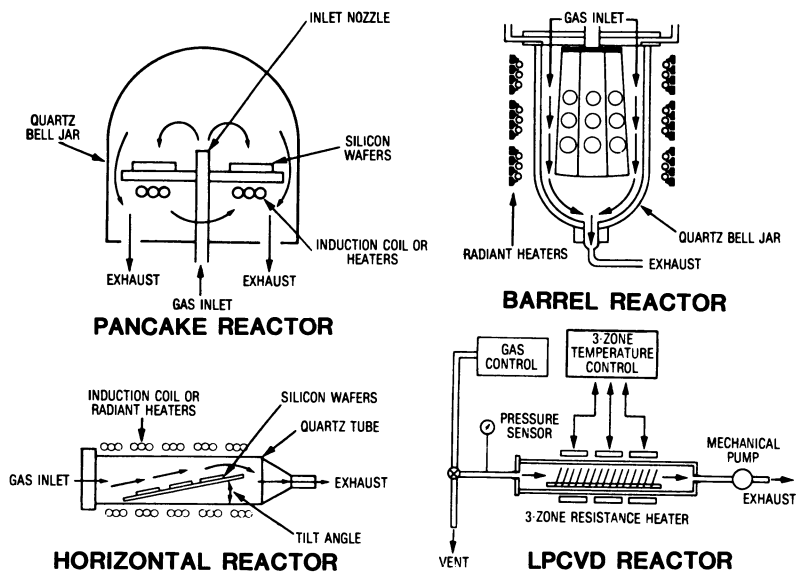
Figure 1. Typical CVD reactors.

There have been a number of modelling studies; in particular
horizontal and barrel reactors have been considered. However, the
usefulness of these models in the optimization of reactor design
and operating conditions is limited by many simplifying assump-
tions which bring empirical constants into the modelling equations.
Shepherd (3) described the deposition of Si from $SiCl_4$ in a hori-
zontal reactor assuming a parabolic velocity profile, linear tem-
perature variation, and diffusion to the susceptor surface while
neglecting the change in gas phase concentration in the flow di-
rection due to the depletion of reactants. Rundle (4,5) included
this axial depletion of reactant, but assumed a plug flow and ne-
glected temperature variations.

Bradshaw (6) and Eversteyn et al. (7,8) considered a stagnant
layer of fluid adjacent to the susceptor coupled with a well-mixed
main flow region between the upper end of this layer and the reac-
tor wall. Eversteyn et al. combined the diffusion equation for the
stagnant layer with a plug flow model for the main flow region. An
empirical relation was used to predict the thickness of the layer
as a function of the gas velocity. The major result of this so-
called stagnant layer model was the prediction that if the suscep-
tor were tilted at a small angle to the horizontal, the uniformity
of silicon growth rates through the reactor would be substantially
improved. This improvement is due to a stabilization of the flow
and a thinning of the boundary layer. The latter effect only en-
ters into the modelling equations through the empirical correlation
of layer thickness and gas velocity. In fact, the stagnant layer
model incorrectly predicts that the reactor efficiency passes
through a minimum and then increases with increasing gas velocity
while the efficiency should approach zero in the limit of very
large flow rates.

The stagnant layer concept originated from flow visualization
experiments with TiO_2 particles showing an almost particle free
layer close to the susceptor and natural convection cells in the
main gas stream. This was interpreted as evidence for a stagnant
layer, but because of the large temperature gradients in the reac-
tor, the particle free layer more likely arises from thermodiffu-
sion of TiO_2 particles away from susceptor (9). Takahashi et al.
(10) have also observed natural convection structures in a hori-
zontal CVD reactor. They present finite difference simulations of
velocity and gas phase concentration profiles for pure laminar flow
and for the spiralling flow caused by natural convection effect.
Unfortunately, as was the case with previous investigators, they
limit the analysis to cases where the surface reaction rate is
very large so that mass transfer to the surface controls the depo-
sition process. However, both kinetic and transport effects are
important in the majority of CVD processes.

The two major modelling approaches based on either boundary
layer approximations or well developed laminar flow have also been
applied to the barrel reactor. Dittman (11) used a Chilton-
Colburn analogy for flow over a flat plate to predict Si growth

rates, but such an approach is limited to the mass transfer con-
trolled regime and the specific reactor for which the correlation
is developed. Fujii et al. (12) split the annular flow region into
three concentric layers where convection dominates in the central
one and diffusion governs the transport in both the layers next to
the wall and the susceptor. By adjusting the relative thickness
of the layers the authors could match experimental data. Again,
this type of approach only applies to the reactor at hand and pro-
vides no new insight into the deposition process. Manke and
Donaghey (13) assumed fully developed laminar flow and treated the
mass transfer in the annular region between reactor wall and sus-
ceptor as an extended Graetz problem neglecting all kinetics.

The so far most complete analysis of the barrel reactor is
given by Juza and Cermak (9,14) making use of the 2D momentum,
mass, and energy balances to demonstrate the development of the
transverse velocity, concentration, and temperature profiles along
the susceptor. They include overall surface kinetics for the sur-
face reaction: $SiCl_4 + 2H_2 \rightarrow Si + 4HCl$, and by comparison with
the previous studies they demonstrate the importance of kinetic
effects. They also show that thermodiffusion should be included
because of the steep thermal gradients and the large difference in
molecular weight between H_2 and Si-species. The gas phase reac-
tions associated with Si deposition from $SiCl_4$ (cf. (15)) are not
included in the analysis although they influence the growth rate
predictions.

Experimental Reactor Systems

There have been several experimental studies using the horizontal
reactor, but most of these have been limited to simple measurements
of film thickness. Only a few studies have been performed on the
gas phase, notably by Sedgwick, Ban, and their coworkers. Sedgwick
et al. (16) used laser Raman scattering techniques to measure the
transverse concentration and temperature profiles in a horizontal
reactor. Ban et al. (15,17) determined gas phase contractions by
mass spectrometry. However, the horizontal reactor is not suitable
for mechanistic studies of CVD since it is virtually impossible to
separate physical and kinetic rate processes for this complex re-
actor geometry. On the other hand, rotating disk or stagnation
point flow reactors are attractive for detailed investigations
since the hydrodynamics are characterized. Thus, the use of these
configurations makes it possible to decouple the transport effects
more accurately from the chemical kinetics.

The rotating disk has long been used to study electrochemical
reactions and has also found early use in CVD (18). Sugawara (19)
has presented an analysis of epitaxial growth of Si from $SiCl_4$.
His treatment includes natural convection but is limited to mass
transfer controlled deposition and equilibrium distributions in
the gas phase. Pollard and Newman (20) detail Si deposition on a
rotating disk treating the multicomponent mass and heat transfer

problem and including simultaneous homogeneous and heterogeneous
reactions. In addition, the physical parameters vary across the
deposition zone. Their treatment clearly demonstrates that both
homogeneous and heterogeneous reactions are important in CVD of Si,
but they observe some discrepancy between model predictions and ex-
periments presumably because of poorly known kinetic constants and
natural convection effects. Hitchman et al. (21,22) also consider
the rotating disk reactor and find that the inlet gas flow perturb
the ideal fluid flow pattern. They hypothesize that the difficulty
of rotating disk CVD experiments to confirm to theoretically pre-
dicted flow patterns could be caused by this inlet effect which is
not apparent in liquid phase systems.

The stagnation point flow reactor, where the flow impinges on
the heated substrate, appears to be an attractive alternative to
the rotating disk configuration. There is no ambiguity in the way
the gas is introduced into the deposition region. Moreover, nat-
ural convection driven instabilities may be avoided by inverting
the reactor so that the buoyancy force and the inlet gas velocity
point in the same direction. Donaghey (23) discusses the use of
the stagnation point flow in crystal growth and reviews several CVD
applications. The contributions by Wahl (24,25) seem to be the
most significant. He solves the two-dimensional momentum, species,
and energy balances for an incompressible gas flow in an enclosed
stagnation point flow reactor by using finite differences. The
model predictions compare well with flow visualization experiments.

The conventional stagnation point configuration, where the gas
flows downward, has been used in several CVD studies. However,
none of these researchers seem to have accounted for the fact that
in a region close to the flow axis, the surface of the stagnation
plate is "equally accessible" to transport implying that the film
growth rate is independent of the radial position. Graves and
Jensen (26,27) have recently analyzed this case detailing the
transformation of the general partial differential modelling equa-
tions to a set of ordinary differential equations. These are in
turn solved by a Galerkin finite element technique. The authors
consider various general chemical mechanisms for film growth to
demonstrate how the stagnation point flow configuration may be
used to distinguish whether homogeneous or heterogeneous reactions
dominate the overall deposition process.

Low Pressure CVD Reactors

Low pressure CVD (LPCVD) has become a dominant process in the
growth of thin films of microelectronic materials. It is widely
used to deposit thin films of polycrystalline Si, SiO_2, and Si_3N_4.
In addition it has been demonstrated for deposition of metals,
specifically Al and W. The process is carried out in tubular, hot
wall reactors where the wafers are placed perpendicular to the
flow direction as illustrated in Figure 2. The very large packing
densities that can be realized in LPCVD reactors without adverse
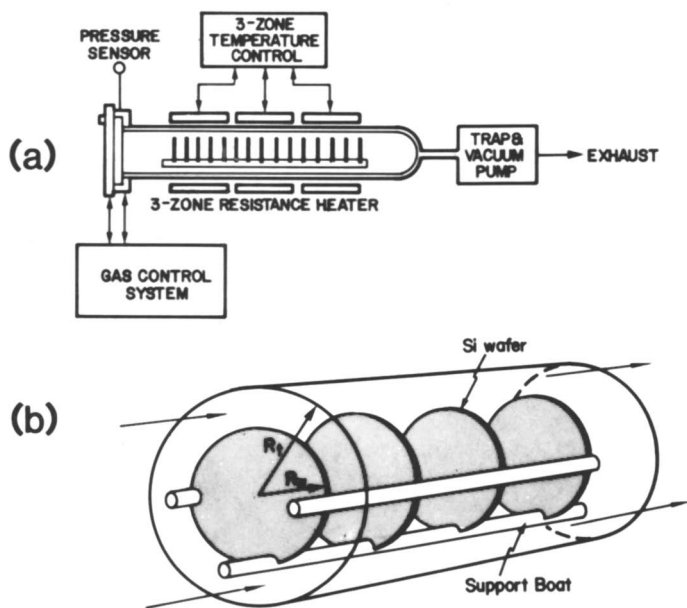
Figure 2. LPCVD reactor system.

effects in film uniformity are possible because of the reduced
pressure (~ 1 torr) where the diffusion coefficients are three
orders of magnitude larger than at atmospheric pressure. This
implies that the chemical reactions at the surface of the wafers
are rate controlling rather than mass transfer processes. More-
over, in spite of the low pressures, rates of deposition in LPCVD
reactors are only an order of magnitude less than those obtained
in atmospheric CVD since the reactants are used with little or no
dilution in LPCVD whereas they are strongly diluted in the conven-
tional cold wall processes reviewed above.

There appear to have been few modelling efforts for hot-wall
LPCVD reactors. Gieske et al. (28) and Hitchman et al. (29) pre-
sent experimental data and discuss flow fields, mass transfer
effects, and possible kinetics in rather general terms. A recent
model by Kuiper et al. (30) cannot account for diffusion in the
spaces between the wafers and the significant volume expansion
commonly associated with LPCVD processes. Furthermore, it is
restricted to isothermal conditions and plug flow in the main flow
region in spite of the large diffusivities associated with LPCVD.

In the following we present a detailed model of the commercial,
multiple-wafer-in-tube reactor illustrated in Figure 2. We have
selected the LPCVD as an example because of its central role in
the microelectronics industry and because it nicely demonstrates
the analogies to heterogeneous catalytic reactors, in particular
the fixed bed reactor.

LPCVD Reactor Model

The modelling approach behind the LPCVD reactor model is not re-
stricted to any specific deposition kinetics. However, to limit
the algebraic complexity and to be able to compare model predic-
tions with experiments we consider the simplest major deposition
process, the deposition of polycrystalline Si from SiH_4. The
model is based on the following kinetic mechanism:

$$SiH_4(g) \rightleftharpoons SiH_2(g) + H_2(g)$$

$$SiH_2(g) \rightleftharpoons SiH_2(ads)$$

$$SiH_2(ads) \rightarrow Si(s) + H_2(g)$$
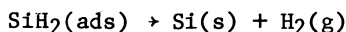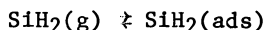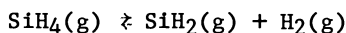
and it is assumed that the surface reaction is rate controlling
and follows the rate expression:

$$\mathscr{R} = \frac{k\ P_{SiH_4}}{1 + K_1 P_{H_2} + K_2 P_{SiH_4}} \tag{1}$$

This particular form may be justified by the experimental observa-
tions: the rate is inhibited by H_2, first order in SiH_4 at low
SiH_4 partial pressures and approaches zero order in SiH_4 at high

partial pressures (31). The details of the development of the
model are given in ref. (32) and follow the same approach as com-
monly used in modelling fixed bed reactors. The complete descrip-
tion of the physicochemical processes in the tubular LPCVD reactor
entails partial differential equations in the radial and axial
coordinates. However, at low pressures the time scale associated
with deposition is of the same order or larger than that for dif-
fusion so that one may assume perfect radial mixing in the narrow
annular flow region. Similarly, since the wafer spacing is small
compared to the radius of the wafer, we may neglect variations in
the axial direction within each cell formed by adjacent wafers.
Under those conditions the reactor equation takes the form:

$$D_o \frac{d}{dz}\left(\psi \frac{d\chi}{dz}\right) + v_o \frac{d\chi}{dz} - \frac{2}{(R_t^2 - R_w^2)c_{10}}\left[R_t(1+\alpha) + \frac{R_w^2}{\Delta}\eta\right]\mathcal{R}(\chi(z)) = 0 \tag{2}$$

where $\quad \psi = -\dfrac{(1+\varepsilon)}{(1+\varepsilon\chi)^2}\left(\dfrac{T}{T_o}\right)^{0.65}$

and the boundary conditions are:

$$D_o \frac{d\chi}{dz}\bigg|_0 = v_o(1 + \chi\varepsilon)\chi \quad ; \quad \frac{d\chi}{dz}\bigg|_L = 0 \tag{3}$$

Here χ is the conversion of SiH_4. ψ combines the effect of the
molar expansion in the deposition process as well as the change in
the volumetric flow and the dispersion coefficient, D, with temper-
ature. At low pressures and small Re in LPCVD reactors the dis-
persion occurs mainly by molecular diffusion, therefore, we have
used $(D/D_o) = (T/T_o)^{1.65}$. ε is the expansion coefficient and the
stoichiometry implies that $\varepsilon = (x_1)_0$, the entrance mole fraction
of SiH_4. The expansion coefficient, ε is introduced as originally
described by Levenspiel (33). The two reaction terms refer to the
deposition on the reactor wall and wafer carrier and that on the
wafers, respectively. The remaining quantities in these equations
and the following ones are defined at the end of the paper. The
boundary conditions are equivalent to the well known Danckwerts'
boundary conditions for fixed bed reactor models.
    The reaction and diffusion of SiH_4 between the wafers is
governed by the continuity equation:

$$D_o c_o \left(\frac{T}{T_o}\right)^{0.65} \frac{1}{r}\frac{d}{dr}\left(\frac{r}{1+\varepsilon\chi}\frac{d\chi}{dr}\right) + \frac{2}{\Delta}\mathcal{R}(\chi(r)) = 0 \tag{4}$$

with the boundary conditions:

$$\chi(r = R_w) = \chi_b(z) \quad ; \quad \frac{d\chi}{dr}\bigg|_0 = 0 \tag{5}$$

where the center boundary condition is the usual symmetry condition. The factor $1/(1+\varepsilon\chi)$ comes about because of the increase in the number of moles in the deposition reaction. The quantity η, connecting the descriptions for the flow region (2) and the wafers (4) is defined as:

$$\eta = \frac{2}{R_w^2} \int_0^{R_w} r \cdot \frac{\mathcal{R}_{(\chi(r))}}{\mathcal{R}(x_b)} \, dr \qquad (6)$$

It plays the same role as the effectiveness factor in heterogeneous catalysis and is a measure of the film thickness uniformity. It represents the ratio of the total reaction rate on each pair of wafers to that we would obtain if the concentration in the cell formed by the two wafers were equal to the bulk concentration everywhere. Thus, if the surface reaction is the rate controlling step, $\eta = 1$, whereas if the diffusion between the wafers controls, $\eta < 1$. In the limit of strong diffusion resistance the deposition is confined to a narrow outer band of the wafers and a strongly nonuniform film results.

As in the analysis of catalytic reactions we make the modelling equations dimensionless and establish the characteristic dimensionless parameter combinations associated with the LPCVD process. By defining:

$$Da_1 = \frac{2L\,R_t\,(1+\alpha)}{v_o(R_t^2 - R_w^2)c_{10}} \mathcal{R}(\chi=0) \ , \quad Da_2 = \frac{2L\,R_w^2/\Delta}{v_o(R_t^2 - R_w^2)c_{10}} \mathcal{R}(\chi=0)$$

$$g(\chi) = \frac{\mathcal{R}(\chi)}{\mathcal{R}(\chi=0)} \qquad , \quad Pe = \frac{v_o\,L}{D_o} \qquad (7)$$

$$\zeta = \frac{z}{L} \qquad , \qquad \xi = \frac{r}{R_w} \qquad , \quad \phi^2 = \frac{2R_w^2\mathcal{R}(\chi=0)}{\Delta c_{10}D_{1m0}(T/T_o)^{0.65}}$$

the reactor equation (2) then takes the form:

$$\frac{d}{d\zeta}\left(\psi\frac{d\chi}{d\zeta}\right) + Pe\frac{d\chi}{d\zeta} - Pe(Da_1 + \eta\,Da_2)g(\chi) = 0 \qquad (8)$$

with boundary conditions:

$$\left.\frac{d\chi}{d\zeta}\right|_0 = Pe\bigl(1 + \chi(0)\varepsilon\bigr)\chi(0) \qquad \text{and} \qquad \left.\frac{d\chi}{d\zeta}\right|_1 = 0 \qquad (9)$$

and

$$\eta = 2 \int_0^1 \xi\,\frac{g(\chi(\xi))}{g(x_b)}\,d\xi \qquad (10)$$

The reaction-diffusion problem (4) governing the wafers becomes:

$$\frac{1}{\xi}\frac{d}{d\xi}\left(\frac{\xi}{1 + \epsilon\chi}\frac{d\chi}{d\xi}\right) + \Phi^2 g\left(\chi(\xi)\right) = 0 \tag{11}$$

with boundary conditions

$$\chi(\xi=1) = \chi_b(\zeta) \qquad , \qquad \frac{d\chi}{d\xi}\bigg|_0 = 0 \tag{12}$$

In these equations the Damköhler numbers Da_1 and Da_2 represent the ratios of reactor space time to the characteristic time for deposition on the reactor wall and on the wafers, respectively. Pe is the axial Peclet number which represents the ratio of the time constant for convective transport to that for diffusive transport. The parameter, Φ, is equivalent to the Thiele modulus used extensively in analysis of heterogeneous reactions. It denotes the ratio of the characteristic time for diffusion in between the wafers to the characteristic time for deposition of Si on the wafer surfaces. Thus, if Φ is large the deposition is hindered by diffusion and a nonuniform film results. This effect is completely analogous to that of a large Thiele modulus for a porous catalyst. In fact, the modelling equations (8-12) are completely equivalent to those for a heterogeneous one-dimensional dispersion model for a fixed bed reactor with intraparticle resistance in the catalyst phase (cf. (34)). Thus, the extensive literature on the behavior of fixed bed reactors can readily be applied to the LPCVD reactor. For example, for large Pe the reactor will behave as a plug flow reactor and large differences in film thickness between the front and the back of the reactor may be expected. While for small Pe the reactor resembles a continuous stirred tank reactor (CSTR) and the film thickness should then be nearly uniform through the reactor.

The similarity between the wafer problem (11-12) and the cylindrical catalyst particle problem has already been mentioned. For an isothermal first order reaction with negligible volume change it is possible to solve (11-12) analytically and evaluate η (35, p. 114). Hence, one can determine a priori the necessary wafer spacing to obtain uniform film growth across each wafer, i.e. $\eta \doteq 1$. In commercial reactors the spacing is typically 3/16" (4.7 mm) which corresponds to the spacings in the cassettes used to store the wafers between process steps. This spacing exceeds the one necessary to ensure uniform growth in polycrystalline Si deposition. At the low pressures encountered in LPCVD, Knudsen diffusion becomes important with wafer spacings < 2 mm. For faster surface reactions than those involved in Si deposition, the diffusion of reactants between wafers could be rate controlling with standard 3/16" spacings. This appears to be the case in some SiO_2 and Si_3N_4 deposition schemes (36).

The modelling equations (8-12) form two nonlinear boundary value problems which we solve by orthogonal collocation. This

method has been applied successfully to fixed bed reactor problems
(37 and references within) and the solution to the LPCVD reactor
case is similar (32). Here we turn to the comparison of model
predictions with experimental observations.

Model Predictions

Since detailed kinetic data for the deposition of Si from SiH_4 are
scarce and somewhat contradictory, the kinetic parameters are eval-
uated from experimental data in ref. (31). Figure 3 shows the ex-
perimental data and the predicted growth rates. The model pre-
dicts the decrease in growth rates along the reactor length due to
depletion of SiH_4 as well as the inhibiting effect of increased H_2
concentration.
In addition to providing a fit to specific experimental data,
a good mathematical model should also predict process performance
over a range of conditions. Therefore, to test our LPCVD model,
the same kinetic parameters were used in the analysis of deposi-
tion data obtained by Rosler (36) with a different LPCVD reactor
and at two orders of magnitude larger SiH_4 concentrations. Figure
4 illustrates the measured growth rates and the predicted ones for
a ± 15% change in SiH_4 feed rates around the base case of 47 SCCM
pure SiH_4 feed. The reactor temperature is increased along the
length of the reactor by using a three-zone furnace to produce a
nearly uniform thickness profile in the base case. The model
accurately predicts the trends in the experimental data. When the
feed rate of SiH_4 is stepped up 15%, the growth rates increase
along the length of the reactor sice there is an excess of reactant
available relative to the base case. A flat thickness profile
could clearly be achieved by lowering the temperature gradient
along the length of the reactor. Analogously, if the flow of SiH_4
is dropped, the rates of deposition tail off. The slight wavelike
appearance of the model predictions arises from the compensation
of decreasing reactant by a piecewise linearly increasing reactor
temperature.
The ultimate goal in LPCVD deposition of polycrystalline Si is
to grow Si films with constant thickness and material properties.
Because of the distributed nature of the LPCVD reactor, it is nec-
essary to vary the wafer temperature along the length of the reac-
tor to at least approach this goal. A continuously stirred tank
reactor would give uniform films, but there are particulate and
wafer loading problems associated with the design and operation of
a CSTR reactor. On the other hand, these problems are avoided in
the tubular LPCVD reactor. By recycling a fraction of the reactor
effluent to the reactor inlet one can combine the benefits of the
CSTR and the conventional LPCVD reactor. This modification pro-
vides highly uniform films as shown in (32) along with additional
comparison of model predictions and experimental data.
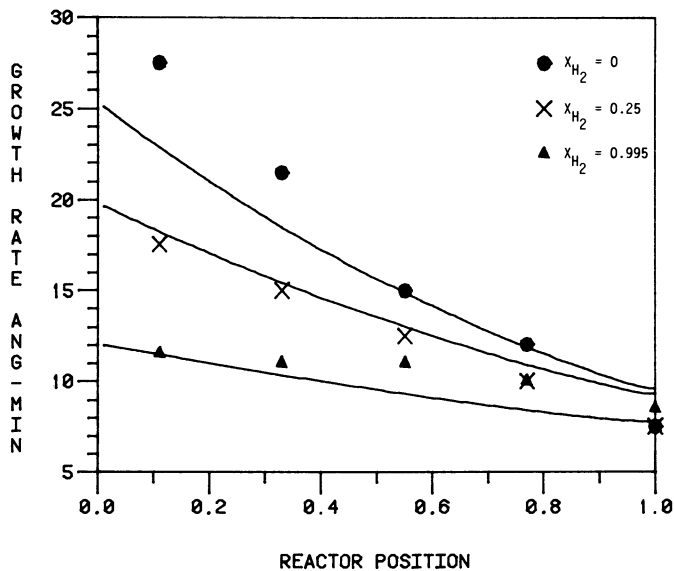
Figure 3. Model predictions (solid line) vs. experimental data of growth rate profiles as function of inlet H_2 concentration. x_{SiH_4} = 0.0047.
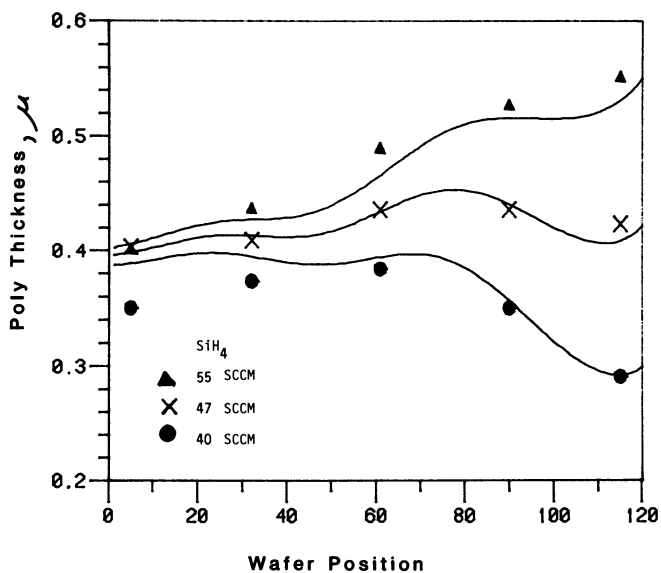
Figure 4. Model predictions (solid line) vs. experimental data of film thickness profiles as a function of (pure) SiH_4 flow rate.

Conclusions

Chemical vapor deposition is a key process for thin film formation in the development and manufacture of microelectronic devices. It shares many kinetic and transport phenomena with heterogeneous catalysis, but CVD reactor design has not yet reached the level of sophistication used in analyzing heterogeneous catalytic reactors. With the exception of the tubular LPCVD reactor, conventional CVD reactors may be viewed as variations on the original horizontal reactor. These reactors have complex flow fields and it is consequently difficult to control and predict the effect of operating conditions on the film thickness and composition.

The LPCVD reactor example illustrates that chemical reaction engineering concepts can readily be applied to CVD processes. Moreover, the similarity between the LPCVD reactor model and fixed bed reactor models means that it is possible to predict qualitatively the effect of operating conditions on the film growth without solving the modelling equations. The good quantitative agreement of model predictions with experimental observations further supports the modelling approach. The model also provides the ability to estimate kinetic parameters and to predict process conditions where variations in film thickness and composition are minimized.

The treatment in this paper has focused on Si derived materials since these are the most widely used materials in the microelectronics industry. However, the modelling approach can be also applied to the new III-V semiconductors. In fact, because of high demands on film thickness and composition uniformity in these systems this promises to be an area where chemical reaction engineering could play a major role.

Acknowledgments

Legend of Symbols

c_0	total inlet concentration
D	dispersion coefficient $\cong D_{1m}$
D_{1m}	diffusivity of component i in the gas mixture
Da_1, Da_2	Damköhler numbers see eqn. (7)
$g(\chi)$	dimensionless rate see eqn. (7)
k, K_1, K_2	rate constants see eqn. (1)
L	reactor length
Pe	Peclet number see eqn. (7)
r	radial coordinate
R	gas constant
$\mathcal{R}$	reaction rate see eqn. (1)

R_w	radius of wafer
R_t	radius of reactor tube
T	temperature
v	linear velocity in annulus
x_i	mole fraction component i
z	axial coordinate
α	area of wafer carrier relative to reactor tube area
Δ	wafer spacing
ε	volume expansion coefficient
ζ	dimensionless axial coordinate see eqn. (7)
η	effectiveness factor see eqn. (6)
ξ	dimensionless radial coordinate see eqn. (7)
Φ	Thiele modulus see eqn. (7)
χ	conversion
ψ	see eqn. (2)

Subscripts

b	bulk conditions
1	SiH_4

Literature Cited

1. Walker, K. L.; Harvey, J. W.; Geyling, F. T.; Nagel, R. S. J. Am. Cer. Soc. 1980, 63, 69.
2. Hawkins, D. T., "Chemical Vapor Deposition 1960-1980, A Biography"; IFI/Plenum: New York, 1981.
3. Shepherd, W. H. J. Electrochem. Soc. 1965, 112, 988.
4. Rundle, P. C. Int. J. Electron. 1968, 24, 405.
5. Rundle, P. C. J. Crystal Growth 1971, 11, 6.
6. Bradshaw, S. E. Int. J. Electron 1967, 23, 381.
7. Eversteyn, F. C.; Severin, P. J. W.; van den Brekel, C. H. J.; Peek, H. L. J. Electrochem. Soc. 1970, 117, 925.
8. Eversteyn, F. C.; Peek, H. L. Philips Res. Rep. 1970, 25, 472.
9. Juza, J.; Cermak, J. J. Electrochem. Soc. 1982, 129, 1627.
10. Takahashi, R.; Koga, Y.; Sugawara, K. J. Electrochem. Soc. 1972, 119, 1406.
11. Dittman, F. W. Adv. Chem. Ser. 1974, 133, 463.
12. Fujii, E., Nakamura, H., Haruna, K., Koga, Y. J. Electrochem. Soc. 1972, 119, 1106.
13. Manke, C. W.; Donaghey, L. F. J. Electrochem. Soc. 1977, 124, 561.
14. Juza, J.; Cermak, J. Chem. Eng. Sci. 1980, 35, 429.
15. Ban, V. J. Electrochem. Soc. 1978, 125, 317.
16. Sedgwick, T. O.; Smith, J. E.; Ghez, R.; Cowher, M. E. J. Crystal Growth 1975, 31, 264.
17. Ban, V. S.; Gilbert, S. L. J. Crystal Growth 1975, 31, 284.
18. Orlander, D. R. Ind. Eng. Chem. Fundam. 1967, 6, 188.
19. Sugawara, K. J. Electrochem. Soc. 1972, 119, 1749.
20. Pollard, R.; Newman, J. J. Electrochem. Soc. 1980, 127, 744.

21. Hitchman, M. L.; Curtis, B. J. J. Crystal Growth 1982, 60, 43.
22. Hitchman, M. L.; Curtis, B. J.; Brunner, H. R.; Eichenberger, V. in "Physicochemical Hydrodynamics"; Spalding, D. B., Ed.; Advance Publications: London, 1977; Vol. 2.
23. Donaghey, L. F. in "Crystal Growth"; Pamplin, B. R., Ed.; Pergamon Press, 1980; p. 65.
24. Wahl, G. Thin Solid Films 1977, 40, 13.
25. Wahl, G. Rev. Int. Hautes. Temper. Refract., Fr. 1980, 17, 7.
26. Graves, D. B.; Jensen, K. F. Proc. 4th Euro. Conf. CVD, Eindhoven, The Netherlands, 1983.
27. Graves, D. B.; Jensen, K. F. Chem. Eng. Sci., submitted.
28. Gieske, R. J.; Mcmullen, J. J.; Donaghey, L. F Proc. 6th Int. Conf. CVD, Electrochem. Soc. Princeton, 1977, p. 183.
29. Hitchman, M. L.; Kane, J.; Widmer, A. E. Thin Solid Films 1979, 59, 231.
30. Kuiper, A. E. T.; van den Brekel, C. J. H.; de Groot, J.; Veltkamp, G. W. J. Electrochem. Soc. 1982, 129, 2288.
31. Claassen, W. A. P., Bloem, J.; Valkenburg, W. G. J. N.; van den Brekel, C. H. J. J. Crystal Growth 1982, 57, 259.
32. Jensen, K. F.; Graves, D. B. J. Electrochem. Soc. 1983, in press.
33. Levenspiel, O. "Chemical Reaction Engineering"; Wiley: New York, 1972; 2nd Ed.
34. Hlavacek, V.; Votruba, V. "Chemical Reactor Theory, A Review"; Amundson, N. R.; Lapidus, L., Eds.; Prentice Hall: Englewood Cliffs, NJ, 1977; p. 314.
35. Aris, R. "The Mathematical Theory of Diffusion and Reaction in Permeable Catalysts"; Oxford, 1975.
36. Rosler, R. S. Solid State Tech. 1977, 20 (4), 63.
37. Jensen, K. F.; Ray, W. H. Chem. Eng. Sci. 1982, 37, 199.

Multicomponent Diffusion and Reaction in Porous Catalysts

HENRY W. HAYNES, JR.

Department of Chemical Engineering, University of Wyoming, Laramie, WY 82071

This tutorial paper begins with a short introduction to multicomponent mass transport in porous media. A theoretical development for application to single and multiple reaction systems is presented. Two example problems are solved. The first example is an effectiveness factor calculation for the water-gas shift reaction over a chromia-promoted iron oxide catalyst. The methods applicable to multiple reaction problems are illustrated by solving a steam reformer problem. The need to develop asymptotic methods for application to multiple reaction problems is apparent in this example.

Most textbook discussions of effectiveness factors in porous, heterogeneous catalysts are limited to the reaction A → Products where the effective diffusivity of A is independent of reactant concentration. On the other hand, it is widely recognized by researchers in the field that multicomponent single reaction systems can be handled in a near rigorous fashion with little added complexity, and recently methods have been developed for application to multiple reactions. Accordingly, it is the intent of the present communication to help promote the transfer of these methods from the realm of the chemical engineering scientist to that of the practitioner. This is not, however, intended to be a comprehensive review of the subject. The serious reader will want to consult the works of Jackson, et al. (1,2,3), Sorensen and Stewart (4) and others (5,6). Much of the material contained herein is borrowed from these previous authors.

Two illustrative examples will be discussed. The first example, the chromia-promoted iron oxide catalysis of the water-gas shift reaction, can be solved to engineering accuracy on a hand calculator. The second example, steam reforming of methane over a supported nickel catalyst, involves multiple

reactions and the computations are a bit more involved. Still, the solution over a wide range of parameter values is readily obtained on a modern digital computer at very low computation expense.

Constitutive Equations

Mass transport in porous catalysts generally takes place by one or a combination of the following mechanisms: ordinary molecular diffusion, Knudsen diffusion, viscous flow, configurational diffusion and surface diffusion. Our analysis will, however, be limited to situations in which only ordinary diffusion and Knudsen diffusion contribute to mass transfer. Viscous flow will seldom, if ever be of significance in problems of diffusion and reaction in porous catalysts despite the presence of gradients in total pressure (7). Configurational diffusion is important only when molecular dimensions are comparable in magnitude to pore dimensions. This happens frequently in zeolite catalysis and in heavy oil processing over noncrystalline catalysts. Surface diffusion is not very well understood, but it can be argued that surface diffusion effects are small in comparison to gas phase transport at elevated temperatures where many reactions of practical importance take place (8). It will also be assumed that the catalyst particle is isothermal. This assumption is reasonable for most gas phase reactions where the major resistance to heat transfer tends to be external to the particle. The nonisothermal particle can be treated with little increased complexity, however.

In this treatment only the ordinary and Knudsen diffusion mechanisms will be considered. Then, mass transport in isothermal, multicomponent gas phase systems is described by the following constitutive equation:

$$- \frac{dC_i}{dX} = \frac{N_i}{\mathcal{D}^e_{Ki}} + \sum_{j=1}^{n} \frac{y_j N_i - y_i N_j}{\mathcal{D}^e_{ij}} \quad , \quad i = 1, 2 \ldots n \qquad (1)$$

Here n is the number of components (including inerts), $\mathcal{D}^e_{Ki}$ is the effective component $\underline{i}$ Knudsen diffusivity, and $\mathcal{D}^e_{ij}$ is the effective ordinary diffusivity for the i,j-binary pair. These equations are derived, for example, from the Dusty Gas Theory of Mason, et al. (9). Strictly speaking, the N_i in these equations are the diffusive molar fluxes. However, by our basic assumption, the viscous flux contribution is zero, so the N_i may be viewed as total molar fluxes. Note that the driving force for mass transfer in these equations is the gradient in concentration. A

number of authors have used equations analogous to these written in terms of a gradient in mole fraction in calculations of diffusion and reaction in heterogeneous catalysts. When this is done, contradictions arise. For example the component mole fractions may not sum to unity (10).

Single Reactions

Consider an n-component system in which a single reaction takes place with m components participating in the reaction:

$$\nu_1 A_1 + \nu_2 A_2 + \nu_3 A_3 + \dots + \nu_m A_m = 0 \qquad (2)$$
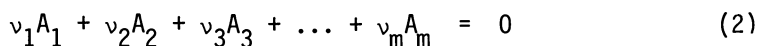
As written, the stoichiometric coefficients are negative for reactants and positive for products. From reaction stoichiometry it is clear that the component fluxes are related according to:

$$N_i = \frac{\nu_i}{\nu_1} N_1 \qquad i = 1,2, \dots m$$

$$= 0 \qquad i = m+1, \dots n \qquad (3)$$

Often it can be assumed with good justification that the component i effective diffusivities are constant, i.e.

$$N_i = - \mathcal{D}_i^e \frac{dC_i}{dX} \quad , \quad i = 1,2, \dots n \qquad (4)$$

This is the situation, for example, when Knudsen diffusion dominates. Then Equations 1, for $\mathcal{D}_{ij} \gg \mathcal{D}_{Ki}$, clearly reduce to Equations 4 with $\mathcal{D}_i^e = \mathcal{D}_{Ki}^e$.

   Another constant diffusivity case arises when one of the components, designated component ℓ, is in large excess. All component mole fractions except for component ℓ are approximately zero and the mole fraction of component ℓ is approximately unity. In this circumstance Equation 1 for $i \neq \ell$ reduces to Equation 4 with:

$$\frac{1}{\mathcal{D}_i^e} = \frac{1}{\mathcal{D}_{Ki}^e} + \frac{1}{\mathcal{D}_{i\ell}^e} \quad , \quad \begin{array}{l} i = 1,2, \dots n \\ (i \neq \ell) \end{array} \qquad (5)$$

Equation 5 is generally referred to as the Bosanquet equation. When component ℓ participates in the reaction, the effective diffusivity for that component can be derived by substituting the stoichiometric relations, Equations 3, into Equations 1 to obtain:

$$\frac{1}{\mathcal{D}_\ell^e} = \frac{1}{\mathcal{D}_{K\ell}^e} - \frac{1}{\nu_\ell} \sum_{\substack{j=1 \\ j \neq \ell}}^{n} \frac{\nu_j}{\mathcal{D}_{\ell j}^e} \tag{6}$$

One can easily show that the component concentrations are linearly related when the effective diffusivities are constant. The first step is to eliminate N_i between Equations 3 and 4 to obtain:

$$\frac{dC_i}{dX} = -\frac{\nu_i}{\nu_1} \frac{N_1}{\mathcal{D}_i^e} \quad , \quad i = 1, 2, \dots m$$
$$= 0 \qquad\qquad i = m+1, \dots n \tag{7}$$

for $i = 1$:

$$\frac{dC_i}{dX} = -\frac{N_1}{\mathcal{D}_1^e} \tag{8}$$

Now divide Equation 7 by Equation 8 to obtain:

$$\frac{dC_i}{dC_1} = \frac{\nu_i}{\nu_1} \frac{\mathcal{D}_1^e}{\mathcal{D}_i^e} \qquad i = 1, 2, \dots m \tag{9}$$

This equation is now integrated from the particle surface to any point within the particle to give the desired result:

$$C_i = C_{i,S} - \frac{\nu_i}{\nu_1} \frac{\mathcal{D}_1^e}{\mathcal{D}_i^e} (C_{1,S} - C_1) \quad , \quad i = 1, 2, \dots m$$
$$= C_{i,S} \qquad\qquad\qquad , \quad i = m+1, \dots n \tag{10}$$

Thus all component concentrations are linearly related to the key component concentration, component 1, using Equations 10. The

reaction rate expression at constant temperature is generally a function of any or all component concentrations, i.e. $R_W = R_W$ $(C_1, C_2, \ldots C_n)$. With the aid of Equations 10, the rate expression can be written as $R_W = R_W (C_1)$.

For slab geometry, the key component mass balance takes the form:

$$\mathcal{D}_1^e \; \frac{d^2 C_1}{dX^2} \; = \; \rho_p R_W \tag{11}$$

with boundary conditions:

$$C_1 (X_0) \; = \; C_{1,S} \tag{12}$$

$$\frac{dC_1}{dX} (0) \; = \; 0 \tag{13}$$

Substitution of the rate expression in the form $R_W = R_W(C_1)$ completes the problem statement. Since the rate expression is usually nonlinear, numerical methods are generally required for obtaining a solution to the problem. A particularly convenient method of solution is described by Weisz and Hicks ([11]).

A simplification is often employed for effectiveness factor calculations in the asymptotic limit of strong intraparticle diffusion resistance ([12],[13]). In this situation, an alternative form of the key component mass balance can be written as follows:

$$M \; = \; \frac{\ell_0 \rho_p R_{W,S}}{\sqrt{2}} \left\{ \int_{C_{1,E}}^{C_{1,S}} \mathcal{D}_1^e \rho_p R_W dC_1 \right\}^{-\frac{1}{2}} \tag{14}$$

where M is the "Generalized Thiele Modulus". In the asymptotic limit, i.e., for M greater than about 3, the effectiveness factor, η, is the reciprocal of M. Outside the asymptotic limit a good approximation to the effectiveness factor can be obtained from:

$$\eta \; = \; \frac{\tanh (M)}{M} \tag{15}$$

provided that the reaction is normal. (A normal reaction is one whose rate decreases with decreasing reactant concentration.)

Example 1:

The chromia-promoted iron oxide catalyzed water-gas shift reaction:

$$CO + H_2O \rightleftarrows CO_2 + H_2$$
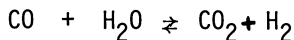
can be described by the following empirical kinetics expression:

$$R_W = k\, P_{CO}^{0.9}\, P_{H2O}^{0.3}\, P_{CO2}^{-0.6} \left(1 - \frac{P_{CO2}\, P_{H2}}{K_E\, P_{CO}\, P_{H2O}}\right)$$

Estimate the effectiveness factor at a point in a shift converter where T = 400°C, P = 25 atm, and the gas composition is (mol %): 10% CO, 60% H_2O, 8% CO_2, and 22% H_2. The catalyst is in the form of 3/8" x 3/8" cylinders. The particle density is 1.84 g/cc, the porosity is 0.623, and the pore structure is unimodal with an average pore diameter of 660 Å. At 400°C, k = 2.05 x 10^{-4} mol/s·g·atm$^{0.6}$ and K_E = 12.0.

Solution

The effective diffusivities were estimated using methods in (8) and the results are presented in Table I. Assume constant diffusivities. For H_2O in excess, we have:

$$\frac{1}{\mathcal{D}_{CO}^e} \cong \frac{1}{\mathcal{D}_{K,CO}^e} - \frac{1}{\mathcal{D}_{H2O-CO}^e} = \frac{1}{0.0326} + \frac{1}{0.00810}$$

or $\mathcal{D}_{CO}^e$ = 0.00649 cm^2/s. Similarly for CO_2 and H_2 we calculate: $\mathcal{D}_{CO2}^e \cong$ 0.00494 cm^2/s and $\mathcal{D}_{H2}^e$ = 0.0231 cm^2/s. For H_2O, the component in excess:

$$\frac{1}{\mathcal{D}_{H2O}^e} \cong \frac{1}{\mathcal{D}_{K,H2O}^e} - \frac{1}{\nu_{H2O}} \sum_{j \neq H2O} \frac{\nu_j}{\mathcal{D}_{H2O-j}^e}$$

$$= \frac{1}{0.0406} + \left\{ \frac{-1}{0.00810} + \frac{1}{0.00610} + \frac{1}{0.0285} \right\}$$

or $\mathcal{D}^e_{H2O} = 0.0098$ cm^2/s. Then, taking CO as the key component:

$$P_{H2O} = P_{H2O,S} - \frac{\nu_{H2O}\, \mathcal{D}^e_{CO}}{\nu_{CO}\, \mathcal{D}^e_{H2O}} [P_{CO,S} - P_{CO}]$$

$$= (0.60)(25) - \frac{(-1)(0.00649)}{(-1)(0.00998)} [(0.10)(25) - P_{CO}]$$

or

$$P_{H2O} = 13.37 + 0.6503\, P_{CO}$$

and similarly for the other components.

$$P_{CO2} = 5.284 - 1.314\, P_{CO}$$

$$P_{H2} = 6.205 - 0.2822\, P_{CO}$$

(Where the partial pressures are in atmospheres). These relations when substituted into the rate expression give:

$$R_W = R_W (P_{CO})$$

Generalized Thiele Modulus:

$$M = \frac{\ell_o \rho_p R_{W,S}}{\sqrt{2I}}$$

$$I = \int_{C_{CO,E}}^{C_{CO,S}} \mathcal{D}^e_{CO}\, \rho_p\, R_W\, dC_{CO} = \frac{\mathcal{D}^e_{CO}\, \rho_p}{RT} \int_{P_{CO,E}}^{P_{CO,S}} R_W\, dP_{CO}$$

By numerical integration:
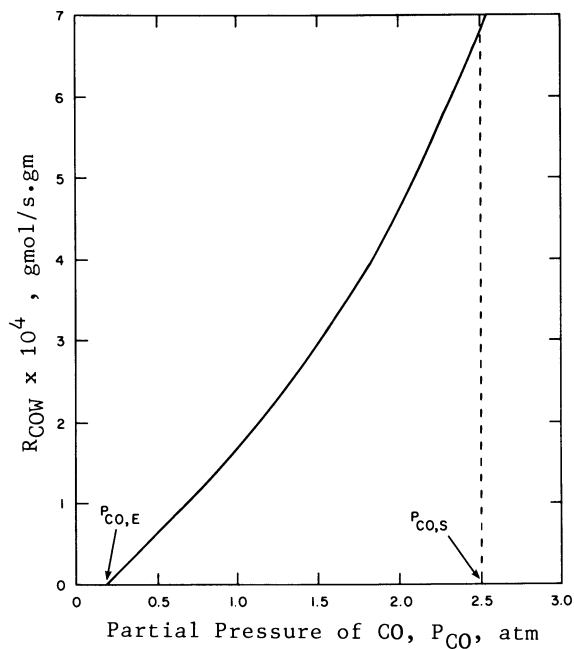
Figure 1. Evaluation of the integral of Example 1.

$$\int_{P_{CO,E}}^{P_{CO,S}} R_W \, dP_{CO} = 6.497 \times 10^{-4} \text{ mol} \cdot \text{atm/g} \cdot \text{s}$$

$$I = \frac{(0.00649 \text{ cm}^2/\text{s})(1.84 \text{ g/cm}^3)(6.497 \times 10^{-4} \text{ mol} \cdot \text{atm/g} \cdot \text{s})}{(82.05 \text{ atm} \cdot \text{cm}^3/\text{mol} \cdot \text{K})(673.2 \text{ K})}$$

$$= 1.405 \times 10^{-10} \text{ mol}^2/\text{s}^2 \cdot \text{cm}^4$$

$$M = \frac{(0.1588 \text{ cm})(1.84 \text{ g/cm}^3)(6.784 \times 10^{-4} \text{ mol/g} \cdot \text{s})}{\sqrt{(2)}(1.405 \times 10^{-10}) \text{ mol}^2/\text{s}^2 \cdot \text{cm}^4}$$

$$= 11.83$$

Therefore:

$$\eta = \frac{1}{M} = \frac{1}{11.83} = \underline{\underline{0.0845}}$$

Table I. Estimated Effective Diffusivities, Example 1
(T = 400°C, P = 25 atm)

Component	$\mathcal{D}^e_{Ki}$ (cm^2/s)	$\mathcal{D}^e_{ij,S}$ (cm^2/s)		
		H$_2$O (2)	CO$_2$ (3)	H$_2$ (4)
CO (1)	0.0326	0.00810	0.00532	0.0246
H$_2$O (2)	0.0406	---	0.00610	0.0285
CO$_2$ (3)	0.0260	0.00610	---	0.0211
H$_2$ (4)	0.1219	0.0285	0.0211	---

The above example illustrates how an approximate hand calculation can be carried out to obtain the effectiveness factor for a single reaction in a multicomponent reaction mixture. It has of course been necessary to make a number of assumptions. One

assumption that might be questioned is that of constant effective diffusivities. Equations 5 and 6 were derived for the situation in which one component is in large excess. A H_2O mole fraction of 0.60 would hardly seem to meet this criterion. Let us now see how the restriction to constant diffusivities can be removed.

The Equations 10 were obtained by substituting the stoichiometric relations, Equations 3, for the component fluxes in Equations 4. Had we employed the more general Equations 1 instead of Equations 4, the following set of mutual concentration relations would have been obtained:

$$\frac{dC_i}{dC_1} = \frac{\dfrac{\nu_i}{\mathcal{D}^e_{Ki}} + \dfrac{RT}{P_S}\left[\displaystyle\sum_{j=1}^{m}\frac{C_j\nu_i - C_i\nu_j}{\mathcal{D}^e_{ij,S}} + \nu_i\sum_{j=m+1}^{n}\frac{C_j}{\mathcal{D}^e_{ij,S}}\right]}{\dfrac{\nu_1}{\mathcal{D}^e_{K1}} + \dfrac{RT}{P_S}\left[\displaystyle\sum_{j=1}^{m}\frac{C_j\nu_1 - C_1\nu_j}{\mathcal{D}^e_{1j,S}} + \nu_1\sum_{j=m+1}^{n}\frac{C_j}{\mathcal{D}^e_{1j,S}}\right]} \tag{16}$$

for $i = 1,2,\ldots m$ and

$$\frac{dC_i}{dC_1} = -\frac{\dfrac{RTC_i}{P_S}\displaystyle\sum_{j=1}^{m}\frac{\nu_j}{\mathcal{D}^e_{ij,S}}}{\dfrac{\nu_1}{\mathcal{D}^e_{K1}} + \dfrac{RT}{P_S}\left[\displaystyle\sum_{j=1}^{m}\frac{C_j\nu_1 - C_1\nu_j}{\mathcal{D}^e_{1j,S}} + \nu_1\sum_{j=m+1}^{n}\frac{C_j}{\mathcal{D}^e_{1j,S}}\right]} \tag{17}$$

for $i=m+1, \ldots n$. These equations are analogous to results derived previously for the constant diffusivity case, Equations 10. Like the previous results, no assumption has been made regarding the form of the kinetics expression. Thus, the mutual concentration relations defined by Equations 16 and 17 are valid for all single reaction systems. It does not appear possible to analytically integrate Equations 16 and 17 to obtain results analogous to the constant diffusivity result, Equations 10. However, despite their complex appearance, Equations 16 and 17 are readily solved numerically with the initial conditions $C_i(C_{1,S}) = C_{i,S}$ using, for example, the Runge-Kutta algorithm.

Calculations of catalyst effectiveness are readily carried out using the generalized Thiele modulus. For the key component we can write:

$$N_1 = -\mathcal{D}_1^e \frac{dC_1}{dX} \tag{18}$$

where:

$$\frac{1}{\mathcal{D}_1^e} = \frac{1}{\mathcal{D}_{K1}^e} + \frac{RT}{P_S}\left[\sum_{j=1}^{m} \frac{\nu_1 C_j - C_1 \nu_j}{\mathcal{D}_{1j,S}^e} + \sum_{j=m+1}^{n} \frac{C_j}{\mathcal{D}_{1j,S}^e}\right] \tag{19}$$

This equation is obtained by writing Equation 1 for component 1 and then eliminating the other component fluxes using the stoichiometric relations, Equations 3. Substitution into the generalized Thiele modulus, Equation 14, provides:

$$M = \frac{\ell_o \rho_p R_{W,S}}{\sqrt{2}}\left\{\int_{C_{1,E}}^{C_{1,S}} \frac{\rho_p R_W dC_1}{\frac{1}{\mathcal{D}_{K1}^e} + \frac{RT}{P_S}\left[\sum_{j=1}^{m}\frac{\nu_1 C_j - C_1\nu_j}{\mathcal{D}_{1j,S}^e} + \sum_{j=m+1}^{n}\frac{C_j}{\mathcal{D}_{1j,S}^e}\right]}\right\}^{\frac{1}{2}} \tag{20}$$

The problem of Example 1 was reformulated in terms of Equations 16, 17 and 20, and the generalized Thiele modulus was found to be M = 11.40 corresponding to an effectiveness factor of η = 0.0877. Thus the error introduced by the constant diffusivities assumption amounts to less than 5% for this example. Had there been a substantial volume change accompanying the reaction, agreement between the two methods of computation would not have been as good.

Multiple Reactions

Now let us consider an n-component system in which m components participate in two or more chemical reactions. It will be supposed that r reactions among the various components proceed at a sufficient rate that they must be considered in the analysis. These will be called the "kinetics" reactions. The number of kinetics reactions is equivalent to the number of significant reaction paths. The number of kinetics reactions must not be confused with the number of independent stoichiometric reactions, s. Whereas the number of independent stoichiometric reactions among a system of n-components is limited, we can in principle have any number of significant reaction paths. Quite often r exceeds s in practice.

Consider the system of $\underline{r}$ kinetics reactions:

$$\nu_{11}A_1 + \nu_{12}A_2 + \ldots + \nu_{1m}A_m = 0$$

$$\nu_{21}A_1 + \nu_{22}A_2 + \ldots + \nu_{2m}A_m = 0 \qquad (21)$$

$$\vdots$$

$$\nu_{r1}A_1 + \nu_{r2}A_2 + \ldots + \nu_{rm}A_m = 0$$

where, as before, the stoichiometric coefficients are negative for reactants and positive for products. A stoichiometric coefficient ν_{ki} of zero simply means that the i-th component does not participate in the k-th reaction. More conveniently, these equations may be summarized as follows:

$$\sum_{i=1}^{m} \nu_{ki} A_i = 0 \qquad , \qquad k = 1,2, \ldots r \qquad (22)$$

Now let $R_{W,k}$ be the rate (per unit mass of catalyst) of the k-th reaction. A mass balance on the i-th component then provides:

$$\frac{dN_i}{dX} = \sum_{k=1}^{r} \nu_{ki} \, \rho_p \, R_{W,k} \qquad , \qquad i = 1,2, \ldots m \qquad (23)$$

(Slab particle geometry has been assumed.) For components not participating in the reactions, the flux is zero, i.e.,

$$N_i = 0 \qquad\qquad i = m+1, \ldots n \qquad (24)$$

For a multicomponent gas phase system, the appropriate constitutive equations are Equations 1 written in terms of component concentrations. (The reaction mixture is assumed to be an ideal gas.):

$$\frac{dC_i}{dX} = -\frac{N_i}{\mathcal{D}_{Ki}^e} - \frac{RT}{P_S} \sum_{j=1}^{n} \frac{C_j N_i - C_i N_j}{\mathcal{D}_{ij,S}^e} \quad , \quad i = 1,2 \ldots n \qquad (25)$$

Equations 23, 24 and 25 constitute a set of $\underline{2n}$ ordinary differential equations with boundary conditions:

$$N_i(0) = 0 \qquad\qquad i = 1,2 \ldots n \qquad (26)$$

$$C_i(X_o) = C_{i,S} \qquad i = 1,2 \ldots n \qquad (27)$$

These equations can, in principle, be solved for the 2n unknowns, i.e., n values of N_i and n values of C_i. However, it is usually more desirable to simplify the problem by making use of the reaction stoichiometry. In general we can write m-s stoichiometric equations relating the N_i at steady state, and these equations may be used to eliminate differential equations from among Equations 23.

Analysis of the reaction stoichiometry may be based on any set of s independent stoichiometric reactions which encompasses all m components of the system taking part in the reactions. As pointed out earlier, the stoichiometric reactions do not necessarily correspond to the sequence of kinetics reactions, Equations 22, in kind or number. The sequence of independent stoichiometric reactions may be written as:

$$\sum_{i=1}^{m} \nu'_{ki} A_i = 0 \qquad , \qquad k = 1,2, \ldots s \qquad (28)$$

where the prime distinguishes the stoichiometric coefficients from the same in Equations 22.

To aid in the derivation of the stoichiometric flux relations, it is convenient to define a "stoichiometric reaction flux", Γ_k, for each of the s independent stoichiometric reactions, k = 1,2, ... s. The reaction flux for a particular reaction, k, when multiplied by the stoichiometric coefficient for a particular component, i, gives the rate of disappearance of the component i in the region (O-X) by the reaction k per unit cross-sectional area. The net component flux is obtained by summing over all the stoichiometric reactions, i.e.,

$$N_i = \sum_{k=1}^{s} \nu'_{ki} \Gamma_k \qquad , \qquad i = 1,2, \ldots m \qquad (29)$$

The stoichiometric flux relations between the N_i are obtained by eliminating the Γ_k from Equations 29. Upon eliminating the s values of Γ_k from the set of m Equations 29, we are left with m-s relations between the component fluxes, N_i.

Even with this simplification, we still must solve a split boundary value problem. A particularly convenient method of solution appears to be a "shooting" technique in which the

centerline concentrations, $C_i(0)$, are guessed and the system equations, Equations 23 and 25, integrated until the external surface is reached. The calculated $C_i(X_o)$ are then compared with the $C_{i,S}$ and, if necessary, the $C_i(0)$ are adjusted and the integration is repeated in an iterative fashion until agreement to the desired accuracy is achieved. Integration from the "inside-out" is preferred to the alternative in which the $N_i(X_o)$ are guessed and the integration performed toward the center of the particle. Experience has taught that this alternative procedure often gives rise to an ill-conditioned boundary value problem in the sense discussed by Morrison, et al. (14).

The matching of the surface concentrations can be formulated as an optimization problem. One approach is to choose the $C_i(0)$ in such a fashion as to make the least squares criterion

$$\phi = \sum_{i=1}^{n} \{C_i(X_o) - C_{i,S}\}^2 \tag{30}$$

a minimum. The $C_i(X_o)$ are approximated by a truncated Taylor series about estimates of the particle center concentrations, $b_i = C_i(0)$. Thus:

$$C_i(X_o) = f_i (b_1, b_2, \ldots b_n)$$

or, approximately:

$$C_i(X_o) \cong f_i^{(o)} + \Delta b_1 \left(\frac{\partial f_i}{\partial b_1}\right)^{(o)} + \Delta b_2 \left(\frac{\partial f_i}{\partial b_2}\right)^{(o)} + \ldots + \Delta b_n \left(\frac{\partial f_i}{\partial b_n}\right)^{(o)} \tag{31}$$

where the (o) superscripted quantities are based on initial estimates of the b_i and the $\Delta b_j = b_j - b_j^{(o)}$ are corrections to the $b_j^{(o)}$. The derivatives in Equation 31 are approximated here by finite differences. Minimization of the objective function gives rise to a set of linear algebraic equations which can be solved to obtain corrections to the original $C_i(0)$. The procedure is repeated with the revised $C_i(0)$ until convergence is achieved.

This scheme converges rapidly when it converges, but of course convergence is not guaranteed. One procedure to insure good initial guesses of the $C_i(0)$ (and therefore increased likelihood of convergence) is to begin a computation at low temperatures where the concentrations are nearly uniform throughout the particle. The temperature is gradually increased in steps to the desired temperature and in each successive integration the $C_i(0)$ are guessed from previous experience.

Example 2:

De Deken, et al, (15) found that the steam reforming of methane over Ni/Al$_2$O$_3$ could be described in terms of the reactions:

$$CH_4 + H_2O \rightleftarrows CO + 3H_2 \qquad \text{(react. no. 1)}$$

$$CH_4 + 2H_2O \rightleftarrows CO_2 + 4H_2 \qquad \text{(react. no. 2)}$$
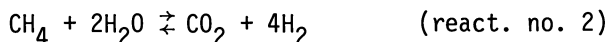
with the intrinsic kinetics given by:

$$R_{W1} = \frac{k_1 \left(P_{CH4} P_{H2O}/P_{H2}^3 - P_{CO}/K_{E,1} \right)}{\left(1 + K_{CO}P_{CO} \right)^2}$$

$$R_{W2} = \frac{k_2 \left(P_{CH4} P_{H2O}^2/P_{H2}^4 - P_{CO2}/K_{E,2} \right)}{\left(1 + K_{CO}P_{CO} \right)^3}$$

where

$$k_1 = 3.139 \times 10^{19} \exp(-43750/T) \qquad , \qquad \frac{kmol \cdot kPa}{kg \cdot s}$$

$$k_2 = 1.022 \times 10^{17} \exp(-38100/T) \qquad , \qquad \frac{kmol \cdot kPa}{kg \cdot s}$$

$$K_{CO} = 3.50 \times 10^{-10} \exp(+16470/T) \qquad , \qquad kPa^{-1}$$

with T in K. The quantities $K_{E,1}$ and $K_{E,2}$ are the thermodynamic equilibrium constants for reactions 1 and 2 respectively. The catalyst particle density is 2.338 g/cc and the effective length is 0.1588 cm. The mean pore radius is 1600 Å (unimodal) and the particle porosity is 0.362. Plot the effectiveness factor for each reaction vs. temperature at a position in the reactor where $y_{CH4} = 0.30$, $y_{H2O} = 0.50$, and $y_{H2} = y_{CO} = y_{CO2} = y_{N2} = 0.05$. The total pressure is 2500 kPa.

Solution

Calculated effective diffusivities are tabulated in Table II. This problem was solved on the computer by the "shooting method" for a range of temperatures. Integrations were by the 4th order Runge-Kutta algorithm. The system equations are summarized below.

Table II. Estimated Effective Diffusivities, Example 2
(T = 900 K, P = 2500 kPa)

Component	$\mathcal{D}^e_{Ki}$ (cm^2/s)	$\mathcal{D}_{ij,S}$ (cm^2/s)				
		H_2O (2)	H_2 (3)	CO (4)	CO_2 (5)	N_2 (6)
CH_4 (1)	0.1403	0.00832	0.0226	0.00713	0.00579	0.00708
H_2O (2)	0.1324	---	0.0277	0.00799	0.00619	0.00796
H_2 (3)	0.396	0.0277	---	0.0232	0.0201	0.0229
CO (4)	0.1062	0.00799	0.0232	---	0.00512	0.00638
CO_2 (5)	0.0847	0.00619	0.0201	0.00512	---	0.00509
N_2 (6)	0.1062	0.00796	0.0229	0.00638	0.00509	---

Component Mass Balances:

$$\frac{dN_{CH4}}{dX} = -\rho_p \, R_{W1} - \rho_p \, R_{W2}$$

$$\frac{dN_{H2O}}{dX} = -\rho_p \, R_{W1} - 2 \, \rho_p \, R_{W2}$$

Constitutive Equations:

$$\frac{dC_i}{dX} = -\frac{N_i}{\mathcal{D}^e_{Ki}} - \frac{RT}{P_S} \sum_{j=1}^{6} \frac{C_j N_i - C_i N_j}{\mathcal{D}^e_{ij,S}} \quad , \quad i=1,2, \ldots 6$$

Stoichiometric Relations:

$$N_{H2} = -N_{H2O} - 2 \, N_{CH4}$$

$$N_{CO} = N_{H2O} - 2 \, N_{CH4}$$

$$N_{CO2} = N_{CH4} - N_{H2O}$$

$$N_{N2} = 0$$

Boundary Conditions:

$$N_i(0) = 0 \quad , \quad i = 1, 2, \ldots n$$

$$C_i(X_o) = C_{i,S} \quad , \quad i = 1, 2, \ldots n$$

Computational results are plotted in Figures 2, 3 and 4. The effectiveness factors are very small at elevated temperatures in line with the observations of Van Hook (16). Note that this simulation has been kept as simple as possible for illustrative purposes. At steam-carbon ratios below about 1.4, carbon forming reactions should be considered. The water-gas shift reaction might also be a factor, but the experimental evidence suggests that both CO and CO_2 are primary reaction products (16) in agreement with the assumed kinetics model.

Natural gas steam reformers typically operate over temperatures ranging from about 500 to 800°C. Attempts to extend the effectiveness factor plot of Fig. 2 to higher temperatures were unsuccessful. At temperatures greater than 910 K, the initial guesses of the $C_i(0)$ must be extremely accurate to bring about convergence of the optimization scheme employed in the calculations. A probable explanation for this behavior can be deduced from Figure 4 where the approach to equilibrium at the particle center is plotted for both reactions. At temperatures greater than about 910 K, the concentrations at the particle center are essentially in equilibrium. In this region, small errors in the assumed $C_i(0)$ are magnified greatly when the integrations are terminated at the external particle surface.

A brief effort was made to solve Example 2 in the high temperature region using a collocation method (finite differences) with quasilinearization of the reaction rate terms similar to the method of Lee (17). This method also gave good results at low temperatures, but failed in the high temperature region. The problem is similar to that described above. One must have an extremely accurate estimate of the concentration profiles in order for the linearization of the reaction rate terms to approximate reality. Kaza and Jackson (3) and Sorensen and Stewart (4) used orthogonal collocation methods to solve problems involving multiple reactions. In this approach, one must solve a set of nonlinear algebraic equations by iterative
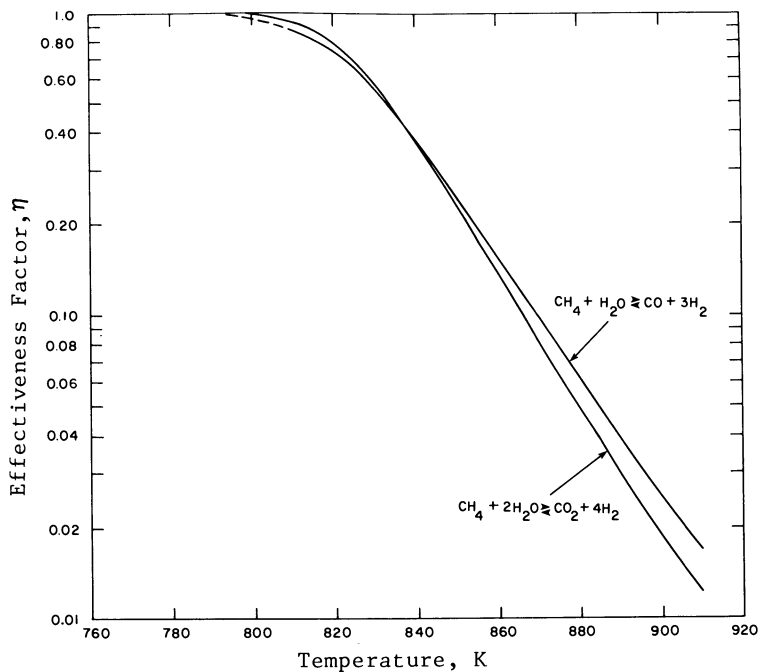
Figure 2. Effectiveness factor plots for Reactions 1 and 2.
Example 2.
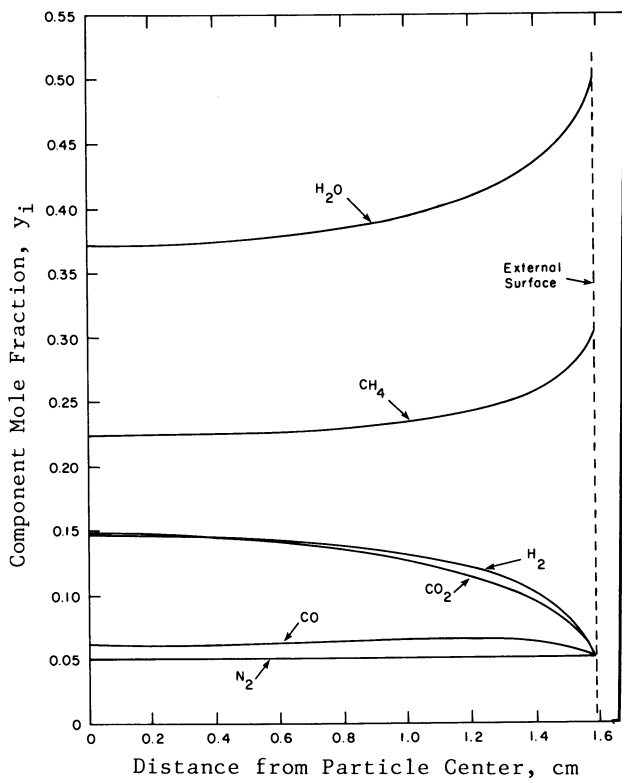
Figure 3.   Concentration profiles at 900 K.   Example 2.
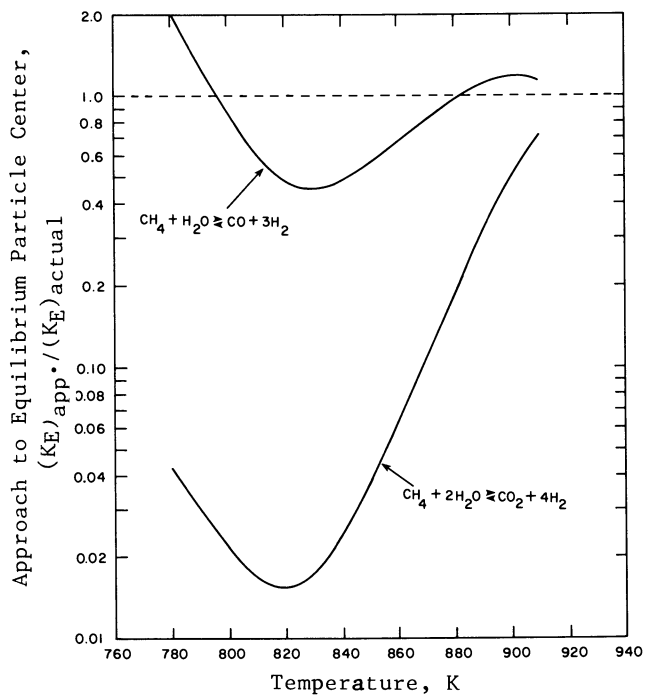
Figure 4.   Approach to thermodynamic equilibrium at particle center.

techniques such as the Newton-Raphson procedure. Sorensen and Stewart's example problem was only "mildly nonlinear", and the effectiveness factors reported by Kaza and Jackson do not extend below $\eta = 0.1$. It is not known how these methods would work on highly nonlinear problems in regions characterized by strong intraparticle diffusion resistances, but one might anticipate difficulties similar to those encountered in the present example. It seems that an investigation of asymptotic methods for application to multiple reaction problems might be a fruitful area for future research.

Notation

b_i = Component i concentration at particle center, $kmol/m^3$

C_i = Component $\underline{i}$ concentration, $kmol/m^3$.

$\mathcal{D}_{ij}^e$ = Effective ordinary diffusivity, i,j-binary pair, m^2/s.

$\mathcal{D}_{Ki}^e$ = Component $\underline{i}$ effective Knudsen diffusivity, m^2/s.

$\mathcal{D}_i^e$ = Component $\underline{i}$ effective diffusivity, m^2/s.

ℓ_o = Particle length parameter, m.

M = Generalized Thiele modulus.

m = Number of components participating in reaction.

N_i = Component $\underline{i}$ flux, $kmol/s \cdot m^2$.

n = Number of components (including inerts).

P = Pressure, kPa.

R = Gas constant, $kN \cdot m/kmol \cdot K$.

R_W = Reaction rate on particle weight basis, $kmol/s \cdot kg$.

r = Number of kinetics reactions.

s = Number of independent stoichiometric reactions.

T = Temperature, K.

X = Distance coordinate, m.

y_i = Component $\underline{i}$ mole fraction.

Γ_k = Stoichiometric reaction flux for k-th reaction.

$\eta^{\cdot}$ = Effectiveness factor.

ν' = Stoichiometric coefficient, stoichiometric reactions.

ν = Stoichiometric coefficient, kinetics reactions.

ρ_p = Particle density, kg/m^3.

ϕ = Least squares objective function.

Subscripts:

S = Quantity at external surface.

W = Weight or mass basis.

p = Particle quantity.

o = Particle center.

Literature Cited

1. Jackson, R. "Transport in Porous Catalysts", Elsevier, Amsterdam, 1977.
2. Kaza, K.R.; Villadsen, J. and R. Jackson Chem. Eng. Sci. 35, 17(1980).
3. Kaza, K.R. and R. Jackson Chem. Eng. Sci. 35, 1179(1980).
4. Sorensen, J.P. and W.E. Stewart Chem. Eng.Sci. 37, 1103(1982).
5. Wong, R.L. and V.E. Denny Chem. Eng. Sci. 30, 709(1975).
6. Hugo, P. Chem. Eng. Sci. 20, 975(1965).
7. Haynes, H.W. Jr Can. Jour. Chem. Eng. 56, 582(1978).
8. Satterfield, C.N.   "Mass Transfer in Heterogeneous Catalysis", M.I.T. Press, Cambridge, 1970.
9. Mason, E.A.; Malinauskas, A.P. and R.B. Evans, III J. Chem. Phys. 46, 3199(1967).
10. Schneider, P. Chem. Eng. Commun. 1, 239(1974).
11. Weisz, P.B. and J.S. Hicks Chem. Eng. Sci. 17, 265(1962).
12. Petersen, E.E. "Chemical Reaction Analysis", Prentice-Hall, 1965.
13. Bischoff, K.B. AIChE Jour. 11, 351(1965).
14. Morrison, D.D.; Riley, J.D. and J.F. Zancanaro Commun. of ACM 5, 613(1962).
15. De Deken, J.C.; Devos, E.F. and G.F. Froment ACS Symp. Ser. 196, 181(1982).
16. Van Hook, J.P. Catal. Rev. - Sci. Eng. 21, 1(1980).
17. Lee, S.E. AIChE Jour. 14, 490(1968).

Analysis of Fixed-Bed Catalytic Reactor Models

S. I. PEREIRA DUARTE

Dto. Ingeniería Química, Universidad Nacional de La Plata, 1 esquina 47, 1900 La Plata, Argentina

N. O. LEMCOFF

PINMATE (CONICET–UBA), Facultad de Ciencias Exactas y Naturales, Ciudad Universitaria, 1428 Buenos Aires, Argentina

A generalized method to predict the deviations of
the different types of fixed-bed catalytic reactor
models with respect to an heterogeneous two-dimen-
sional model is presented. Very good agreement
with numerically calculated errors is found. The
differences in the responses between the one and
two-dimensional versions of each type of model
are analyzed. The conditions in which the different
types of models should be used are discussed.

The development of mathematical models for the simulation of non-
adiabatic fixed-bed catalytic reactors has received considerable
attention. In previous work, we have analyzed the two-dimensional
and one-dimensional versions of the models ($\underline{1}$, $\underline{2}$) which, in turn,
were classified as: (I) pseudohomogeneous, (II) heterogeneous,
but conceptually wrong, and (III) heterogeneous, written in the
correct way (Table I). Model equations are in the Appendix.
     The objective of this work is to stress the importance of
type III models, both in their two-dimensional version, proposed
a decade ago ($\underline{3}$), and in the recently proposed one-dimensional
version ($\underline{2}$). Although these models correctly represent the trans-
fer phenomena in and between phases for tubular fixed-bed reac-
tors, they have seldom been used up to now. Type II models have
been included in this analysis because they have been used very
frequently and it is of special importance to show that their
responses may greatly deviate with respect to the response of
type III models.

Mathematical Development

In order to simplify the analysis of the differences between
models, a series of assumptions have been made (constant physical
properties, plug flow, negligible axial dispersion, and negligible
influence of temperature on fluid velocity) that do not affect
the generality of the results. An irreversible reaction of order

Table I. Classification of Heterogeneous Catalytic Reactor
                              Models

	One-dimensional	Two-dimensional
Pseudohomogeneous	I-0	I-T
Radial heat transfer in fluid phase only (lumped parameter)	II-0	II-T
Separate radial heat transfer in solid and fluid phases	III-0	III-T

(The leftmost column has the vertical label "Heterogeneous" spanning the last two rows.)

n has been considered:

$$r_A = k \, c^n \tag{1}$$

where $k = A_0 \cdot \exp(-E/RT)$. Intraparticle temperature gradients have
been neglected (1, 4) and the analytical expression derived by
Gottifredi et al.(5) for the isothermal effectiveness factor has
been used.
     The steady-state heat and mass balance equations of the
different models were numerically integrated using a fourth-order
Runge-Kutta-Gill method for the one-dimensional models, while the
Crank-Nicholson finite differences method was used to solve the
two-dimensional models.

Analysis of the Responses of the Different Models

Considering the models in Table I, it follows that the response
of model III-T will be more close to reality due to: (i) the
correct way the transfer phenomena in and between phases is set
up, and (ii) radial gradients are taken into account. Therefore,
the responses of the different models will be compared to that
one. It is obvious that the different models can be derived from
model III-T under certain assumptions. If the mass and heat trans-
fer interfacial resistances are negligible, model I-T will be
obtained and its response will be correct under these conditions.
If the radial heat transfer is lumped into the fluid phase, model
II-T will be obtained. This introduces an error in the set up of
the heat balances, and the deviations of type II models responses
will become larger when the radial heat flux across the solid
phase becomes more important. On the other hand, the one-dimensio-
nal models are obtained from the integration on a cross section
of the respective two-dimensional versions. In order to adequately
compare the different models, the transfer parameters of the
simplified models must be calculated from the basic transfer

parameters of model III-T. The correlations used for these basic parameters are the same as those used by Pereira Duarte et al. (2) and therefore will not be described here.

Transfer parameters of the simplified models. The pseudohomogeneous two-dimensional parameters λ_{er} and a_w have been extensively studied. Although several analytical expressions in terms of the basic parameters have been proposed (6, 7), we consider that there is no general criteria on the relations that have to be established between the models to obtain those parameters. One alternative is to assume equal heat fluxes, and for models I-T and III-T it follows that:

$$\lambda_{er} \left(\frac{\partial^2 T}{\partial r^2} + \frac{1}{r} \frac{\partial T}{\partial r} \right) = \lambda_{er}^f \left(\frac{\partial^2 T_f}{\partial r^2} + \frac{1}{r} \frac{\partial T_f}{\partial r} \right) +$$

$$+ \lambda_{er}^s \left(\frac{\partial^2 T_s}{\partial r^2} + \frac{1}{r} \frac{\partial T_s}{\partial r} \right) \qquad \forall (r,z) \qquad (2)$$

and: $\quad a_w (T-T_w) = a_w^f (T_f - T_w) + a_w^s (T_s - T_w) \qquad \forall (R_t, z) \qquad (3)$

In order to obtain λ_{er} and a_w from Equations 2 and 3, the pseudohomogeneous temperature of model I-T must first be defined. Equal axial heat convection flux will be obtained if:

$$T = T_f \qquad (4)$$

If Equations 2-4 are satisfied exactly, the resulting values of λ_{er} and a_w will vary along the bed. In actual case, they should be numerically evaluated. This is an impractical method and further analysis of this problem is being carried out in order to obtain relatively simple expressions (8). In this work, a sum of parameters is used to calculate λ_{er} and a_w:

$$\lambda_{er} = \lambda_{er}^f + \lambda_{er}^s \qquad (5)$$

$$a_w = a_w^f + a_w^s \qquad (6)$$

These equations permit the correct evaluation of the radial heat flux when the interfacial temperature gradients are negligible. Even when these gradients are important, the error introduced by the use of Equations 5 and 6 is not as significant as that due to the inexact calculation of the reaction rate (1).

The heterogeneous one-dimensional heat transfer parameters a_i^f and a_i^s can be obtained from (2):

$$a_i^f = a_w^f / (1 + Bi_{sh}/4) \qquad (7)$$

$$a_i^s = a_w^s/(1 + Bi_{sh}/4) \qquad\qquad (8)$$

where $Bi_{sh} = (a_w^f + a_w^s)R_t/(\lambda_{er}^f + \lambda_{er}^s)$. The coefficients a_i^f and a_i^s will generally vary along the reactor and therefore the use of constant values will introduce a certain error, but the use of these values in predicting the difference between models is more than adequate.

For the coefficient a_i of the one-dimensional models I-O and II-O we have used the well known expression in terms of the two-dimensional pseudohomogeneous parameters (9):

$$\frac{1}{a_i} = \frac{1}{a_w} + \frac{R_t}{4\,\lambda_{er}} \qquad \text{or} \qquad a_i = \frac{a_w}{1 + Bi_{sh}/4} \qquad (9)$$

Although the experimental measurements of certain parameters of type III model are somewhat scarce (a_w^s, λ_{er}^s) or affected by a relatively high degree of dispersion (a_w^f), more research work in these areas will allow to reduce these uncertainties.

Differences in the Responses of the Different Types of Models. The basic differences that exist in the heat and mass balances for the different types of models determine deviations of the responses of types I and II with respect to type III. In a previous work (1) a method was developed to predict these deviations but for conditions of no increase in the radial mean temperature of the reactor ($T_O \gg T_w$). In this work, the method is generalized for any values of T_O and T_w and for any kinetic equation. The proposed method allows the estimation of the error in the radial mean conversions of models I and II with respect to models III. Its validity is verified by comparing the predicted deviations with those calculated from the numerical solution of the two-dimensional models. A similar comparison could have been made with the numerical solution of the one-dimensional models.

The numerically calculated error is defined as:

$$e_i = \frac{\bar{x}_i - \bar{x}_{III}}{\bar{x}_{III}} \cdot 100 \qquad i = I, II \qquad (10)$$

where $\bar{x}$ is the radial mean conversion obtained at a length L_c, the same for the different models. Since the error varies with L_c (Figure 1), it is convenient to define a characteristic length. This was defined as the length at which the hot spot (maximum T_f), according to model III-T, is attained. When no hot spot is found ($T_O \gg T_w$), the characteristic length is defined as that corresponding to the maximum T_s for model III-T. Although these definitions seem arbitrary, they have shown to be appropriate for the comparison of errors. Errors calculated at the reactor inlet ($L_c \to 0$) have also been compared.
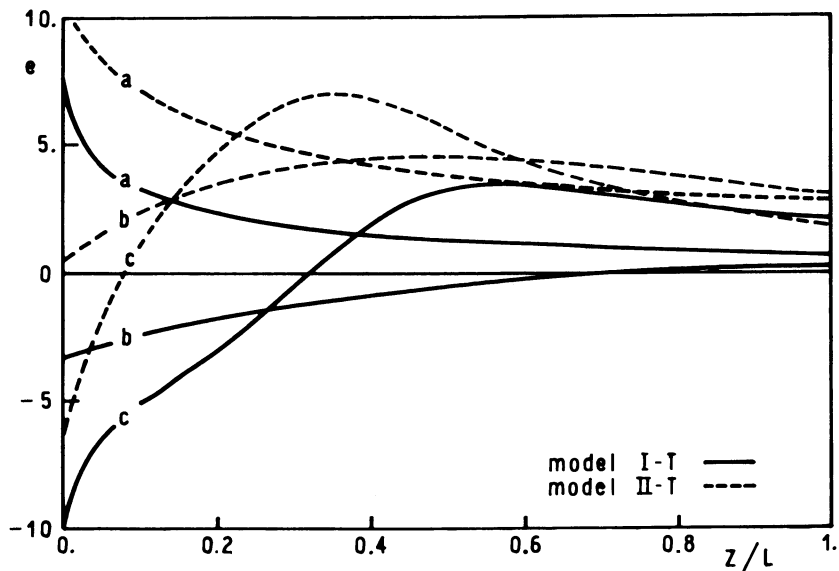
Figure 1. Axial variation of the error of models I-T and II-T with respect to model III-T. γ_O = 20, n = 1, Re = 200, A_O = 9.13x10^{12} h^{-1}, d_p = 0.01 m, L = 1 m. a) T_w = 543 °K; b) T_w = 643 °K; c) T_w = 703 °K.

<u>Method of Prediction of Deviations of Type I and II Models</u>. The radial mean conversion is proportional to the volumetric mean reaction rate:

$$\bar{x} = \frac{F_{Ao} - F_A|_{Lc}}{F_{Ao}} = \frac{L_c}{u_{so}C_o} \frac{\int_{V_{Lc}} \eta \, r_A \, dV}{V_{Lc}} = \frac{L_c}{u_{so} \, C_o} \overline{\overline{\eta r_A}} \qquad (11)$$

where one overbar indicates radial mean values, while two overbars indicate volume averaged values. If ηr_A can be estimated for the different types of models, a predicted error can be evaluated as:

$$e_{ie} = \frac{(\overline{\overline{\eta r_A}})_{ie} - (\overline{\overline{\eta r_A}})_{IIIe}}{(\overline{\overline{\eta r_A}})_{IIIe}} .100 \qquad i = I, II \qquad (12)$$

The subscript e denotes an estimated value and it is used to differentiate it from a numerically calculated value. If the volume mean composition and temperature are known for all models, $\overline{\overline{\eta r_A}}$ can be estimated from the equations for one-dimensional models:

For type I model:

$$(\overline{\overline{\eta r_A}})_{Ie} = (\eta r_A)_{(\overline{\overline{C}}, \overline{\overline{T}})_{Ie}} \qquad (13)$$

For type II and III models, the system of algebraic equations consisting of the solid phase heat and mass balances for models II-O and III-O, respectively, must be solved.
For type II model:

$$(\overline{\overline{\eta r_A}})_{IIe} = k_g \, a_v \, (\overline{\overline{C}}_f - \overline{\overline{C}}_s) = (\eta r_A)_{(\overline{\overline{C}}_s, \overline{\overline{T}}_s)} \qquad (14a)$$

$$h_f \, a_v \, (\overline{\overline{T}}_s - \overline{\overline{T}}_f) = (-\Delta H) \, (\eta r_A)_{(\overline{\overline{C}}_s, \overline{\overline{T}}_s)} \qquad (14b)$$

and for type III model:

$$(\overline{\overline{\eta r_A}})_{IIIe} = k_g \, a_v \, (\overline{\overline{C}}_f - \overline{\overline{C}}_s) = (\eta r_A)_{(\overline{\overline{C}}_s, \overline{\overline{T}}_s)} \qquad (15a)$$

$$h_f \, a_v \, (\overline{\overline{T}}_s - \overline{\overline{T}}_f) = (-\Delta H)(\eta r_A)_{(\overline{\overline{C}}_s, \overline{\overline{T}}_s)} - \frac{4 \, a_i^s}{d_t}(\overline{\overline{T}}_s - T_w) \qquad (15b)$$

Recently, a sufficiently exact method to predict conditions at the hot spot has been developed (<u>8</u>) and therefore the volume averaged conditions can be estimated assuming a linear variation of composition and a parabolic variation of temperature up to the hot spot:

$$\overline{\overline{x}} = \bar{x}_{hs}/2 \qquad\qquad \overline{\overline{T}} = T_o + 2/3 \, (\overline{T}_{hs} - T_o) \qquad (16a, b)$$

where $\bar{x}_{hs}$ and $\bar{T}_{hs}$ are the estimated values at the hot spot, which may be different for each model.

<u>Analysis of the Deviations</u>. The axial variation of the errors of models I-T and II-T calculated according to Equation 10 are represented in Figure 1. Values of the parameters shown in Table II remain constant in all the analyzed cases while the values of the remaining parameters are shown in each figure.

Table II.   Numerical Values of the Parameters

C_p = 0.26 kcal/kg°K	D_e = 0.001224 m²/h	d_t = 0.05 m
ρ_g = 0.561 kg/m³	P = 1 atm	T_o = 643°K
ρ_p = 2280 kg/m³	p = 0.8	β = 0.7
λ_g = 0.0468 kcal/m°Kh	μ_f = 0.126 kg/mh	ϵ = 0.4
λ_s = 1.0 kcal/m°Kh	Sc = 2.06	$(-\Delta H)$ = 30000 $\frac{kcal}{kmol}$

From Equations 14 and 15, it follows that the error in the evaluation of the reaction rate for type II models is mainly due to the incorrect evaluation of the solid temperature, since the radial heat dispersion is not included in the solid phase heat balance. It is easy to deduce from Equation 15b the influence that the magnitude and sign of $(\bar{T}_s - T_w)$ will have on the solid phase temperature and hence on the error of type II models.

The analysis of the deviations of type I models is slightly more complex since the error in the evaluation of the reaction rate is due to neglecting the interfacial temperature and concentration gradients. These generally have opposite effect on the error. For positive reaction orders, the effect of the conversion gradient is of a positive sign, while that of the temperature gradient depends on $(T_s - T_f)$, which not always is positive, as could be expected for an exothermic reaction. This somewhat anomalous situation occurs if the radial dispersion term in the solid phase heat balance equation is greater than the heat generation term and of opposite sign. For low Reynolds numbers, a high percentage of the heat flux to the refrigerant occurs through the solid phase and if, in addition, $T_w \ll T_o$, there exists a large driving force. Therefore, positive errors are found for case (a) in Figure 1 since $T_s < T_f$ and both the effects of conversion and temperature are positive. For cases (b) and (c), these effects are of opposite sign since $T_s > T_f$, being more important those of temperature close to the inlet (negative errors) and those of conversion far from the inlet (positive errors).

It can be seen that the maximum errors are generally found close to the hot spot or at the inlet, depending on the difference

between T_O and T_w. The method developed above allows us to pre-
dict these errors quite accurately, as can be seen in Figure 2,
where the predicted errors (Equations 12-16) are plotted together
with the numerically calculated ones (Equation 10). For the pre-
diction of the error at the inlet, feed conditions are used,
while for the prediction at the characteristic length, conditions
defined by Equation 16 are used. As T_w decreases, the temperature
attained at the characteristic length decreases and finally rea-
ches the inlet temperature. At this point the characteristic
length is equal to zero and all the curves coincide. The accuracy
of the prediction of the error can be seen from Figures 2-4 and
confirms the close relationship between the one and two-dimension-
al versions of the different types of models. Although not impo-
ssible, it is complicated to present a qualitative analysis of
the influence of the system parameters, since the temperature
and conversion profiles for each model and each case should be
known. However, some conclusions may be drawn:

The errors for different Re and d_p/d_t are compared in Figures
3 and 4. In order to analyze their influence only through the
effect on the transport phenomena, the ratio between the radial
heat transfer capacity and the heat generation rate at the inlet,
$4\,a_i/[\,d_t\,(-\Delta H)\,(\eta r_A\,)_o]$, is kept constant. Therefore, A_o is ade-
quately modified and, in the analysis of the effect of d_p/d_t, η
is assumed to be equal to one in order to avoid changes in the
apparent activation energy. A decrease in Re generates higher
absolute values of type II model errors due to the increase in
the relative importance of the radial heat dispersion through
the solid phase. A decrease in d_p/d_t leads to a better agreement
between the models due to the decrease in the interfacial gra-
dients (Figure 4). At low Re and d_t/d_p, the use of type III models
is very important. For very low Re, axial dispersion terms should
also be included in the heat and mass balance equations (10). How-
ever, the effect of the axial dispersion should be similar for the
different models, so that the method presented here is still valid.

The effect of the reaction order on the errors is also shown
in Figure 4. As it could be predicted, the increase in the order
shifts the errors of type I models to more positive values due
to the increase in the influence of the interfacial conversion
gradient. It has also been shown, that as γ_o or β increase, a
higher thermal sensitivity exists and the errors of type II
model increase (1).

When conditions are such that parametric sensitivity is
possible (11), the assumptions made in the method for predicting
the hot-spot (8) cause the prediction of the error for the
characteristic length to be less accurate. Although it may not be
reliable, it is sometimes necessary to design a reactor operating
in these conditions, and it is convenient in this case to use
model III-T because it will represent more closely the actual
behaviour.
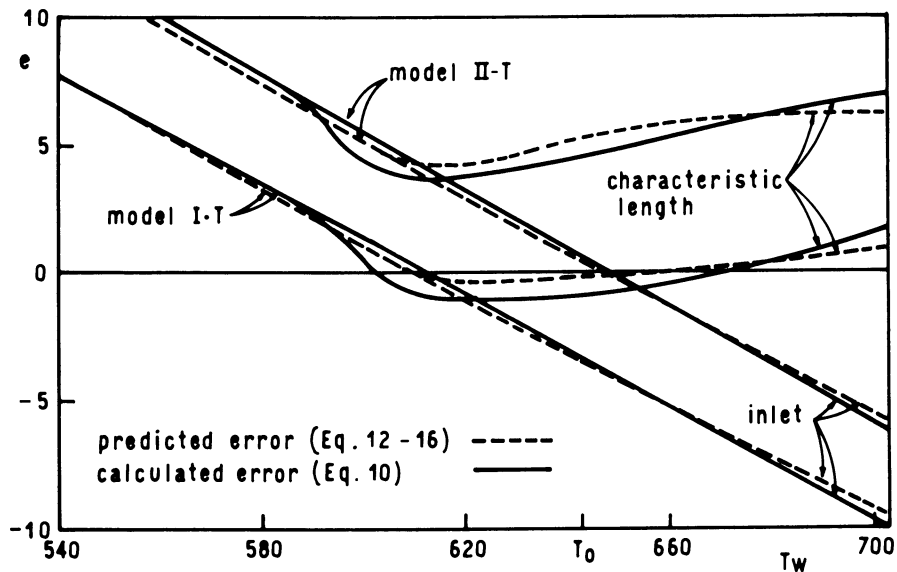
Figure 2.   Errors of models I–T and II–T as a function of
T_w. Conditions as in Figure 1.
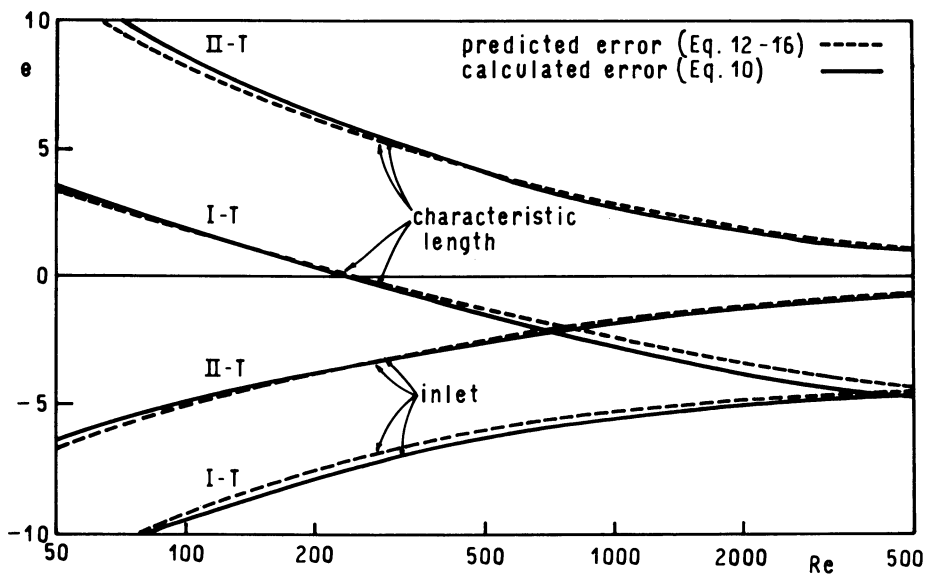
Figure 3.   Errors of models I–T and II–T as a function of
Re. $4\,a_i/[\,d_t(-\Delta H)(\eta r_A)_o\,] = 0.03777\ °K^{-1}$, $\gamma_o = 20$, n = 1,
$d_p = 0.01$ m, $T_w = 683\ °K$.
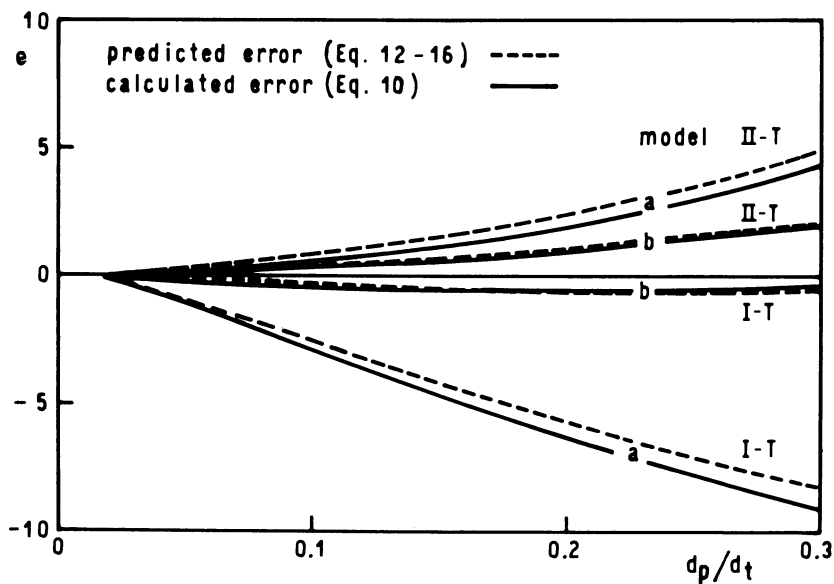
Figure 4. Errors of models I–T and II–T evaluated at the characteristic length as a function of d_p/d_t. $4 \, a_i/[d_t \cdot (-\Delta H)(\eta r_A)_o]$ = 0.03777 $°K^{-1}$, γ_o = 10, T_w = 643 °K, Re = 2000. a) n = 0.5; b) n = 2.

Comparison between One and Two-Dimensional Models. In a recent article (2), the differences between the responses of the one and two-dimensional versions of the same type of model were compared. It was found that they depend to a greater extent on kinetic parameters (β and γ) than on physical parameters (Re and d_p/d_t). In order to explain this behaviour, an analysis of the error in the evaluation of the reaction rate for a one-dimensional model is carried out. Since the reaction rate at radial mean concentration and temperature generally differs from the radial mean reaction rate, we can define:

$$e_r = \frac{r_A (\bar{x}, \bar{T})}{\bar{r}_A} - 1 \qquad (17)$$

For an irreversible reaction, and assuming parabolic radial temperature profiles and that the radial change in conversion is small, it follows that:

$$e_r = \frac{a}{\sinh a} - 1 \qquad (18)$$

with:

$$a = \bar{\gamma} \left(1 - \frac{T_w}{\bar{T}}\right) \frac{1}{1 + 4/Bi_{sh}}$$

From the analysis of Equation 18, it follows that the main variables that affect the error in the reaction rate are E and β due to their effect on $\bar{\gamma}$ and $\bar{T}$. Thus, very good responses are obtained from a one-dimensional model when reaction conditions are mild (moderate values of E and β). It can also be seen that for these conditions, the influence of the distribution of the radial heat transfer resistances between the bed and the wall, given by the Biot number, is small. E.g., for $\bar{T} = 673°K$, $T_w = 643°K$ and E = 12.5 kcal/mol, the maximum $|e_r|$, found for $Bi_{sh} \to \infty$ is 2.8%.

When Re and d_p/d_t vary, while both the activation energy and the ratio between the radial heat transfer and heat generation rate at the inlet are kept constant, the values of $\bar{\gamma}$ and $\bar{T}$ do not vary significantly. On the other hand, since the effect of the Biot number on the error is small, no variations in the difference between models are expected.

Conclusions

An extensive analysis of the behaviour of different types of non-adiabatic fixed bed reactor models is carried out and the importance of the heterogeneous one and two-dimensional models III-O and III-T is stressed. Although in these models the heat and mass transfer phenomena are correctly taken into account, they

have seldom been used up to now. A generalized method to predict
the deviations of the other types of models, namely types I and
II, with respect to type III is presented. The errors in conver-
sion predicted by this method are in very good agreement with
numerically calculated errors over a wide range of conditions.

As a result of the analysis carried out in this and previous
work (1, 2), conditions in which each model is to be used can be
established. The selection of the adequate type of model can be
carried out with the prediction method proposed in this article,
while the selection between a one or two-dimensional version will
depend on the thermal conditions. In this final analysis, type II
models have not been considered since they are conceptually
wrong. For large d_t/d_p ratios, a pseudohomogeneous type I model
can be used, while for small ratios, interphase resistances are
high, and a heterogeneous type III model should be used. For large
values of $\bar{\gamma}$ and $(\bar{T} - T_w)$, that is, extreme thermal conditions, a
two-dimensional model is recommended, while for low values of
these parameters, a one-dimensional model could be used. Obvious-
ly, model III-T will have the best performance in any situation,
but it must be taken into account that programming and computing
time is greater than for the other models.

Acknowledgments

Legends of Symbols

A_o: frequency factor $(kmol/m^3)^{1-n} h^{-1}$
a_v: external particle surface area per unit reactor volume (m^{-1})
C: reactant molar concentration $(kmol/m^3)$
C_p: specific heat of fluid (kcal/kg°K)
D_e: effective diffusivity within the particle (m^2/h)
d_p: pellet diameter (m)
d_t: internal tube diameter (m)
E: activation energy (kcal/kmol)
F_A: reactant molar flow rate (kmol/h)
$-\Delta H$: heat of reaction (kcal/kmol)
h_f: heat transfer coefficient between fluid and pellet $(kcal/hm^2°K)$
k: reaction rate coefficient $(kmol/m^3)^{1-n} h^{-1}$
k_g: mass transfer coefficient between fluid and pellet (m/h)
L: bed length (m)
n: order of reaction
p: emissivity of the solid
P: total pressure
Re: Reynolds number $(d_p u_s \rho_g/\mu_f)$
Rt: reactor tube radius

r: radial coordinate (m)

r_A: rate of reaction per unit bed volume (kmol/m^3 h)

Sc: Schmidt number (μ_f/ρ_g D)

T: temperature (°K) T_r T_s – fluid and solid temperature, resp.

u_s: superficial fluid velocity (m/h)

x: fractional conversion $(C_O - C)/C_O$

z: axial coordinate (m)

a_i, a_i^f, a_i^s: one-dimensional heat transfer coefficient on the bed side: lumped; for fluid phase; for solid phase (kcal/m^2 h °K),

a_w, a_w^f, a_w^s: wall heat transfer coefficient: lumped; for fluid phase; for solid phase (kcal/m^2 h °K)

β: dimensionless adiabatic temperature rise, $(-\Delta H)C_O/\rho_g c_p T_O$

γ: dimensionless activation energy (E/RT)

ϵ: bed void fraction

η: effectiveness factor

λ_{er}, λ_{er}^f, λ_{er}^s: radial effective thermal conductivity: lumped; for fluid phase; for solid phase (kcal/hm °K)

λ_g, λ_s: thermal conductivity of fluid and of solid particle (kcal/hm °K)

μ_f: fluid phase viscosity (kg/hm)

ρ_g, ρ_p: fluid and pellet density (kg/m^3)

Literature Cited

1. Pereira Duarte, S.I.; Barreto, G.F.; Lemcoff, N.O. XI Jornadas Investig. en Ciencias de Ingeniería Química y Química Aplicada Buenos Aires, 1980.
2. Pereira Duarte, S.I.; Ferretti, O.A.; Lemcoff, N.O. Proc. 32nd. Can. Chem. Engn. Conf. Vancouver, 1982.
3. De Wasch, A.P.; Froment, G.F. Chem. Eng. Sci. 1971, 26,629.
4. Prater, C.D. Chem. Eng. Sci. 1958, 8, 284.
5. Gottifredi, J.C.; Gonzo, E.E.; Quiroga, O.D. Chem. Eng. Sci. 1981, 36, 713.
6. Olbrich, W.E. Proc. Chemeca 70 Conf;Butterworths: London, 1970, p.101.
7. Dixon, A.G.; Cresswell, D.L. AIChE J. 1979, 25, 663.
8. Pereira Duarte, S.I.; Martínez, O.M., unpublished results.
9. Froment, G.F.; Bischoff, K.B. "Chemical Reactor Analysis and Design"; J. Wiley: New York, 1979.
10. Mears, D.E. Ind. Eng. Chem. Fundam. 1976, 15, 20.
11. Van Welsenaere, R.J.; Froment, G.F. Chem. Eng. Sci. 1970, 25, 1503.

APPENDIX: TABLE AI

BALANCE EQUATIONS FOR THE FIXED BED CATALYTIC REACTOR MODELS

MODEL I-0

$$u_s \frac{d\bar{C}}{dZ} = - \eta r_A$$

$$u_s \rho_g C_p \frac{d\bar{T}}{dZ} = (-\Delta H)\eta r_A - \frac{4a_i}{d_t}(\bar{T} - T_w)$$

MODEL II-0

$$u_s \frac{d\bar{C}_f}{dZ} = - k_g a_v (\bar{C}_f - \bar{C}_s)$$

$$k_g a_v (\bar{C}_f - \bar{C}_s) = \eta r_A$$

$$u_s \rho_g C_p \frac{d\bar{T}_f}{dZ} = h_f a_v (\bar{T}_s - \bar{T}_f) - \frac{4a_i}{d_t}(\bar{T}_f - T_w)$$

$$h_f a_v (\bar{T}_s - \bar{T}_f) = (-\Delta H)\eta r_A$$

MODEL III-0

$$u_s \frac{d\bar{C}_f}{dZ} = - k_g a_v (\bar{C}_f - \bar{C}_s)$$

$$k_g a_v (\bar{C}_f - \bar{C}_s) = \eta r_A$$

$$u_s \rho_g C_p \frac{d\bar{T}_f}{dZ} = h_f a_v (\bar{T}_s - \bar{T}_f) - \frac{4a_i^f}{d_t}(\bar{T}_f - T_w)$$

$$h_f a_v (\bar{T}_s - \bar{T}_f) = (-\Delta H)\eta r_A - \frac{4a_i^s}{d_t}(\bar{T}_s - T_w)$$

Initial conditions for one-dimensional models

$$\bar{C} = \bar{C}_f = C_o$$
$$\qquad\qquad \text{at } Z = 0$$
$$\bar{T} = \bar{T}_f = T_o$$

Model I-T

$$u_s \frac{\partial C}{\partial Z} = \varepsilon\, D_{er} \left(\frac{\partial^2 C}{\partial r^2} + \frac{1}{r}\frac{\partial C}{\partial r}\right) - \eta r_A$$

$$u_s \rho_g C_p \frac{\partial T}{\partial Z} = \lambda_{er} \left(\frac{\partial^2 T}{\partial r^2} + \frac{1}{r}\frac{\partial T}{\partial r}\right) + (-\Delta H)\eta r_A$$

MODEL II-T

$$u_s \frac{\partial C}{\partial Z} = \varepsilon\, D_{er} \left(\frac{\partial^2 C_f}{\partial r^2} + \frac{1}{r}\frac{\partial C_f}{\partial r}\right) - k_g a_v (C_f - C_s)$$

$$k_g a_v (C_f - C_s) = \eta r_A$$

$$u_s \rho_g C_p \frac{\partial T_f}{\partial Z} = \lambda_{er} \left(\frac{\partial^2 T_f}{\partial r^2} + \frac{1}{r}\frac{\partial T_f}{\partial r}\right) + h_f a_v (T_s - T_f)$$

$$h_f a_v (T_s - T_f) = (-\Delta H)\, \eta r_A$$

Boundary Conditions for Models I-T and II-T

$$\left.\begin{aligned} C &= C_o \\ T &= T_o \end{aligned}\right\} \quad \text{at } Z = 0 \text{ all } r$$

$$\left.\begin{aligned} \frac{\partial C}{\partial r} &= 0 \\ \frac{\partial T}{\partial r} &= 0 \end{aligned}\right\} \quad \text{at } r = 0 \text{ all } Z$$

$$\left.\begin{aligned} \frac{\partial C}{\partial r} &= 0 \\ -\lambda_{er}\frac{\partial T}{\partial r} &= \alpha_w (T - T_w) \end{aligned}\right\} \quad \text{at } r = R_t \text{ all } Z$$

C, T are fluid conditions for model II-T

Model III-T

$$u_s \frac{\partial C_f}{\partial Z} = \varepsilon \, D_{er} \left(\frac{\partial^2 T_f}{\partial r^2} + \frac{1}{r} \frac{\partial C_f}{\partial r} \right) - k_g a_v \, (C_f - C_s)$$

$$k_g a_v \, (C_f - C_s) = \eta r_A$$

$$u_s \rho_g C_p \frac{\partial T}{\partial Z} = \lambda_{er}^f \left(\frac{\partial^2 T_f}{\partial r^2} + \frac{1}{r} \frac{\partial T_f}{\partial r} \right) + h_f a_v \, (T_s - T_f)$$

$$h_f a_v \, (T_s - T_f) = \lambda_{er}^s \left(\frac{\partial^2 T_f}{\partial r^2} + \frac{1}{r} \frac{\partial T_s}{\partial r} \right) + (-\Delta H) \eta r_A$$

Boundary Conditions for Model III-T

$$\left. \begin{aligned} C_f &= C_o \\ T_f &= T_o \end{aligned} \right\} \quad \text{at } Z = 0 \text{ all } r$$

$$\left. \begin{aligned} \frac{\partial C_f}{\partial r} &= 0 \\[6pt] \frac{\partial T_f}{\partial r} &= \frac{\partial T_s}{\partial r} = 0 \\[6pt] \frac{\partial C_f}{\partial r} &= 0 \end{aligned} \right\} \quad \text{at } r = 0 \text{ all } Z$$

$$\left. \begin{aligned} - \lambda_{er}^f \frac{\partial T_f}{\partial r} &= \alpha_w^f \, (T_f - T_w) \\[6pt] - \lambda_{er}^s \frac{\partial T_s}{\partial r} &= \alpha_w^s \, (T_s - T_w) \end{aligned} \right\} \quad \text{at } r = R_t \text{ all } Z$$

RECEIVED July 19, 1983

The Optimal Design of a Reactor for the Hydrogenation of Butyraldehyde to Butanol

J. B. CROPLEY, L. M. BURGESS, and R. A. LOKE

Union Carbide Corporation, South Charleston, WV 25303

The optimal design of a plant-scale catalytic
reactor must effectively utilize capital, energy,
and raw material resources to achieve the lowest
possible product cost, consistent with
constraints imposed by business plans and the
overall plant environment. The paper illustrates
an effective strategy that was used recently to
develop the optimum reaction system design for a
real process -- the hydrogenation of butyraldehyde
to butanol -- in a total time of less than six
months. The basic approach involved the
development of Langmuir-Hinshelwood kinetics for
the reaction from Berty autoclave data,
incorporation of these kinetics into a tubular
reactor simulation and optimization program,
validation of the combined reaction and reactor
models with data from an existing pilot-plant,
and constrained optimization using easily-
developed economic criteria. The final design
exhibited superior economic performance, largely
as a result of greater catalyst productivity and
more efficient energy utilization and integration.

Union Carbide manufactures normal- and iso-butanol by the
hydrogenation of the corresponding butyraldehydes produced by its
rhodium-catalyzed, low-pressure Oxo process. The hydrogenation
process has been noted for a long time as a highly-selective,
economical route to high-purity butanol. Nevertheless, changes
in the relative costs of capital, energy, and raw materials over
the last several years led to a review of alternate technologies
for the hydrogenation of butyraldehyde, followed by complete
optimization of some of the more promising candidates. This
paper describes the optimization of one of these, the vapor-phase

catalytic hydrogenation of butyraldehyde in a shell-and-tube
fixed-bed catalytic converter.
      The optimization study comprised several distinct steps:

  o   Identification of the most suitable catalyst,

  o   Development of reaction kinetics models for primary and
      byproduct reactions,

  o   Development of reactor simulation and optimization
      computer programs specifically for the vapor-phase
      tubular reactor system,

  o   Validation of the simulation models using existing
      catalytic pilot-scale equipment,

  o   Development of economic criteria that could be evaluated
      rapidly by the optimization program, and finally,

  o   Reaction system design and optimization.

Identification of the Most Suitable Catalyst

The most important characteristics of a hydrogenation catalyst
are, for a particular reaction, its productivity and selectivity
to the desired product over economical ranges of temperature and
pressure. These ranges in turn depend heavily upon the overall
plant context in which the catalyst is to be used.
      For example, the most economical pressure range for typical
vapor-phase processes is between about five and thirty atmos-
pheres, based on both equipment and energy costs. Similarly,
the reaction temperature should permit the heat of reaction to
be recovered as steam at pressures between perhaps 3 and 45
atmospheres, corresponding roughly to 134 and 258°C.
      The useful and economical ranges for both the reaction
temperature and pressure vary widely within these ranges from
one plant to another and so it is important when optimizing a
process design for a particular location to understand exactly
how the process will fit into the overall plant, especially from
an energy conservation and utilization standpoint.
      It is apparent that optimum utilization of raw materials,
capital, and energy resources will influence the choice of
catalyst. Catalytic activity alone is not a sufficient
criterion. A hypothetical catalyst might be wonderfully active
and selective at 25°C and one atmosphere, but it would be
difficult to build an economical process around it.
      Union Carbide's Research and Development Department maintains
active programs in catalyst research and screening for a number
of major processes, and the candidate catalyst was selected for

this project on the basis of its chemical performance at
attractive temperatures and pressures.

We have not discussed catalyst life as one of the
determinants in the selection of a catalyst, although it
obviously can be of critical importance. In the absence of
poisoning, hydrogenation catalysts frequently last for several
years in plant service, and catalyst costs are thus relatively
minor in the overall product cost breakdown. Candidate
catalysts that did not exhibit exceptional life in laboratory
tests were simply excluded from consideration for our purposes.

Development of Reaction Kinetics Models

In reaction engineering, kinetic models are used to predict
reaction rates at specified conditions of temperature and the
partial pressures or concentrations of reactants and products.
The emphasis must be, therefore, upon accuracy of prediction,
even at the expense, if need be, of mechanistic rigor. For this
reason, kinetic models for design purposes should be developed
using the same pellet size and geometry as will be used in the
commercial process, and over the ranges of temperature and
component partial pressures expected for it. Finally, the
kinetics should be studied at realistic plant-scale gas
velocities so that the data are not influenced by physical
transport phenomena like heat- and mass-transfer.

Note that only temperature and partial pressures or
concentrations have been mentioned as variables. For a
catalytic reaction, these are the only variables of importance
from a kinetics standpoint. Time variables like space-velocity,
space-time, or residence-time, are reac<u>tor</u> variables rather than
reac<u>tion</u> variables, and will be involved in the development
of the reactor simulation model.

The choice of experimental reactor is important to the
success of the kinetic modeling effort. The short bench-scale
reaction tubes sometimes used for studies of this sort give
little or no insight into best mathematical form of the kinetic
model, conduct the reaction over varying temperatures and
partial pressures along the tube, and inevitably operate at
velocities that are a small fraction of those to be encountered
in the plant-scale reactor. Rate models from laboratory
reactors of this sort rarely scale-up well. The laboratory
differential reactor suffers from velocity problems but does at
least conduct the reaction at known and relatively constant
temperature and partial pressures. However, one usually runs
into accuracy problems because calculated reaction rates are
based upon the small observed differences in concentration
between the reactor inlet and outlet.

In recent years these problems have been largely overcome
with the development of gas-phase continuous back-mixed reactors
like the Berty reactor. This reactor recirculates the gas

rapidly through the catalyst bed and thus operates at uniform temperatures and partial pressures, and generally at rather high conversion levels. It is necessary, however, to control the outlet concentrations of both reactants and products in the course of the experimental program because the temperatures and partial pressures inside the reactor are the same as those at the outlet, rather than the inlet. Generally, it is necessary to feed reaction products as well as reactants to the reactor in order to control both product and reactant concentrations independently. A Berty reactor was used in the study described here. For more complete discussions of experimental reactors the reader is referred to Satterfield (1) and to Berty (2) (3).

The experimental program for the kinetic study comprised only 17 experiments altogether, but the formal program was not started until the ability to obtain quality data had been established. This meant that we had fine-tuned analytical methods and experimental procedures so that good material balances could be obtained routinely at any desired reaction conditions. Also, by the time the formal program was started, the catalyst activity in the autoclave had declined to a relatively constant level from the hyperactivity characteristic of new hydrogenation catalysts.

The core of the experimental program comprised a small statistically-designed set of eleven experiments in four variables: temperature, and the partial pressures of hydrogen, butyraldehyde, and butanol. (For discussions of the design of kinetic experiments, see Timoshenko (4) and Cropley (5).) Six additional experiments were made in order to approach desired conditions more closely, and ultimately all seventeen were used for model development. Both butyraldehyde and butanol were fed to control the outlet partial pressures at the desired levels. We used high-purity mixed normal- and iso-butyraldehyde and butanol for our work. Little difference in reaction kinetics were observed with either normal- or iso-species.

The kinetic model developed from these data for the reversible production of butanol is of the form:

$$ r = \frac{k_o e^{-E/RT} P_{H2} P_{BAL} - \frac{k_o e^{-E/RT}}{K_{eq}} P_{BOL}}{(1 + K_1 P_{BAL} + K_2 P_{BOH} + K_3 P_{H2})^2} $$

The expression for the equilibrium constant K_{eq} was developed from component standard free energies of formation published by Stull (6) and has the general form

$$ K_{eq} = K_o e^{-\Delta H_r/RT}, $$

where ΔH_r is the overall heat of reaction.

The kinetic parameters were evaluated numerically using the heuristic procedures of Cropley (5). The algebraic form of the kinetic model had been shown previously to describe adequately the kinetics of reactions of this type. Note that in spite of its apparent complexity, only one parameter is associated with each variable. The basic two level experimental design is thus adequate if the form of the rate law is fixed, though one might like to have the time to develop a more complete data set.

The overall quality of the model is excellent, with a coefficient of determination of 0.987 and a relative standard deviation of the error of 14.5 percent. Nonetheless, the values for K_1, K_2, and K_3 are jointly confounded with one another and thus represent only one of many families of values for the parameters that would fit the data virtually equally well. This means that inferences that these parameters really represent chemisorption equilibrium constants are unwarranted, but the model is nonetheless useful for its intended purpose. If it had been desirable to do so, additional experiments could have been run to narrow the joint confidence intervals of these parameters.

Simpler models for byproduct formation were developed from the same set of experiments. These models are of simple power-series or exponential form and serve adequately to predict the small amounts of byproducts formed by the reaction.

Note that the mathematical form of the model implies that the rate-limiting step is a dual-site surface reaction between chemisorbed hydrogen and chemisorbed butyraldehyde, and that the reverse reaction is the monomolecular dehydrogenation of chemisorbed butanol. Models of this sort should not be over-interpreted from a mechanistic standpoint. Kinetics models are at best ambiguous indicators of mechanism in that several models typically fit the data equally well.

Although this model is entirely adequate to fit the data from which it was developed, its form was selected for an entirely different and even more pragmatic reason. Since the hydrogenation reaction is desirably conducted to virtual extinction of the butyraldehyde to avoid problems and losses in the refining system, the model must readily collapse to a predicted rate of zero at equilibrium partial pressures of hydrogen, butyraldehyde, and butanol. This requires that all three components appear in the numerator of the equation. If in fact some other rate controlling step prevails early in the reaction, the model will not predict as well at that point. In actual fact, validation of the model in the pilot-plant showed that the model does a reasonably good job throughout the reaction.

Development of Reactor Simulation and Optimization Programs

Numerical simulation techniques were used to investigate the performance characteristics of alternative fixed-bed reactor designs. The complexity of a model used for simulation depends

largely upon the objective of the simulation and the nature of the available data. For the hydrogenation project described in this paper, we used a relatively simple one-dimensional simulation that comprised a set of ordinary differential equations for axial distance versus the mol fractions of hydrogen, inert gases, butyraldehyde, butanol, principal byproducts, water, reaction temperature, coolant temperature, and mean molecular weight. This last item is important because it leads to an easy way to accommodate the molar contraction of the gas as the reaction proceeds. The program calculates steady-state profiles of each of these down the length of the tubular reactor, given the reaction kinetics models, a description of the reactor and catalyst geometries, and suitable inlet gas flow-rate, pressure and composition information. Reactor performance is calculated from the flow-rate and composition data at the reactor outlet. Other data, such as the calculated pressure drop across the reactor and the heat of reaction recovered as steam, are used in economic calculations. The methods of Dixon and Cresswell (7) are recommended for heat-transfer calculations.

The equations comprising the simulation model for the hydrogenation of butyraldehyde are:

For each chemical species i:

$$\frac{dY_i}{dZ} = \frac{R_i n \pi D^2}{4F} + \frac{Y_i}{\overline{MW}} \frac{d(\overline{MW})}{dZ} \quad , \quad R_i = \sum \alpha_{ij} \beta_j r_j$$

For Reaction and Coolant Temperatures:

$$\frac{dT_r}{dZ} = \frac{n \pi D^2}{4FC_p} \sum \beta_j r_j \Delta H_j - \frac{n U \pi D (T_r - T_c)}{FC_p}$$

$$\frac{dT_c}{dZ} = \frac{n \pi D U (T_r - T_c)(MODE)}{F_c C_c}$$

For Pressure:

$$\frac{dP}{dZ} = \frac{-150 u v_o (1.-e)^2}{D_p^2 e^3} + \frac{1.75 \rho_g v_o^2 (1.-e)}{D_p^2 e^3} \Big/ 144. / 32.3 / 14.7$$

For Mean Molecular Weight:

$$\frac{d(\overline{MW})}{dZ} = MW_{BAL} \frac{dY_{BAL}}{dZ} + MW_{H2} \frac{dY_{H2}}{dZ} + MW_{BOH} \frac{dY_{BOH}}{dZ} + \ldots + MW_n \frac{dY_n}{dZ}$$

Although these equations incorporated the best information we had at the time of their development, the model had to be validated before its accuracy could be relied upon for actual design and optimization of the reaction system.

Model Validation

The one-dimensional model is by no means descriptive of everything that goes on in the reactor, because it provides calculated temperatures, concentrations, pressures, and so on only in one dimension -- lengthwise, down the axis of the tube. Actually, transport processes and diffusion cause variations and gradients not only axially but also radially within tubes and within individual catalyst pellets. Furthermore, the reactor may not actually operate at steady-state, and so time might also be included as a variable. All of these factors can be described quite easily by partial differential equations in as many as four dimensions (tube length, tube radius, pellet radius, and time).
    But there are problems with multi-dimensional models. From a purely pragmatic standpoint, even two-dimensional models require too much computer time to be really practicable for optimization purposes. In addition, multi-dimensional models require values for parameters that are difficult or impossible either to estimate with sufficient accuracy, or to measure.
    In practice, it generally will be found that one-dimensional models are entirely adequate for optimization, provided that they are validated in some kind of pilot-scale tubular reactor. Validation comprises the adjustment of parameters in the reactor model equations so that observed and predicted temperature and concentration profiles match as closely as possible. Typical parameters are the relative catalyst activity factors β_j and, if necessary, the overall heat-transfer coefficient, U. A statistically-designed set of experiments in the pilot-plant is invaluable for model validation, and such a set was used in this project.
    Figure 1 illustrates typical performance of a validated one-dimensional model in the prediction of temperature profiles in a plant-scale tubular hydrogenation reactor. Note that the major problem area is in the relatively low-temperature region near the inlet. The peak temperature is properly located in the tube, but is slightly lower than the actual temperature. With reactions and reactors of this type, the major reaction is over slightly after the peak temperature has been reached, and the remainder of the reactor is described primarily by a cooling curve. The outlet composition of the reactor will be essentially at equilibrium with respect to the principal reaction.
    We have identified several probable causes of the "hook" phenomena -- the failure of the one-dimensional model to predict the inlet temperature profile accurately, as shown in Figure 1. The major causes are:
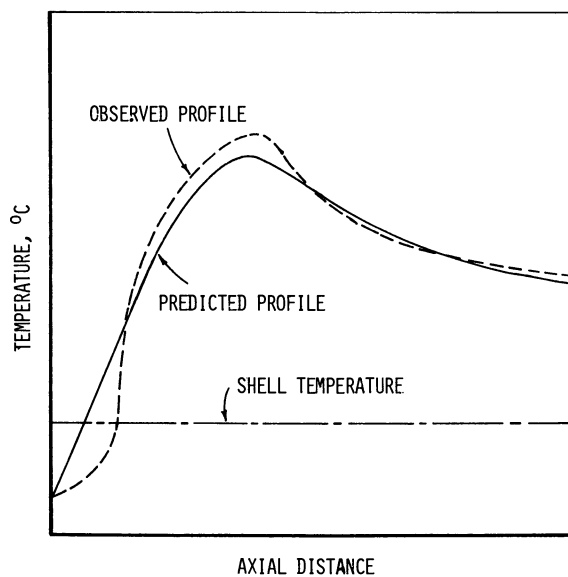
Figure 1. Typical temperature profiles using a validated
one-dimensional reactor simulation model.

a) Deactivation of the catalyst in the bed by progressive poisoning or deactivation or by condensation of liquids in the smallest pores of the catalyst pellet.

b) Axial and radial thermal dispersion in the catalyst bed.

c) Non-uniform shell temperatures, especially in reactors in which both gas and relatively cool steam condensate enter at the bottom.

There are other possible causes as well, but it is essential to point out that the effect has little apparent impact on the overall performance of the reactor or the model's ability to predict it, based on outlet composition and product distribution.

If progressive deactivation is a factor, it may be desirable to describe the β_j catalyst activity factors as functions of axial distance and catalyst age. In any event, the final design must be checked over a realistic range of catalyst activities to ensure operability and performance over the projected life of the catalyst.

In our judgment, it is not necessary that the exact geometry of the final reactor design be duplicated in the pilot plant to be used for validation, provided that appropriate ranges of mass and space velocities, pressure, temperature, feed composition, and so on can be effectively matched, and that critical recycle loops can be closed.

Fortunately for our project, a pilot-plant suitable for validation purposes was available as part of the R&D facilities at the projected plant site.

Development of Economic Optimization Criteria

In principle, almost any economic parameter that reflects changes in the reaction system may be used for optimization. In practice there are constraints and limitations that historically have limited the direct use of economic criteria. The most common of these is the complexity of economic evaluations, which typically have required vast amounts of computer time in their preparation.

Nevertheless, it is entirely possible and practicable to develop optimization criteria that are simultaneously relevant to the reaction system design and readily calculable.

Most economic studies of chemical processes show the projected performance of the process with respect to some parameter like return on investment, profit on sales, or net present value at some future year. These studies are appropriate for project evaluation by management, and may include cost components related to capital, energy, utilities, raw materials, labor, overhead, working capital, and so on. They may or may not include sensitivity analyses of the effects

of reactor size, raw material utilization, or reactant conversion. And they invariably include sales price projections.

Reaction system optimization seeks to reduce the cost of manufacturing a particular product, and is typically unconcerned with sales price unless more than one saleable product is produced. For plant design and optimization, it is convenient to separate overall product costs into components that directly reflect the attributes of the reaction system. Thus instead of capital, utilities, and raw material utilization costs, one calculates costs that are related to reactor size, gas recycle volume, raw material inefficiencies and vent and purge losses. Each of these may have components related both to capital and operating costs that are of interest to management but which are not particularly useful for optimization. It is desirable to summarize costs in a way that is simultaneously meaningful to management and to the reaction system designer.

One such way is to prepare a table of the following type, to be used to summarize each of several base cases. The hypothetical example shown here is reproduced from an earlier paper (8), but it effectively illustrates the kind of summary used in this project. The actual numbers for the butyraldehyde hydrogenation process, of course, are confidential.

Sample Table of Base Summaries

	Capital ¢/lb	Utilities ¢/lb	Raw Mat'ls ¢/lb	Total ¢/lb
Reactor (Incl. Catalyst)	1.0		0.5	1.5
Gas Recycle System				
Compressors	1.5	0.8		2.3
Heat Exchangers	0.6	0.2		0.8
Product Recovery System	2.0	0.2		2.2
Raw Material A				
Losses to Byproducts	0.5		6.2	6.7
Physical Losses			1.0	1.0
Stoichiometric Req'ts			20.0	20.0
Raw Material B				
Losses to Byproducts	0.1		1.0	1.1
Physical Losses			1.0	1.0
Stoichiometric Req'ts			3.0	3.0
Semi-Fixed Costs (Labor, Inventory, Overhead, etc.)	2.0	1.0		3.0
Totals	7.7	2.2	32.7	42.6

Armed with the summaries of several well-conceived case studies, the reaction system designer can readily plot the economic impact of catalyst productivity, product concentration, or reaction selectivity -- the primary chemical responses of the reaction system -- as reflected by reactor size, cycle gas volume, and raw material utilization.

As it turns out, plots of these responses are typically simple monotonic functions like straight lines or curves that are easily described algebraically. Figure 2 is typical of the graphs and relationships used in the optimization of the butyraldehyde hydrogenation reactor. Given these, we easily determined the total cost of producing butanol from butyraldehyde by simply adding up the component costs and adding in the stoichiometric cost requirements and semi-fixed costs.

The equations that describe these graphs are entirely adequate to evaluate the production cost in the optimization program, and comprised a total of fewer than 50 FORTRAN statements, even with provisions for multiple options and constraints.

Obviously, the optimum reaction system design will reflect assumptions about the relative costs of capital, energy, and raw materials. These will inevitably change as one studies the optimum timing to build the new unit and its actual location. But the economic criteria developed here are readily changed to reflect different assumptions. A strength of the method is that it can quickly lead to changes in the optimum plant design based on projected changes in the overall economic climate.

Optimization of the Reaction System

The business department established the production rate for the new system, and the plant context determined certain other quantities, such as the pressure and purity of the hydrogen feed stream. Given these, optimization of the reaction system was accomplished by iteratively solving the simulation equations to arrive at the lowest cost for the product butanol, which was calculated according to the scheme described in the last section. The optimization procedure utilized a non-linear optimum-seeking algorithm, and involved the manipulation and calculation of search variables, response variables, and constraints.

The search variables included both reactor design and operating variables. The former included quantities like the number of tubes in the reactor and their diameter and length. Operating variables included quantities like the mol fraction of aldehyde in the reactor feed (and hence the cycle gas flow rate), reactor inlet and shell temperatures, and reactor inlet pressure.

The response variables included virtually everything that one might observe in a real reactor -- reactor maximum and outlet temperatures, reactor outlet concentrations of butyraldehyde, butanol, and byproducts, inlet and outlet dewpoint temperatures, catalyst productivity, reactor pressure drop, and so on.
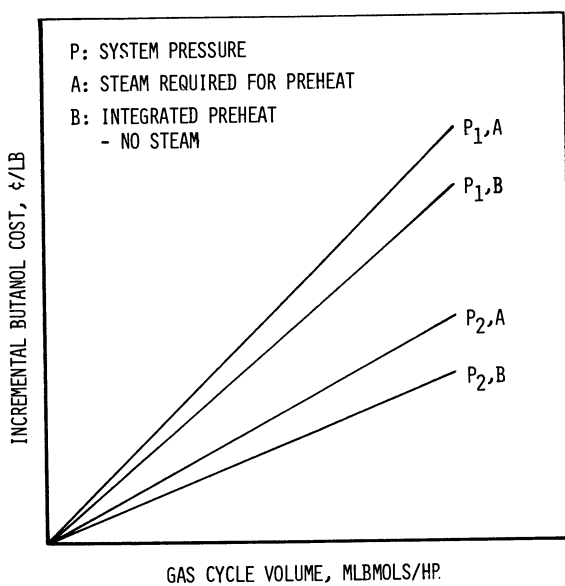
Figure 2. Incremental butanol cost vs. gas cycle volume.

The constraints changed from one trial configuration of the reaction system to the next, but typically included things like the minimum coolant temperature to permit efficient utilization of the heat of reaction as process steam, the maximum allowable aldehyde concentration in the condensed crude product to avoid refining and product specification problems, and a prescribed reactor pressure drop to insure adequate flow distribution among the reactor tubes at a minimum energy cost. All of these are implicit constraints -- they establish the maximum or minimum levels for certain response variables. Explicit constraints comprise the ranges for search variables.

We proceeded to develop the entire reaction system network for the optimum case, by setting implicit and explicit constraint levels that realistically described each new version of the system as we perceived it. Most of these versions involved changes external to the reactor that were primarily concerned with the most efficient utilization of the heat of reaction. But they frequently necessitated changes in reactor outlet temperature or shell temperature to adjust the fraction of the heat of reaction to be generated as steam. These changes in turn made changes necessary throughout the system, and the optimization program determined the best combination of these. A simplified flow diagram of a typical hydrogenation system is shown in Figure 3.

The result of the effort was a precise definition of the values for all of the fixed, search, and response variables for the optimum case, as well as an economic breakdown of the costs. We'll see how these compared with the previous technology in the next section.

Comparative Economics of the Optimized Vapor-Phase Tubular Reaction System

At the outset of the project, we established as a yardstick for economic comparison, an entirely new unit based on the old hydrogenation process technology. No attempt was made to improve it, either in the light of experience or knowledge gained from the study described in this paper. Dubbed irreverently the "Rubber Stamp", the old process, while chemically efficient, was characterized by significantly higher product costs than was the new optimized process.

The comparative costs are shown in Figure 4. Note that they exclude the stoichiometric requirements for butyraldehyde and hydrogen, as well as the semi-fixed costs discussed earlier.

The most striking reduction in costs was achieved by energy integration, specifically by establishing the recovery of usable energy and the minimization of expended energy as important components of the overall economic optimization process.

Raw material usage was reduced largely by lowering the hydrogen concentration in the cycle gas in order to reduce the
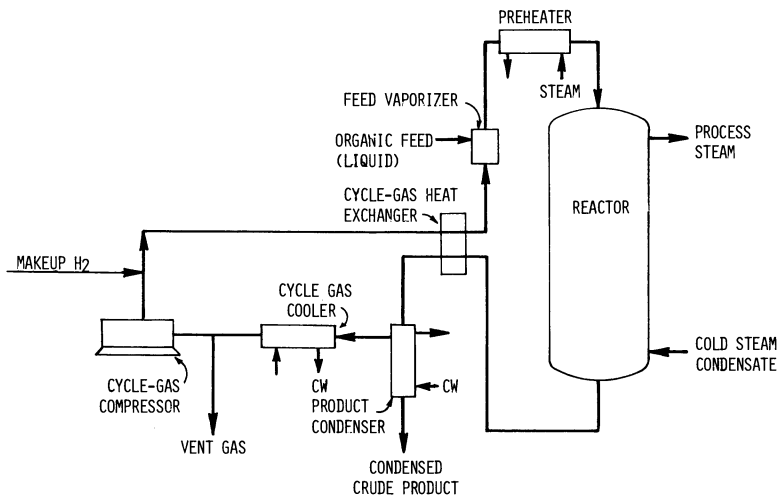
Figure 3. Conceptual flow diagram for a typical vapor-phase hydrogenation reaction system.
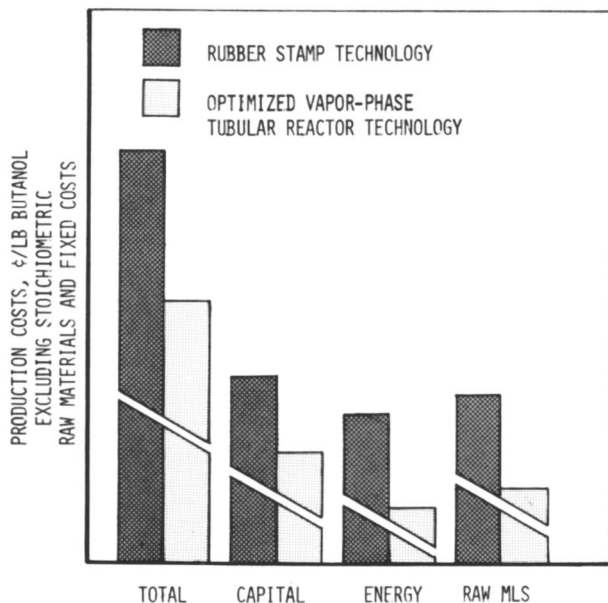
Figure 4. Economic comparison of existing "Rubber Stamp" and optimized tubular reaction systems.

hydrogen vented with the purge. (The "Rubber Stamp" process was already highly efficient from a purely chemical standpoint.)

Capital costs were reduced virtually everywhere in the reaction system, but the utilization of a highly reactive catalyst that was suitable for operation at economical temperatures and pressures was probably the most important single factor. It is thus important to establish economic criteria for catalyst selection or development early in the development and design of a new process.

As with most commodity chemicals, the stoichiometric chemical costs remain the dominant component of overall process economics, but success in the marketplace depends critically upon the most efficient utilization of capital, energy, and raw material resources to gain and retain the economic upper hand. Programs like the one described in this paper are designed to do just that.

Legend of Symbols

C_c	Coolant heat capacity, Btu/Lb/°C
C_p	Gas heat capacity, Btu/LbMol/°C
D	Tube diameter, ft.
D_p	Catalyst pellet diameter, ft.
E	Reaction activation energy, Cal/Gmol
e	Catalyst bed void fraction
F	Gas flow-rate, LbMols/Hr
ΔH_{r_j}	Heat of reaction for reaction j, Btu/LbMol
k_o	Pre-exponential rate constant
K_{eq}	Reaction equilibrium constant (dimensionless)
K_i	Kinetic parameter
MODE	Heat transfer mode: -1 for coolant countercurrent to gas
	0 for isothermal shell-side
	+1 for coolant co-current with gas
$\overline{MW}$	Mean molecular weight of gas, Lb/LbMol
MW_i	Molecular weight of component i, Lb/LbMol
n	Number of tubes in reactor
P_i	Partial pressure of component i, atmospheres
r_j	Reaction rate for reaction j, LbMols/Ft^3/Hr
R	Gas constant, 1.987 Cal/Gmol°C
R_i	Net rate of reaction for component i, LbMols/Ft^3/Hr
T_r, T	Reaction temperature, °C
T_c	Coolant temperature, °C
U	Overall heat-transfer coefficient, Btu/Ft^2/Hr/°C
v_o	Superficial gas velocity, ft/sec.
Y_i	Mole fraction of component i
Z	Axial distance from reactor inlet, ft.
α_{ij}	Stoichiometric coefficient for component i in reaction j
ρ_g	Gas density, Lb/ft^3
β_j	Relative activity factor for reaction j
u	Gas viscosity, Lb/ft-sec.

Literature Cited

1. Satterfield, C. N. "Heterogeneous Catalysis in Practice,"
   McGraw-Hill Book Company, New York, 1976.
2. Berty, J. M. Chem. Eng. Prog. 1974, 5 (5).
3. Berty, J. M. Catal. Rev.-Sci. 1979, 20, 76-96.
4. V. I. Timoshenko, et al. Kinetika i Kataliz, 1968, 9,
   1358-1363.
5. Cropley, J. B., in "Chemical Reaction Engineering -
   Houston"; Weekman, V. W., Jr.; Luss, D., Eds; ACS SYMPOSIUM
   SERIES No. 65, American Chemical Society: Washington, D.C.,
   1978; pp. 292-302.
6. Stull, R. D.; Westrum, E. F., Jr.; Sinke, G. C. "The
   Chemical Thermodynamics of Organic Compounds," John Wiley
   and Sons: New York, 1969.
7. Dixon, A. G.; Cresswell, D. L. AIChEJ 1979, 25, 663-676.
8. Cropley, J. B. Proc. Pittsburgh AIChE Section Reactor
   Engineering Industrial Applications Symposium, 1982.

Problems in the Design of the Countercurrent Moving-Bed Catalytic Reactor

A Geometric Approach

DIMITRY ALTSHULLER[1]

School of Chemical Engineering, Purdue University, West Lafayette, IN 47907

We consider a reactor with a bed of solid catalyst moving in the direction opposite to the reacting fluid. The assumptions are that the reaction is irreversible and that adsorption equilibrium is maintained everywhere in the reactor. It is shown that discontinuous behavior may occur. The conditions necessary and sufficient for the development of the internal discontinuities are derived. We also develop a geometric construction useful in classification, analysis and prediction of discontinuous behavior. This construction is based on the study of the topological structure of the phase plane of the reactor and its modification, the input-output space.

Consider a physical system shown schematically in Figure 1. A fluid stream containing reactant A is moving upwards in plug flow with a constant velocity U. The reactant is adsorbed by a stream of solid catalytic particles falling downwards with a constant velocity V and occupying the void fraction of $1 - \varepsilon$. On the surface of catalyst an irreversible chemical reaction $A \rightarrow B$ is occurring and the product B is then rapidly desorbed back into the fluid phase. Instantaneous adsorption equilibrium for the species A is assumed.

    The advantage of the moving-bed reactor over the convention-al fixed-bed reactor is the possibility of continuous recharging of fresh catalyst, thus eliminating the need for shutdown to replace it. It has also been shown (1, 2) that the residence time required for a given conversion is shorter in a moving-bed reactor. This system has received a considerable attention at the University of Minnesota. Viswanathan and Aris (1) studied the behavior of the reactor assuming that the adsorption isotherm was convex and using the Langmuir equation as an example. The

[1] Current address: Dept. of Mathematics, University of Missouri, Columbia, MO 65211.
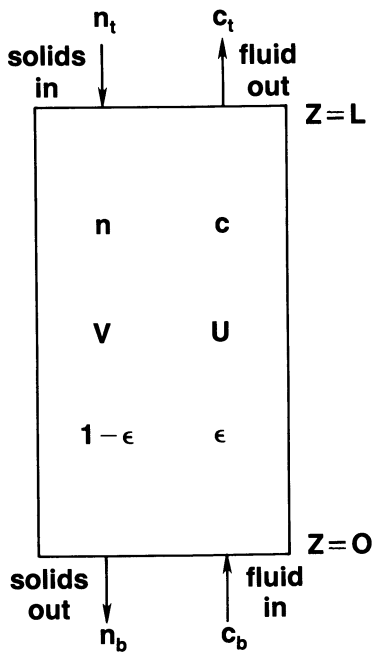
Figure 1. Moving bed reactor schematic.
(Reproduced with permission from Ref. 8.
Copyright 1983, Chem. Eng. Commun.)

results for continuous steady states for arbitrary form of adsorption equilibrium were derived in the earlier paper (2). In that paper we have also discussed some features of transient and discontinuous behavior.

This work may be viewed as a continuation of the previous work (2). We want to describe the steady-state discontinuous behavior of the reactor, thus generalizing some of the results obtained by Viswanathan and Aris (1). We want to derive the necessary and sufficient conditions for the development of the internal discontinuities. Then, we shall see how the geometric methods can be used in analysis and prediction of the discontinuous behavior.

The presence of the internal discontinuities makes the use of the standard design equations impossible. Therefore it is necessary to know at what degree of conversion will the discontinuity occur. Then the design equation will tell us at what point in the reactor this happens.

After these preliminary remarks we now proceed to construct the mathematical model of the system.

The Equations of the System

We begin our analysis by making a mass balance for the reactant. It leads to the following equation for the steady state

$$\frac{d}{dz} [U\varepsilon c_A - V(1 - \varepsilon)n_A] + R(n_A) = 0 \qquad (1)$$

The concentration of the product B can be established, if desired, by overall mass balance. The above equation can be made dimensionless by introducing the new variables

$$u = c_A/c_A^o, \quad w = n_A/n_A^o \qquad (2)$$

$$x = kz/\varepsilon U, \quad X = kL/\varepsilon U \qquad (3)$$

where k is the coefficient which has a dimension of the first-order rate constant and relates the function $R(n_A)$ to the dimensionless function $F(v)$:

$$R(n_A) = kn_A^o F(v) \qquad (4)$$

Therefore we have two important dimensionless parameters

$$\mu = n_A^o/c_A^o \qquad (5)$$

and,

$$\gamma = p(1 - \varepsilon)V/\varepsilon U \qquad (6)$$

The parameter γ is a ratio of the transport capacities of the two phases, while μ is a ratio of the reference concentration of the reactant in these phases.

The Equations 1 and 2 then become

$$\frac{d}{dx}[u - \gamma v] + \mu F(v) = 1 \qquad (7)$$

The following boundary conditions can be imposed on u and v

$$u(o_-) = u_b \qquad (8)$$

$$v(x_+) = v_t \qquad (9)$$

i.e., we specify the conditions just outside of the reactor which do not have to coincide with those just inside of the reactor since the adsorption equilibrium is attained instantaneously.

Adsorption equilibrium which we have assumed can be described in two ways: $u = f(v)$ and $v = g(u)$. The advantages and limitations of these two expressions were discussed earlier (2). In this work we shall assume that the function $f(v)$ is monotonic and use primarily the function $v = g(u)$.

The introduction of the adsorption equilibrium leads to the equation:

$$[1 - \gamma g'(u)] \frac{du}{dx} + \mu G(u) = 0 \qquad (10)$$

where $G(u) = F(g(u))$

In order to solve the Equation 10, we rearrange it to obtain

$$\frac{du}{dx} = \frac{\mu G(u)}{\gamma g'(u) - 1} \qquad (11)$$

Solution of Equation 11 seems to be quite easy. The separation of variables and integration leads to:

$$\mu(x - x_o) = \int_{u_o}^{u} \frac{\gamma g'(u) - 1}{G(u)} \, du \qquad (12)$$

The desired reactor length therefore is

$$\mu X = \left| Z(u_{t-}) - Z(u_{b+}) \right| \qquad (13)$$

where $Z(u)$ is an auxiliary function defined as an integral

$$Z(u) = \int_{lower-limit}^{u} \frac{\gamma g'(u) - 1}{G(u)} \, du \qquad (14)$$

The lower limit of integration may be omitted since the function $Z(u)$ can appear only in a difference relationship.

However, if we look at Equation 11 more carefully, we notice that its right-hand side becomes discontinuous at the points where $\gamma g'(u) = 1$. If such a point is between u_{b+} and u_{t}, continuous solutions (and only for them Equation 13 is valid) fail to exist. Therefore, we need to analyze the discontinuous behavior of the reactor. In order to do that, we must first establish some general properties of the discontinuities often referred to as shocks.

The General Properties of Shocks

Let us make a mass balance over the plane of the discontinuity as shown in Figure 2. Insisting that there is no accumulation of matter in the shock plane, we obtain

$$u_1 - \gamma v_1 = u_2 - \gamma v_2 \qquad (15)$$

Therefore, every discontinuity can be represented on a plane v **vs.** u by a segment of a straight line having a slope of $1/\gamma$ often called a shock path.

We can distinguish between two kinds of shocks depending on where they occur: boundary and internal. The former ones are caused by the difference between the inlet and the equilibrium concentrations. The nature of the latter ones is more subtle.

For the boundary discontinuities, we have the following two equations:

$$u_b - \gamma v_b = u_{b+} - \gamma v_{b+} \qquad (16)$$

$$u_{t-} - \gamma v_{t-} = u_t - \gamma v_t \qquad (17)$$

From the boundary conditions, we know u_b and v_t. Since equilibrium is maintained just inside the reactor, we have

$$v_{b+} = g(u_{b+}) \qquad (18)$$

$$v_t = g(u_{t-}) \qquad (19)$$

Therefore, one end of the path of the boundary discontinuity must lie on the isotherm. The outlet concentrations u_t and v_b can be determined by combining Equations 16-19.
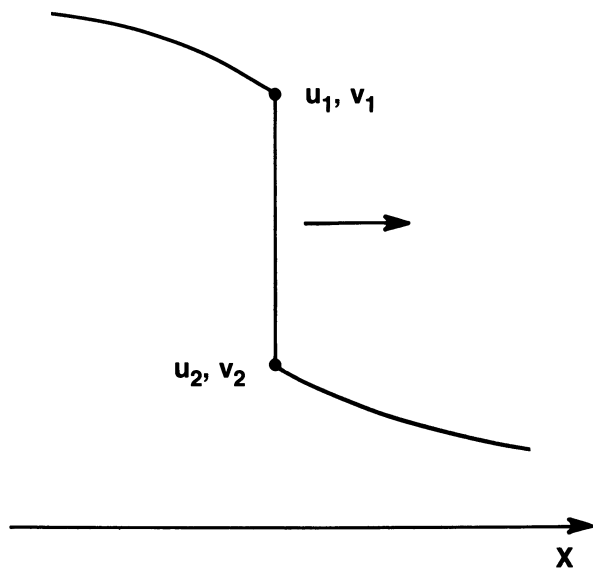
Figure 2. The shock plane.
(Reproduced with permission from Ref. 8.
Copyright 1983, Chem. Eng. Commun.)

$$v_b = \frac{1}{\gamma}[u_b - u_{b+} + \gamma g(u_{b+})] \qquad (20)$$

$$u_t = u_{t-} - \gamma g(u_{t-}) + \gamma v_t \qquad (21)$$

For the internal discontinuity, both ends of the path must lie on the isotherm. Using this condition together with Equation 15 we obtain

$$g(u_2) - g(u_1) = \frac{1}{\gamma}(u_2 - u_1) \qquad (22)$$

Since the function $g(u)$ is continuous and differentiable everywhere between u_1 and u_2, we may apply the theorem from Analysis known as La Grange's formula (3). It states that there exists a point u^* such that

$$g(u_2) - g(u_1) = g'(u^*)(u_2 - u_1) \qquad (23)$$

Together with Equation 29 this implies

$$g'(u^*) = 1/\gamma \qquad (24)$$

Equation 24 is a necessary condition for the presence of the internal discontinuity. If it is satisfied, for some $g(u)$ and γ, then Equation 11 fails to meet Lipschitz condition (see, for example, (4) for discussion of this as well as some other facts from the theory of differential equations) and continuous solutions cannot exist. Therefore, Equation 24 is also a sufficient condition for the presence of the internal discontinuity. Thus, we have proved the following:

THEOREM. A necessary and sufficient condition for the existence of the internal discontinuity is the existence of a point u^* such that $g'(u^*) = 1/\gamma$.

Geometrically, this theorem means that there must be a straight line tangent to the isotherm having a slope of $1/\gamma$. Therefore the point $u = u^*$ will hereafter be called the tangency point.

In the following section, we will look at the geometry of the adsorption equilibrium curve (isotherm) and see how it can be related to the above discussion. When we speak about tangents or chords hereafter, we shall always mean that they have a slope of $1/\gamma$.

The Adsorption Isotherm and the Structure of the Phase Plane

A number of equations have been proposed to describe adsorption equilibria. None of them can be considered universal and some of them cannot be used in the theoretical studies because they do not conform to certain constraints imposed by the physical nature of adsorption (5).

Two types of isotherms are most common. The first is type I of Brunauer's classification (6) with Langmuir's equation being the simplest example. The curves corresponding to this type are convex everywhere and have a v = 1 asymptote. This type was studied in the framework of the moving bed reactor by Viswanathan and Aris (1). According to the result of the previous section we cannot have more than one internal discontinuity.

The second type of isotherm which commonly occurs arises when the lateral interactions between adsorbed molecules are taken into account or the Van der Waals type of equation is used to describe the state of the adsorbate (7). The equations for these isotherms usually have the form $u = f(v)$, for example, the Fowler-Guggenheim isotherm studied with some care in the earlier work (2).

For these isotherms, different geometries may be possible for one equation. If the lateral interactions are weak, the isotherm is convex. On the other hand, if these interactions are very strong, the function $f(v)$ is not monotonic and the function $v = g(u)$ is multi-valued. The case we study here is an intermediate between these two extremes. We assume that the function $f(v)$ is monotonic but has an inflection point $(\tilde{u}, g(\tilde{u}))$. The function $g(u)$ is thus defined, perhaps, implicitly. We assume that $g(u)$ is concave for $u < \tilde{u}$ and convex for $\tilde{u} < u$ and also that $v = 1$ is an asymptote.

From the previous section, it is clear that we need to know the number and the locations of the tangency points. For the isotherm considered here, four cases may be distinguished. They are shown in Figure 3.

If $\gamma < 1/g'(\tilde{u})$ (Figure 3a), there are no tangency points. It has been proved (2) that the behavior of the reactor is similar to that with the fixed-bed. The discontinuity may occur only on top of the reactor. The fact that the isotherm is not convex does not give rise to any new qualitative features. Therefore, we do not study this case in detail here.

Let us dispose of another relatively simple case. If $\gamma > 1/g'(0)$ as shown in Figure 3b, there is one and only one tangency point located on the convex part of the isotherm. Again, this case is qualitatively similar to that of convex isotherm thoroughly analyzed by Viswanathan and Aris (1).

The effects of nonconvexity are present when $1/g'(\tilde{u}) < \gamma < 1/g'(0)$. In this case, there are two tangency points $u = u^*$ and $u = u_*$. Therefore, we may have two internal discontinuities, the case not possible if the isotherm is convex. The tangent at the point $u = u^*$ may pass either above the origin if $1/g'(\tilde{u}) < \gamma < u^*/g(u^*)$, or below it if $u^*/g'(u^*) < \gamma < 1/g'(0)$. These two situations are shown in Figures 3d and 3c, respectively.

It is important to know the direction of the shock paths in order to establish the exact locations of the discontinuities. Viswanathan and Aris (1) have shown that the shock paths are
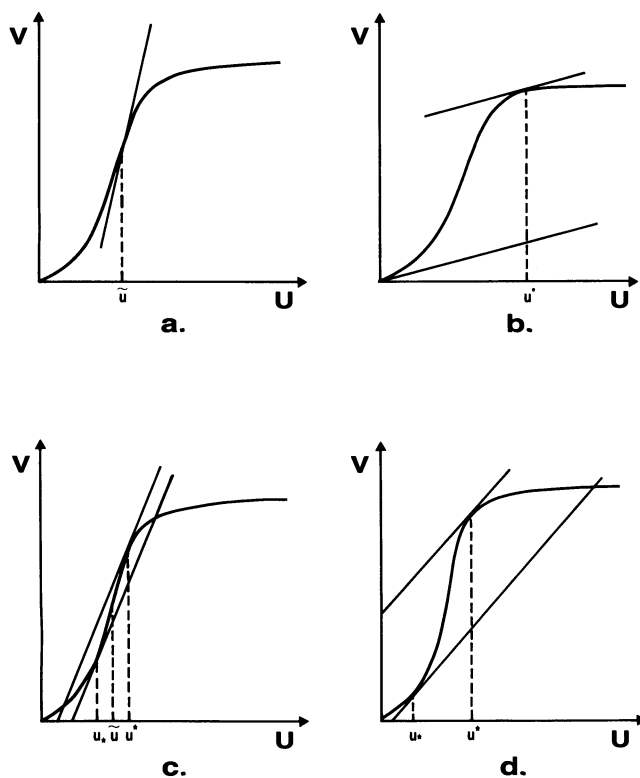
Figure 3. Isotherm and tangents. Key: a, $\gamma < 1/g'(\tilde{u})$;
b, $\gamma > 1/g'(0)$; c, $1/g'(\tilde{u}) < \gamma < u^*/g(u^*)$; and d, $u^*/g(u^*)$
$< \gamma < 1/g'(0)$.

directed upwards above the isotherm and downwards below it.
Therefore, we can distinguish between stable and unstable parts
of the isotherm depending upon whether the shock paths point
towards or away from it. In Figures 4a – 4c, the stable parts of
the isotherm are shown with the solid line and the unstable ones
with the broken line. If there are no tangency points, the entire
isotherm is unstable (Figure 4a). If there is only one tangency
point, the part below it is stable (Figure 4b). If there are two
tangency points, the stable part lies between them (Figure 4c).
From Equation 11, we know that $du/dx < 0$ if $g'(u) < 1/\gamma$ and
$du/dx > 0$ otherwise. Therefore, the trajectories are directed
towards the upper tangency point and away from the lower tangency
point (Figures 4b and 4c).

A stable part of the isotherm has an attraction area associ-
ated with it. By attraction area we mean the region in which all
the discontinuity paths and on the isotherm. The attraction areas
are bounded by the tangents as well as some portions of the
unstable parts.

If a tangent intersects the isotherm at some point other
than the tangency point, such an intersection will be called a
limitation point. If this does not happen, the limitation point
will be defined as an end of the chord beginning at the origin.
The former situation occurs if $u^*/g(u^*) < \gamma < 1/g'(0)$ and the
latter one if $1/g'(\tilde{u}) < \gamma < u^*/g(u^*)$. In any case, we have two
limitation points $u = u^\ell$ and $u = u_\ell$. Figures 5a and 5b show the
complete topological structure of the phase plane when
$1/g'(\tilde{u}) < \gamma < 1/g'(0)$.

Every chord drawn to the isotherm associates a point on the
unstable part with a point on the stable part. Mathematically,
this association can be expressed by a function $J(u)$ which we
shall call a jump function. This function can be defined implic-
itly using Equation 22, but then we would have two values u_2
corresponding to some values of u_1. This difficulty is eliminated
if an additional condition that $u_* \leq J(u) \leq u^*$ for every u is
imposed.

The same difficulty arises if we attempt to define an in-
verse of the function $J(u)$ also needed in our analysis. Two
inverses must be defined which we shall call upper and lower
inverses denoted by $J^1(u)$ and $J_1(u)$, respectively. The distinc-
tion is that $J^1(u) > u^*$ and $J_1(u) < u_*$ for every u. The function
$J^1(u)$ always maps the interval (u_*, u^*) onto the interval
(u^*, u^ℓ) and $J^1(u_*) = u^\ell$. For the function $J_1(u)$, the domain and
the range depend on whether γ is greater or less than $u^*/g(u^*)$.
In the former case, this function maps the interval (u_*, u^*) onto
the interval $u_\ell, u_*)$ and $J_1(u^*) = u_\ell$. In the latter case, the
domain is (u_*, u_ℓ) and the range is $(0, u_*)$ with $u_\ell = J(0)$.

Having established the geometric properties of shocks and
the structure of the phase plane, including appropriate functions
needed in the analysis, we may look at the discontinuous solutions
as a whole.
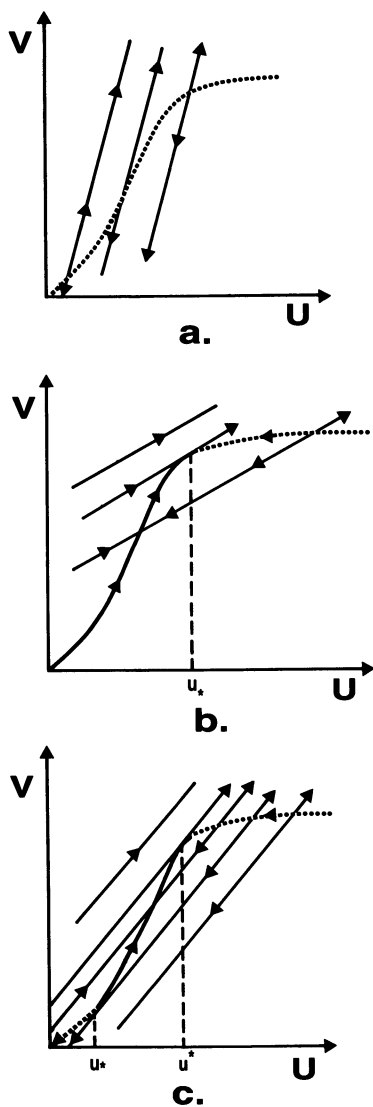
Figure 4. Stability of isotherm. Key: a, no tangency
points; b, one tangency point; and c, two tangency points.
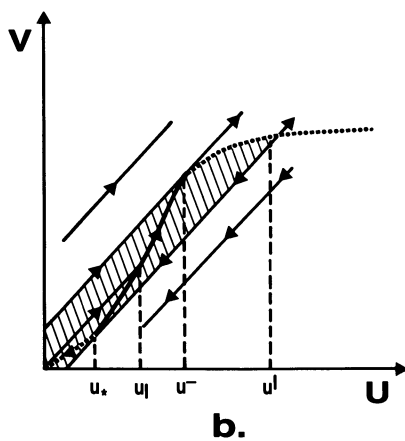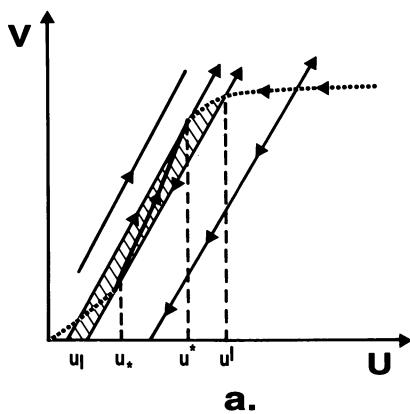
Figure 5. The phase plane of the reactor. Key: a, $1/g'(\tilde{u})$
$< \gamma < u^*/g(u^*)$; and b, $u^*/g(u^*) < \gamma < 1/g'(0)$.

The Structure of the Discontinuous Solutions

From the previous two sections, it is clear that every phase trajectory of the moving-bed reactor consists of the segments of the isotherm and the segments of the straight line having a slope of $1/\gamma$. Let us classify the solutions which may be encountered. First, we have two trivial types: the totally discontinuous solution denoted D and a solution continuous everywhere, denoted C. These two solutions are shown on the Figures 6a and 6b, respectively. The trajectory for the solution D is a straight segment which either starts or ends on the isotherm. The length of the reactor is in this case zero. The trajectory of the solution C lies entirely on the isotherm and may contain a tangency point only at the end. The reactor length corresponding to this solution can be calculated in a straightforward way from Equation 13 :

$$\mu X_C = \left| Z(f(v_t)) - Z(u_b) \right| \qquad (25)$$

Among the solutions with one discontinuity, we may distinguish between three types corresponding to their location which may be bottom, top or middle. We shall denote them B, T and M respectively. Figures 7a-c show some examples of these solutions.
    The solution of the type B starts in the attraction area of the stable part of the isotherm. It consists of a straight segment followed by segment of the isotherm lying on its stable part. The end point of the shock path will be called a drop point and denoted $(u_d, g(u_d))$. The length of the reactor is calculated by applying the design equation to the continuous part:

$$\mu X_B = \left| Z(f(v_t)) - Z(u_d) \right| \qquad (26)$$

with $u_d = u_{b+}$ in this case.
    The solution of type T (Figure 7b) is to some extent a reverse of the solution of type B. It consists of an arc of the unstable part of the isotherm followed by a shock path. The starting point of the shock path will be called a junction point, $(u_j, g(u_j))$, the equation for the reactor length is

$$\mu X_T = \left| Z(u_j) - Z(u_b) \right| \qquad (27)$$

where $u_j = u_{t-}$.
    Type M (Figure 7c) is in some sense a combination of the types B and T. Its structure contains an unstable part, junction point, drop point, and stable part. Of course, the junction point must belong to the attraction area. We may compute the reactor length as follows:
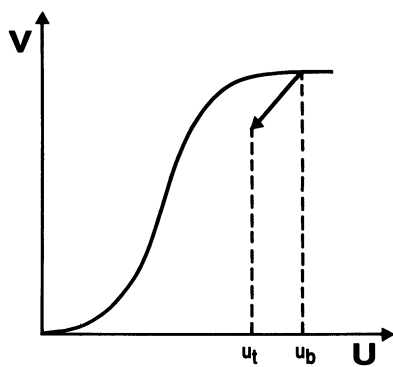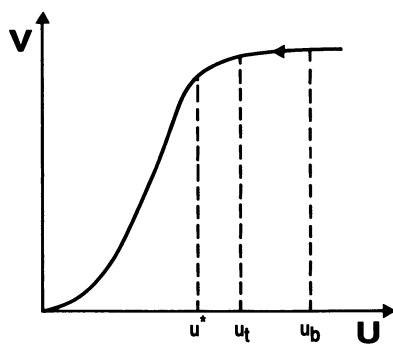
Figure 6. Solution types. Key: a, solution of type D;
b, solution of type C.
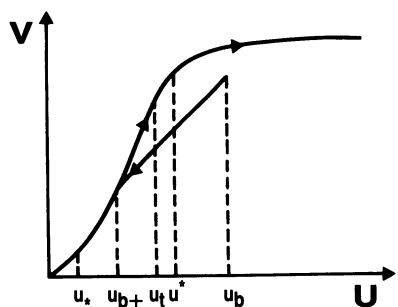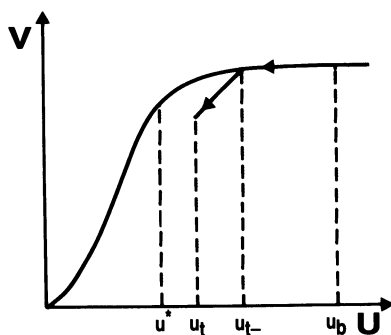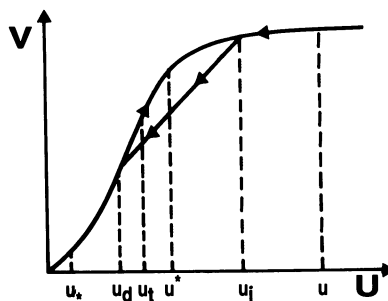
Figure 7. Solutions with one discontinuity. Key: a, type B; b, type T; and c, type M.

$$X_M = X_B + X_T \tag{28}$$

but the equalities $u_d = u_{b+}$ and $u_j = u_{t-}$ are no longer valid.

Let us now look at the solutions with the two discontinuities. Here we may distinguish four types: BT, MT, BM and MM. Some examples are shown on the Figures 8a-d. All of these trajectories involve the transition from stable to the unstable part of the isotherm.

The BT type has the following components. Shock path – drop point – stable part – unstable part – junction point – shock path. Therefore, the only point which can be a junction point is the upper tangency, i.e. $u_{t-} = u^*$ (Figure 8a). The length of the reactor is

$$\mu X_{BT} = \left| Z(u^*) - Z(u_{b+}) \right| \tag{29}$$

The structure of the MT solution combines the structures of the types M and T. The sequence of the components is: unstable part – junction point – drop point – stable part – unstable part – junction point – shock path. This structure contains two junction points u_{j1} and u_{t-}. Some restrictions apply to the locations of these points. The first one must lie in the attraction area of the stable part and the second must be the upper tangency point so that $u_{t-} = u^*$. The equation for the reactor length is

$$\mu X_{MT} = \left| Z(u_{j1}) - Z(u_b) \right| + \left| Z(u_{d1}) - Z(u^*) \right| \tag{30}$$

The solutions of the types BM (Figure 8c) and MM (Figure 8d) do not occur if the isotherm is convex. The reason for that is that convex isotherms do not have lower tangency point which serves as a drop point for both of these types. The reactor length may be calculated for BM type from the following equation

$$\mu X_{BM} = \left| Z(u_{j1}) - Z(u_{b+}) \right| + \left| Z(f(v_t)) - Z(u_{d1}) \right| \tag{31}$$

The solution of the type MM includes three continuous parts. The reactor length is computed by applying the design equation to each of them and adding the results:

$$\mu X_{MM} = \left| Z(u_{j1}) - Z(u_b) \right| + \left| Z(u_{j2}) - Z(u_{d1}) \right| + \left| Z(f(v_t) - Z(u_{d2}) \right| \tag{32}$$

We must also note that $u_{j1} = u^\ell$ for MM type of solutions.

Like BM and MM types, the solutions, with three discontinuities never occur if the isotherm is convex. Only two kinds belonging to this group are possible. They are BMT (Figure 9a) and MMT (Figure 9b). They have very restrictive conditions for their junction and drop points. For BMT solution we must have $u_{b+} = u_*$
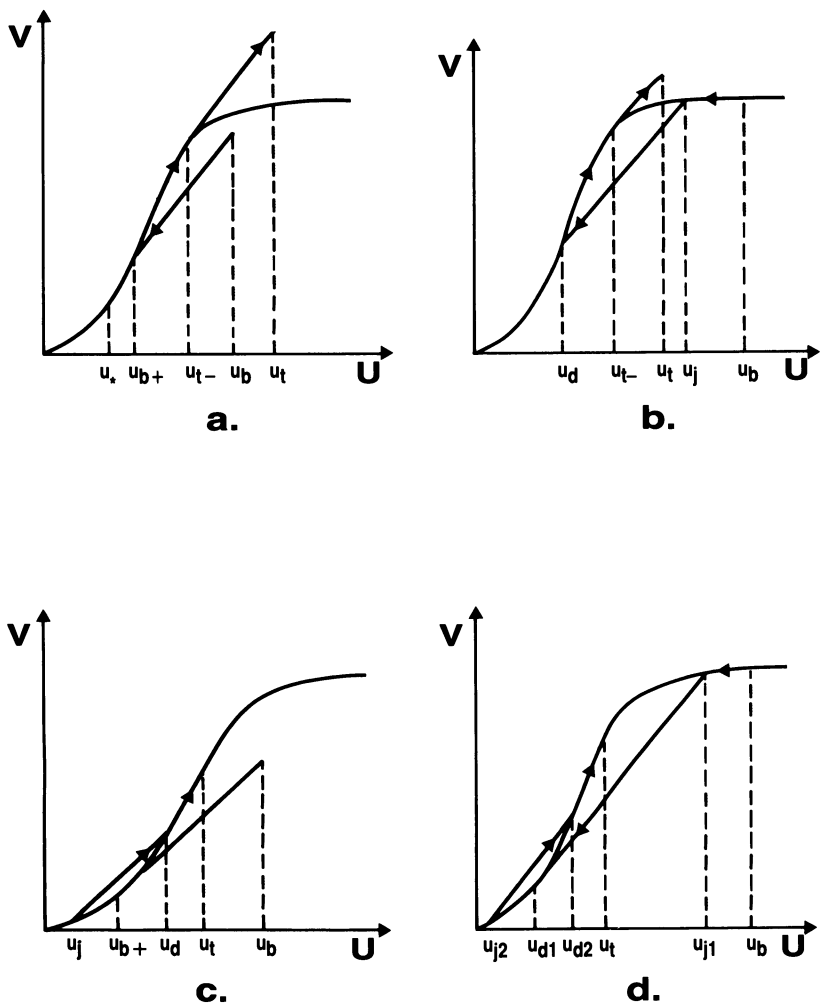
Figure 8. Solutions with two shocks. Key: a, type BT; b, type MT; c, type BM; and d, type MM.
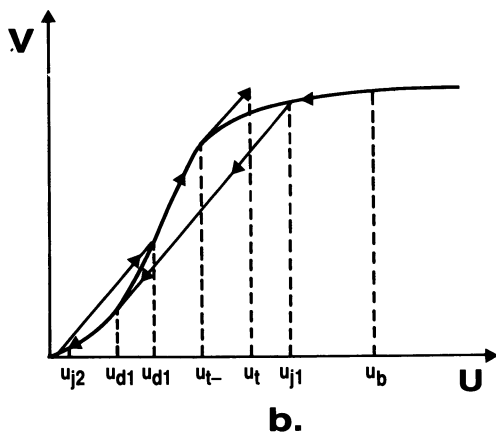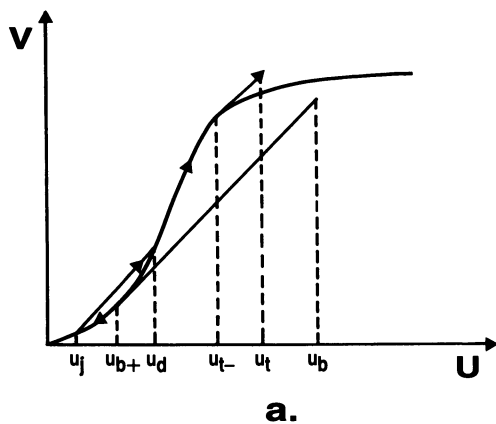
Figure 9. Solutions with three shocks. Key: a, type BMT; and b, type MMT.

and $u_{t-} = u^*$. Likewise, for MMT solution both tangency points
are involved as drop (lower) and junction (upper) points. The
equations for the length of the reactor are analogous to the
previous case. They are:

$$\mu X_{BMT} = |Z(u_{j1}) - Z(u_*)| + |Z(u^*) - Z(u_{d1})| \qquad (33)$$

$$\mu X_{MMT} = |Z(u) - Z(u_b)| + |Z(u_{j2}) - Z(u_*)| + |Z(u^*) - Z(u_{d2})| \qquad (34)$$

The question which has not yet been answered is how the
boundary conditions affect these discontinuous solutions and what
are the conditions for the existence of each of them. In the
following section we shall develop a geometric construction which
will help us in answering this question.

The Input – Output Space

So far in our analysis the boundary conditions (8) and (9) have
not been incorporated. In this section we shall see how they fit
into the topological structure of the phase plane.

The condition $u(0_-) = u_b$ prescribed by Equation 8, here-
after called the input condition states that every phase tra-
jectory starts on a vertical line $u = u_b$. At the same time, the
condition $v(x_+) = v_t$ imposed by Equation 9 which we shall call
the output condition demands that every trajectory ends on a
horizontal line $v = v_t$. Thus we have a point (u_b, v_t) associated
with each solution. The set of all such points constitutes a
structure which we call the input – output space of the reactor.
For the case of convex isotherm, this was done by Viswanathan and
Aris (1).

The position in the input – output space together with the
value of γ determines the available types of the discontinuous
solutions. Which of them actually occurs is uniquely determined
by the length of the reactor.

Let us study the topological structure of the input – output
space. We have already seen that the structure of the phase
plane changes significantly when the parameter γ passes through
$u^*/g(u^*)$. The same should be expected from the input – output
space.

The input – output space for the case when
$1/g'(\tilde{u}) < \gamma < u^*/g(u^*)$ is shown in Figure 10. We may distin-
guish 15 regions according to the types of the discontinuous
behavior encountered. The ranges and/or the locations of the
discontinuities are summarized in Table I. The solutions
corresponding to each region are listed in the order of the
increasing reactor length. The first one is thus always a dis-
continuous solution D (zero reactor length). The last solution
for each region corresponds to infinitely long reactor is
labelled with subscript ∞. It can have any type of the
discontinuity.

Table I. Steady-State Solutions for the Case when $1/g'(\bar{u}) < \gamma < u^*/g(u^*)$

Region	Type	u_{b+}	u_{j1}	u_{d1}	u_{j2}	u_{d2}	u_{t-}
A	D	—	—	—	—	—	—
	T	u_b	—	—	—	—	(u^*,u_b)
	T	u_b	(u^*,u_ℓ)	$J(u_{j1})$	—	—	u^*
	MT	u_b	u_ℓ	u^*	—	—	u^*
	MMT	u_b	u_ℓ	u^*	(u_ℓ,u_*)	$J(u_{j2})$	u^*
	MT	u_b	u_ℓ	u^*	—	—	u_ℓ
	MT	u_b	u_ℓ	u^*	—	—	$(0,u_\ell)$
	MT$_\infty$	u_b	u_ℓ	u^*	—	—	0
B	D	—	—	—	—	—	—
	T	u_b	—	—	—	—	$(f(v_t),u_b)$
	C	u_b	—	—	—	—	$f(v_t)$
	T	u_b	(u^*,u_ℓ)	$J(u_{j1})$	—	—	(u_*,u_b)
	T	u_b	u_ℓ	u^*	—	—	u^*
	MT	u_b	u_ℓ	u^*	—	—	u^*
	MMT	u_b	u_ℓ	u^*	(u_ℓ,u_*)	$J(u_{j2})$	u
	MT	u_b	u_ℓ	u^*	—	—	u_ℓ
	MT	u_b	u_ℓ	u^*	—	—	$(0,u_\ell)$
	MT$_\infty$	u_b	u_ℓ	u^*	—	—	0
C	D	—	—	—	—	—	$(J^i(f(v_t)),u_b)$
	T	u_b	—	—	—	—	$J^i(f(v_t))$
	T	u_b	(u^*,u_ℓ)	$J(u_{j1})$	—	—	$f(v_t)$
	M	u_b	u_ℓ	u^*	—	—	$f(v_t)$
	M	u_b	u_ℓ	u^*	—	—	$f(v_t)$
	MM	u_b	u_ℓ	u^*	$(J_i(f(v_t)),u_*)$	$(u_*,f(v_t))$	$f(v_t)$
	MT	u_b	u_ℓ	u^*	—	—	$J_i(f(v_t))$
	MT	u_b	u_ℓ	u^*	—	—	$J_i(f(v_t))$
	MT$_\infty$	u_b	u_ℓ	u^*	—	—	$(0,J_i(f(v_t)))$
							0

	Type						Boundary
D	D	—	—	—	—	—	—
	T	u_b	—	—	—	—	(u^l, u_b)
	T	u_b	u^l	—	—	—	$(f(v_t), u_*)$
	MT	u_b	u^l	u_*	—	—	$f(v_t)$
	M	u_b	u^l	u_*	—	—	$(0, u_*)$
	MT	u_b	u^l	u_*	—	—	0
	MT_∞	u_b	u^l	u_*	—	—	
E	D	—	—	—	—	—	—
	T	u_b	—	—	—	—	(u_*, u_b)
	T	u_b	(u_*, u_b)	—	—	—	u_*
	MT	$J(u_b)$	—	$J(u_{j1})$	—	—	u_*
	BT	$(u_*, J(u_b))$	—	—	—	—	u_*
	BMT	u_*	—	—	—	—	u_*
	BT	u_*	(u_l, u_*)	$J(u_{j1})$	—	—	u_*
	BT	u_*	—	—	—	—	u_l
	BT	u_*	—	—	—	—	$(0, u_l)$
	BT_∞						0
F	D	—	—	—	—	—	$((fv_t), u_b)$
	T	u_b	—	—	—	—	$f(v_t)$
	C	u_b	(u_*, u_b)	—	—	—	(u_*, u_b)
	T	u_b	—	—	—	—	u_*
	T	u_b	—	$J(u_{j1})$	—	—	u_*
	MT	$J(u_b)$	—	—	—	—	u_*
	BT	$(u_*, J(u_b))$	—	—	—	—	u_*
	BT	u_*	(u_l, u_*)	$J(u_{j1})$	—	—	u_*
	BMT	u_*	—	—	—	—	u_l
	BT	u_*	—	—	—	—	$(0, u_l)$
	BT	u_*					0
	BT_∞						

Table I. Continued

Region	Type	u_{b+}	u_{j1}	u_{d1}	u_{j2}	u_{d2}	u_{t-}
G	D	—	—	—	—	—	$(u_*, J^i(f(v_t)))$
	T	u_b	—	—	—	—	$J^i(f(v_t))$
	T	u_b	$(J^i(f(v_t)), u_b)$	$J(u_{j1})$	—	—	$f(v_t)$
	M	u_b	—	—	—	—	$f(v_t)$
	B	$J(u_b)$	—	—	—	—	$f(v_t)$
	B	$(u_*, J(u_b))$	$(J^i(f(v_t)), u_*)$	$(u_*, f(v_t))$	—	—	$f(v_t)$
	B	u_*	—	—	—	—	$f(v_t)$
	BM	u_*	—	—	—	—	$J^i(f(v_t))$
	BT	u_*	—	—	—	—	$(0, J_i(f(v_t)))$
	BT	u_*	—	—	—	—	0
	BT$_\infty$	u_*	—	—	—	—	
H	D	—	—	—	—	—	—
	B	$(u_*, f(v_t))$	—	—	—	—	$f(v_t)$
	B	u_*	$(u_*(f(v_t)), u_*)$	$(u_*, f(v_t))$	—	—	$f(v_t)$
	BM	u_*	—	—	—	—	$f(v_t)$
	BT	u_*	—	—	—	—	$J_i(f(v_t))$
	BT	u_*	—	—	—	—	$0, J_i(f(v_t))$
	BT$_\infty$	u_*	—	—	—	—	0
I	D	—	—	—	—	—	—
	BT	u_*	—	—	—	—	$(f(v_t), u_*)$
	B	u_*	—	—	—	—	$f(v_t)$
	BT	u_*	—	—	—	—	$(0, u_*)$
	BT	u_*	—	—	—	—	0
J	D	—	—	—	—	—	—
	BT	(u_b, u_*)	—	—	—	—	u_*
	T	u_b	(u_ℓ, u_*)	$J(u_{j1})$	—	—	u_*
	BT	(u_*, u_b)	—	—	—	—	u_*
	BMT	u_*	—	—	—	—	u_*
	BT	u_*	—	—	—	—	u_ℓ
	BT	u_*	—	—	—	—	$(0, u_\ell)$
	BT$_\infty$	u_*	—	—	—	—	0

		(1)	(2)	(3)	(4)	(5)	(6)
K	D	–			–	–	–
	B	$(u_b, f(v_t))$			–	–	$f(v_t)$
	C	u_b			–	–	$f(v_t)$
	B	(u_*, u_b)			–	–	$f(v_t)$
	B	u_*			–	–	$f(v_t)$
	BM	u_*	$(J_i f(v_t), u_*)$	$(u_* f(v_t))$	–	–	$f(v_t)$
	BT	u_*			–	–	$J_i(f(v_t))$
	BT	u_*			–	–	$(0, J_i(f(v_t)))$
	BT$_\infty$	u_*			–	–	0
L	D	–			–	–	–
	BT	(u_*, u^*)			–	–	u^*
	BT	$J(u_b)$	$(J(u_b), u^*)$		–	–	u^*
	MT	u_b			–	–	u^*
	T	u_b			–	–	u_ℓ
	T	u_b			–	–	$(0, u_\ell)$
	T$_\infty$	u_b			–	–	0
M	D	–			–	–	
	B	$(u_*, f(v_t))$			–	–	$f(v_t)$
	B	$J(u_b)$	$(J_i f(v_t), u_b)$	$(u_*, f(v_t))$	–	–	$f(v_t)$
	M	u_b			–	–	$f(v_t)$
	T	u_b			–	–	$J_i(f(v_t))$
	T	u_b			–	–	$(0, J_i(f(v_t)))$
	T$_\infty$	u_b			–	–	0
N	D	–			–	–	–
	T	u_b			–	–	$(0, u_b)$
	T$_\infty$	u_b			–	–	0
O	D	–			–	–	–
	T	u_b			–	–	$(f(v_t), u_b)$
	C	u_b			–	–	$f(v_t)$
	T	u_b			–	–	$(0, u_b)$
	T$_\infty$	u_b			–	–	0

Let us examine the region G with some care. It is suffi-
ciently complex to clarify the method being used. Figure 11
shows the types of the phase trajectories which may occur. First,
we have a trivial discontinuous solution labelled $\underline{1}$. Then we may
have a continuous path followed by a jump (Type T, trajectory $\underline{2}$).
The trajectory $\underline{3}$ is a limiting case of $\underline{2}$ corresponding to the
longest reactor for which we may have a type T behavior. We must
have $u_{t-} = J^1 (f(v_t))$. Longer reactors will have a discontinuity
in the middle (trajectory $\underline{4}$) or in the bottom (trajectories $\underline{6}$, $\underline{7}$).
Trajectory $\underline{5}$ represents the transition between the type M and
type B while $\underline{7}$ is a limiting case of $\underline{6}$ with $u_{b+} = u_*$. The latter
must hold for all the remaining trajectories ($\underline{7}$ - $\underline{10}$). The tra-
jectory $\underline{7}$ is a BM type and $\underline{8}$ is its limiting case with a drop
point at $u = J_i(f(v_t))$ belonging to the type BT. The trajectories
$\underline{9}$ and $\underline{10}$ are also of type BT with $\underline{10}$ being the limiting case
corresponding to the infinitely long reactor with $u_{t-} = 0$.

The input - output space when $u^*/g(u^*) < \gamma < 1/g'(0)$ is
shown in Figure 12. We can notice at the first sight that it is
more complicated. Instead of 15 regions like in the previous
case, we now have 30. If we look at the Table II summarizing the
solutions we see greater variety in behavior.

Let us again examine in detail the region G. The possible
phase trajectories are displayed in Figure 13. Like in the
previous case, we may have a trivial solution D labelled $\underline{1}$. Tra-
jectories $\underline{2}$ - $\underline{4}$ have a continuous part from $u = u_{t-}$ followed by
downward ($\underline{2}$) or upward ($\underline{4}$) discontinuity. Trajectory $\underline{3}$ just
happens to be continuous because $u_{t-} = f(v_t)$. The limiting case
for this type is the trajectory $\underline{5}$ with $u_{t-} = u^*$ corresponding to
the longest reactor for which the solutions of type T can exist.
Longer reactors must have an internal discontinuity (trajectory $\underline{6}$)
or bottom discontinuity (trajectory $\underline{7}$). The trajectory $\underline{8}$ is a
limiting case of $\underline{7}$ having $u = u_*$ as a drop point. The latter
must also be true for the trajectory $\underline{9}$ which belongs to the type
BMT and its limiting case ($\underline{10}$) corresponding to an infinitely long
reactor.

Concluding Remarks

It is very common in the reaction engineering calculations to
assume the continuity of all the functions involved. Problems
arising in the design of the moving bed catalytic reactor show
that this assumption is not always valid. Therefore, the direct
application of the Equation 13 may result in confusion. For
some concentrations of the reactant it will give two values for
the reactor length, yet for some others it will fail to give any
result at all. In order to avoid this, the designer must first
examine the input - output space for the given operating condi-
tions then locate the discontinuities and only after that apply
Equation 13 to the continuous parts.
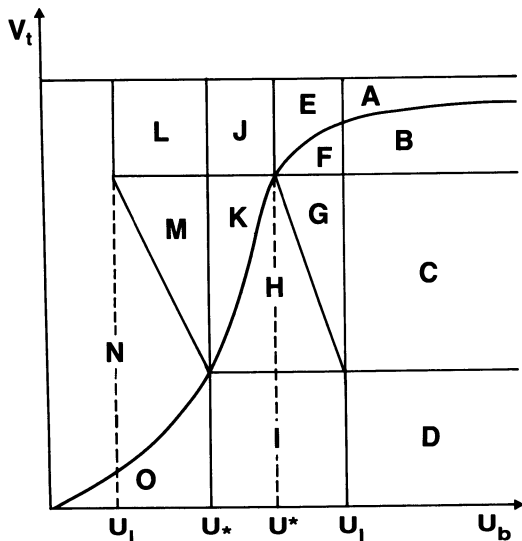
Figure 10. Input-output space for $1/g'(\tilde{u}) < \gamma \, u^*/g(u^*)$.
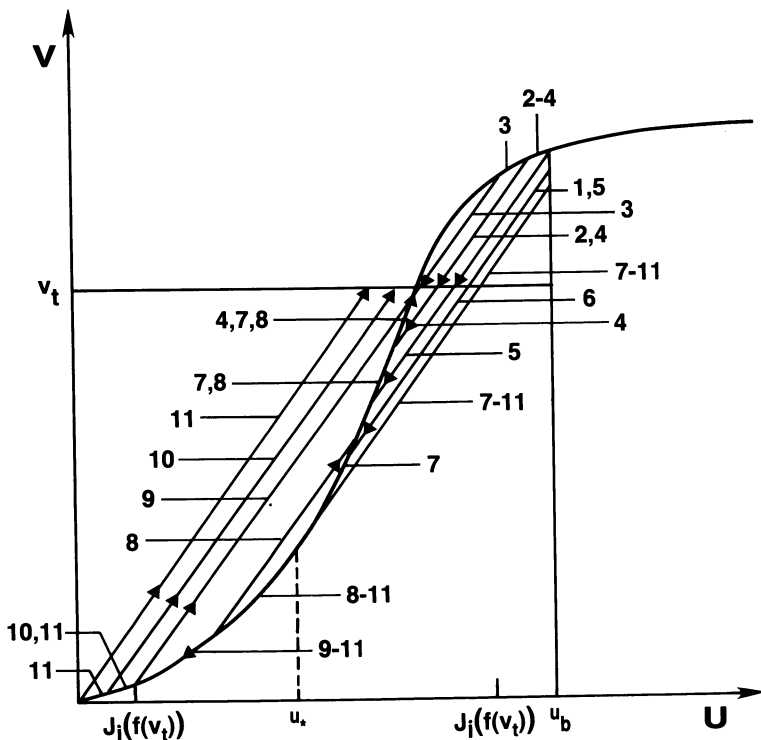
Figure 11. Trajectories for region G (see Figure 10).

Table II. Steady-State Solutions for the Case when $u^*/g(u^*) < \gamma < 1/g'(0)$

Region	Type	u_{b+}	u_{j1}	u_{d1}	u_{j2}	u_{d2}	u_{t-}
A	D	—	—	—	—	—	—
A	T	u_b	(u^*, u_ℓ)	—	—	—	(u^*, u_b)
A	T	u_b	u_ℓ	—	—	—	u^*
A	MT	u_b	u_ℓ	$J(u_{j1})$	—	—	u^*
A	MT	u_b	u_ℓ	u^*	—	—	u^*
A	MMT	u_b	u_ℓ	u^*	$(0, u^*)$	$J(u_{j2})$	u^*
A	MMT$_\infty$	u_b	u	u^*	0	u_ℓ	u^*
B	D	—	—	—	—	—	—
B	T	u_b	—	—	—	—	$f(v_t)$
B	C	u_b	—	—	—	—	$f(v_t)$
B	T	u_b	(u^*, u_ℓ)	—	—	—	(u^*, u_b)
B	T	u_b	u_ℓ	—	—	—	u^*
B	MT	u_b	u_ℓ	$J(u_{j1})$	—	—	u^*
B	MT	u_b	u_ℓ	u^*	—	—	u^*
B	MMT	u_b	u_ℓ	u^*	$(0, u^*)$	$J(u_{j2})$	u^*
B	MMT$_\infty$	u_b	u	u^*	0	u_ℓ	u^*
C	D	—	—	—	—	—	—
C	T	u_b	—	—	—	—	$(J^i(f(v_t)), u_b)$
C	T	u_b	—	—	—	—	$J^i(f(v_t))$
C	M	u_b	$(J^i(f(v_t)), u_\ell)$	$(u^*, f(v_t))$	—	—	$f(v_t)$
C	M	u_b	u_ℓ	u^*	—	—	$f(v_t)$
C	MM	u_b	u_ℓ	u^*	$(0, u^*)$	$J(u_{j2})$	$f(v_t)$
C	MM$_\infty$	u_b	u_ℓ	u^*	0	u_ℓ	$f(v_t)$
D	D	—	—	—	—	—	—
D	T	u_b	—	—	—	—	$(J^i(f(v_t)), u_b)$
D	T	u_b	—	—	—	—	$J^i(f(v_t))$
D	M	u_b	$(J^i(f(v_{t\ell})), u_\ell)$	$(u^*, f(v_t))$	—	—	$f(v_t)$
D	M	u_b	u_ℓ	u^*	—	—	$f(v_t)$
D	MM	u_b	u_ℓ	u^*	—	—	$f(v_t)$
D	MT	u_b	u_ℓ	u^*	$(J_i(f(v_t)), u^*)$	$(u^*, f(v_t))$	$J_i(f(v_t))$
D	MT	u_b	u_ℓ	u^*	—	—	$(0, J_i(f(v_t)))$
D	MT$_\infty$	u_b	u	u^*	—	—	0

E						
D	—	—	—	—	—	—
T	u_b	—	—	—	—	(u_ℓ, u_b)
T	u_b	—	—	—	—	u_ℓ
MT	u_b	u_ℓ	$u*$	—	—	$(f(v_t), u*)$
M	u_b	u_ℓ	$u*$	—	—	$f(v_t)$
MT	u_b	u_ℓ	$u*$	—	—	$(0, u*)$
MT$_\infty$	u_b	u_ℓ	$u*$	—	—	0
F						
D	—	—	—	—	—	—
T	u_b	—	—	—	—	$(u*, u_b)$
T	u_b	—	—	—	—	$u*$
MT	u_b	$(u*, u_b)$	$J(u_j1)$	—	—	$u*$
BT	$J(u_b)$	—	—	—	—	$u*$
BT	$(u*, J(u_b))$	—	—	—	—	$u*$
BMT	$u*$	$(0, u*)$	$J(u_j1)$	—	—	$u*$
BMT$_\infty$	$u*$	0	u_ℓ	—	—	$u*$
G						
D	—	—	—	—	—	—
T	u_b	—	—	—	—	$(f(v_t), u_b)$
C	u_b	—	—	—	—	$f(v_t)$
T	u_b	—	—	—	—	$(u*, u_b)$
T	u_b	—	—	—	—	$u*$
MT	u_b	$(u*, u_b)$	$J(u_j1)$	—	—	$u*$
BT	$J(u_b)$	—	—	—	—	$u*$
BT	$(u*, J(u_b))$	—	—	—	—	$u*$
BT	$u*$	—	—	—	—	$u*$
BMT	$u*$	$(0, u*)$	$J(u_j1)$	—	—	$u*$
BMT$_\infty$	$u*$	0	u_ℓ	—	—	$u*$

Table II. Continued

Region	Type	u_{b+}	u_{j1}	u_{d1}	u_{j2}	u_{d2}	u_{t-}
H	D	—	—	—	—	—	—
	T	u_b	—	—	—	—	$(J^i(f(v_t)), u_b)$
	T	u_b	—	—	—	—	$J^i(f(v_t))$
	M	u_b	—	—	—	—	$f(v_t)$
	B	$J(u_b)$	$(J^i(f(v_t)), u_b)$	$(J(u_b), f(v_t))$	—	—	$f(v_t)$
	B	$(u_*, J(u_b))$	—	—	—	—	$f(v_t)$
	BM	u_*	$(0, u_*)$	$J(u_{j1})$	—	—	$f(v_t)$
	BM$_\infty$	u_*	0	u_*	—	—	$f(v_t)$
I	D	—	—	—	—	—	—
	T	u_b	—	—	—	—	$(J^i(f(v_t)), u_b)$
	T	u_b	—	—	—	—	$J^i(f(v_t))$
	M	u_b	—	—	—	—	$f(v_t)$
	B	$J(u_b)$	$(J_i(f(v_t)), u_b)$	$(J(u_b), f(v_t))$	—	—	$f(v_t)$
	B	$(u_*, J(u_b))$	—	—	—	—	$f(v_t)$
	B	u_*	$(J_i(f(v_t)), u_*)$	$(u_*, f(v_t))$	—	—	$f(v_t)$
	BM	u_*	—	—	—	—	$f(v_t)$
	BT	u_*	—	—	—	—	$J_i(f(v_t))$
	BT	u_*	—	—	—	—	$(0, J_i(f(v_t)))$
	BT	u_*	—	—	—	—	0
J	D	—	—	—	—	—	—
	B	$(u_*, f(v_t))$	—	—	—	—	$f(v_t)$
	B	u_*	—	—	—	—	$f(v_t)$
	BM	u_*	$(0, u_*)$	$(0, u_{j1})$	—	—	$f(v_t)$
	BM$_\infty$	u_*	0	u_ℓ	—	—	$f(v_t)$
K	D	—	—	—	—	—	—
	B	$(u_*, f(v_t))$	—	—	—	—	$f(v_t)$
	B	u_*	—	—	—	—	$f(v_t)$
	BM	u_*	—	—	—	—	$f(v_t)$
	BT	u_*	$(J_i(f(v_t)), u_*)$	$(u_*, f(v_t))$	—	—	$J_i(f(v_t))$
	BT	u_*	—	—	—	—	$(0, J_i(f(v_t)))$
	BT$_\infty$	u_*	—	—	—	—	0

L	D	—	—	—	—	—	—
	BT	u_*	—	—	—	—	$(f(v_t), u_*)$
	B	u_*	—	—	—	—	$f(v_t)$
	BT	u_*	—	—	—	—	$(0, u_*)$
	BT$_\infty$	u_*	—	—	—	—	0
M	D	—	—	—	—	—	$—^*$
	BT	(u_b, u^*)	$(0, u_*)$	—	—	—	u^*
	T	u_b	0	—	—	—	u^*
	BT	(u_*, u_b)	—	$J(u_{j1})$	—	—	u^*
	BT	u_*	—	u_ℓ	—	—	u^*
	BMT	u_*	—	—	—	—	u^*
	BMT$_\infty$	u_*	—	—	—	—	u
N	D	—	—	—	—	—	—
	B	(u_b, u^*)	$(0, u_*)$	—	—	—	$f(v_t)$
	C	u_b	0	—	—	—	$f(v_t)$
	B	(u_*, u_b)	—	$J(u_{j1})$	—	—	$f(v_t)$
	B	u_*	—	u_ℓ	—	—	$f(v_t)$
	BM	u_*	—	—	—	—	$f(v_t)$
	BM$_\infty$	u_*	—	—	—	—	$f(v_t)$
O	D	—	—	—	—	—	—
	B	(u_b, u^*)	$(J_i(f(v_t)), u_*)$	$(u_*, f(v_t))$	—	—	$f(v_t)$
	C	u_b	—	—	—	—	$f(v_t)$
	B	(u_*, u_b)	—	—	—	—	$f(v_t)$
	BM	u_*	—	—	—	—	$f(v_t)$
	BT	u_*	—	—	—	—	$J_i^{-1}(f(v_t))$
	BT	u_*	—	—	—	—	$(0, J_i(f(v_t)))$
	BT$_\infty$	u_*	—	—	—	—	0
P	D	—	—	—	—	—	$—^*$
	BT	$(J(u_b), u^*)$	$(0, u_b)$	$(J(u_b), u_\ell)$	—	—	u^*
	BT	$J(u_b)$	0	u_ℓ	—	—	u^*
	MT	u_b	—	—	—	—	u^*
	MT$_\infty$	u_b	—	—	—	—	u

Table II. Continued

Region	Type	u_{b+}	u_{j1}	u_{d1}	u_{j2}	u_{d2}	u_{t-}
Q	D	$-$	$-$	$-$	$-$	$-$	$-$
	B	$(J(u_b),f(v_t))$	$-$	$-$	$-$	$-$	$f(v_t)$
	B	$J(u_b)$	$-$	$-$	$-$	$-$	$f(v_t)$
	M	u_b	$(0,u_b)$	$(J(u_b),u_\ell)$	$-$	$-$	$f(v_t)$
	M_∞	u_b	0	u_b	$-$	$-$	$f(v_t)$
R	D	$-$	$-$	$-$	$-$	$-$	$-$
	B	$(J(u_b),f(v_t))$	$-$	$-$	$-$	$-$	$f(v_t)$
	B	$J(u_b)$	$-$	$-$	$-$	$-$	$f(v_t)$
	M	u_b	$(J_i(f(v_t)),u_b)$	$(J(u_b),u_\ell)$	$-$	$-$	$f(v_t)$
	T	u_b	$-$	$-$	$-$	$-$	$J_i(f(v_t))$
	T	u_b	$-$	$-$	$-$	$-$	$(0,J_i(f(v_t)))$
	T	u_b	$-$	$-$	$-$	$-$	0
S	D	$-$	$-$	$-$	$-$	$-$	$-$
	T	u_b	$-$	$-$	$-$	$-$	$(0,u_b)$
	T_∞	u_b	$-$	$-$	$-$	$-$	0
T	D	$-$	$-$	$-$	$-$	$-$	$-$
	T	u_b	$-$	$-$	$-$	$-$	$(f(v_t),u_b)$
	C	u_b	$-$	$-$	$-$	$-$	$f(v_t)$
	T	u_b	$-$	$-$	$-$	$-$	$(0,u_b)$
	T_∞	u_b	$-$	$-$	$-$	$-$	0

Figure 12. Input-output space for u*/g(u*) < γ < 1/g'(0).
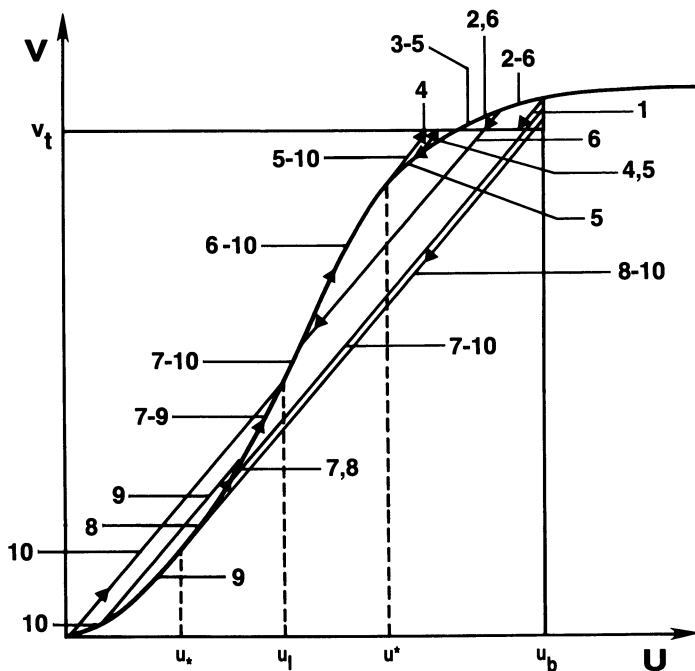
Figure 13. Trajectories for region G (see Figure 12).

If the reactor operates close to, but not quite at adsorption equilibrium, or if small diffusion effects are present, then instead of the discontinuities we may expect very rapid changes of concentration. This can still be a problem for numerical calculations and the study of the discontinuities in the ideal model can still be very useful.

Moving-bed reactors are probably not the only systems in which the discontinuous behavior can occur. The techniques developed in this paper can also be applied to other such systems,

Acknowledgment

Legend of Symbols

c	Concentration in the fluid phase
$F(v)$	Dimensionless reaction rate expression
$f(v)$	Dimensionless expression for adsorption isotherm
$G(u)$	Dimensionless reaction rate expression
$g(u)$	Dimensionless expression for adsorption isotherm
$J(u)$	Jump function defined in the text
$J^i(u)$	Upper inverse of the jump function
$J_i(u)$	Lower inverse of the jump function
k	Coefficient in Equation 5
L	Length of the reactor
n	Concentration in the solid phase
$R(n_a)$	Reaction rate expression
$r(u, v)$	Dimensionless adsorption rate expression
U	Interstitial fluid velocity
u	Dimensionless concentration of A in the fluid phase
$\tilde{u}$	Dimensionless concentration of A at the isotherm inflection point
V	Solid phase velocity
v	Dimensionless concentration of A in the solid phase
X	Dimensionless reactor length
x	Dimensionless distance
$Z(u)$	Function defined by the Equation 21
z	Distance

Greek Letters

γ	$\mu(1 - \varepsilon)V/\varepsilon U$
ε	Void fraction of the fluid
γ	Parameter in Equation 7
μ	n_A^o/c_A^o

Subscripts

A, B	Chemical species
b	Fluid phase entrance
ℓ	Lower limitation point
t	Entrance of the solid phase
1, 2	Left- and right-hand sides of the shock
o	Initial value or reference point
*	Lower tangency point
+, -	Sides

Superscripts

ℓ	Upper limitation points
o	Reference concentration
$'$	Derivative
*	Upper tangency point

Literature Cited

1. Viswanathan, S. and R. Aris, "An Analysis of the Counter-current Moving Bed Reactor," SIAM-AMS Proceedings, v. 8, pp. 99-124 (1974).
2. Altshuller, D., "Design Equations and Transient Behavior of the Countercurrent Moving-Bed Chromatographic Reactor," Chem. Eng. Commun., v. 19, pp. 3630375 (183).
3. Smirnov, V., A Course in Higher Mathematics, v. 1, Pergamon Press, 1964.
4. Cronin, J., Differential Equations. Introduction and Qualitative Theory, Marcel Dekker, Inc., New York, N. Y., 1980.
5. Sircar, S.; R. Gupta AIChE J, 27, No. 4, pp. 806-812 (1981).
6. Brunauer, S. Adsorption of Gases and Vapors, v. 1, Princeton University Press, Princeton, N. J., 1945.
7. Adamson, A. W., Physical Chemistry of Surfaces, 3rd ed., Wiley, 1976.

Optimization in Tubular Reactor Systems

E. B. NAUMAN and RAMESH MALLIKARJUN

Department of Chemical Engineering and Environmental Engineering, Rensselaer Polytechnic Institute, Troy, NY 12181

Tubular reactors often have large velocity or temperature gradients in the radial direction. These give rise to a broad distribution of thermal times which in turn leads to non-uniformities in product composition, at least in laminar flow systems with modest molecular diffusivities. In this paper, the focus is on reaction systems where, along with a specified average yield, one is interested in obtaining a uniform product across the reactor outlet. Functional optimization of the wall temperature represents one means of approaching this goal. Initially, a simplified parallel plate system was investigated. Preliminary results on the wall temperature optimization of tubular polymerizers are also presented.

In designing tubular reactors, one aims at progressive flow with little or no internal recycle and at a uniform distribution of residence times or thermal times. In actual realization, however, this design goal is sometimes difficult to achieve. Often, different fluid elements will experience substantially different reactor environments. The problem is especially acute in polymerization systems which are characterized by large radial gradients in composition and viscosity that lead to elongated velocity profiles and potential flow instabilities (1). Further, large radial gradients in temperatures may occur and can develop into thermal runaways with the reaction suddenly going to completion at very high temperatures. The radial gradients in velocity and temperature will lead to a radial distribution in conversion and in average molecular weights. Good product quality requires control over these distributions. The present paper explores the feasibility of minimizing radial com-

position distributions and of achieving required product proper-
ties through steady-state control of reactor wall temperatures.

Most of the work in reactor optimization concerns maxi-
mizing yield in catalytic reactors (2-6) and tube-wall reactors
(7). For consecutive reactions in riser reactors, Robertson and
Pratt (8) concluded that the imposition of an optimal isothermal
temperature profile gave as good a yield as that obtained by
having wall temperatures varying along the reactor length. The
present work falls in the category of optimization involving
distributed parameter systems that are mathematically described
by partial differential equations. Butkovskiy (9) discusses a
number of cases where the system equations are distributed in
space and time. In his review on recent applications to distri-
buted parameter control theory, Ray (10) briefly touches upon
reactor engineering applications.

Except for the cases where the optimal temperature profile
is of the 'bang-bang' type, analytical solutions for axially
varying optimal profiles are almost impossible. Denn et. al.
(11) used a variational approach for a wide class of distributed
parameter systems where the optimizing decisions may enter into
the state equations or boundary conditions. When intermediate
control is involved, one can only obtain numerical approxima-
tions to the optimal solution.

In this paper, the problem of product non-uniformity is
placed in perspective as we consider the simple case of flow
between parallel plates with a flat velocity profile accompanied
by a first order reaction. The system equations involved are
non-dimensionalized and four parameters identified. A systema-
tic attempt is made to explore a host of constrained and
unconstrained wall temperature profiles that alleviate the
problem of product non-uniformity at the reactor outlet. Work
is already underway to study similar problems in complex poly-
merization systems, and some preliminary results are reported
here.

Problem statement

Consider the parallel-plate reactor system shown in Figure 1.
It is assumed that the system is operating under
1. Flat velocity profile,
2. First order reaction,
3. No heat of reaction
4. Conductivity of the reactor wall is extremely high compared
   to that of the reactor fluid.
This comparitively simple problem represents a starting point
for functional optimization and exhibits similar qualitative
behavior to the more complex systems to be considered later.

After non-dimensionalizing the system equations with
respect to inlet conditions and reactor geometry, the mathemati-
cal model for the system becomes

$$\frac{\partial C}{\partial z} = -[k_o \bar{t}] \, C \, \exp\left[-E\left(\frac{1}{T}-1\right)\right] \tag{1}$$

$$\frac{\partial T}{\partial z} = \left[\frac{\alpha \bar{t}}{R^2}\right] \frac{\partial^2 T}{\partial x^2} \tag{2}$$

where $\bar{t}$ is the mean residence time and $k_o \bar{t}$ is the Damkohler number. The boundary conditions are

$$C(x,0) = 1 \quad , \qquad T(x,0) = 1 \tag{3}$$

$$\frac{\partial T}{\partial x}(0,z) = 0 \quad , \qquad T(1,z) = T_w(z) \tag{4}$$

where $T_w(z)$ is the prescribed wall temperature and is the only means of control in the system. The optimization problem concerns the prescription of an optimal wall temperature that minimizes the variation at the reactor outlet from the desired concentration, C_d, in a mean square sense. Thus, the objective functional becomes

$$J[T_w(z)] = \text{Min} \left\{ \int_o^1 [C(x,1)-C_d]^2 \, dx \right\} \tag{5}$$

An additional equality constraint may be imposed so that the average outlet concentration exactly equals the desired concentration.

$$K[T_w(z)] = \int_o^1 [C(x,1)-C_d] \, dx = 0 \tag{6}$$

When Equation 5 is used alone the functional optimization will be called a 'free case' and when Equations 5 and 6 are used the optimization will be a 'constrained case'.
In this paper, we consider three types of optimization problems:
1.   Constrained optimization in a two-zone reactor where the wall temperature is prescribed as two constant temperature regions, the zone lengths being equal.
2.   Free optimization in a two-zone reactor.
3.   Constrained optimization with continuously varying wall temperatures.
If the set of admissible controls is bounded, closed and convex, then it follows (12) that a unique minimizing optimal profile $T_w(z)$ always exists. Denn et. al. (11) employed the variational approach in determining the necessary and sufficient conditions for an optimal solution. An iterative scheme for approximating the optimal profile was then developed based on the solution of the system equations in the forward direction

and the solution of a set of adjoint equations in the backward direction. In this paper, however, a function fitting approach has been employed for approximating continuous optimal profiles.

Given the set of system Equations 1 through 6, it is imperative to develop the smallest set of independent parameters that fully describe the system. With an aim of imparting physical meaning to these parameters, the following groups were developed.

1. P_1 is the desired average conversion, $1-C_d$.
2. P_2 is the conversion obtained when $T_w = T_0 = T_{inlet}$.
3. P_3 represents the fractional approach of the average temperature at the reactor exit to a uniform wall temperature
4. P_4 is a dimensionless activation energy.

Mathematical definitions of the various parameters and of the temperature groups used in this study are given in Tables I and II.

Since P_1, P_2, P_3 have a theoretical range of 0 to 1 and P_4 has a practical range of 10 to 50, it becomes easy to vary these parameters in order to study the entire range of allowable optimal temperature profiles.

Results for simplified problem

The two-zone reactor has wall temperatures of the 'bang-bang' type where

$$T_w(z) = \begin{cases} T_1 & , \quad 0 \leqslant z \leqslant 0.50 \quad , \quad \text{zone 1} \\ T_2 & , \quad 0.50 < z \leqslant 1.00 \quad , \quad \text{zone 2} \end{cases} \tag{7}$$

as shown in Figure 2.

The objective functionals become functions of the parameters T_1 and T_2:

$$J_2(T_1,T_2) = \text{Min}\left\{ \int_o^1 [C(x,1)-C_d] \, dx \right\} \tag{8}$$

subject to

$$K_2(T_1,T_2) = \int_o^1 [C(x,1)-C_d] \, dx = 0 \tag{9}$$

Equations 1 through 4 were solved by finite difference methods for all the cases. For the constrained case, the numerical procedure consisted of first determining T_{avg} by a root-finding method: $K_2(T_{avg}, T_{avg}) = 0$. Then for fixed values of T_1 near T_{avg}, T_2 was determined by solving $K_2(T_1, T_2) = 0$. The set of (T_1, T_2) feasible points was then fitted with a cubic spline and the minimum found by differentiation.

For the case of free minimization without the equality constraint, the problem can be written in terms of equation 8
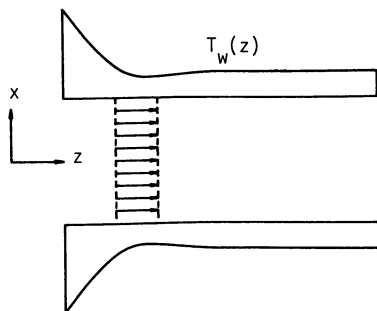
Figure 1.   Parallel Plate System.
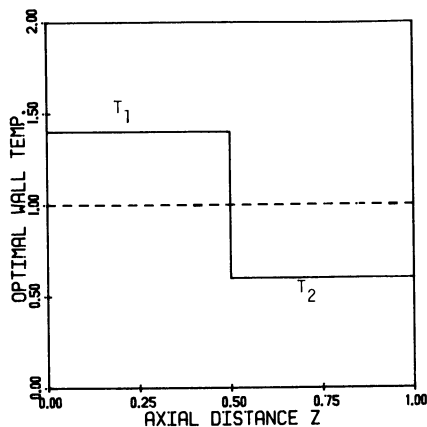
Figure 2.   Typical two-zone wall temperature profile normalized by T_{in}.

Table I. Parameter Definitions

Parameter	Equivalent Equation	Range
P1	$[1.0 - C_d]$	$[0,1]$
P2	$[1.0 - e^{-k_o \bar{t}}]$	$[0,1]$
P3	$\dfrac{\bar{T}_L - T_o}{T_u - T_o} = f\,\dfrac{(\alpha \bar{t})}{R^2}$	$[0,1]$
P4	$[\dfrac{\Delta E}{RT_s}]$	$[10,50]$

Table II. Temperature Definitions

TEMP.	DEFINITION
T_o	Inlet temp., also called T_{inlet}
T_s	Represents that temp. $(T_o = T_{wall} = T_s)$ at which 50% conversion is obtained
T_{avg}	Represents that constant wall temp. $(T_{wall} = T_{avg})$ at which desired conversion is obtained, for a given T_o
T_{unif} or T_u	Is that temp. $(T_o = T_{wall} = T_{unif})$ at which desired conversion is obtained.
T_1, T_2	Are the constant zone temp. in zone 1 & 2 respectively of a two-zone reactor

alone and a two-parameter unconstrained optimization was carried out using a NAG (Numerical Algorithms Group, U.K.) routine that employs a quasi-newton method.

The optimal zone temperatures, T_1 and T_2, were calculated for various values of P_1 and P_2 in the range 0 to 1 while P_3 and P_4 were fixed at physically plausible values of 0.63 and 16.0 respectively. Our primary aim was to determine how the objective function and optimal temperatures varied as a function of the inlet temperature and desired outlet conversion. Figures 3 and 4 present plots of the optimal temperature in the first zone normalized by the inlet temperature and T_{avg} respectively, as a function of desired conversion P_1. The results are not unexpected and show increasing first zone temperatures for higher desired conversions with second zone temperatures changing appropriately to maintain the average conversion. This variation in the zone temperatures is clearly seen in Figure 5 as both P_1 and P_2 are varied. At about $P_1 = 0.75$, a shift is seen in the movement of T_2 with changing T_1.

Figures 6 and 7 present values of the objective functional for various desired concentrations in the constrained and free cases respectively. The most dramatic variation in both cases is the drop in objective functional values as the inlet temperature is increased. The constrained objective values are always higher than that for the free case as expected. The highest possible values for the objective functional are shown for the free case in Figure 7 as the envelope around the curves. This envelope is given by

$$J_{worst} = \begin{cases} P_1^2 & , \ P_1 \leqslant 0.50 \\ (1-P_1)^2 & , \ P_1 \geqslant 0.50 \end{cases} \tag{10}$$

For the case of continuous wall temperature profiles, a function fitting approach was used. Although there are no end conditions on $T_w(z)$ to be satisfied, for all the cases considered in this paper $T_w(z)$ is expected to be high near the entrance to the reactor and lower near the exit. Thus, with a decreasing optimal wall temperature sequence in mind, a Laguerre expansion (with exponential weighting) of the wall temperature was chosen. The expansion can be represented as

$$T_w(z) = \sum_{i=1}^{N} a_i L_i^*(z) \tag{11}$$

where a_i are the coefficients of the expansion and $L_i^*(z)$ are the weighted Laguerre polynomials with
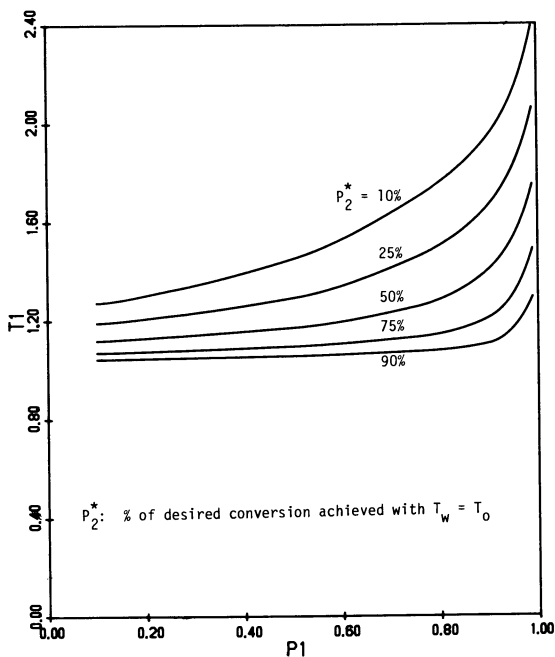
Figure 3.   Effect of desired conversion on the optimal first zone wall temperature (normalized by T_{in}).
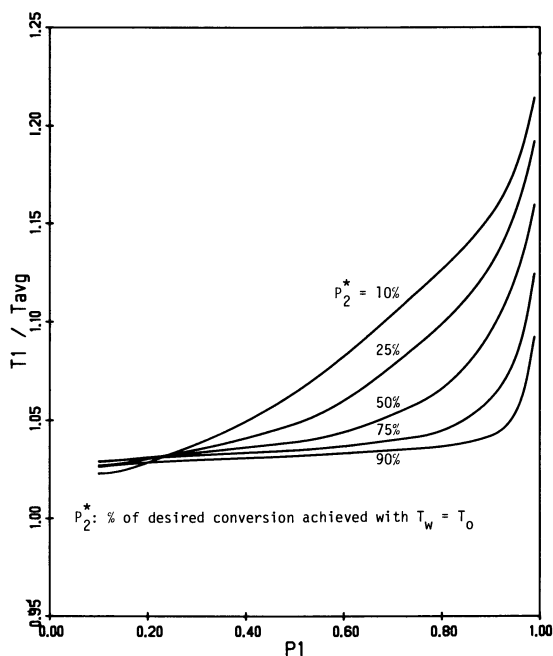
Figure 4.   Effect of desired conversion on the optimal first zone wall temperature (normalized by T_{avg}).
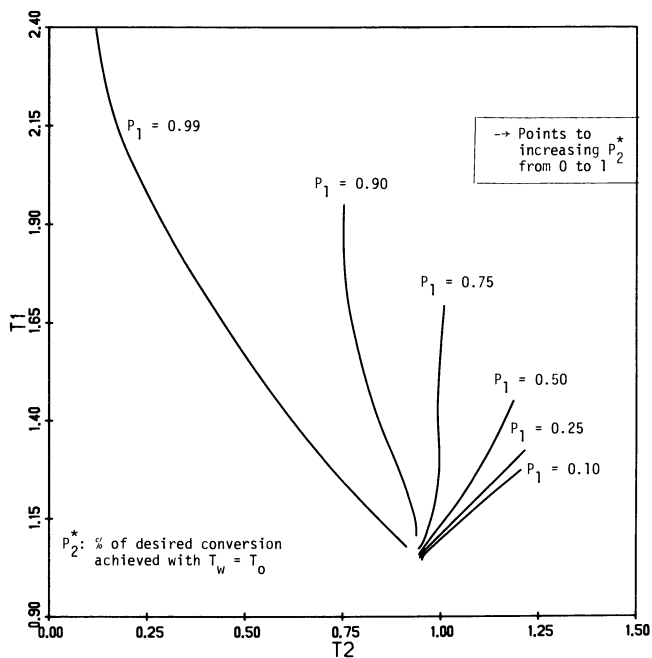
Figure 5. Variation of the optimal first and second zone wall temperatures along lines of constant desired conversion.
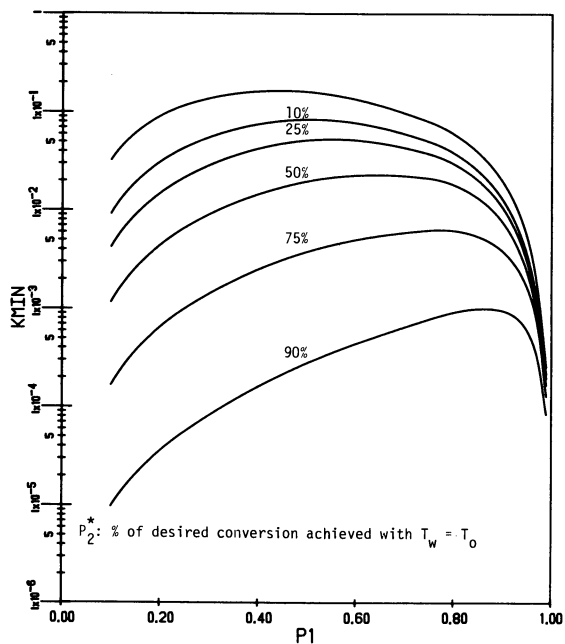
Figure 6.   Variation of the objective functional with desired conversion for the two-zone constrained case.
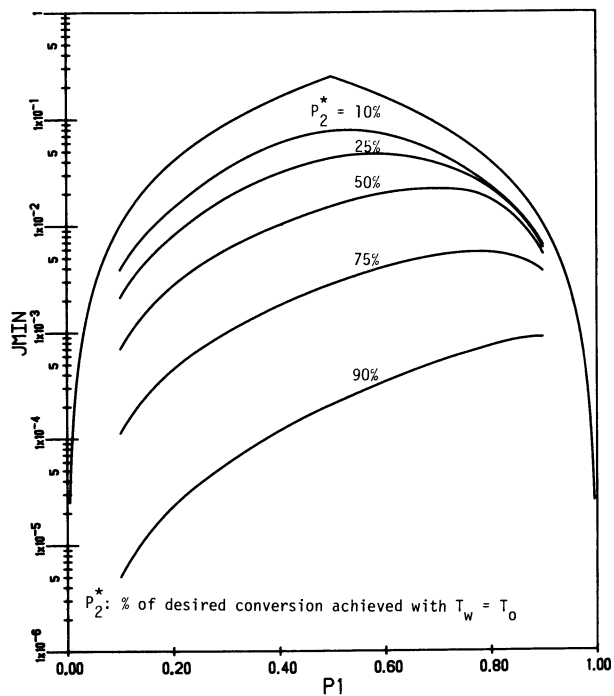
Figure 7. Variation of the objective functional with desired conversion for the two-zone free case.

$$L_i^*(z) = L_i(\omega z) \, e^{-\omega z/2} \qquad\qquad (12)$$

Here $L_i(\omega z)$ are the unweighted Laguerre polynomials and ω is a scaling factor. These polynomials are orthogonal over the semi-infinite interval $(0,\infty)$ with respect to the exponential weighting function. In our case, however, z has a range of $(0,1)$ and this range is expanded by ω to values large enough to be practically infinity. A range of ω values from 10 to 30 was tried and the best value of ω was obtained through interpolation. With the optimization scheme presently employed, it has not been possible to directly include ω along with the coefficients a_i. Thus the problem of obtaining the best value of ω automatically has not yet been resolved. Instead of directly fitting the approximation to $T_w(z)$ which has a range of $[0,\infty)$ it is fitted to a function g(T) with a range of $(-\infty,\infty)$ where g(T) maps $T(0,\infty)$ onto $(-\infty,\infty)$ and is given by

$$g(T) = \left[\frac{T^2 - T_u^2}{T} \right] \qquad\qquad (13)$$

The optimization was carried out for a fixed ω and for N=4 using a constrained NAG routine employing a sequential augmented Lagrangian method, the minimization sub-problems involved being solved by a quasi-newton method. Convergence of the approximate profile to the optimum was checked by running a number of cases with N=2,3,4,5. It was found that the optimal profile remained the same and the coefficients did not change for N > 3. Thus convergence to the optimal profile is assured with N=4. The optimization gives us the four best coefficients a_i, i=1,4 such that the optimal temperature is closely approximated. The resulting optimal wall temperature profile is shown in Figure 8 for one set of parameters. This method is computationally efficient, and CPU times of about 1-2 min depending on the initial guess coefficients are typical of the IBM 3033. A more detailed study into obtaining approximate continuous wall temperature profiles is underway. The goal is to include the determination of the best ω in the optimization routine as well as the determination of the a_i.

A comparison between the two equal-zone, variable-zone and the continuous profile cases is presented in Table III for one set of parameters. It is noted that the objective function value registers only a marginal improvement as we do from the equal-zone case to the continuous profile case. Figure 9 shows this feature by graphing the exit conversion profiles for various cases. Although a more in-depth comparison is necessary, it seems apparent that a 'bang-bang' type profile does the job almost as well as that using a continuous profile and is simpler to work with theoretically and experimentally.
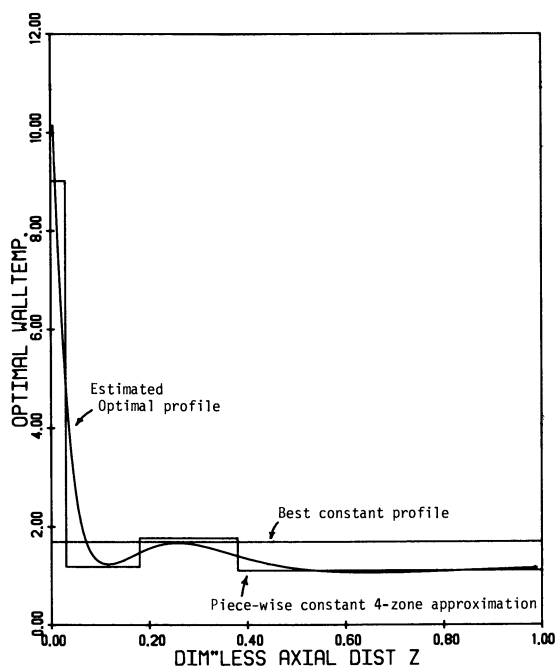
Figure 8. Example of fourth order Laguerre approximation of the continuous optimal wall temperature.

Table III. Comparison of Two-Zone and Continuous Profile Cases
            for P1 = 0.90, P2 = 0.09, P3 = 0.63, P4 = 16.0

Profile	Type	Approx. CPN Time Sec	Objective Function Value	Outlet Conversion X out
Two-Zone	Free	15-20	0.634×10^{-2}	0.960
Continuous	Constrained	100-120	1.203×10^{-2}	0.900
Two-Zone	Constrained	25-35	1.305×10^{-2}	0.900
Two-Zone (Variable Zone)	Constrained	~80*	1.280×10^{-2}	0.900
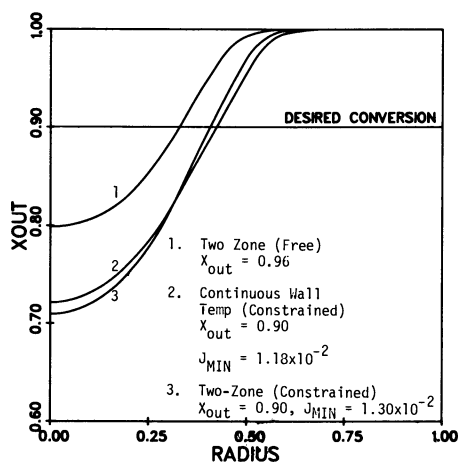
Figure 9. Comparison of exit conversion profiles for dif-
ferent cases.

Styrene polymerization

As a sequel to the simple reactor model described above, two-zone cases for the bulk polymerization of styrene were also studied. Polymerizations in straight, empty tubes give rise to unfavorable temperature and velocity profiles which can lead to hydrodynamic or thermal instabilities. These instabilities may be avoided or postponed by manipulating the wall temperature.

There is limited range of tube sizes over which wall temperature optimization can be effective as a stand-alone method of stabilizing tubular polymerizers. At large tube sizes, the radial variations in temperature and concentration become unmanageably high and often lead to a thermal runaway as the heat produced in the center of the tube cannot be effectively removed. At intermediate diameters, radial composition and viscosity gradients become significant, but manageable as appreciable control over the temperature within the tube is still possible. Capillary size tubes provide even better control over the temperature and concentration within the tube as radial gradients tend to be negligible. The product quality functionals are similar to Equations 8 and 9, but now include weighting by the velocity profile.

$$J[T_w(z)] = M_{in} \left\{ \int_o^R r\, v_z(r)\, [M(r,L) - M_{desired}]^2\, dr \right\} \quad (14)$$

subject to the equality constraint

$$K[T_w(z)] = \int_o^R r v_z(r)\, [M(r,L) - M_{desired}]\, dr = 0 \quad (15)$$

which requires that the desired mixing cup average concentration be achieved exactly.

For the bulk polymerization of styrene using thermal initiation, the kinetic model of Hui and Hamielec (13) was used. The flow model (Harkness (1)) takes radial variations in temperature and concentration into account and the velocity profile was calculated at every axial point based on the radial viscosity at that point. The system equations were solved using the method of lines with a Gear routine for solving the resulting set of ordinary differential equations.

In this paper, a tube of size 1/4" in diameter was considered with styrene monomer preheated to 135 C. The radial variations in temperature are minimal and good control over the concentration profile was possible. Some typical variations in conversion with radial position are shown in Figure 10. The zone temperatures for this example represent a sub-optimal case. However, it is readily seen that as we approach the optimal solution, the first zone temperature converges to an upper limit, while the second zone temperature goes to absolute zero. Figure 11 shows this trend. We also note that as the optimal temperatures are approached, there is a steady drop in the

	$T_{w1}(°K)$	$T_{w2}(°K)$	$\bar{R}_W$	$\bar{R}_N$
1.	400.6	400.5	3670	2004
2.	408.3	385.0	3484	1849
3.	410.4	370.0	3273	1717
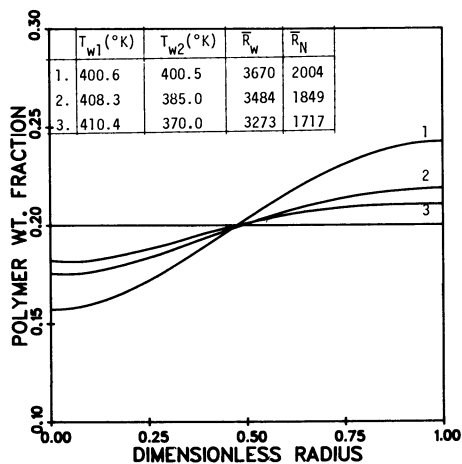
Figure 10. Comparison of exiting polymer weight fraction profiles as the optimal two-zone wall temperatures are approached.

	$\bar{R}_W$
1.	3670
2.	3484
3.	3273
4.	3115
5.	3056
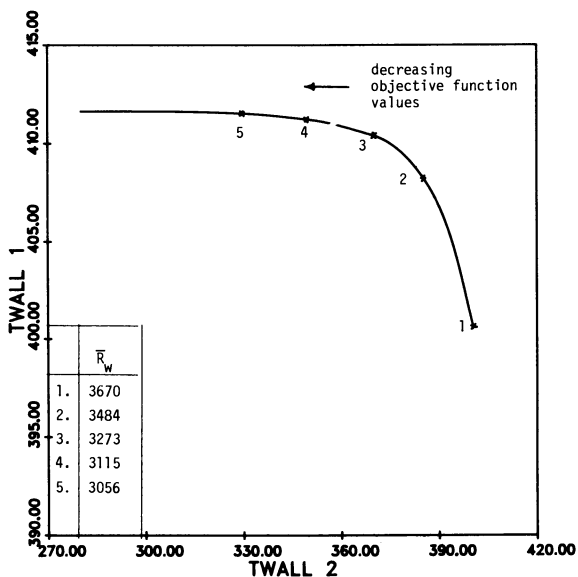
Figure 11. Approach of the two-zone wall temperatures to the optimum and the corresponding variation in weight averaged chain length of the polymer.

average molecular weight of the polymer due to increasing first
zone temperatures. In practice, molecular weights must also be
controlled through the use of additional objective functionals
or constraints.   Such optimization problems are very complex
(14), but practical reactor designs using wall temperature opti-
mization appear possible which satisfy commercial constraints on
the molecular weight distribution.

Conclusions

1. Simple methods have been presented to study constrained and
    free optimization in two-zone reactor systems and in systems
    with a continuous wall temperature profile.
2. Four parameters are identified for the simplified system and
    results are presented for various values of parameters P_1
    and P_2 indicative of desired conversion and inlet tem-
    perature respectively.
3. A computationally efficient method of function fitting using
    an orthogonal polynomial expansion is presented for approxi-
    mating continuous wall temperature profiles.
4. It is seen that a 'bang-bang' type wall temperature performs
    just as well as a continuously variable wall temperature,
    the former also being computationally efficient and simpler
    to work with.
5. Initial results on the two zone wall temperature optimiza-
    tion of bulk polymerizers in tubular reactors shows that the
    molecular weight distribution and product 'quality' can be
    controlled for conversion levels aroung 20%. Further
    investigations into the use of optimal wall temperatures in
    tubular polymerizers are underway.

Nomenclature

a_i — Coefficients of the Laguerre expansion for $T_w(z)$
C — Dimensionless reactant concentration, $C(x,z)$
C_d — Desired exit reactant concentration
ΔE — Activation energy of the reaction
E — Dimensionless activation energy, $\Delta E/R_g T_s$
J — Objective functional to be minimized in the continuous case
J_2 — Objective function to be minimized in two-zone case
K_o — Reaction rate constant at T_o
K — Equality constraint in continuous case
K_2 — Equality constraint in two-zone case
L_i — Laguerre polynomial set
M — Dimensionless monomer concentration, $M(r,z)$
N — Number of terms in the Laguerre expansion for $T_w(z)$
P_i — (i=1,2,3,4) see Table I
r — Dimensionless radial position in tubular polymerizer
R — Radius of the tubular polymerizer
$\overline{R}_n$ — Number averaged degree of polymerization
R_g — Universal gas constant

$\underline{R}_w$ Weight averaged degree of polymerization
t Mean residence time
T Dimensionless reactor temperature, $T(x,z)$
T_i (i=1,2,0,s,avg,u) see Table II
T_w Continuous dimensionless wall temperature, $T_w(z)$
T_L Average temperature at reactor outlet
v_z Axial velocity in tubular polymerizer, $v_z(r)$
x Dimensionless distance from center of the parallel plates
z Dimensionless axial distance

Greek Symbols
α Thermal diffusivity
ω Scale factor in the Laguerre expansion

Literature Cited

1. Harkness, M. M.S. Thesis, Rensselaer Polytechnic Institute, Troy, New York, 1982.
2. Earp, R.G.; Kershenbaum, L.S. Chem. Eng. Sci. 1975, 30, 35.
3. Espiau, B.; Laurgeau, C. Chem. Eng. Sci. 1976, 31, 393.
4. Crowe, C.M. Chem. Eng. Sci. 1976, 31, 959.
5. Gruyaert, F.; Crowe, C.M. AIChE J. 1976, 22, 985.
6. Choi, C.Y.; Perlmutter, D.D. AIChE J. 1978, 24, 193.
7. Smith, T.G.; Carberry, J.J. Chem. Eng. Sci. 1975, 30, 221.
8. Robertson, A.D.; Pratt, K.C. Chem. Eng. Sci. 1981, 36, 471.
9. Butkovskiy, A.G. "Distributed Control Systems"; American Elsevier, 1969.
10. Ray, W.H., Proceedings 2nd IFAC Symposium on Distributed Parameter Control Theory, Coventry 1977.
11. Denn, M.M.; Grey, R.D.; Ferron, J.R., Ind. Eng. Chem. Fundamentals 1966, 5, 59.
12. Lions, J.L., "Optimal Control of Systems Governed by Partial Differential Equations"; Springer-Verlag, Berlin and New York 1971.
13. Hui, A.W.; Hamielec, A.E. J. Appl. Polym. Sci. 1972, 16, 74
14. Tsoukas, A.; Tirrell, M.; Stephanopoulos, G. Chem. Eng. Sci. 1982, 37, 1785.

Safe Design of Cooled Tubular Reactors
for Exothermic Multiple First Order Reactions

K. R. WESTERTERP, K. J. PTASINSKY, and R. R. M. OVERTOOM

Chemical Reaction Engineering Laboratories, Department of Chemical Engineering, P.O. Box 217, Twente University of Technology, 7500 AE Enschede, The Netherlands

Available criteria for the prevention of runaway have been derived for single reactions only. In this paper results are presented for multiple reactions. For multiple reactions not only runaway has to be prevented, but also selectivity or yield have to be maintained. By carefully separating dimensionless groups describing the properties of the reaction system from those describing the operating or design conditions, criteria could be developed to maintain the selectivity or the yield of the cooled, tubular reactor. These criteria require more strict operating conditions than the prevention of runaway and always lead to safely operating reactors.

At designing a cooled (catalytic) tubular reactor for exothermic reactions much care is required to avoid excessive reactor temperatures with respect to reactor temperature runaway. To this end in the past several authors developed criteria for the safe design and operation of cooled tubular reactors. All these criteria are based on single reactions and on the phenomenon of parametric sensitivity. In a certain range of the values of the relevant design and operating parameters, such as the tube diameter d_t, the cooling medium temperature T_c, the reactor inlet temperature T_0 or the concentration c_{A0} of the reactant in the reactor feed, the tubular reactor has been proven to be extremely sensitive to the value of one of these parameters: after a small change of a parameter in the critical region the reactor suddenly starts to operate at a much higher temperature level, the reactor temperatures "run away".

All criteria developed up to now have been based on the conception that this should be avoided and that the reactor should operate outside of the region of high parametric sensitivity. Moreover, the available criteria have been based on a single reaction taking place and on a specified maximum allowable tempe-

rature T_{ma}, which must not be surpassed. The criteria developed
up to now are then based on determining the process conditions at
which the reactor for the specified T_{ma} is at the boundary of the
regions of high and low parametric sensitivity, so that the pro-
cess conditions can be chosen such that runaway is prevented.

    The available criteria exhibit some imperfections. Firstly
because if really only one reaction takes place, it does not mat-
ter that the reactor temperature gets very high; the higher the
temperature the shorter the reactor can be, provided the construc-
tion materials remain strong enough and the catalyst remains ac-
tive. Secondly because specifying a T_{ma} in itself can be rather
arbitrary, although usually it is based on small scale laboratory
experiments, which, of course, does give strong indications for
industrial reactors despite the scale-up problems. A maximum allo-
wable temperature can be specified for various reasons e.g. such
as catalyst life, reactor selectivity, strength of construction
materials, temperature runaway or explosion limits. Here we will
discuss <u>multiple reactions</u> and limit ourselves to <u>runaway</u> and
<u>selectivity</u> aspects. We first will derive criteria for maintaining
a required reactor selectivity or yield and later we will demon-
strate that temperature runaway will not occur, if the desired
selectivity or yield criteria are adhered to. We will restrict
ourselves to exothermic first order reactions in a one dimensional
pseudo-homogeneous, cooled tubular reactor.

Literature survey

Bilous and Amundson [1] were the first to describe the phenomenon
of parametric sensitivity in cooled tubular reactors. This para-
metric sensitivity was used by Barkelew [2] to develop design
criteria for cooled tubular reactors in which first order, second
order and product- inhibited reactions take place. He presented
diagrams from which for a certain tube diameter d_t the required
combination of C_{Ao} and T_c can be derived to avoid runaway or vice
versa. Later van Welsenaere and Froment [3] did the same for first
order reactions, but they also used the inflexion points in the
reactor temperature T versus relative conversion X_A trajectories,
which describe the course of the reaction in the tubular reactor.
With these trajectories they derived a less conservative criterion.
Morbidelli and Varma [4] recently devised a method for single
order reactions based on the isoclines in a temperature conversion
plot as proposed by Oroskar and Stern [5].

    Agnew and Potter [6] did the same as Barkelew for heteroge-
neous catalytic reactors and presented design diagrams to prevent
runaway, including also the parameter of the ratio of the tube to
the catalyst particle diameters d_t/d_p. Burghardt and Warmuzinski
[7] considered multiple reactions and also took the heat effect of
the secondary reaction into account; however, they did not study
the selectivities achieved in the reactor.

    Multiple steady states in catalyst particles have been stu-

died by McGreavy and Adderley [8] and by Rajadhyaksha, Vasudeva
and Doraiswamy [9] and they presented criteria to avoid this mul-
tiplicity. However, it has been shown [10,11] that multiplicity
arising from interparticle gradients are not very likely under
industrial operating conditions. Other criteria to avoid runaway
were developed by Dente and Collina [12] and Hlaváček, Marek and
John [13].

   Emig, Hofmann, Hoffmann and Fiand [14] proved experimentally
that the criteria of Barkelew, of Agnew and Potter and of McGreavy
and Adderley all predict runaway remarkedly well for a single
first order reaction in a cooled catalytic tubular reactor.
Only Westerterp [15] up to now also took the required selectivity
into account in a reactor stability study, but only for tank reac-
tors. We will use his study as a starting point and extend it to
multiple reactions in a cooled tubular reactor. Recently Wester-
terp, Ptasinsky [16,17] and Overtoom [18,19] published studies
on multiple reactions in this reactor type.

Existing criteria for single reactions in tubular reactors

For the prevention of runaway the maximum allowable temperature
T_{ma} must be known. For a first order reaction with $k = A \exp(-E/RT)$
Barkelew [2] derived the condition that:

$$\frac{E}{RT_c} * \frac{T_{ma}-T_c}{T_c} \leq 1 \tag{1}$$

Further he derived empirically by calculation the border line
between the regions with and without runaway in a plot of the
cooling capacity of the reactor as a function of the adiabatic
temperature rise of the reaction. Van Welsenaere and Froment [3]
proved that the less strict condition

$$\frac{E}{RT_{ma}} * \frac{T_{ma}-T_c}{T_{ma}} \leq 1 \tag{2}$$

also gives satisfactory results. Moreover, empirically they found
for first order reactions a mathematical expression for the border
line between the regions with and without runaway:

$$\frac{\Delta T_{ad}}{T_{ma}-T_c} = 1 + \sqrt{N} + N \quad \text{with} \quad N = \left(\frac{4U}{\rho c_p d_t k_{ma}}\right) \tag{3}$$

in which $k_{ma} = A \exp(-E/RT_{ma})$. To compare their results with
those of Barkelew and by substitution of $E/RT_c * (T_{ma}-T_c)/T_c = 1$
and introducing $N_c = 4U/\rho c_p d_t k_c$ and $S = E \Delta T_{ad}/RT_c^2$, in which
$k_c = A \exp(-E/RT_c)$ we can rewrite Eq.(3) into:

$$\frac{N_c}{S} = e[\frac{S-1}{S} - \sqrt{\frac{N_c}{eS^2}}] \tag{4}$$

in which e = 2.718. We see that N_c/S reaches a limit e for very high values of the adiabatic temperature rise. The results of van Welsenaere and Froment enable us to calculate a minimum coolant temperature T_c with equation 2 and then a maximum reactant concentration in the reactor feed ($\Delta T_{ad} = (-\Delta H_R)C_{Ao}/\rho c_p$) with Equation 3 for a certain value of N or for a fixed value of feed concentration a minimum value of N. From Equation 3 it follows that no runaway occurs, provided:

$$\frac{U(T_{ma}-T_c)}{d_t C_{Ao}} \geq \frac{(-\Delta H_R)}{4} k_{ma} \ (1 + \frac{1}{\sqrt{N}} + \frac{1}{N})^{-1} \tag{5}$$

This equation can later on be compared with the criteria derived by us.

The mathematical model for the plug flow reactor with multiple reactions

Several authors applied in vain the same method of Barkelew and others to multiple reactions without finding criteria for safe design of tubular reactors. We think this is mainly caused by the fact that the dimensionless groups used by them instrinsically are strongly dependent on the operating conditions. Specially N_c is strongly affected by the coolant temperature to be chosen ($k_c = A \exp(-E/RT_c)$). We therefore should look for dimensionless groups which are either exclusively representative for the reaction system or for the design and operating parameters. We therefore followed a different approach. We consider a tubular reactor in which two parallel or consecutive reactions occur:

$$A \overset{\displaystyle P}{\underset{\displaystyle X}{\diagup\diagdown}} \qquad or \qquad A \to P \to X \tag{6}$$
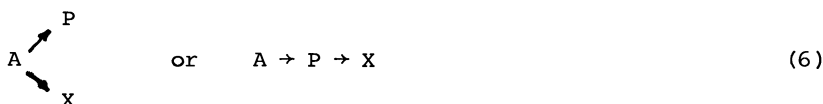
In these reactions A is the reactant, P is the desired and X the undesired product. Both reactions are irreversible, exothermic and of the first order and conversion rates are given by:

$$R_{wP} = k_P C_A \qquad\qquad R_{wP} = k_P C_A - k_X C_P \tag{7}$$
$$\text{or}$$
$$R_{wX} = k_X C_A \qquad\qquad R_{wX} = k_X C_P \tag{8}$$

Here R_w is expressed as kmoles converted per unit of time and per unit of mass of catalyst. The pseudo-homogeneous one-dimensional model of the cooled, tubular reactor used by us is based on the following assumptions:
- the concentration and temperature gradients only occur in the axial direction;
- the only transport mechanism operating in the axial direction is the overall flow itself, which is supposed to be the plug flow;

- the physical and chemical data ρ_g, ρ_B, C_p, ΔH and U are assumed to be independent of temperature;
- the temperature of the cooling medium T_c is constant.

The mass and heat balances for this reactor model are e.g. for consecutive reactions:

$$u \frac{dC_A}{dz} = R_{wA} \rho_B \tag{9}$$

$$u \frac{dC_X}{dz} = R_{wX} \rho_B \tag{10}$$

$$u \frac{dT}{dz} = -(\Delta H_A R_{wA} + \Delta H_X R_{wX}) \frac{\rho_B}{\rho_g C_p} - \frac{4U}{d_t \rho_g C_p} (T-T_c) \tag{11}$$

In order to compare the two competing reactions we use the reference temperature T_R introduced by Westerterp [15]. This is the temperature at which the reaction velocity constants k_P and k_X are equal and have the value of k_R as shown in Figure 1. From this condition follows:

$$k_R \equiv k_P|_{T_R} = k_X|_{T_R} = A_P e^{\frac{-E_P}{RT_R}} = A_X e^{\frac{-E_X}{RT_R}} \tag{12}$$

We now can derive the value of the reference temperature T_R and also a reference reaction velocity constant k_R:

$$T_R = \frac{E_P(p-1)}{R \ln(A_X/A_P)} \quad \text{and} \quad k_R = [A_P^p/A_X]^{\frac{1}{p-1}} \tag{13}$$

in which $p = E_X/E_P$. With T_R and k_R the following dimensionless variables can be introduced: $\mathbf{T} = T/T_R$, the dimensionless temperature; $\kappa = k_P/k_R$ and $\kappa^p = k_X/k_R$, the dimensionless reaction velocity constants. Now κ depends on the dimensionless temperature according to:

$$\kappa = e^{\gamma_P(1-\frac{1}{\mathbf{T}})} \quad \text{with} \quad \gamma_P = E_P/RT_R \tag{14}$$

The reaction velocity constants of both reactions are now defined by the set of parameters: k_R, T_R, γ_P and p instead of by A_P, A_X, E_P and E_X. The ratio of the activation energies p is a measure for the temperature sensitivity of the selectivity of the reacting system. If $p > 1$ the selectivity increases with decreasing temperatures. In this case the reactor has to be operated at a temperature level below the reference temperature in order to obtain high selectivities. For $p < 1$ the reactor should operate at the highest possible temperatures; this case is not of interest for this study.
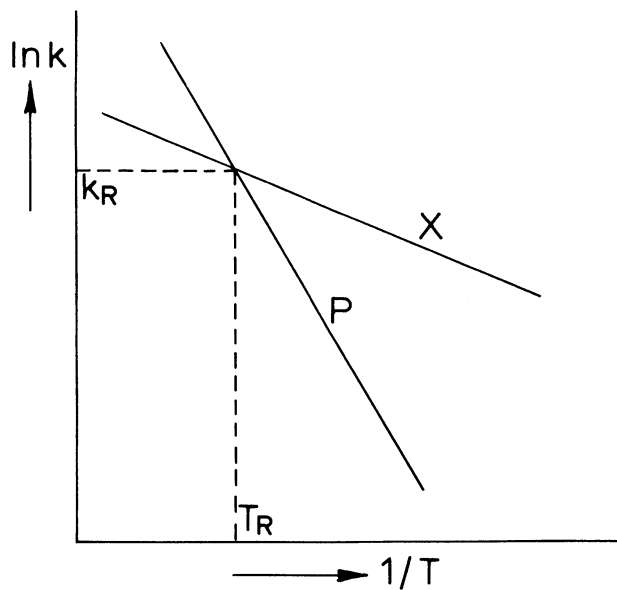
Figure 1. Determination of k_R and T_R, the reference reaction velocity constant and the reference temperature respectively.

Equations 9 to 11 can be made dimensionless after introducing the dimensionless quantities X_P, X_X, Z, H, Da, ΔT_{ad} and U^* (see the list of symbols for their definitions). The transformed equations are for parallel reactions:

$$\frac{dX_P}{dZ} = Da\ \kappa(1-X_P-X_X) \tag{15}$$

$$\frac{dX_X}{dZ} = Da\ \kappa^p(1-X_P-X_X) \tag{16}$$

$$\frac{dT}{dZ} = Da\ \Delta T_{ad}(\kappa+H\kappa^p)(1-X_P-X_X) - Da\ U^*(T-T_c) \tag{17}$$

and for consecutive first order reactions:

$$\frac{dX_A}{dZ} = Da\ \kappa(1-X_A) \tag{18}$$

$$\frac{dX_P}{dZ} = Da[\kappa(1-X_A) - \kappa^p X_P] \tag{19}$$

$$\frac{dT}{dZ} = Da\ \Delta T_{ad}[\kappa(1-X_A) + H\kappa^p X_P] - Da\ U^*(T-T_c) \tag{20}$$

This set of equations describes the behaviour of multiple, first order reactions in a tubular reactor using the relative conversion to desired product X_P and to undesired product X_X, the dimensionless temperature T and the dimensionless reactor length Z. The reaction system is characterized by the ratio of the reaction heats H in addition to k_R, T_R, γ_P and p. The operating and design conditions are determined by: T_c, the dimensionless cooling medium temperature; Da, the dimensionless residence time in the reactor; U^*, the dimensionless cooling capacity per unit of reactor volume and ΔT_{ad}, the dimensionless adiabatic temperature rise for the desired reaction, which, of course, depends on the initial concentration of the reactant A.

  If the reactor feed does not contain any product P or X, the reactor yield of desired product is given by $\theta_P = C_{PL}/C_{Ao} = X_{PL}$, the selectivity of the reactor by $S_P = C_{PL}/(C_{Ao}-C_{AL}) = X_{PL}/X_{AL}$ and the local or differential selectivity at any place in the reactor by $S_P' = -dC_P/dC_A = + dX_P/dX_A$. The selectivity ratio is $S_{PX} = X_P/X_X$, the reciprocal selectivity ratio $S_{XP} = X_X/X_P$ and the differential reciprocal selectivity ratio $S_{XP}' = dX_X/dX_P$. From the basic equations 15 to 20 for the differential selectivity can be derived:

for parallel reactions   : $$S_P' = \frac{1}{1+\kappa^{p-1}} \tag{21}$$

for consecutive reactions:
$$S'_P = 1 - \frac{\kappa^{p-1} X_P}{1 - X_A} \qquad (22)$$

From equations 21 and 22 the striking difference between parallel and consecutive reactions immediately becomes clear; whereas the selectivity for the first type is only a function of the temperature, it is for consecutive reactions also a function of the conversion of A and P. Moreover, for consecutive reactions the selectivity always decreases with increasing conversion! For consecutive reactions two different situations may be considered:

- the reactant A can be recovered from the reactor product: then the reactor should be operated at low conversions, when the selectivity is still high, and the non-converted A should be recycled to the reactor inlet. This case will not be discussed here.

- the reactant A cannot be recovered from the reactor product. In this case, which will be elaborated further, we should operate the reactor at its yield maximum. The maximum yield is found, when $S'_P = 0$. So the reaction must be terminated as soon as $S'_P = 0$.

Derivation of criteria for multiple reactions

The behaviour of the trajectories - the relation between the reactor temperature T and the conversion X_A of the reactant - has been analysed extensively by us [16,17,18,19] for multiple reactions. The basis of this analysis is formed by the so called hot spot temperature in connection with the desired selectivity for parallel reactions or the desired yield for consecutive reactions. The desired selectivity or yield leads to a maximum allowable temperature T_{ma} which further is determined only by reaction system parameters. Table I gives a survey of the results obtained. Once T_{ma} is known, the operating and design conditions can be chosen. We see that the dimensionless group $U^*(T_{ma}-T_c)/\Delta T_{ad}$ - containing only design and operating parameters - has to be kept larger or equal to an expression containing only reaction system parameters and the desired selectivity or yield. The temperature difference $T_{ma}-T_c$ can be chosen at will, but the lower T_c with respect to T_{ma} the lower the average temperature level in the reactor, the lower the average reaction rates and the larger the required reactor tube length. This leads to an additional requirement of $T_{ma} > T_c > T_{c\ min}$ for T_c to obtain practical reactor lengths.

Check for runaway and design procedure

The results obtained were checked for parametric sensitivity. It was found that under all practical conditions and for $S_P > 0.5$ $\Theta_P > 0.5$ <u>runaway can not occur if the selectivity or yield criteria are adhered to.</u> This means that the maintaining of a required selectivity or yield requires more stringent operating and design

Table I. <u>Criteria for the safe design of cooled tubular reactors</u>
<u>with multiple exothermic first order reactions</u>

Parallel reactions	Consecutive reactions

Maximum allowable temperature T_{ma}:

$$T_{ma} = \frac{\gamma_p (p-1)}{\gamma_p (p-1) - \ln(S'_{XP})_{ma}} \qquad\qquad T_{ma} = \frac{\gamma_p (p-1)}{\gamma_p (p-1) - \dfrac{1-\kappa_{ma}^{p-1}}{\kappa_{ma}^{p-1}} \ln(\theta_p)_{ma}}$$

for diff. selectivity ratio $(S'_{XP})_{ma}$ for yield $(\theta_p)_{ma}$

Design or operating conditions $U^\wedge (T_{ma}-T_c)/\Delta T_{ad}$ should be:

$\geqslant (S'_{XP})_{ma}^{\frac{1}{p-1}} \; 1+H(S'_{XP})_{ma} \; P_{1,2}$ $\geqslant \kappa_{ma}^{P_{1,2,3}}$

in which:

$P_1 = 1$
$P_2 = 1- \dfrac{T_{ma}-T_c}{\Delta T_{ad}} * \dfrac{1+\kappa_c^{p-1}}{1+H\kappa_c^{p-1}}$

$P_1 = 1$
$P_1 = [1-(1-H\kappa_{ma}^{p-1}) * \dfrac{T_{ma}-T_c}{\Delta T_{ad}}]$

$P_3 = [\dfrac{\kappa_{hs}}{T_{hs}-T_c} + \dfrac{H\kappa_{hs}^p -\kappa_{hs}}{\Delta T_{ad}}] * \dfrac{T_{ma}-T_c}{\kappa_{ma}}$

in which T_{hs} follows for chosen T_c from:

$$\frac{Hp\kappa_{hs}^{p-1}}{\Delta T_{ad}}(T_{hs}-T_c)^2 + (T_{hs}-T_c) - \frac{T_{hs}^2}{\gamma_p} = 0$$

Cooling medium temperature should be $T_{ma} > T_c > (T_c)_{min}$, where

$$(T_c)_{min} = \frac{\gamma_p}{\gamma_p - \ln[\dfrac{(S'_{XP})_{ma}^{\frac{1}{p-1}}(1+(S'_{XP})_{ma}]}{Da_c/Da_{min}}]} \qquad (T_c)_{min} = \frac{\gamma_p}{\ln(Da_c/Da_{min})+\gamma_p/T_{ma}}$$

and in which $Da_c/Da_{min} = 3 - 5$

conditions than the prevention of runaway. Or in other words, if
design or operating variables are chosen less strict, the selectivi-
ty or yield will deteriorate much earlier then the runaway starts.

The recommended procedure for the design and the safe opera-
tion of a cooled tubular reactor for first order, multiple reac-
tions is given in Table II. Once the reactor has been designed and
installed, the tube diameter cannot be changed anymore. Moreover,
with the requirement $U^*(T_{ma}-T_c)/\Delta T_{ad}$ should be kept constant at
varying operating conditions like changes in c_{Ao} or $\dot{u}$ now values
e.g. for the required coolant temperature can be chosen [17,19]
in order to keep the reactor selectivity or yield constant.

We should warn that the method has been developed for first
order reactions; for reactions of different order and especially
for reactions with Langmuir-Hinshelwood or Eley-Rideal kinetics
the method will not work.

Application of the criteria to industrial processes

To conclude this article two examples of application of the crite-
ria follow.
The industrial production of ethylene oxide is based on the direct
oxidation of ethylene in the gas phase on a silver catalyst in
cooled, tubular reactors. For a large excess of ethylene the reac-
tion scheme can be simplified to:

$$C_2H_4 \begin{array}{l} \nearrow C_2H_4O \qquad (- 210 \text{ MJ/kmole } O_2) \\ \searrow CO_2 + H_2O \qquad (- 473 \text{ MJ/kmole } O_2) \end{array}$$
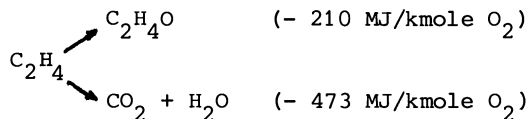
in which both reactions are pseudo-first order in oxygen. A de-
tailed elaboration is given in [17], some results are given in
Table III. We see that reactors with tube diameters from 1" to
2.5" give satisfactory results and lead to the desired selectivity.
The larger the tube diameter, the longer the reactor tube becomes;
a final choice has to be made on economic grounds.
If we would have applied the criteria of van Welsenaere and
Froment [3] for the determination of runaway conditions - using
the kinetic rate expression for the main reaction only - we would
find S = 11.3 and N_c = 20.6 for T_{ma} = 534 K and T_c = 494.4 K.
This would give a tube diameter d_t = 0.14 m, whereas our selecti-
vity requirement asks for a tube diameter $\leq$ 0.06 m. Although the
one-dimensional pseudo-homogeneous model is no more valid for
d_t = 0.14 m, this proves that maintaining the selectivity asks for
much smaller tube diameters than the runaway prevention.

Table II. Design procedures

The following procedure can be followed:

1. Determine from the laboratory data, whether the reactions under consideration can be described by a system of parallel or consecutive reactions.
2. Fit the data obtained in the laboratory by first order rate expressions of the type $R_{wj} = k_j C_j$ in the temperature range of interest. Check whether the use of first order kinetics is allowed.
3. Calculate the reaction parameters k_R, T_R, γ_p, p and H.
4. Choose on economic grounds, especially on raw materials costs and product value, a value of the maximum allowable reciprocal selectivity ratio $(S_{XP})_{ma}$ for parallel reactions or yield for consecutive reactions.
5. Determine T_{ma} from Table I.
6. Determine $U^*(T_{ma}-T_c)/\Delta T_{ad}$ from Table I, preferably with P_2 for parallel and P_3 for consecutive reactions.
7. Choose a value of Da_c/Da_{min} in agreement with the investment costs of the reactor and determine from Table I a minumum value for the cooling medium temperature.
8. Calculate with the criteria the minimum value of $U(T_{ma}-T_c)/d_t C_{Ao}$ and choose practical values for d_t and C_{Ao}.
9. If d_t is larger than required for the process, either a higher selectivity towards desired product or a shorter reactor can be chosen by increasing the coolant temperature. If d_t is too small, lower selectivities and/or lower coolant temperatures have to be accepted.

Table III. The oxidation of ethylene

Reactor configurations for selectivities above 70% as calculated with criterion P_2 for parallel reactions.
C_{Ao} = 6 mole %, T_{ma} = 534 K, oxygen conversion 40%, $(T_c)_{min}$ = 489 K

d_t inch	d_t (mm)	U W/m^{2}K	T_c K	Da_c/Da –	$L_{0.40}$ m	Selectivity
1"	24.3	298	516	1.82	5.7	0.72
1½"	38.1	297	507	2.58	7.4	0.74
2"	49.3	290	499	3.50	10.1	0.76
2½"	59.0	282	491	4.68	13.6	0.78

The industrial production of phthalic anhydride is a.o. based on the direct oxidation of naphthalene with air in cooled tubular reactors filled with catalyst. The reaction scheme can be simplified [15,19] to:

$$C_{10}H_8 \xrightarrow[(-1880\ MJ)]{} C_8H_4O_3 \xrightarrow[(-3280\ MJ)]{} CO_2 + H_2O$$
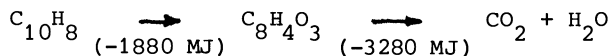
The reactions are pseudo-first order in hydrocarbons.

Table IV The oxidation of napthalene

Reactor configurations for yields above 70% as calculated with criterion P_3 for consecutive reactions.
$C_{A_O} = 0.8$ mole %, $T_{ma} = 693$ K, $(T_c)_{min} = 626$ K

d_t	U	T_c	Da_c/Da_{min}	L_{opt}	X_A	yield X_P
inch	W/m^{2}K	K	–	m	–	–
½"	161	677	1.42	1.20	0.92	0.72
¾"	158	658	2.19	2.40	0.95	0.80
1"	154	643	3.17	3.90	0.96	0.85

Table IV gives some results after applying the criteria for different tube diameters and operating conditions, as given in [19].

Legend of symbols not described in the text

C	Concentration, kmole/m^3
c_p	Sensible heat, J/kg K
H	$\Delta H_X/\Delta H_P$
ΔH	exothermic reaction heat, J/kmole
k	reaction velocity constant, m^3 reactor/kg cat s
L	reactor length, m
T	temperature, K
u	superficial gas velocity, m/s
U	total heat transfer coefficient, W/m^{2}K
U*	$4U/k_R\rho_B\rho_g c_p d_t$
z	distance from reactor inlet
Z	z/L
Da	$k_R\rho_B L/u$
ρ_B	bulk density of catalyst kg/cat/m^3 reactor volume
ρ_g	density of reaction mixture kg/m^3
ΔT_{ad}	$\Delta H_P C_{Ao}/T_R\rho_g c_p$

Subscripts

A	reactant
c	coolant
ma	maximum allowable
P	desired product

X   undesired product
o   inlet conditions
R   reference
hs   "hot spot"

Literature cited

[1] Bilouw O. and Amundson N.R., AIChE J 1956, 2, 117.
[2] Barkelew C.H., Chem. Eng. Progr. Symp. Ser. 1959, 55, 37.
[3] Van Welsenaere R.J. and Froment G.F., Chem. Eng. Sci. 1970, 25, 1503.
[4] Morbidelli M. and Varma A., AIChE J, 1982, 28, 705.
[5] Oroskar A. and Stern S.A., AIChE J, 1979, 25, 903.
[6] Agnew J.B. and Potter O.E., Trans. Instn. Chem. Engrs. 1966, 44, T216.
[7] Burghardt A. and Warmuzinski K., Proc. 5th Int. Congre. Chem. Engng., Chem. Equip., Des. Autom., K2.5, Prague 1975.
[8] McGreavy C. and Adderley C.I., Chem. Eng. Sci. 1973, 28, 577.
[9] Rajadhyaksha R.A., Vasudeva K. and Doraiswamy L.K., Chem. Engng. Sci. 1975, 30, 1399.
[10] Froment G.F., Proc. NATO Adv. Study Inst., Chem. Chem. Engng. Cat. Proc., Ser. E 1980 (39) 535.
[11] Westerterp K.R., van Swaaij W.P.M. and Beenackers A.A.C.M., "Chemical Reactor Design and Operation", J. Wiley, London, 1983.
[12] Dente M. and Collina A., Chim. Ind. (Milan) 1964, 46, 752.
[13] Hlavacek V., Marek M. and John T.M., Coll. Czechoslov. Chem. Comm. 1969, 34, 3868.
[14] Emig G., Hofmann H., Hoffmann V. and Fiand V., Chem. Eng. Sci. 1980, 35, 249.
[15] Westerterp K.R., Chem. Engng. Sci. 1962, 17, 423.
[16] Westerterp K.R. and Ptasinsky K.J.: "Safe design of cooled tubular reactors for exothermic, multiple reactions. Parallel reactions. Development of criteria". Chem. Eng. Sci. in print.
[17] Westerterp K.R. and Ptasinsky K.J.: "The design and operation of an ethylene oxide reactor". Chem. Eng. Sci., in print.
[18] Westerterp K.R. and Overtoom R.R.M.: as [16], but for "Consecutive reactions", submitted to Chem. Eng. Sci.
[19] Westerterp K.R. and Overtoom R.R.M.: "The design and operation of a naphtalene oxidation reactor", submitted to Chem. Eng. Sci.

Stability of Adiabatic Reactors

C. H. BARKELEW

Shell Development Company, Houston, TX 77001

An adiabatic exothermic reaction in a continuous
flow system can develop uncontrollable
"runaways" or "hot-spots" if the extent of
reaction is allowed to increase beyond a
critical limit. This limit depends strongly on
the thermal parameters of the reaction and on
mixing of the reacting fluid in the direction of
its flow. This paper provides broadly
applicable rules for designing such reactors and
operating them safely.

A runaway exotherm in a flow reactor can occur locally if there
are lateral irregularities and insufficient mixing of adjacent
portions of the reactants. It can also occur globally, in
which situation all of the fluid passes through the runaway
zone before it leaves the reactor. This latter type of runaway
reaction is the subject of this paper.
    If the kinetics and thermal parameters of a reaction are
known, and if the characteristics of the fluid flow through a
reactor can be described, a set of differential equations can
be formulated, whose solution will give an estimate of the
temperature profile in that reactor, for a variety of operating
conditions. A collection of such temperature profiles could in
principle be used to design a safe reactor or to provide
operating guidelines for an existing reactor. It is not the
purpose of this paper to exhibit examples of this sort of
computational exercise. Rather, it is to show that with
understanding of the physical circumstances which can lead to
runaway reaction, a simple, accurate, and broadly applicable
set of rules can be developed, which can be used without the
need for extensive numerical analysis.
    In a sufficiently long adiabatic reactor, the temperature
can ultimately increase so strongly with length that it will
appear to be discontinuous. The position of this discontinuity

is rarely fixed; instead it wanders slowly back and forth as
operating conditions vary. A safe reactor is one which is
short enough so that a wandering potential discontinuity never
becomes real. "Short enough" thus means the position of the
discontinuity in the steady state at the average operating
condition, multiplied by a factor (<1) which depends on the
length of the zone of wandering. In this paper, the
characterization of the steady state is developed with design
and operating rules deduced from this characterization. The
user must provide his own "factor." It depends more on the
nature of the disturbances in his particular process than on
anything else.

The ultimate stability criterion developed here is novel,
broadly-applicable, and simpler to use than anything in the
prior art.

Conclusions and Significance

The fundamental rule for safe operation of an adiabatic
exothermic reactor is that it must not be operated with too
much conversion. The definition of "too much" is provided by
the development described herein. It takes one of two nearly
equivalent forms:

$$SD^* < \left[\frac{\sigma^2}{\mu^2} \right]^{\frac{\sigma^2}{\mu^2 - \sigma^2}}$$

or

$$\tau^* < \frac{\mu^2}{\mu^2 - \sigma^2} \log\left(\frac{\mu^2}{\sigma^2} \right)$$

The definition of symbols is in the Table of Nomenclature.
Basically SD^* is a number proportional to the reactor length,
made dimensionless by a proper combination of thermal and
reaction kinetic paramters. τ^* is proportional to the
temperature rise, made dimensionless by a combination of inlet
temperature and activation energy. μ and σ^2 are the mean and
variance, respectively, of the residence-time distribution in
the reactor.

The significant conclusion of this work is that although
mixing of the fluid in the direction of flow has a strong
influence on the stability of a continuous flow reactor, as can
be seen by the way the parameters of the residence-time
distribution are involved, the quantitative criterion for
stability is independent of the mechanism by which such mixing
occurs. The criterion applies equally well to imperfectly-

stirred tanks, nearly-plug-flow packed beds, bubble towers, and trickle beds.

The condition for applicability of the criterion is that it must be possible to relate the local rate of generation of heat to the temperature, over a small initial fraction of conversion, by an Arrhenius-type of kinetic expression involving the conversion of a single component. This is not a severe restriction.

Basis
─────

The fundamental premise of the development to be described is the following: Insofar as its tendency to run away is concerned, the kinetics of a reaction can be adequately described in terms of an equivalent single reaction.

In the analysis, I have taken the rate of this equivalent reaction as being proportional to the product of a function of a single composition variable, which I call "conversion," and normal Arrhenius function of temperature. In particular, there is a specific rate constant, a reaction order, an activation energy, and an adiabatic temperature rise. These four parameters are presumed to be sufficient to describe the reaction well enough to determine its stability characteristics. Finding appropriate values for them may be a bit complicated in some cases, but it can always be done, and in what follows I assume that it has been done.

I also make use of the representation of the Arrhenius function by an exponential function of temperature. This is a conservative approximation, which can be made at the time the rate parameters are determined.

The Adiabatic Plug-Flow Reactor
───────────────────────────────

On the above basis, the rate of the reaction under consideration in a unit volume of reactor can be written as

$$\text{Rate} = k_s \, (1 - x)^n \, \exp \, (-E/RT) \tag{1}$$

The reaction is taken as adiabatic, therefore

$$C \, \Delta T = Hx \tag{2}$$

Then,

$$\text{Rate} = k_s \left(1 - \frac{C \, \Delta T}{H} \right)^n \, \exp \, (-E/RT) \tag{3}$$

The exponential approximation is

$$k_s \exp (-E/RT) = k_s \exp (-E/RT_o) \exp (\gamma \Delta T)$$

$$= k \exp \gamma \Delta T \qquad (4)$$

Let $\gamma \Delta T \equiv \tau$ and $\gamma H/C \equiv S$.

Then,

$$\text{Rate} = k (1 - \frac{\tau}{S})^n \exp(\tau) \qquad (5)$$

The parameter S is the maximum adiabatic temperature rise, scaled by the temperature coefficient of reaction rate. k is the rate at the reactor inlet.

In plug flow,

$$CF \frac{dT}{dz} = H \cdot \text{Rate} \qquad (6)$$

In dimensionless form, this is

$$\frac{d\tau}{dz} = SD (1 - \frac{\tau}{S})^n \exp (\tau) \qquad (7)$$

with $D \equiv kV/F$.

The solution of Equation (7) is:

$$SDz = S^n \exp (-S) \int_{S-\tau}^{S} u^{-n} \exp (u) \, du \qquad (8)$$

For n = 0, SDz = 1 - exp (-τ).

For n = 1, SDz = S exp (-S) [Ei(S) - Ei(S-τ)]

with $Ei(x) \equiv \int_{\infty}^{x} \exp (u) \, du/u$

A review of the physical significance of the dimensionless parameters is appropriate at this point. S is the maximum possible adiabatic temperature rise, scaled by the temperature coefficient of reaction rate. It is a measure of the sensitivity of the reaction to changes in operating conditions, and is sometimes designated by "B" in the literature. "D" is the residence time multiplied by the specific rate constant at the inlet, often called the "number of reaction units". τ is the temperature rise, scaled by the temperature coefficient of reaction rate. The maximum possible value of τ is S.

The form of Equation (8) is indicated in Figure 1, drawn for z = 1. This is basically a plot of temperature rise vs. residence time. A feature is the extremely steep temperature
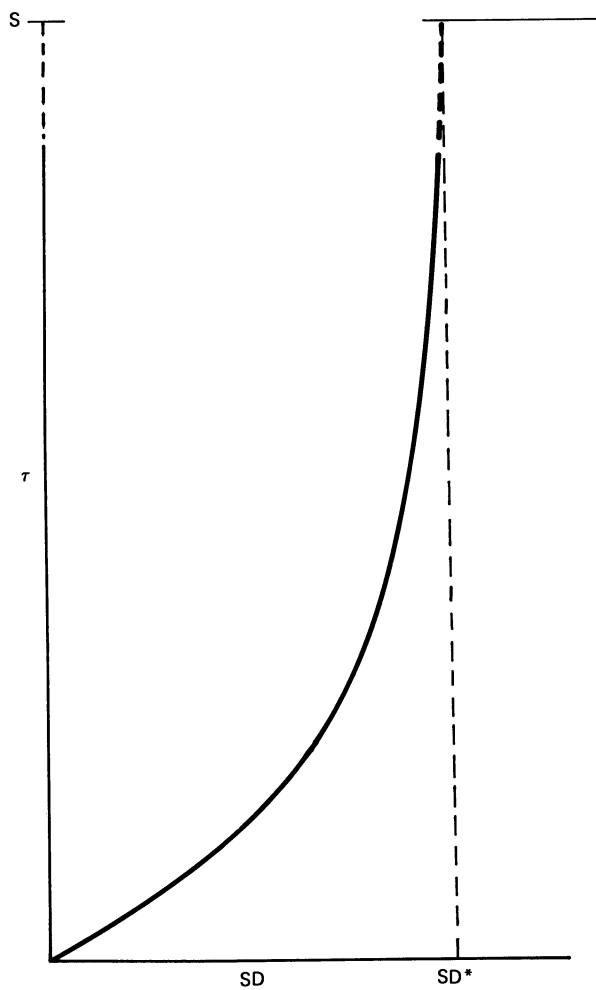
Figure 1.   Temperature Rise in Plug Flow.

rise that occurs if SD is larger than a certain critical
value. A safe reactor would be such that SD never reaches this
value, regardless of disturbances that may occur.   In
particular, SD depends on flow rate, inlet temperature, and
feed composition. A sufficient disturbance in one or more of
these operating variables could cause a runaway if corrective
action were not taken.

The slope of τ vs. SD is always finite. Its maximum is
at $\tau = S - n$. Table I gives values of SD at this inflection
point, called SD*, for a range of values of S and n.

$$\text{Table I.   SD}^* \text{ for Plug Flow}$$

	n = 0.0	n = 0.5	n = 1.0	n = 1.5	n = 2.0
S = 10	1.000	1.061	1.131	1.213	1.309
S = 15	1.000	1.037	1.078	1.123	1.171
S = 20	1.000	1.027	1.056	1.087	1.119
S = 25	1.000	1.021	1.044	1.067	1.092
S = 30	1.000	1.018	1.036	1.055	1.074

These were calculated by numerical integration of Equation
(8). SD must be less than SD^* if an ideal plug-flow reactor is
to be designed and operated.

Real process reactors, for which runaway reaction is a
concern, typically have S-values of 20 or greater.

The Perfectly-Stirred Tank

The temperature rise in a well-mixed reactor is given by:

$$\tau = SD \left(1 - \frac{\tau}{S}\right)^n \exp (\tau) \tag{9}$$

or

$$SD = \tau \exp (-\tau)/\left(1 - \frac{\tau}{S}\right)^n \tag{10}$$

This function is shown in Figure 2. It is different from the
plug-flow reactor in a conspicuous and significant way. It has
a local maximum of SD as τ is increased. If an operating well-
mixed reactor were to be subjected to an increasing SD (say, by
raising the feed temperaure), it would eventually reach a state
where its conversion would jump to near-completion at a rate
determined by its dynamics. Further, this high-temperature
state could not be cleared by simply bringing the feed back to
its orginal condition. SD would have to be reduced to below
its local minimum near $\tau = S$, before τ can drop significantly.
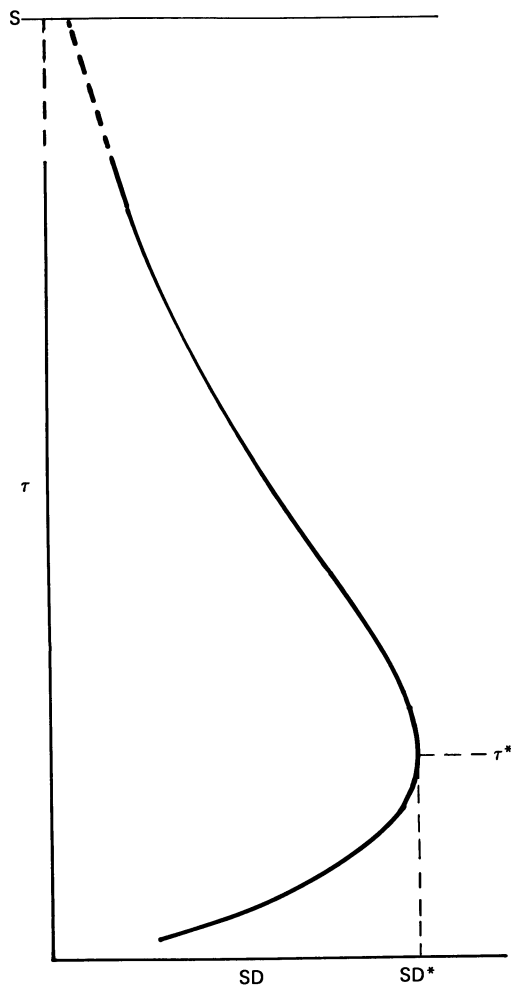
Figure 2.   Temperature Rise with Perfect Mixing.

The value of SD at the local maximum is critical for the
well-mixed reactor, just as that at the inflection is for plug
flow. The value of τ at the maximum SD $\equiv$ SD* is given by:

$$\tau = \left[(S + 1 - n) - \sqrt{(S + 1 - n)^2 - 4S} \right] \Big/ 2 \qquad (11)$$

Some values of SD* are given in Table II.

Table II. SD* for Perfect Mixing

	n = 0.0	n = 0.5	n = 1.0	n = 1.5	n = 2.0
S = 10	0.368 (=e^{-1})	0.388	0.412	0.438	0.468
S = 15	0.368	0.381	0.395	0.411	0.427
S = 20	0.368	0.378	0.388	0.399	0.410
S = 25	0.368	0.376	0.384	0.392	0.401
S = 30	0.368	0.374	0.381	0.388	0.395

Inspection of Tables I and II shows that corresponding
values of SD* differ by almost a factor of 3. This difference
is caused by the physical phenomenon of "backmixing." Hot
products mix with cold reactants in the second case, and
because of the strong non-linearity, the average rate is
enhanced.
      No real reactor is either perfectly mixed or in pure plug
flow. An interpolating procedure to bridge the factor of 3 is
needed for the rational design and safe operation of adiabatic
reactors.
      Much of what I have said thus far is already well known.
In fact, Hlavacek and Hoffman (1) have suggested a way to make
the interpolation. What I offer below is quite different and,
I think, more useful.

Backmixing by Axial Diffusion

The procedure suggested in Reference (1) is to add another term
to Equation (7), giving

$$\frac{d\tau}{dz} = SD \left(1 - \frac{\tau}{S}\right)^n \exp(\tau) + \frac{1}{P} \frac{d^2\tau}{dz^2} \qquad (12)$$

The boundary conditions are $d\tau/dz = P\tau$ at $z = 0$ and $d\tau/dz = 0$
at $z = 1$. Here, P is the axial Peclet number, defined as the
product of velocity and reactor length, divided by the
effective axial diffusivity.

P = 0 corresponds to the well-mixed reactor, P = ∞ to plug flow. Solutions of Equation (12) for a selected set of positive finite values of P fills in the region between the two idealized reactor types. Hlavacek and Hoffman performed the necessary numerical calculations for a few selected values of the parameters and presented their results in a set of plots. Since their plots were intended for illustration rather than for quantatative use in design, I have repeated the calculations for a selected set of parameters.

The critical values of SD and τ for a given P can be found easily by backward numerical integration of Equation (12). The procedure is to perform the integration with a fixed assumed value of SD for a series of assumed values of τ at the reactor outlet. The error in the initial condition, $d\tau/dz - P\tau$ at z = 0, passes through a minimum at some value of the outlet τ. It turns out that the outlet τ at minimum error is very nearly independent of the assumed value of SD. The critical values are those which make the minimum error equal to zero.

Table III gives a few of them, for a zero-order reaction.

Table III.   Critical Parameters for the Diffusion Model

P	SD*	τ *
2	.4802	1.336
4	.5679	1.646
8	.6801	2.112
10	.7846	2.661

Although Equation (12) is widely used as a reactor model, there are reactor types for which it does not represent the physical phenomena in a plausible way. Accordingly, I have investigated five other mathematical decriptions of mixing in reactors, each of which can be said to represent a type of reactor that is used in industrial practice. Comparisons among them has been enlightening.

I have chosen to make the comparison using a zero-order reaction only. Tables I and II indicate that this is conservative for the two ideal reactor types, and it seems plausible to assume that it is also so for real reactors. The degree of conservatism is little more than a few percent in reactor volume. This restriction is thus a useful way to keep the ultimate results in a simple form without compromising their utility.

Descriptions of the various mixing processes and the effects they have on reactor stability follow.

The Imperfectly-Stirred Tank

A common form of stirred-tank reactor has an impeller and a draft tube, which together cause the contents to circulate in a toroidal loop without much mixing except in the region of the feed. This is a simple case of a more general description suggested by van de Vusse (2). Such a reactor can be represented as a loop, described by the differential equation

$$\frac{d\tau}{dz} = \frac{SD \exp (\tau)}{1 + \rho} \tag{13}$$

$$\text{with } \tau(0) = \frac{\rho\tau(1)}{1 + \rho}$$

as the initial condition.

In (13), z is the fractional distance along the loop, SDe^{τ} is the zero-order rate term, and ρ is the ratio of circulation flow rate to feed flow rate. The initial condition states that the temperature at the point where the feed is mixed with the contents of the loop is just the flow average of the two temperatures.

The solution of Equation (13) is

$$SD = (1 + \rho) \left[\exp \left(-\rho\tau/(1+\rho)\right) - \exp \left(-\tau\right)\right] \tag{14}$$

A plot of Equation (14) would resemble Figure 2. There is a maximum value of SD equal to $[\rho/(1+\rho)]^{\rho}$, which occurs at $\tau = (1+\rho) \log [(1+\rho)/\rho]$. As with the perfectly-stirred tank, these can be interpreted as critical values for stability. A few values are listed in Table IV.

Table IV. Critical Values for Loop Model

ρ	SD^{*}	τ^{*}
0.125	0.7598	2.472
0.25	0.6687	2.012
0.5	0.5773	1.648
1.0	0.5000	1.386
2.0	0.4444	1.216
4.0	0.4096	1.116
8.0	0.3897	1.060

Increasing the amount of circulation causes the amount of conversion that can safely be taken, as measured by τ^{*}, to decrease. Equivalently, it decreases the size of a reactor that can be operated safely at the given condition, as measured by SD^{*}.

Series of Stages

An individual reactor in a train can, of course, run away because of its own internal disturbances, but it can also send disturbances ahead to affect the stability of downstream reactors. If there is no intermediate heat exchange, the train acts like a single adiabatic reactor, subject only to disturbances in its feed. Within the stages there is backmixing, but there is none otherwise. A reactor series can also serve as a model for packed-bed reactors, if the upstream propagation implied by Equation (12) is not realistic.

For a zero-order reaction, the temperatures in the stages are given by

$$\tau_1 = \frac{SD}{N} \exp (\tau_1)$$

$$\tau_2 - \tau_1 = \frac{SD}{N} \exp (\tau_2)$$

$$\tau_3 - \tau_2 = \frac{SD}{N} \exp (\tau_3)$$

$$\tau_N - \tau_{N-1} = \frac{SD}{N} \exp (\tau_N)$$

Here the N stages are all presumed to be of equal residence time. The subscripts identify the stage number in the direction of flow.

For a train that is just critical, the last reactor is the one where the incipient runaway occurs. The equation which describes it can be written as:

$$\frac{SD}{N} \exp (\tau_{N-1}) = (\tau_N - \tau_{N-1}) \exp [-(\tau_N - \tau_{N-1})] \qquad (15)$$

which is identical in form to Equation (10). Therefore, its critical conditions are the same, with redefined parameters. Thus,

$$(\tau_N^* - \tau_{N-1}^*) = 1$$

and

$$\frac{SD}{N}^* e^{\tau_{N-1}^*} = \exp (-1)$$

This latter form is equivalent to

$$SD^* = N \exp (-\tau_N^*) \qquad (16)$$

This leads to:

$$\Delta\tau_N^* = 1$$

$$\Delta\tau_{N-1}^* = \exp [-(\tau_N^* - \tau_{N-1}^*)] \qquad (17)$$

$$\Delta\tau_{N-2}^* = \exp [-(\tau_N^* - \tau_{N-2}^*)]$$

$$\Delta\tau_i^* = \exp [-(\tau_N^* - \tau_i^*)]$$

Note that

$$\tau_N^* - \tau_i^* = \Delta\tau_N^* + \Delta\tau_{N-1}^* = \ldots + \Delta\tau_{i+1}^* \qquad (18)$$

and, therefore, that

$$\Delta\tau_{N-1} = \exp (-\Delta\tau_N)$$

$$\Delta\tau_{N-2} = \exp [-(\Delta\tau_N + \Delta\tau_{N-1})] \qquad (19)$$

$$\Delta\tau_{N-3} = \exp [-(\Delta\tau_N + \Delta\tau_{N-1} + \Delta\tau_{N-2})], \text{ etc.}$$

Table V, constructed from Equation (19) and Equation (16), gives values of the critical parameters. The sequence of τ^*'s is the sequence of exponents in Equation (19).

Table V.   Critical Values for a Series of Equal Stages

N	$\Delta\tau_N^*$	τ_N^*	SD^*
1	1.0000	1.0000	.3679
2	.3679	1.3679	.5093
3	.2547	1.6225	.5922
4	.1974	1.8199	.6482
5	.1620	1.9820	.6890
6	.1378	2.1198	.7204
7	.1201	2.2398	.7453
8	.1065	2.3463	.7658
9	.0957	2.4402	.7827
10	.0872	2.5290	.7974

Decreasing the backmixing by increasing the staging
stabilizes the adiabatic reaction in the same sense as for the
circulating loop. Larger values of SD^* and τ^* can be tolerated
for larger values of N.

Interstage Mixing

A bubble tower reactor exhibits some degree of staging, but the
dominant mixing pattern is an intermittent large-scale
circulation caused by rising clumps of bubbles. An approximate
mathematical description is similar to that of the staged
reactor, but with added terms to account for mixing between
adjacent stages. In this description, a model for the nth of N
stages can be written as

$$(1 + 2\varepsilon)\tau_n - (1 + \varepsilon)\tau_{n-1} - \varepsilon\tau_{n+1} = \frac{SD}{N} \exp\ (\tau_n) \qquad (20)$$

where ε is the volumetric ratio of circulation to feed.

For the top stage,

$$(1 + \varepsilon)\ (\tau_N - \tau_{N-1}) = \frac{SD}{N} \exp\ (\tau_N) \qquad (21)$$

For the bottom stage,

$$(1 + \varepsilon)\tau_1 - \varepsilon\tau_2 = \frac{SD}{N} \exp\ (\tau_1) \qquad (22)$$

For a given N, the critical values of SD and τ can be
calculated by assuming a series of values of $\tau_N - \tau_{N-1} \equiv \Delta\tau_N$,
then calculating the corresponding values of $\Delta\tau_{N-1}$,
$\Delta\tau_{N=2}$, . . . to $\Delta\tau_1$ by a cascading procedure similar to that
used for Equation (19). With the calculated $\Delta\tau$'s, SD is given
by Equation (21). The critical value is the maximum possible
value of SD, determined by interpolation among the
assumed $\Delta\tau_N$'s.   A plot of SD vs. τ_N resembles that of
Figure 2.
A few critical values are given in Tables VI and VII.
Again, increasing mixing in the flow direction destabilizes the
reaction.

Mixing by Velocity Distribution

In a packed-bed reactor, the backward flux of energy is limited
to the relatively small effect of conduction through the
packing. The principal dispersion mechanism is variation in
flow rate from point to point, coupled with lateral mixing.
The extent of axial mixing is typically small, compared with
other types of reactors.

Table VI. Critical Values of SD[*] for Interstage Mixing

N	$\varepsilon=$	.1	.2	.5	1	2	5	10
2		.4923	.4784	.4498	.4246	.4030	.3842	.3766
4		.6260	.6051	.5544	.5025	.4534	.4084	.3984
6		.6984	.6782	.6244	.5621	.4958	.4300	.4012
8		.7457	.7262	.6744	.6092	.5530	.4504	.4125
10		.7787	.7605	.7111	.6470	.5658	.4698	.4235

Table VII. Critical Values of τ[*] for Interstage Mixing

N	$\varepsilon=$	.1	.2	.5	1	2	5	10
2		1.3430	1.3147	1.2397	1.1648	1.0998	1.0454	1.0238
4		1.7874	1.7414	1.5886	1.4124	1.2514	1.1144	1.0548
6		2.0826	2.0315	1.8537	1.6231	1.3890	1.1784	1.0932
8		2.3055	2.2507	2.0614	1.8042	1.5180	1.2409	1.1261
10		2.4853	2.4278	2.2307	1.9592	1.6380	1.3025	1.1586

A model by which this can be represented was proposed some years ago by Deans and Lapidus (3). A simple realization of this model is to consider the reactant as being divided into two parallel streams with different velocities, with the two streams being mixed and redivided at intervals. If this representation is to resemble a real packed reactor, the number of mixing-dividing points must be fairly large, say greater than 8 or 10.

With the same notation as before, the reaction in one of the parallel streams can be described by

$$\frac{d\tau}{dz} = \frac{\beta SD}{\alpha N} \qquad (23)$$

where α is the fraction of the total flow in the stream,
β is the fraction of the cross-section it occupies, and
N is the number of mixing points.

There are 2N such equations in this representation. Their solution can be summarized by

$$\exp(\tau_n) = \left(1 - \frac{\beta SD \tau_{n-1}}{\alpha N}\right)^{-\alpha} \left(1 - \frac{(1-\beta)SD \tau_{n-1}}{(1-\alpha)N}\right)^{\alpha-1} \qquad (24)$$

The critical value of SD is that for which the second factor becomes exactly zero for n = N. It can be readily calculated by a one-variable search, for any assumed values of the parameters.

A few values of SD^*, calculated in this way, are given in Table VIII for the special case of $\beta = 1/2$.

Table VIII. Critical SD^* Values for Mix-Separate Model

N	$\alpha=$	.6	.7	.8
8		.9641	.9026	.8003
10		.9706	.9188	.8296
12		.9751	.9302	.8509

Decreasing N and increasing α correspond to increasing degrees of mixing. In this model there is no backmixing whatsoever, in the sense that no energy flows upstream. The temperature profiles of this representation resemble those of Figure 1, with a vertical asymptote rather than a maximum in SD. Formally, the critical value of τ^*, corresponding to SD^*, would be that corresponding to maximum rate, just as it is in plug flow. The critical temperature rise in a real reactor

described by this model would be determined by the disturbances in the process. For this reason a table of τ is not appropriate for this model.

Cross-Mixing with Channeling An alternative description of cross-mixing is to assume that the reactant is divided into two parallel streams which do not remix until the reactor outlet, but which exchange energy and matter laterally as they move downstream. Something like this could happen in a packed bed if there were gross maldistribution of the packing.

The mathematical representation of parallel flow with diffusion crossmixing is

$$\alpha \frac{d\tau_A}{dz} = \beta SD \exp (\tau_A) + \kappa(\tau_B - \tau_A) \qquad (25)$$

$$(1 - \alpha) \frac{\partial \tau_B}{\partial z} = (1 - \beta) SD \exp (\tau_B) + \kappa(\tau_A - \tau_B)$$

where κ is the appropriate Stanton number and the other variables have been defined earler.

Calculation of critical values of SD from Equation (25) requires numerical integration. I used τ_B as the independent variable (the temperature of the slower-moving stream) and integrated to the point where $d\tau_B/dz \geqslant 10^6$. For a series of assumed values of SD, there is a unique value at this point for which z = 1.000. This is the critical SD^*. As with the plug-flow reactor, there is no physically significant τ^* in the absence of disturbances.

A few values of SD^* for this model are given in Table IX.

Table IX. Critical SD^* Values for the Parallel-Flow Model

α	β	κ	SD^*
.75	.5	2	.8359
.75	.5	4	.9012
.6	.2	4	.8570
.6	.2	8	.9219

With this model, if the value of κ is small, local hot-spots will develop within the bed. This type of reactor instability is the subject of another paper. The values from which Table IX was constructed are sufficiently large, as determined by a criterion to be described below.

A Common Characterization of Mixing

With each of the six reactor models just described, the
transport of energy from regions with high conversion to those
with low conversion causes destabilization. Each model has its
own unique way of characterizing the transport process. For
these results to be of practical use, a common measure of
energy transport is required.

This common measure is the variance of the residence-time
distribution. In the absence of reaction, a sudden change in
inlet conditions will be followed by a spread-out change in
outlet conditions. The spreading can be described by common
statistical parameters, the mean, variance, skewness, and so
on.

Ways of calculating these parameters are well-known. For
example, they are simply related to the coefficients in the
Taylor's Series expansion of the Laplace Transform of the
equation which describes the temperature transient without
reaction. With each of the six reactor models, an expression
for the ratio of the variance of the residence-time distribu-
tion to the square of the mean can be derived analytically by
finding the Laplace Transform. The results of such an analysis
are listed in Table X.

In the channel model, the residence-time distribution
function is bimodal if the streams are not sufficiently mixed,
a situation which occurs if σ^2/μ^2 > about 1/20. For larger
values, local hot-spots are likely to develop, and the
correlation to be described does not apply. This puts a lower
limit on the parameter κ of that model.

Figure 3 is a plot of the calculated values of SD^*, for
all six models, vs. σ^2/μ^2. With a deviation of only a few
percent, a single curve can be passed through all the points.
To this degree of precision, the critical value of SD for any
reactor is independent of its mechanism of longitudinal mixing.

Values of σ^2/μ^2 can be found by using existing
correlations, by direct measurement, by modeling, by
simulation, or by using one of the expressions of Table X.

Figure 4 shows a plot of the critical τ^* vs. σ^2/μ^2 .
This graph can be used to predict stable operating limits. The
scatter is a little greater than for SD^*, particularly for low
values of σ^2/μ^2 , where the reactor is nearly in plug flow and
where a critial τ^* may not exist formally.

Analytical forms for the correlating curves of Figures 3
and 4 can be specified by using the exact expressions for SD^*
and τ^* for the circulating loop, derived from Equation (14).

TABLE X. Variance of the Residence-Time Distribution

Model	Mixing Parameters	Variance Ratio, σ^2/μ^2
Axial diffusion	P, the axial Peclet number	$\dfrac{2}{P}\left(1 - \dfrac{1-\exp(-P)}{P}\right)$
Circulating Loop	ρ, circulation flow/feed flow	$\rho/(1+\rho)$
Stages in Series	N, the number of stages	$1/N$
Interstage Mixing	N, the number of stages ϵ, mixing flow/feed flow	$\dfrac{1}{N} + \dfrac{2}{N^2}\sum_{i=1}^{N-1}(N-i)\left(\dfrac{\epsilon}{1+\epsilon}\right)^i$
Mix-Separate	N, the number of stages α, the fraction of flow in one stream β, the fraction of cross-section of that stream	$\dfrac{(\beta-\alpha)^2}{N\alpha(1-\alpha)}$
Channel, w/conduction	α, the fraction of flow in one stream β, the fraction of cross-section of that stream κ, the cross-conduction Stanton number	$\dfrac{2(\alpha-\beta)^2}{\kappa}\left\{1 - \dfrac{\alpha(1-\alpha)}{\kappa}\left[1 - \exp\left(\dfrac{-\kappa}{\alpha(1-\kappa)}\right)\right]\right\}$
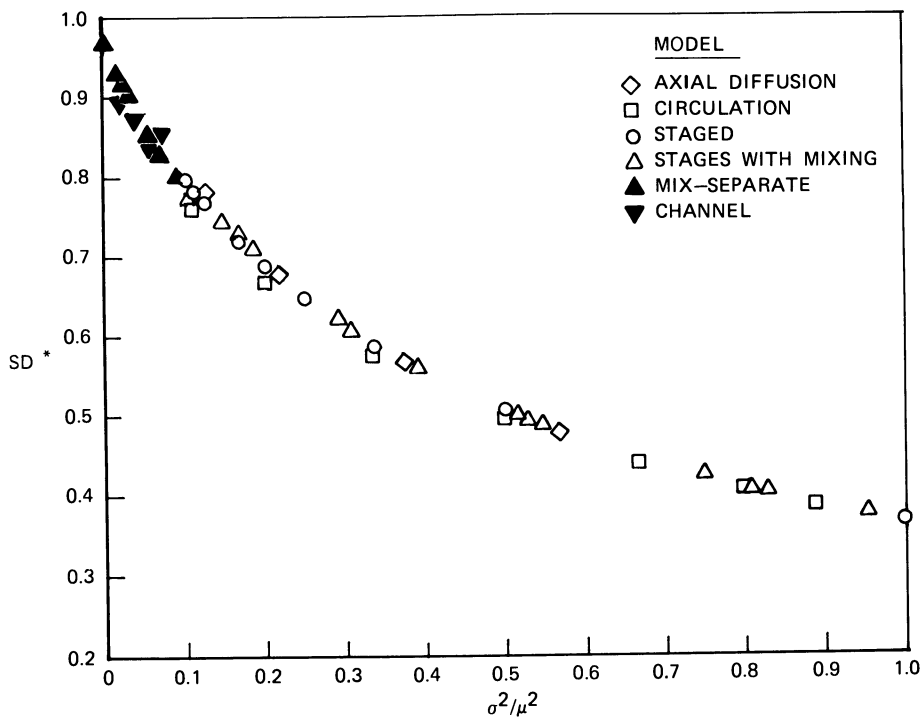
Figure 3.   Critical Residence-Time Parameter.
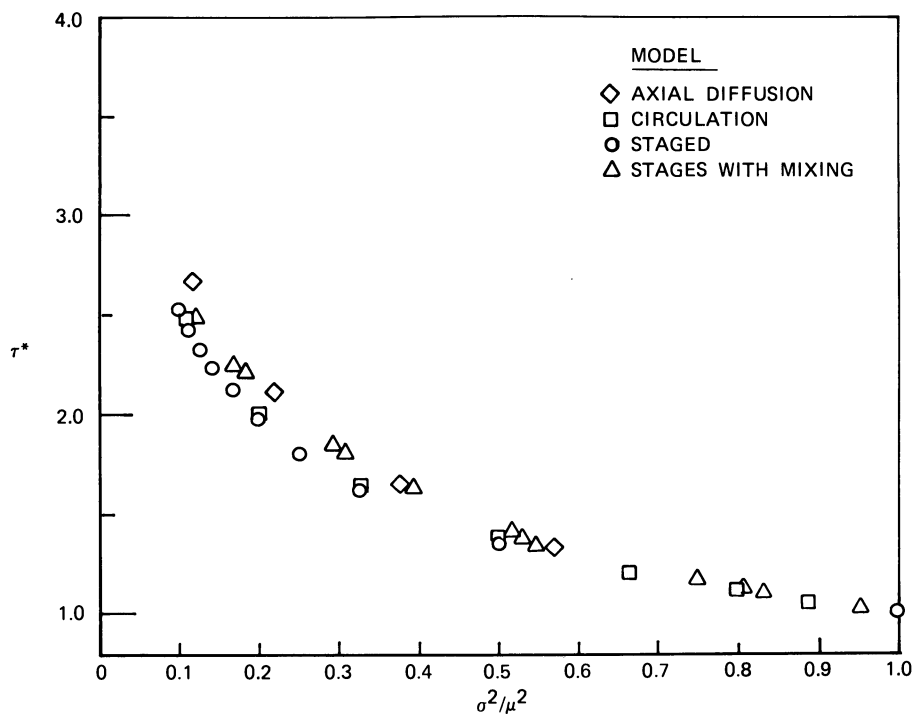
Figure 4. Critical Temperature-Rise Parameter.

They are

$$SD^* = (\frac{\sigma^2}{\mu^2})^{\dfrac{\sigma^2/\mu^2}{1 - \sigma^2/\mu^2}} \qquad (26)$$

$$\tau^* = -\frac{1}{1 - \sigma^2/\mu^2} \log (\sigma^2/\mu^2) \qquad (27)$$

Use of these expressions avoids the inconvenience of attempting to read values off the gridless plots of Figures 3 and 4.

A few comments regarding Equation (26) and (27) are appropriate. They should not be extrapolated beyond $\sigma^2/\mu^2 > 1$. Strongly-skewed distributions for which the inequality holds are physically possible, but they are for systems in which some of the reactants are trapped in a "dead-zone." A runaway reaction in such a system would be local rather than global, and a different procedure for assessing stability would be required.

Otherwise, the expressions are conservative. They were derived from zero-order kinetics and the exponential approximation of the Arrhenius expression, both of which overstate the tendency of a reaction to run away. The conservatism is mild, however, amounting to a few percent at most. Nevertheless, it is possible to compensate for a large part of it and still retain the simplicity of Equation (26) and Equation (27). This can be done by making a minor adjustment to the value of the parameter γ.

In Equation (4), γ was determined by approximating the Arrhenius expression by an exponential, in which the specific rate constant and its temperature derivative were matched at the reactor inlet. A less conservative, but still satisfactory, approximation can be found by matching rates at two different temperatures. My preference is to make this match at T_o and $T_o + 1/\gamma$ (at $\tau = 0$ and $\tau = 1$), because the potential for a runaway is strongly influenced by the course of the reaction in this temperature range, and rather weakly outside it.

In the same way, Equation (26) and (27) can be retained if the order of the reaction is not zero by using the fact that $(1 - \tau/S)^n \approx \exp(-\tau n/S)$ for small τ/S. Since the safe upper limit on τ is in the range of 1 or 2, and typical values of S are 20 or greater, this approximation is not unreasonable.

Taken together, these two adjustments define an effective γ to be used in (26) and (27), as $\gamma(1 - n/S)/(1 + RT_o/E)$. The effective S is the defined S reduced by the same factors. The ultimate result is that the correlations for maximum safe SD and τ can be applied to a much broader set of kinetic expressions than the simple one from which they were derived.

Concluding Remarks

Although much has been published on the stability of adiabatic
reactors, most of it has dealt with conclusions to be drawn
from the assumption that backmixing can be described in a
particular way. Perlmutter (4) has given a review of the
subject, in which the strong effect of backmixing on stability
is clearly recognized. This paper goes beyond the prior art in
that it provides a reasonably convincing demonstration of the
intuitively reasonable proposition that the mechanism of mixing
is relatively unimportant in determining the limits of stable
operation of adiabatic reactors.

Table of Nomenclature

α	Fraction of flow in one of two parallel streams
β	Fraction of reactor cross-section occupied by a stream
γ	E/RT_o^2
C	Heat capacity
d	Axial diffusion coefficient
D	kV/F
ε	Mixing flow/feed flow
E	Activation energy
F	Mass flow rate
H	Heat of reaction
h	Heat transfer coefficient between streams
κ	h/CF
k	Specific reaction rate constant at inlet conditions
k_s	Rate constant
L	Reactor length
μ	V/F
n	Reaction order
N	Number of stages
P	FL/d
ρ	Circulation flow/feed flow
R	Gas constant
σ^2	Variance of residence-time distribution
S	$\gamma H/C$
SD^*	Critical value of SD
τ_*	$\gamma(T-T_o)$
τ^*	Critical value of τ
T	Temperature
T_o	Inlet temperature
V	Reactor volume
x	Conversion, $0 < z < 1$
z	Fraction of reactor length, $0 < z < 1$

Literature Cited

1. V. Hlavacek and H. Hofmann, "Modeling of Chemical Reactors - XVII," Chemical Engineering Science, V. 25, p. 187 (1970).
2. J. G. van de Vusse, "A New Model for the Stirred-Tank Reactor," Chemical Engineering Science, V. 17, p. 507 (1962).

3. H. Deans and L. Lapidus, "A Computational Model for Predicting and Correlating the Behavior of Fixed-Bed Reactors," AIChE Journal, V. 6, p. 656 (1960).
4. D. D. Perlmutter, "Stability of Chemical Reactors," Prentice-Hall, Inc. (1972).

Fundamental Deactivation Data from Laboratory Reactors

EUGENE E. PETERSEN and MICHAEL A. PACHECO

Department of Chemical Engineering, University of California, Berkeley, CA 94720

Fundamental deactivation data are more difficult to obtain than fundamental catalytic reaction rate data because the latter must be known before the nature of the deactivation function can be determined. This is largely due to the kinds of reactors that are used to study deactivation. Many of the usual difficulties experienced in trying to get fundamental deactivation data can be obviated by using a reactor system in which the conversion and hence the compositions of the major components remain constant both in time and in space within the reactor. A description of an apparatus of this type and its utilization to study the deactivation of a real catalytic reaction are presented in this paper. The problem of determining the initial activity in a rapidly deactivating system is also discussed.

When we say that a catalyst deactivates, we mean that under conditions of constant temperature and reaction mixture composition, the conversion of the reactants into products decreases with time. The first question that is asked after a substance has been identified as a catalyst is, "How long will it last?". Accordingly, the phenomenon of deactivation has been the object of an enormous number of research and development projects by companies involved with catalytic processes throughout the world and a lesser, but still significant number of studies, in universities and research institutes. Catalysts are widely used in processes and their finite lifetime is a concern from an economic viewpoint. Therefore, a fundamental understanding of the manner in which catalysts deactivate is important to the selection and development of catalysts for a particular process.

A mathematical definition of the rate of reaction is given by Equation 1:

$$R(0) = F_1(c_1, c_2, c_3, \ldots c_n, T) \tag{1}$$

where the c_i represents the concentrations of the various species in the reaction mixture and T is the absolute temperature. If the system deactivates with time, then the rate expression must be modified to the form given by Equation 2 where t is time:

$$R(t) = F_2(c_1, c_2, c_3 \ldots c_n, T, t) \tag{2}$$

If the function in Equation 2 can be written in the form shown below in Equation 3, the deactivation function is said to be of separable form.

$$R(t) = F_3(t) F_1(c_1, c_2, c_3, \ldots c_n, T) \tag{3}$$

One of the desirable features of the separable form is the natural way in which the activity can be defined.

$$a \equiv \frac{R(t)}{R(0)} = F_3(t) \tag{4}$$

It has been suggested in the literature that homogeneous surfaces of the Langmuir type lead to separable forms and that heterogeneous surfaces lead to non-separable forms [1]. This is partly true in that under many circumstances homogeneous surfaces give separable deactivation forms. Let us consider a simple Langmuir-Hinshelwood mechanism shown below in Equation 5 to bring out three points of concern about deactivating systems:

1)   a mechanistic reason for deactivation through a fouling step,
2)   how a particular mechanism leads to a separable form and,
3)   the importance of the rates of the deactivation process relative to the rate of the main reaction.

$$A + S \underset{k_{-1}}{\overset{k_1}{\rightleftharpoons}} AS \underset{k_{-2}}{\overset{k_2}{\rightleftharpoons}} BS \underset{k_{-3}}{\overset{k_3}{\rightleftharpoons}} B + S \tag{5}$$

$$\underset{k_4}{\overset{}{\downarrow}} \underset{k_{-4}}{\overset{}{\uparrow}}$$

$$F$$
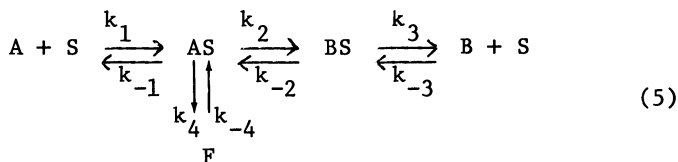
If we make the following assumptions about the rate constants

$$k_{-2} \ll k_2 \ll k_1, \; k_{-1}, \; k_3, \; k_{-3} \qquad (6)$$

$$k_{-4} \ll k_4 \ll k_2$$

then the rate limiting step of the main reaction is

$$AS \xrightarrow{k_2} BS \qquad (7)$$

and quasi-steady conditions prevail.   The site balance equation is

$$X_1 + X_2 + X_3 + X_4 = X_o \qquad (8)$$

where X_1, X_2, X_3, and X_4 are, the concentrations of empty S, adsorbed reactant AS, adsorbed product BS, and foulant F, respectively.   The concentrations of X_2 and X_3 are found in the usual way as shown by Equations 9 and 10 below.

$$X_2 = K_1 \, C_A \, X_1 \qquad (9)$$

$$X_3 = K_3 \, C_B \, X_1 \qquad (10)$$

Hence

$$X_1 + K_1 \, C_A \, X_1 + K_3 \, C_B \, X_1 = X_o - X_4 \qquad (11)$$

and

$$X_1 = \frac{X_o - X_4}{1 + K_1 \, C_A + K_3 \, C_B} \qquad (12)$$

The overall rate of reaction is

$$\text{Rate} = k_2 \, X_2 \qquad (13)$$

while the activity is

$$a = \frac{X_o - X_4}{X_o} \qquad (14)$$

In this way we see that the activity is related to the population of the unpoisoned sites.

Consider now a slight modification of the mechanism shown in Equation 5 to the one shown in Equation 15 below that leads to a non-separable form (2).

$$A + 2S \underset{k_{-1}}{\overset{k_1}{\rightleftarrows}} AS_2 \underset{k_{-2}}{\overset{k_2}{\rightleftarrows}} BS_2 \underset{k_{-3}}{\overset{k_3}{\rightleftarrows}} B + 2S \qquad (15)$$

$$k_4 \downarrow \uparrow k_{-4}$$
$$F$$
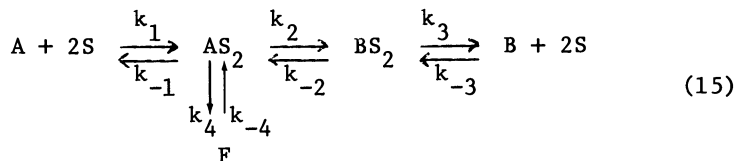
Again assume that Equation 6 applies and the rate limiting step remains the same. However, X_2 and X_3 are now given by

$$X_2 = K_1 \, C_A \, X_1^2 \qquad (16)$$

$$X_3 = K_3 \, C_B \, X_1^2 \qquad (17)$$

thereby making the site balance equation nonlinear.

Now

$$X_1 = \frac{-1 + \sqrt{1 + 8(K_1 C_A + K_3 C_B)(2X_4 - X_o)}}{4(K_1 C_A + K_3 C_B)} \qquad (18)$$

and the activity shown in Equation 18 cannot be put in the form shown in Equation 3, i.e.,

$$a = \left\{ \frac{-1 + \sqrt{1 + 8(K_1 C_A + K_3 C_B)(X_o - 2X_4)}}{-1 + \sqrt{1 + 8(K_1 C_A + K_3 C_B) X_o}} \right\}^2 \qquad (19)$$

Whether the deactivation is separable or non-separable, one normally gets some measure of the activity of a deactivating catalyst by comparing the conversion at zero time to the conversion at some later time. The utility of this type of activity depends in part upon the goal of the study and how fundamentally the data are to be interpreted. For example, the integral reactor shown in Figure 1 is frequently used in pilot plant scale operations and can often produce data of value to interpret and

improve the operation of plant reactors as well as to provide data for direct scale up to commercial scale reactors. However, the activity obtained from integral reactors is a complex average of the local activities in various positions within the reactor bed and the time on-stream. Such data are not easily used to determine the dependence of deactivation on the concentrations within the reaction mixture. However, this is often not a handicap because the variations in the pilot plant and in the commercial plant are presumed similar enough to permit direct utilization. Accordingly, this type of reactor serves a very important role in industry to verify results obtained from more fundamental studies and to improve the operation of existing reactors.

The difficulties that spatial variation of concentrations and temperature cause in trying to get fundamental information from integral reactors can be obviated by using the recycle reactor shown in Figure 2. In this type of reactor, the amount of catalyst in the reactor is chosen so that only a differential amount of reaction takes place per pass, but multiple passes are obtained by recycling the reactants many times over the catalyst before they exit the reactor. In this manner, integral conversion takes place in the reactor, but the concentrations and the temperature to which each catalyst particle is exposed is the same and known. This type of reactor offers an enormous improvement over an integral reactor to provide fundamental data. However, it too has a problem for interpretation because as the catalyst deactivates, the conversion decreases and the concentrations and temperature within the reactor change. As a consequence, the decrease in rate owing to the deactivation can be obtained only after the effects of concentrations and temperature changes have been taken into account.

This difficulty too can be obviated by decreasing the flow rate to just compensate for the decrease in activity owing to catalyst deactivation. To accomplish this, it is necessary to incorporate some device to sense conversion in a recycle reactor as shown in Figure 3. The signal from this sensor is then fed back to a motor valve and positions it to follow a flow rate profile in time so that the conversion is maintained constant. This type of reactor provides data on a deactivating catalyst in which the catalyst is exposed to reactant and product concentrations for a particular reaction and temperature that are constant in both space and time. In principle, then, the kinetics of deactivation are obtained directly from this type of reactor if the kinetic rate law remains unchanged. For example, under the conditions of constant temperature and constant reaction mixture composition, a reactor having a very large recycle ratio behaves like a well-stirred reactor. The conservation equation for this type of reactor is
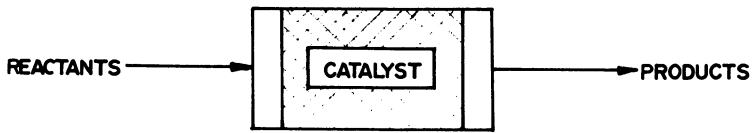
Figure 1.   Concentrations within reactor vary in time and space for a deactivating catalyst.
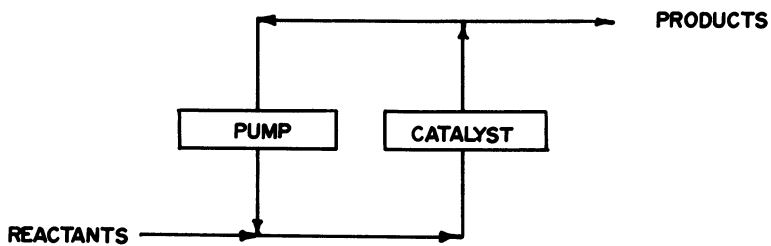
Figure 2.   Concentrations vary in time for a deactivating catalyst.
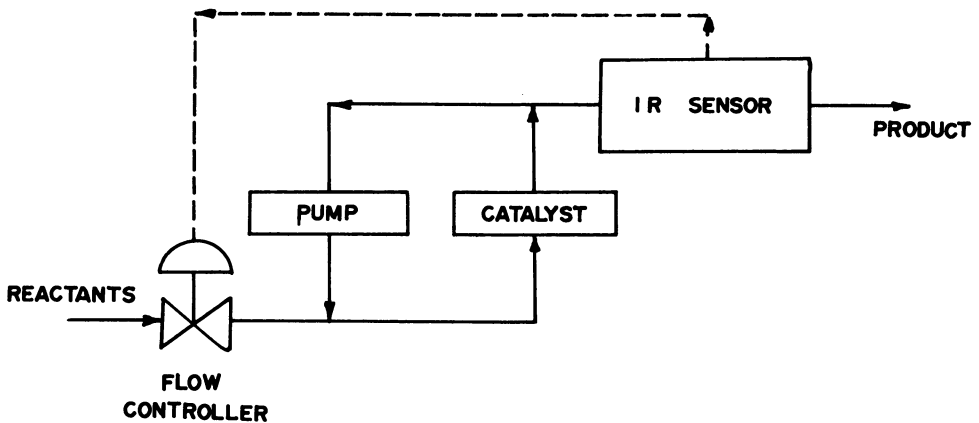
Figure 3.   Concentrations constant in time and space for a deactivating system.

[Flow Rate] $[C_{IN}-C_{OUT}]$ = [Reactor Volume] [Reaction Rate]   (20)

Upon rearrangement, the reaction rate is obtained directly from the flow rate as shown below.

$$[\text{Reaction Rate}] = [\text{Flow Rate}] \, \frac{[C_{IN}-C_{OUT}]}{[\text{Reactor Volume}]} \qquad (21)$$

Under these conditions, the activity of the catalyst is easily calculated from the flow rates

$$a = \frac{Q(t)}{Q(0)} \qquad (22)$$

where Q = Flow Rate.

The reader will note that varying the flow rate to maintain constant conversion does not ensure constant reaction mixture composition if more than one stoichiometric equation is involved in the reaction system.   Decreasing the flow rate can, in principle, maintain only the products from one stoichiometric equation constant.
        Up to this point, we have accepted without comment that we can get a value for $R(0)$. To find $R(0)$, all we have to do, in principle, is to measure the rate of reaction at time equal to zero.   For many systems, in particular, those that deactivate with a time constant long compared to the time scale on which conversion measurements are made, determining the initial rate is relatively easy as depicted on Figure 4.   In other systems, the deactivation rate is fast and the problem of determining the initial reaction rate is very difficult.   A well-known example of this kind of system is the cracking of hydrocarbons.
Figure 5 shows the loss of cracking activity measured by Blanding (3). On this figure, one can observe that the catalyst has an order-of-magnitude loss in activity during the first second on stream.   Accordingly, these curves were extrapolated over a considerable time to get the initial activity.   We note that the abscissa on this plot is unusual in that the scale is the fourth root of time in order to get a zero time on the graph.   Although the extrapolations seem reasonable, it is fair to point out that the first measurements on that curve were taken after about one second on stream.   The extrapolations add about an order of magnitude to the first measurement.   In order to develop a less arbitrary method of extrapolation, we propose
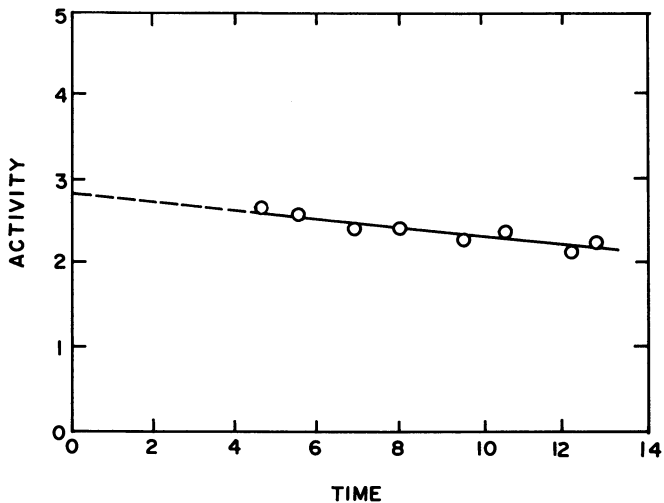
Figure 4.   Activity versus time plot for a reactor.
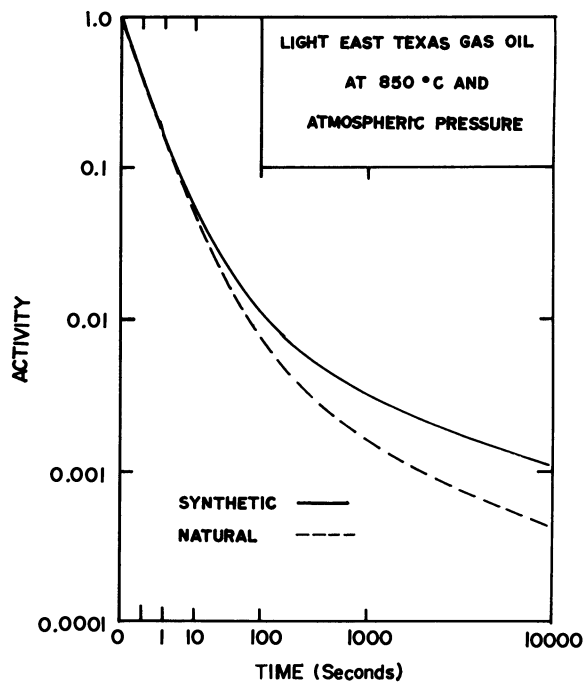
Figure 5.   Instantaneous activity versus time on stream
for cracking.

to use transient conservation equations to assist in determining the initial rate of reaction.

Consider the parallel deactivation scheme of Equation 23:

$$A \xrightarrow{k_m} B$$
$$A \xrightarrow{k_f} F \tag{23}$$

where A is the reactant, B is the desired product, and F is the foulant or undesired product. The transient conservation equations in a recycle reactor with a high recycle ratio are:

$$V_R \frac{dC}{dt} = Q (C_o - C) - a_m W k_m C^n \tag{24}$$

$$\frac{df}{dt} = - a_f k_f C^m \tag{25}$$

$$\text{when } t = 0; \ C = 0 \text{ and } f = 1 \tag{26}$$

where a_m, a_f = catalyst activity for the main and fouling reactions.

These equations can be transformed to dimensionless form to obtain:

$$\frac{dX}{d\tau} = - X + \theta_m f (1-X)^n \tag{27}$$

and

$$\frac{df}{d\tau} = - \theta_d f^6 (1-X)^m \tag{28}$$

where

$$X \equiv \frac{C_o - C}{C_o} \quad ; \quad \theta_m \equiv \frac{W k_m C_o^{n-1}}{Q}$$

$$\tau \equiv \frac{Qt}{V_R} \quad ; \quad \theta_d \equiv \frac{V_R k_f C_o^m}{Q}$$

$$a_m = f \quad ; \quad a_f = f^6$$

Equations 27 and 28 have been solved for m = 0, 1 and 2 and for θ_d = 0.1, 1 and 100. These are shown on Figures 6 and 7.
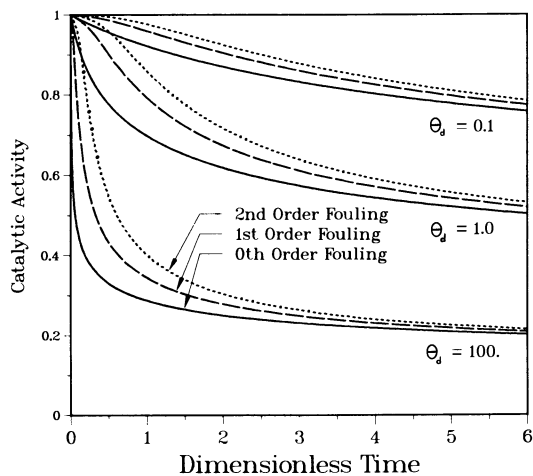
Figure 6.   Catalytic activity in a transient CSTR.
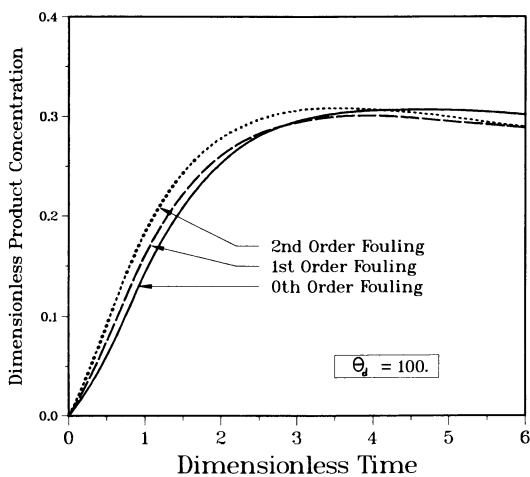
Figure 7.   Product concentration in a transient CSTR.

Figure 6 reveals that the activity after five time constants is insensitive to the order of the fouling reaction with respect to the reactant concentration. For this functionality of a_f on f, however, the activity is quite sensitive to the magnitude of θ_d . Although not shown here, the activity is also sensitive to the dependence of a_f on f.

Figure 7 shows that the magnitude of the maximum in the product concentration is insensitive to reactant concentration dependence of the fouling reaction. These curves have been developed by adjusting θ_m to give a product concentration of 0.3 at five time constants.

We observe that the initial activity can be extrapolated using Equations 27 and 28 if we know the dependence of a_f on f   and if we know θ_d . A general approach to finding these quantities and the reason why we use $a_f = f^6$ is an involved story that will be the subject of a later publication.

Legend of Symbols

a	catalyst activity
a_m, a_f	activity for main and fouling reactions
C, C_o	concentration of reactant leaving and entering reactor
f	fraction of sites unfouled
F_1, F_2	mathematical expression for rate of reaction with and without deactivation
F_3	mathematical expression for activity
k_1, k_{-1}	forward and reverse reaction rate constants
k_m, k_F	rate constants for main and fouling reactions
K_i	equilibrium constants
m, n	order of fouling and main reactions with respect to reactant
Q	volumetric flow rate of reactor feed
R	rate of main reaction
t, τ	time and dimensionless time
V_R	reactor volume
W	catalyst loading (weight)
θ_m, θ_d	dimensionless main and fouling reaction rate constants

Literature Cited

1. Butt, J. B., Wachter, C. K. and Billimoria, R. M., <u>Chem.</u>
    <u>Eng. Sci.</u> <u>33</u>, 1321 (1978).

2. Reiff, E. K. and K. B. Spall, private communication.

3. Blanding, Forest, <u>Ind. Eng. Chem.</u> <u>45</u>, 1186 (1953).

Poisoning Effects in Temperature-Increased Fixed-Bed Reactor Operation

A Comparison of Experimental Results and Model Simulation

GEORGE J. FRYCEK and J. B. BUTT

Department of Chemical Engineering, Northwestern University, Evanston, IL 60201

A variation of the constant conversion policy has been used to investigate the poisoning of a Ni-kieselguhr catalyst by thiophene. Hydrogenation of benzene was used as the model exothermic reaction. This alternative policy required that the conversion be allowed to decline under deactivating conditions in an isothermal fixed bed reactor. Upon reaching a lower conversion limit, the feed impurity was removed from the feed and the bed temperature was increased to bring the average bed activity to a higher level and thus also the conversion of benzene. Comparison of experimental conversion vs. time and average isothermal bed temperature were made against a one-dimensional pseudohomogeneous plug flow reactor model utilizing separable kinetics. Generally, excellent agreement between experiment and simulation were obtained for the first deactivation cycle. However, beyond the first cycle, the match between model and experiments was less satisfactory. In particular, the experimental results declined in a convex manner while the simulation decayed exponentially; temperature increase requirement (TIR) and decay times were reasonably well predicted for most cycles.

Industrially, catalyst activity maintenance is often screened via "temperature increase requirement" (TIR) experiments. In these experiments, constant conversion is established and the rate of temperature increase required to do so is used as a measure of the resistance of the catalyst to deactivation. However, this type of operation may mask the effect of particle size, temperature, temperature profile, and heat of reaction on poison coverage, poison profile, and the main reaction rate. This masking may be particularly important in complicated reactions and reactor systems where the TIR experiment may produce positive feedback. The alternative approach presented here has been used in an attempt to determine the importance of some of the above parameters. Another primary objective of this research has been to determine how well one might model the dynamic behavior of the system in an a priori fashion where the parameters used in the

modeling were determined via independent experimentation, as
reported in prior work (2-4).

Experimental

A stainless steel tubular reactor, which was approximately 16mm
I.D., was used to maximize the rate of heat transfer to and from a
glass bead diluted bed. The diluted bed was used to minimize
local heat generation and was approximately 50cm in length. Two
temperature controllers and five autotransformers were used to
control the reactor temperature profile along the axial length of
the reactor as shown in Figure 1. The controller thermocouples
were placed at the top and bottom of the reactor. The top
controller was responsible for maintaining a constant inlet feed
temperature. The bottom controller and the five variacs were used
to maintain the desired temperature profile. A centerline
thermocouple was used to measure this axial temperature profile as
well as to serve as a guide for changes in variac settings. These
changes were a result of a moving active zone from poisoning.
Thermocouples used were of type J, 0.040"O.D., and were grounded
to minimize response time. An outer thermowell was occasionally
used to give an indication of radial gradients.
     Solutions of benzene and benzene-thiophene were fed via a
parallel-reciprocal syringe pump. These solutions were then
vaporized and mixed with hydrogen. Either the poisoned or pure
feed streams could be passed through the reactor, as shown in
Figure 2, through the use of a four-way valve and a by-pass
reactor. Gas compositions were measured by a thermal conductivity
gas chromatograph. Experimental conditions are given in Table I.

Table I. Experimental Operating Conditions

Run	6	7	8	9	10	11
Average pressure (10^{-5})[Pa]	1.1961	1.1961	1.2198	1.1961	1.1851	1.2063
Bed length (10^1)[m]	4.667	4.659	4.667	4.699	4.699	4.667
Benzene molar flow (10^7)[Kg-mole/min]	8.795	8.795	22.069	8.720	8.720	22.147
Mole fraction benzene (10^2)	2.151	2.151	5.397	2.132	2.132	5.416
Mole fraction hydrogen (10^1)	9.784	9.784	9.457	9.783	9.783	9.457
PPM thiophene	134	134	336	341	341	122

All experiments: Cross sectional area for flow = 2.026

$\times 10^{-4}$[m^2]; catalyst weight = 2.00 g; glass bead weight

= 150.0g; exit volumetric flow=1000 [ml/min]$\pm$5% (STP)
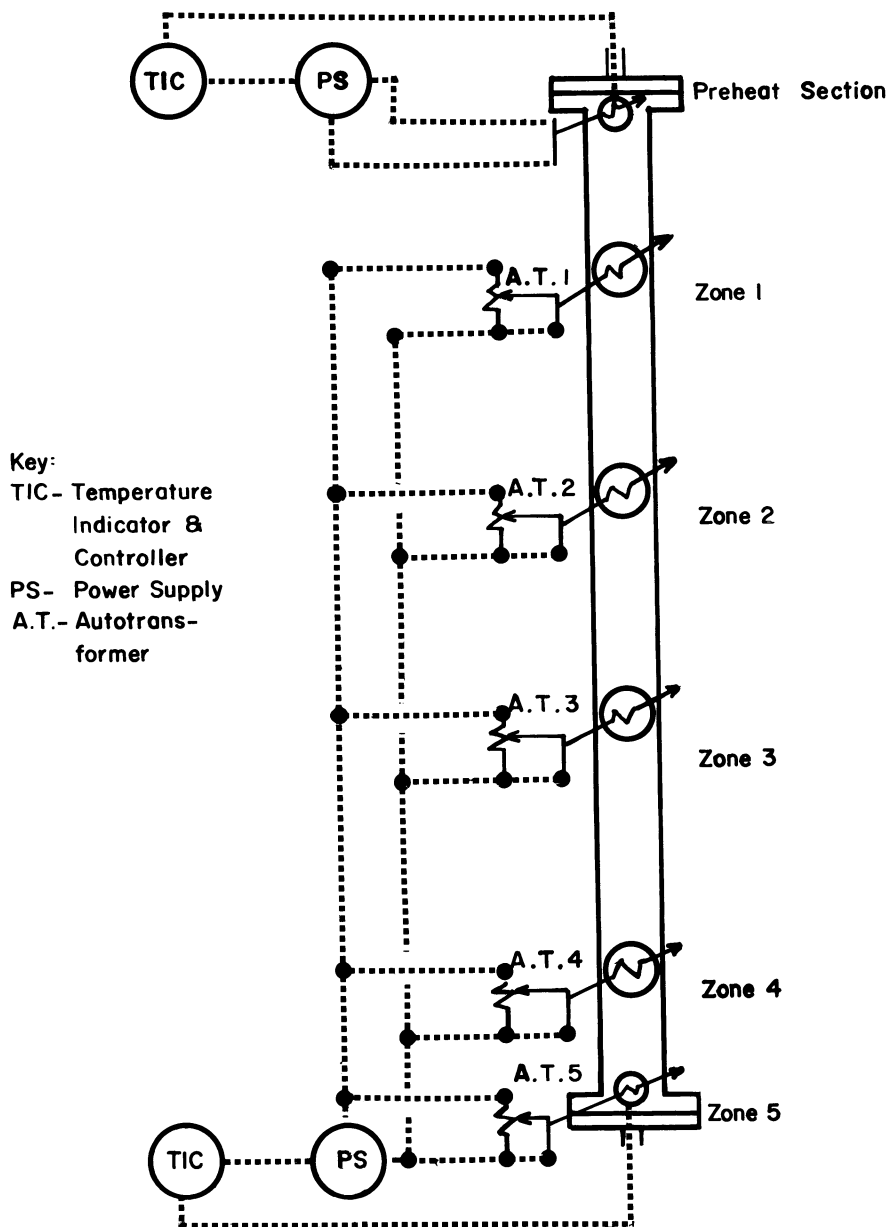
Figure 1. Temperature Maintenance Schematic.

Figure 2.   Experimental Apparatus.

GC: Gas Chromatograph
TC: Thermocouple
ΔP: Pressure Gauge
FV: Four-way Valve
BP: Bypass
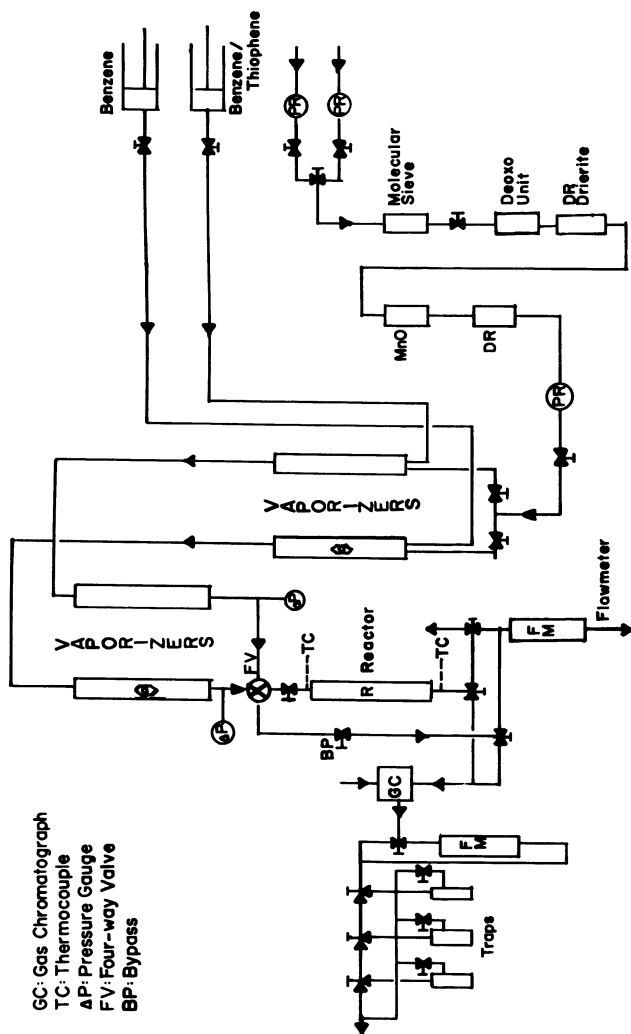
The hydrogenation catalyst used for this study was Harshaw Ni-0104T. The catalyst is 58% by weight Ni on kieselguhr and was crushed to 60-70 mesh (250-210 microns) for use in these experiments. The granules were then mixed with similar sized glass beads and reduced for 4 hours in hydrogen at 375°C.

Reactor Model

A one-dimensional pseudohomogeneous plug flow reactor model assuming isothermality was used to simulate experimental results. The continuity and kinetic expressions used were as follows:

Benzene Continuity Equation

$$\frac{\partial X_B}{\partial t} = \frac{\rho_{cat} \cdot MW_g}{\varepsilon \cdot \rho_g} \; r_B \cdot s \; - \; V_z \frac{\partial X_B}{\partial z} \tag{1}$$

Thiophene Continuity Equation

$$\frac{\partial X_T}{\partial t} = \frac{-\rho_{cat} \cdot MW_g}{\varepsilon \cdot \rho_g} \; r_T \cdot s \; - \; V_z \frac{\partial X_T}{\partial z} \tag{2}$$

In equations (1)&(2) "s" is the activity variable and is assumed to be separable from the intrinsic kinetics [1]. The active site balance is as follows, where the deactivation kinetics were determined by [2] and may be found in Table II:

$$\frac{\partial s}{\partial t} = r_D = \frac{-r_T}{M_T} = -k_D^o \; \exp[-E_D/RT]P \cdot X_T \cdot s \tag{3}$$

The hydrogenation rate equation for benzene, as investigated by [3] is:

$$-r_B = \frac{k^o K^o \exp[(Q-E)/RT] \; P^2 X_B X_H}{1 + K^o \exp[Q/RT] \; PX_B} \tag{4}$$

Table II. Kinetic Parameters

k[Kg-mole/Kg-s-Pa]	7.3506E-3	Ed[J/Kg-mole]	4.534E+6
K[1/Pa]	2.2652E-9	kd[1/(Pa-s)]	1.802E-4
E[J/Kg-mole]	5.3398E+7	*M_T[Kg-mole/Kg]	8.1E-4
Q[J/Kg-mole]	4.6585E+7		

*M_T was determined empirically and found to be well within the bounds found by previous researchers [2,5,6].

The benzene kinetic parameters used for the above expression were those reported by Onal [4] and are given in Table II. The boundary conditions used in the simulation were:

$$z=0 \quad X_B = X_B^{\;o} \;\;;\;\; X_T = X_T^{\;o}$$
$$t=0$$
$$s(z) = 1.0 \tag{5}$$

A major assumption in the above modeling was that one could assume that the poisoning process was slow enough that the assumption of quasi steady-state could be made. This eliminated the accumulation terms in equations (1)&(2) and allowed them to be solved by a 4th order Runge-Kutta method. Further, by assuming that the thiophene term in equation (3) was a constant, one could preserve its integrated exponential characteristics. The integrated activity balance was then solved for each interior point within the reactor. The time step size was governed by the rate at which the catalyst deactivated. The criterion used to control the time step allowed a maximum drop in conversion of no more than 7%. Violation of this requirement resulted in a halving of the time step. Further assumptions were that the poisoning process was irreversible, the benzene concentration was low enough that volume changes were negligible and that heat and mass transfer limations were absent. These restrictions were all obeyed in the experimentation reported here.

Reactor Dynamics and Simulation

Start Up Dynamics. Introduction of benzene into a fresh bed resulted in an initial non-isothermal temperature profile. Through the use of the autotransformers, one was able to override the system control and thus line out the temperature profile. Figure 3 depicts a typical reactor start up for a fresh bed.

First Cycle Poisoning Dynamics. Upon attaining an isothermal temperature profile for an impurity free feed, the next phase of the experiment was begun. Thiophene was introduced into the benzene feed as the feed impurity. The thiophene also caused another problem which manifested itself as a migrating temperature depression, a result of the active zone moving towards the end of the reactor. This movement of the reaction zone decreased the heat generation at the upper section of the reactor and therefore a temperature depression resulted. A comparsion between the simulated activity profile and the temperature migration in Fig.4 illustrates the above phenomena.

Temperature Increase Dynamics after the First Cycle. As with the start up of the bed, subsequent temperature cycles resulted in the formation of a mild hot spot. The occurrence of this temperature fluctuation is undesirable since the past history of the catalyst may be altered. The adsorption of thiophene upon the active hydrogenation sites was assumed to be irreversible and therefore unaffected by temperature. However, as will become apparent later, the effect of temperature may have altered the poison coverage/or profile. Lyubarski, et. al [7] determined that, as a result of the hydrogenation of thiophene and subsequent hydrogenolysis to butane, the adsorption capacity of a suported Ni
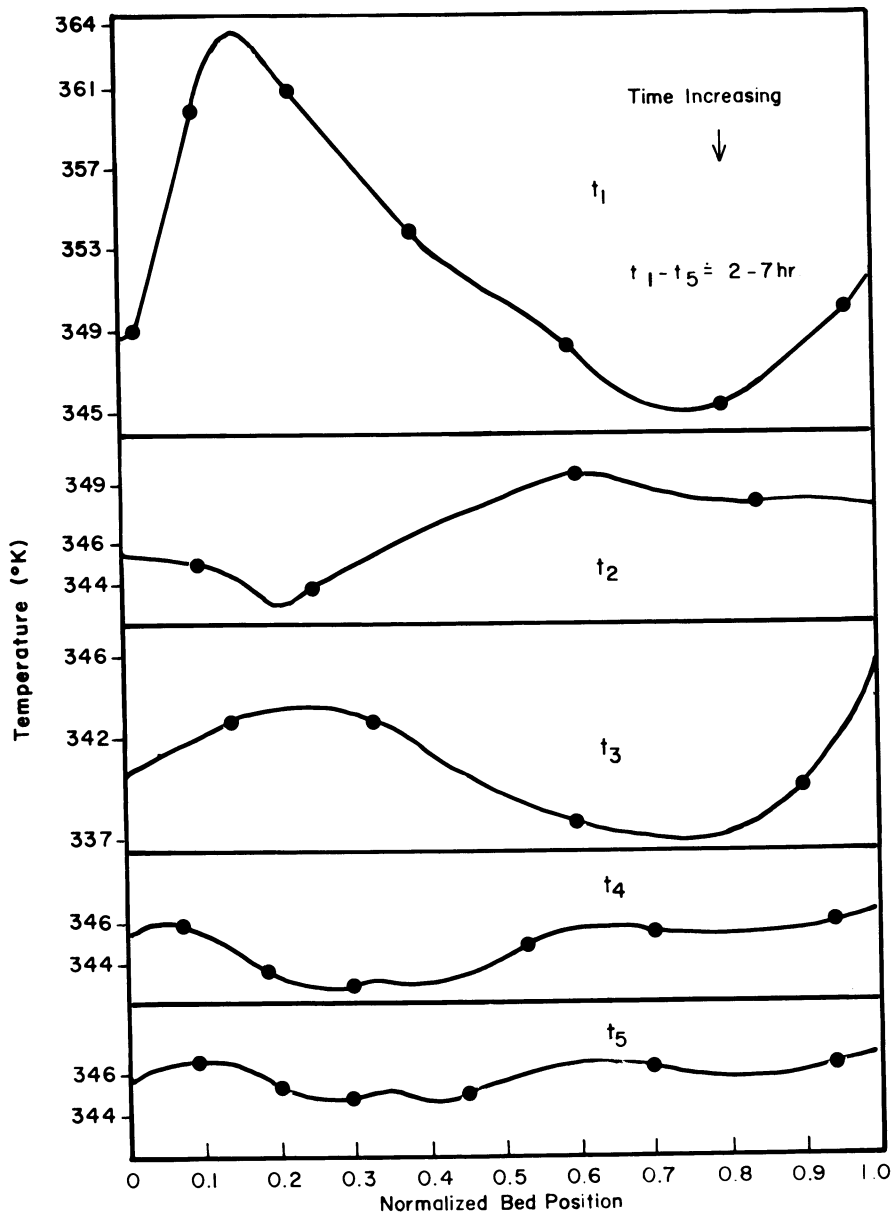
Figure 3.   Representative Axial Temperature Profiles:
Start Up Run 6: Low Benzene.
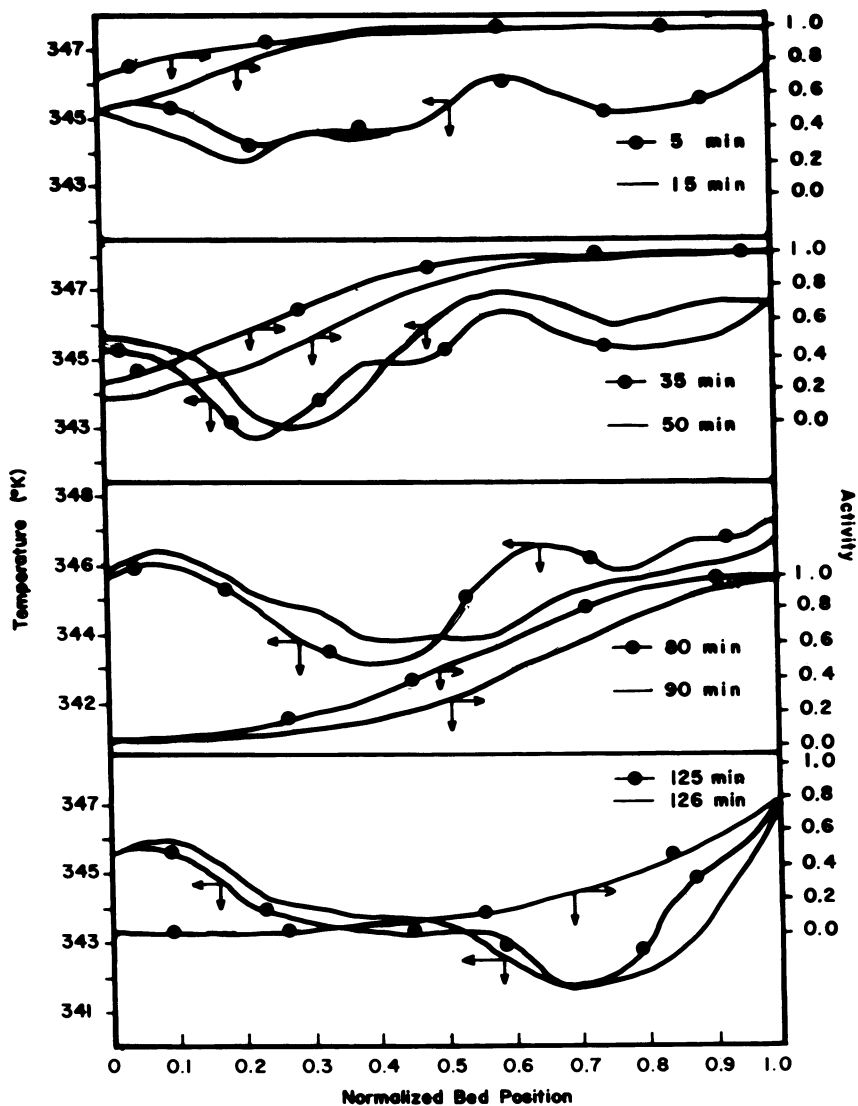
Figure 4.　Axial Profiles During First Cycle Deactivation
Run 6: Low Thiophene.

was altered for temperatures of 100-150°C. This temperature
simulation and experimental TIR and conversion decay profiles.

Decay Behavior and Simulation. Comparison of experimental versus
simulated results yields some very interesting insights into the
behavior of both the model used to simulate the deactivation and
the experimental system itself. Parametric values used in
simulation of the dynamics of the system may be found in Tables I
and II. Each experiment may be divided into distinct sections
which will be termed cycles. The end of a cycle was followed by a
temperature increase and a concomitant increase in conversion.
Good agreement was found to exist between simulation and
experiment during the first cycle as shown in Figure 5 through
Figure 10. This agreement supports the kinetic model which was
used to simulate the system. Temperature and decay times were
reasonably well predicted for both regimes of slower and faster
deactivation. Figure 8, which describes Run 9, shows that the
catalyst prematurely deactivated with respect to the model.
Examination of Run 9, Figure 8, and Run 10, Figure 9, shows that
for the first cycle the experimental data are below the simulation
curve. This may indicate that the assumption of quasi steady-
state may have been questionable at this point. However,
reproducibility for all experiments was very good. This
reproducibility is important when experiment and model begin to
deviate. Such is the case for the cycles after the first.
Looking at Figure 5 through Figure 10 one observes that the
simulation temperature prediction for a desired conversion in the
2nd and some 3rd cycles was usually good. However, the conversion
decay profiles deviate substantially from each other. The
experimental results decay in a convex manner while the simulated
results decay exponentially. This deviation may have been a
result of the temperature excursions which resulted on each TIR.
Thus, as mentioned earlier, the past history of the catalyst may
have been altered. Despite this, the decay times are fairly well
predicted. Some 3rd cycle predictions completely failed as shown
in Figures 8 and 10. These appear to be a result of the
temperature affecting the chemisorption of the thiophene on the
active catalyst. In separable kinetic terms, the resistance to
deactivation in the above outwardly manifests itself as an
increase in the activation energy for deactivation. As the bed
temperature is increased, the catalyst appears to have a higher
resistance to poisoning.

Conclusions

The single cycle, falling conversion TIR experiment seems to be a
reliable measure of decay rate. However, for multiple cycles,
this system appears to be vulnerable to problems similar to those
of the constant conversion TIR policy. Elimination of temperature
upsets and regulated temperature increases need to be addressed in
the future.
    The kinetic model used to simulate the reaction and poisoning
process appears to be adequate for the experiments performed.
However, the influence exerted by small temperature upsets after
each cycle may necessitate a more detailed simulation of heat
tranfer effects if more quantitative agreement with experiment is
required.
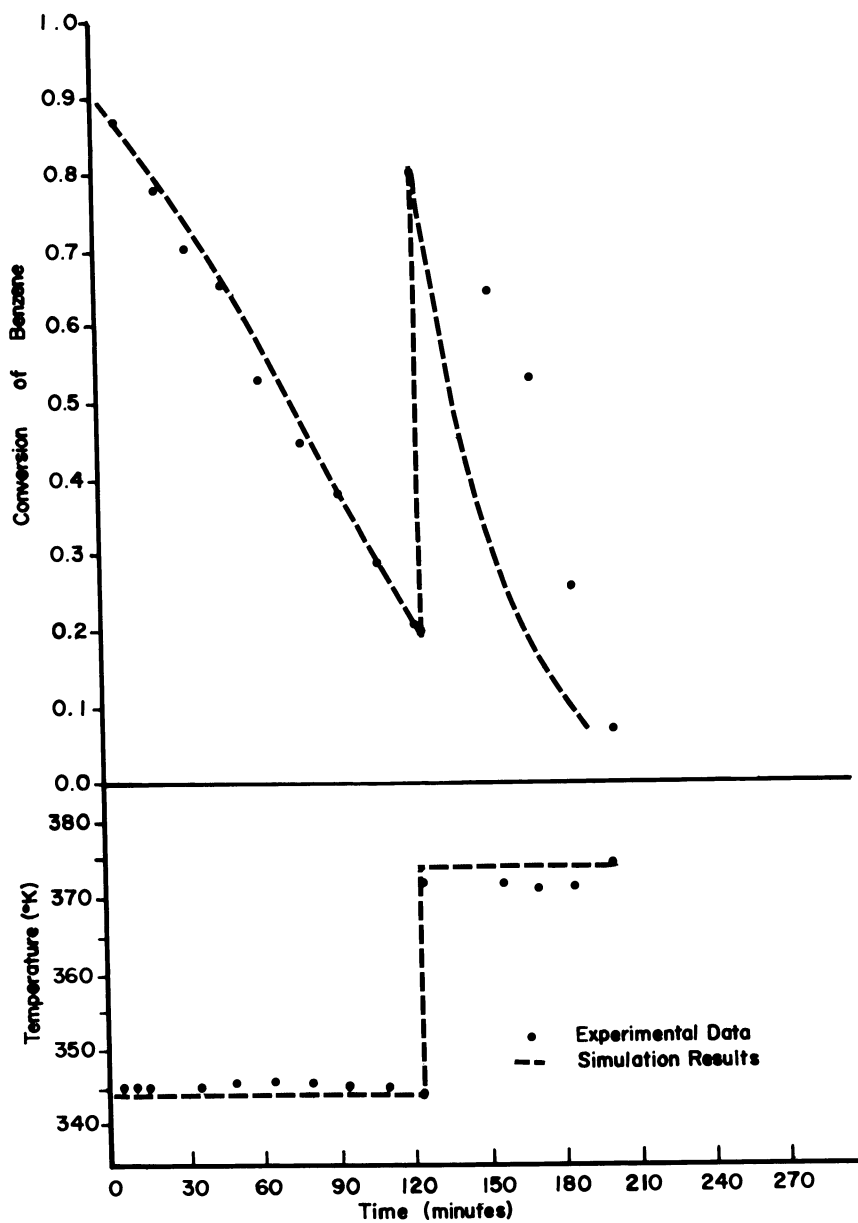
Figure 5.   Simulation of Run 6: Low Benzene and Low
Thiophene.
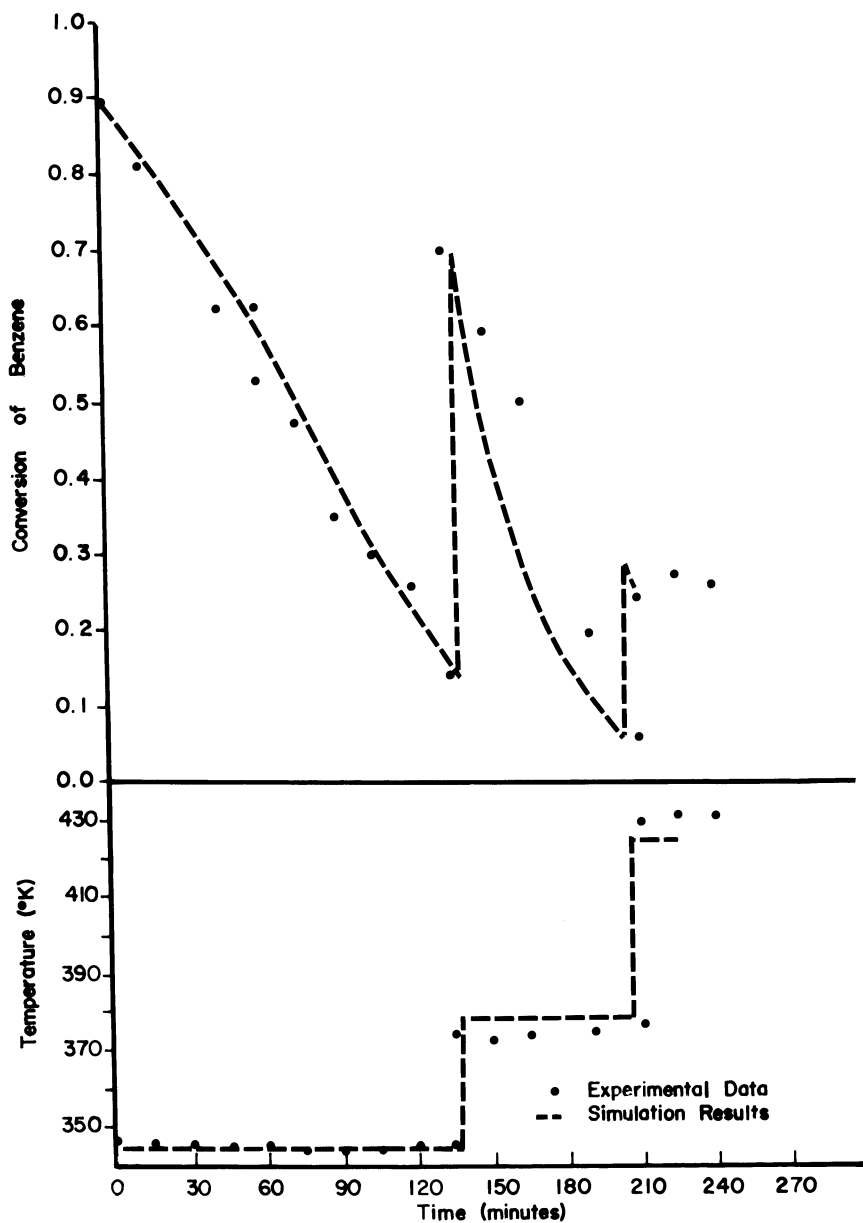
Figure 6.   Simulation of Run 7: Low Benzene and Low Thiophene.
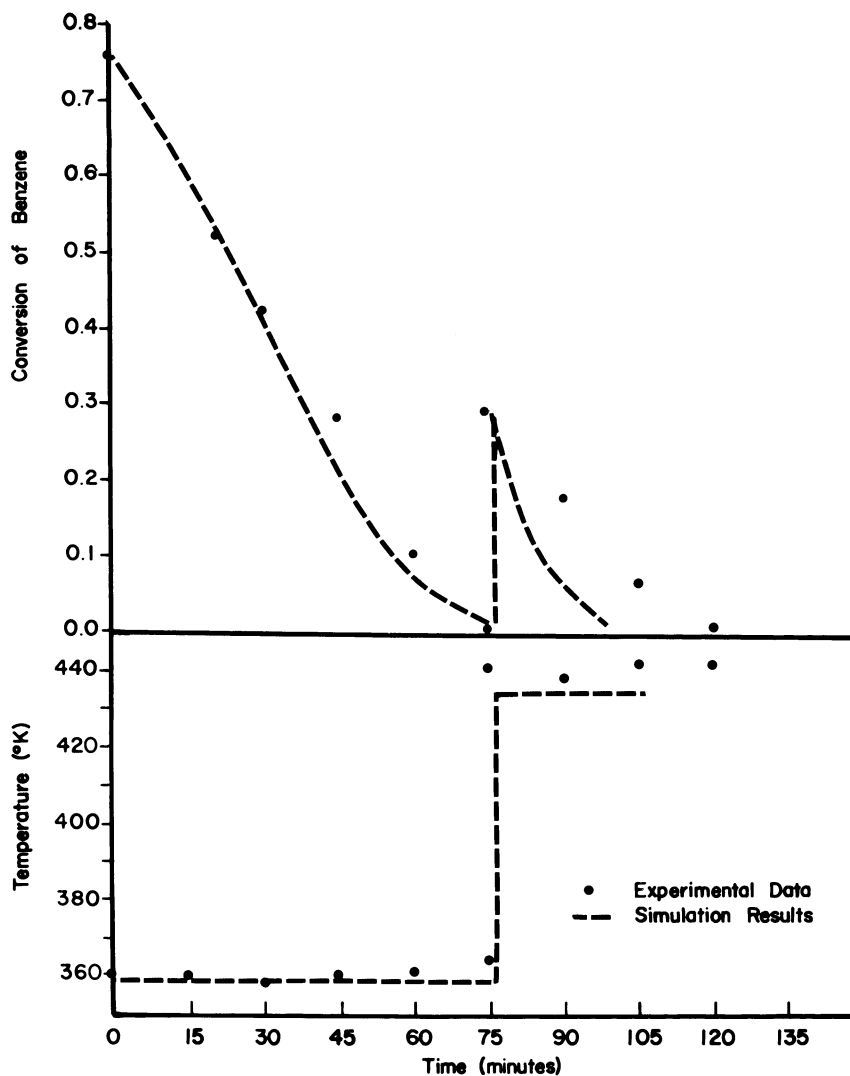
Figure 7. Simulation of Run 8: High Benzene and High Thiophene.
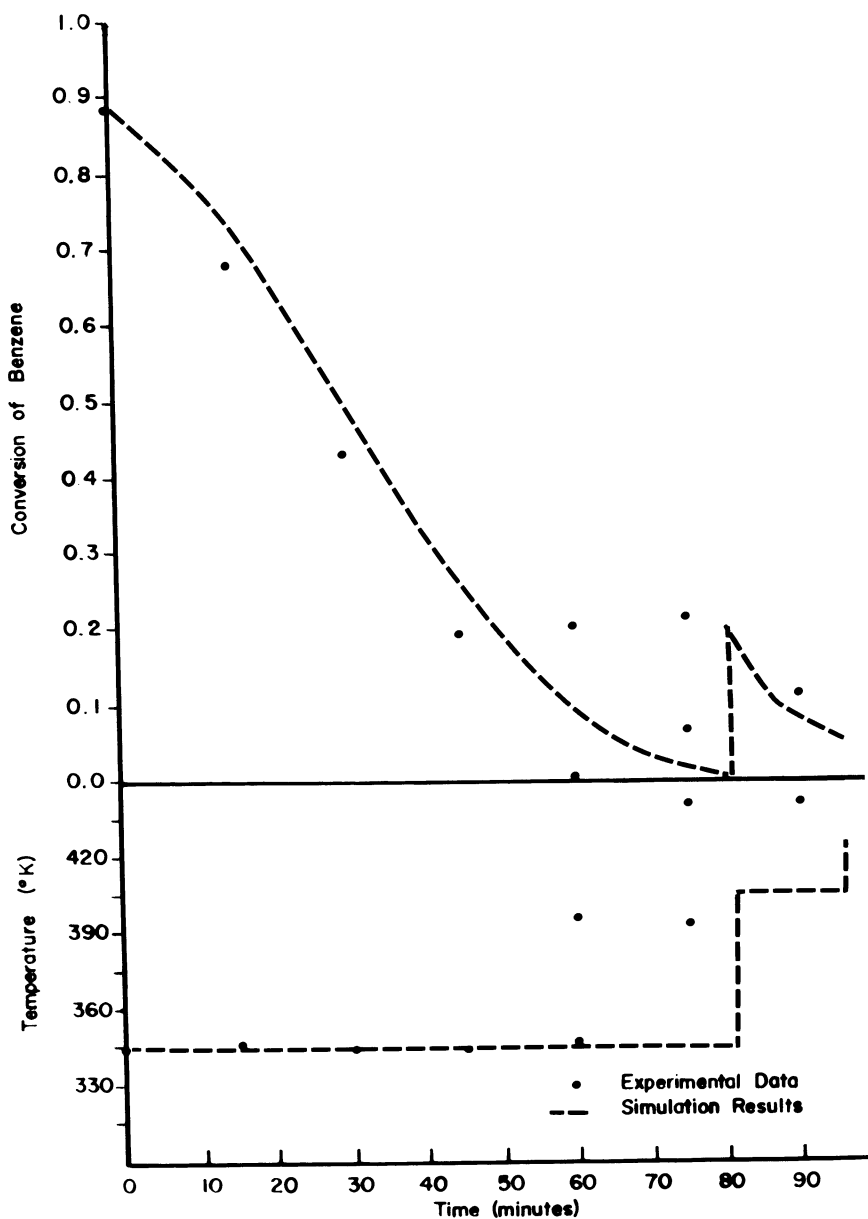
Figure 8.   Simulation of Run 9: Low Benzene and High
Thiophene (sufficient conversion to conduct a 3rd Cycle
was not obtained for T up to 490°K).
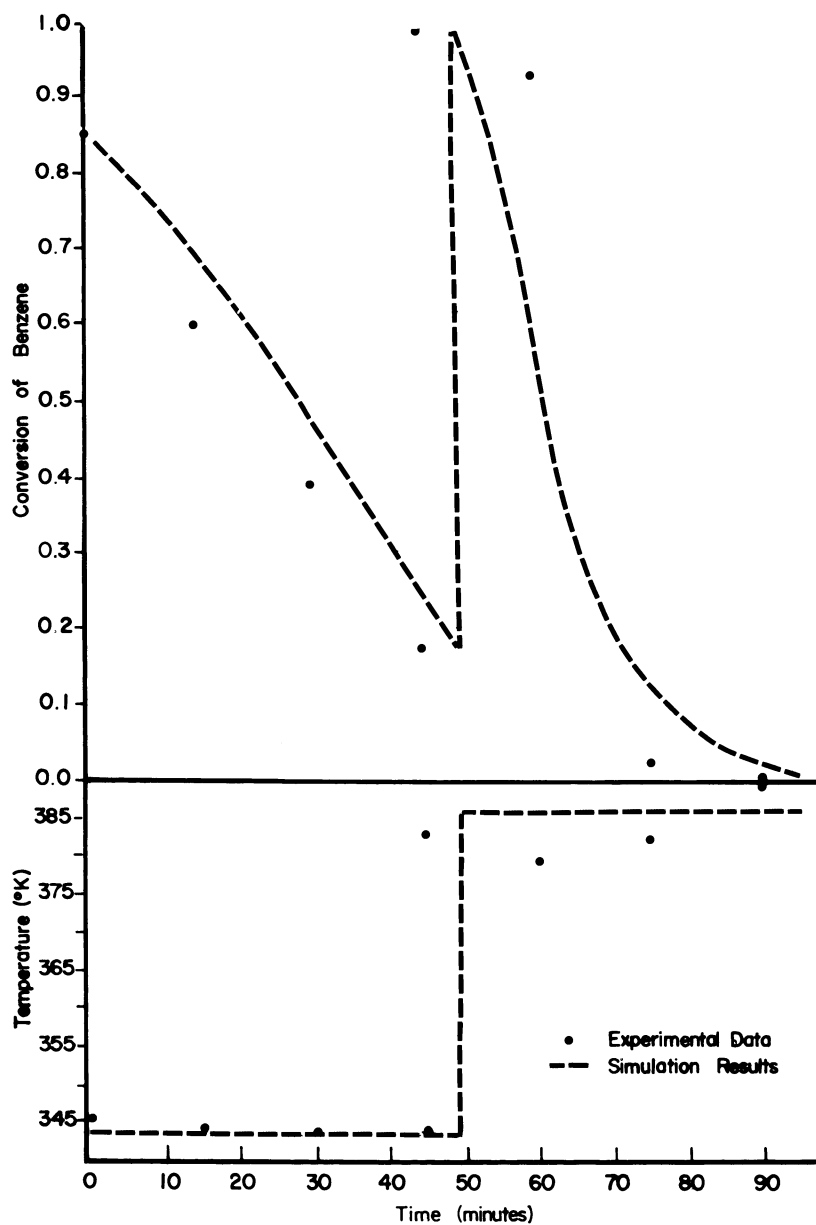
Figure 9.   Simulation of Run 10: Low Benzene and High Thiophene.
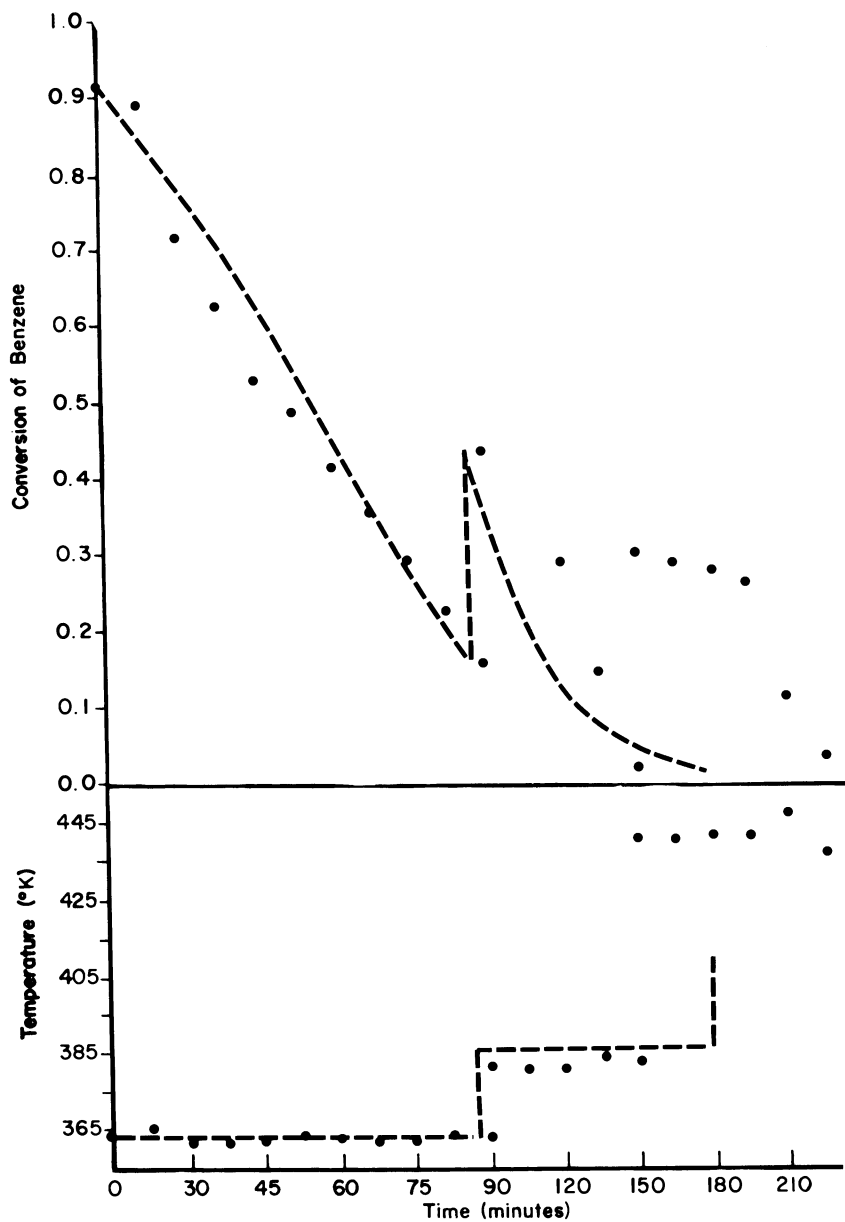
Figure 10. Simulation of Run 11: High Benzene and Low Thiophene (sufficient conversion to conduct a 3rd Cycle was not obtained for T up to 490°K).

NOMENCLATURE

E, E_D	Activation energies for benzene hydrogenation and thiophene poisoning, respectively (J/Kg-mole)
k^o	Pre-exponential factor for benzene hydrogenation rate constant (Kg-mole/Kg(catalyst)-sec-Pa)
k_D^o	Pre-exponential constant for thiophene poisoning $(Pa-sec)^{-1}$
K^o	Pre-exponential factor for adsorption rate constant $(Pa)^{-1}$
L	Catalyst bed length (m)
M_T	Adsorption capacity of catalyst for thiophene (Kg-mole (thiophene)/Kg(cat))
MW_g	Molecular weight of the gas phase (Kg/Kg-mole)
P	Average pressure (Pa)
Q	Benzene heat of adsorption (J/Kg-mole)
$-r_B$	Rate of benzene hydrogenation (Kg-mole/Kg(catalyst)-sec) and (Kg-mole/m^3 (particle)-sec)
$-r_D$	Rate of deactivation (sec^{-1})
$-r_T$	Rate of thiophene chemisorption (Kg-mole(thiophene) /Kg(catalyst)-sec)
R	Universal gas constant (J/Kg-mole-^{o}K)
s	Catalytic activity
t	Time (sec)
T	Temperature (^{o}K)
V_z	Interstitial gas velocity (m/sec)
X_B, X_H, X_T	Mole fraction of benzene, hydrogen, and thiophene
X_B^o, X_T^o	Initial mole fraction of benzene and thiophene
z	reactor axial position (m)

Greek Symbols

ε	Bed void fraction (m^3 void/m^3 total)

ρ_g Density of gas phase (Kg/m^3)

ρ_{cat} Bulk density of catalyst (Kg/m^3)

Literature Cited

1.   Szepe, S.; Levenspiel, O.; Proc. 45h Euro. Symp. Chem. Reac. Eng., 1968: 265- Pergamon Press, Oxford.

2.   Weng, H.S.; Eigenberger, G.; Butt, J.B.; Chem. Eng. Sci. 1975 30, 1281.

3.   Kehoe, J.P.G.; Butt, J.B. J. Appl. Chem. Biotechnol. 1972, 23, 22.

4.   Onal, I., Ph.D. Dissertation, Northwestern University, Evanston, IL, 1981.   Available from University Microfilms.

5.   Price, T.H.; Butt, J.B. Chem. Eng. Sci. 1977, 32, 393.

6.   Billimoria, R.M.; Butt, J.B. Chem. Eng. J. 1981, 22, 71.

7.   Lyubarski, G.D.; Ardeeva, L.B.; Kul'kova, N.V. Kinet. and Catal. 1962, 3, 102.

Modeling of Tubular Nonisothermal Nonadiabatic Packed-Bed Reactors with Catalyst Poisoning

QAMARDEEP S. BHATIA and VLADIMIR HLAVACÈK

Department of Chemical Engineering, State University of New York at Buffalo, Amherst, NY 14260

One-and two dimensional models are used to des-
cribe deactivation of nonadiabatic packed bed reactors.
The models are based on the quasistationary assump-
tions. Numerical methods of integration of both
models are described. It is shown that the deacti-
vation process can be reasonably described by the
one-dimensional model. The two-dimensional model
must be used only for a deactivation process
having high activation energy which is carried out
in tubes of large diameter. Two major regimes of
deactivation are described: (a) standing wave deac-
tivation and (b) travelling wave deactivation.
The former corresponds to low rates of deactiva-
tion,while for high deactivation rates,travelling
wave deactivation occurs. For the standing wave
deactivation,the hot spot temperature decreases
during deactivation, while for the travelling wave deac-
tivation,constant pattern profiles exist and the
hot spot temperature increases.

Catalyst deactivation is of major concern in catalyst deve-
lopment and design of packed bed reactors. Decay of catalytic
activity with time can be caused by several mechanisms such as
fouling, sintering and poisoning. Although much fundamental
experimental work has been done on deactivation,very little atten-
tion has been focused on modelling and systematic analysis of non-
adiabatic fixed bed reactors where a deactivation process occurs.
Theoretical and experimental results on deactivation have
been summarized in two reviews by Butt (1,2). Previous work of
particular interest to the present study has been done by Blaum
(3) who used a one-dimensional two-phase model to explore the dy-
namic behavior of a deactivating catalyst bed. Butt and coworkers
(4,5,6)have performed deactivation studies in a short tubular
reactor for benzene hydrogenation for both adiabatic and nonadia-
batic arrangements. They experimentally observed both the stand-
ing (6) and travelling (4) deactivation wave. Hlavacek

et. al. (7, 8) have shown that the deactivation process give rise to transient hot spots which move downstream and may grow beyond the adiabatic temperature limit. This growing transient hot spot is a certain type of the "wrong-way" behavior of a packed bed. The growing transient hot spot may damage the catalyst and result in complications in reactor operation (9).

   At present there is no systematic work on simulation and design of packed bed nonadiabatic reactors of industrial size where a deactivation process occurs. The purpose of this work is to analyze the operation of a nonadiabatic deactivating cata- lyst bed and to develop simple techniques for simulation. Based on hydrogenation of benzene, full-scale reactor behavior is calcu‐ lated for a number of different operational conditions. Radial transport processes are incorporated in the model, and it is shown that the two-dimensional model is necessary in some cases.

Mathematical Models

   Both one-and two-dimensional quasi-homogeneous models have been used to simulate the reactor. The following major assumptions have been made: (a) the heterogeneous system, consisting of the solid particles and reacting gas, is treated as though it were ho- mogeneous and a hypothetical anisotropic continuum is considered. (b) axial dispersion processes are neglected. Since systematic analysis by Puszynski et al.(10) reveals that for reactions with a lower activation energy (e.g., hydrogenation reactions) the axial dispersion term does not play an important role in modelling of a full size reactor and may be omitted, and (c) the deactivation pro- cess is very slow and hence a quasi-steady state assumption can be made.

   One-dimensional model. Reactant balance:
$$u \frac{dC}{dz} = -\theta \rho\, r_c \qquad (1)$$

Poison balance:
$$u \frac{dC_p}{dz} = -\theta \rho\, r_p \qquad (2)$$

Energy balance:
$$u < \rho C_{pf} > \frac{dT}{dz} = \theta(-\Delta H)\, r_c \rho + \frac{2U}{R_o}(T_c - T) \qquad (3)$$

Activity balance:
$$\frac{d\theta}{dt} = r_D \qquad (4)$$

Initial conditions: t=0, z=0: $C=C_o$, $C_p = C_{po}$, $T = T_o$, $\theta = 1.0$ (5)

   Two-Dimensional Model. Reactant balance:
$$\varepsilon D_r \left(\frac{\partial^2 C}{\partial r^2} + \frac{1}{r} \frac{\partial C}{\partial r} \right) - u \frac{\partial C}{\partial z} - \theta \rho\, r_c = 0 \qquad (6)$$

Poison balance:
$$\varepsilon D_{pr} \left(\frac{\partial^2 C_p}{\partial r^2} + \frac{1}{r} \frac{\partial C_p}{\partial r} \right) - u \frac{\partial C_p}{\partial z} - \theta \rho\, r_p = 0 \qquad (7)$$

Energy balance:

$$\lambda_{er}(\frac{\partial^2 T}{\partial r^2} + \frac{1}{r}\frac{\partial T}{\partial r}) - u <\rho C_{pf}> \frac{\partial T}{\partial z} + \theta(-\Delta H)\rho r_c = 0 \qquad (8)$$

Activity balance:

$$\frac{d\theta}{dt} = r_D \qquad (9)$$

Boundary conditions:

$$0 < z < L, r=0: \quad \frac{\partial C}{\partial r} = \frac{\partial C_p}{\partial r} = \frac{\partial T}{\partial r} = 0 \qquad (10)$$

$$r=R_0: \frac{\partial C}{\partial r} = \frac{\partial C_p}{\partial r} = 0 \qquad (11)$$

$$-\lambda_{er}\frac{\partial T}{\partial r} = h_w(T - T_w) \qquad (12)$$

$$t=0: \quad \theta=1.0 \qquad (13)$$

Model Reaction. The benzene hydrogenation on nickel-kieselguhr has been selected as a model reaction. This reaction is well understood and can serve as a typical representative of hydrogenation reactions. Butt (4,5) and Pexider et al.(11) have studied this reaction in laboratory and pilot plant reactors, respectively. Pexider's data have been obtained from a nonadiabatically operated reactor. The reaction rate expression has:

$$r_c = 86.7 \exp(-\frac{4,260}{RT})p_B^{0.685} \quad p_H^{0.362} \qquad (14)$$

The reactant mixture contains excess of hydrogen and thus the concentration of hydrogen does not change appreciably during the course of the reaction. Therefore, there is no need for a hydrogen balance. The benzene hydrogenation is an exothermic reaction with $(-\Delta H)=49.9$ kcal/mol.

Catalyst deactivation is assumed to take place by a poisoning mechanism only. The deactivation of catalyst by thiophene will serve as a model deactivation reaction. Weng et al. (4) analyzed the deactivation data and proposed a rate equation, linear in concentration of poison, x_p, and activity θ:

$$r_D = -k_d^\circ \exp(-\frac{E_D}{RT})Px_p\theta \qquad (15)$$

Thiophene consumption is given by:

$$r_p = -M_T r_D \qquad (16)$$

where M_T is the thiophene adsorption capacity. It accounts for an irreversible adsorption on the catalyst surface. Weng et al. (4), found a value $M_T = 1.03 \times 10^{-3}$ kmol/kg cat. In our study, we will also analyze poisoning processes having different activation energy and pre-exponential factors as well.

The values of parameters used in this study are reported in Table I.

Table I.

Parameters Used for Modeling the Reactor

Reactor length, $L=2 - 3.5$[m]
Reactor radius, $R_o=1.27 \times 10^{-2}$ and $R_o=2.54 \times 10^{-2}$[m]

Bed void fraction, $\varepsilon=0.36$

Temperature of cooling medium, $T_c=373$[K]

Concentration of benzene, $C_o=18.24$[mol/m^3]

Concentration of poison, $C_{po}=0.00958-0.02$[mol/m^3]

Initial temperature, $T_o=298-373$[K]

Radial dispersion coefficients for benzene and poison,

$$D_r=D_{pr}=3.94 \times 10^{-4}[m^2/sec]$$

Overall heat transfer coefficient, $U=125$[kcal/hr m^2 K]

Particle diameter, $d_p = 0.3175 \times 10^{-2}$[m]

Reynolds number, $Re=209$

Reaction heat, $(-\Delta H)=49.9$[kcal/mol]

Average heat capacity, $< C_{pf} >=7.7$[kcal/m^{3}K]

Molar ratio in feed, $H_2/C_6H_6 = 20$

Numerical Solution of Governing Equations

One-dimensional Model. This model is represented by a set of hyperbolic first order equations, Eqs. 1-5.   These equations can be integrated by using a splitting strategy, i.e. by sequential integration in space and time. The splitting algorithm will reduce the two-dimensional problem to a sequence of one-dimensional equations.

The initial value problem, Eqs. 1-3, can be integrated by any marching algorithm which is based on the Runge-Kutta or Adams-Moulton techniques. Based on the calculated space profiles of C, C_p and T Eq. 4 is integrated and a new space distribution of θ is evaluated. This distribution is used for a new integration of Eqs. 1-3, etc. Since both in the z and t direction the old profiles must be stored to calculate a new profile, the simplest algorithm for integration should be preferred provided it is stable. We have used an explicit Euler technique. The mass and energy balances, Eqs. 1-3, have been integrated by a trapezoidal rule. This type of integration simplifies the bookkeeping process.

Two-dimensional Model. The same strategy has been used for a two-dimensional model. The mass and energy balances Eqs. 6-8 and Eqs. 10-13, have been integrated by a Crank-Nicolson procedure. After completing the calculation a new distribution of activity is evaluated from Eq. 9 by an explicit Euler integration.

    For the deactivation process studied, the time step $\Delta t=30$ min-
utes has been found to be satisfactory for both the one-and two-
dimensional models. The axial step size $\Delta z=0.02m$ has been used for
both models and 10 grid points in the radial direction have been
adapted for the two-dimensional descriptions. To improve the or-
der of approximation of the explicit integration process, the non-
linear reaction rate term has been evaluated at the $(i+1/2)$ level.
The values of concentration and temperature at $(i+1/2)$ have been
determined by extrapolation from the profiles $i-1$ and i.
    The computer time for simulating 50 hours of deactivation
was 13 seconds for the one-dimensional model and 15 seconds for
the two-dimensional model on the CDC Cyber 174 (13).

Results and Discussion

    The deactivation process in a tubular nonisothermal nonadia-
batic reactor depends on a number of kinetic and operational
parameters. There are two major questions which we would like to
answer: (a) can we use the one-dimensional model for simulation
of a deactivating bed and under what circumstances should the two-
dimensional model be considered?, (b) are there any general fea-
tures of a deactivating bed which would classify different condi-
tions of deactivation? We shall try to find general answers to
these questions.

    Agreement Between One-and Two-dimensional Models. From the
computational point of view, the simulation of a one-dimensional
model represents a rather simple problem than the calculation of
a two-dimensional case. Former systematic analysis (12),
indicated that the one-dimensional description is satisfactory for
parametrically insensitive regimes. The low sensitivity regimes
typically feature convex axial temperature profiles and not
excessive values of the hot spot temperature. Numerical
simulation of reactor operation under low parametric sensitivity
reveals an absence of inflection points of the radial temperature
profiles. Owing to the low values of the activation energy for
hydrogenation reactions parametrically insensitive regimes should
prevail for operation of these reactors. As a result, there are
good reasons that the two-dimensional model can be well approxi-
mated by the one-dimensional approximation.
    A comparison between axial temperature profiles of temperature,
activity, poison, and benzene concentrations calculated from one-
and two-dimensional models is presented in Figures 1-4, respecti-
vely. The values calculated from a two-dimensional model are
drawn in Figures 1-4 at the radial position $r=0.707R_0$. The theory
reveals (12) that the axial profile taken for a two-dimensional
model at $r = 0.707R_0$ should well agree with the one-dimensional
approximation. The calculated results prove that there is a very
good agreement between the one- and two-dimensional models.
There is a small difference in the vicinity of the hot spot.
The concentration profile are identical for both models.
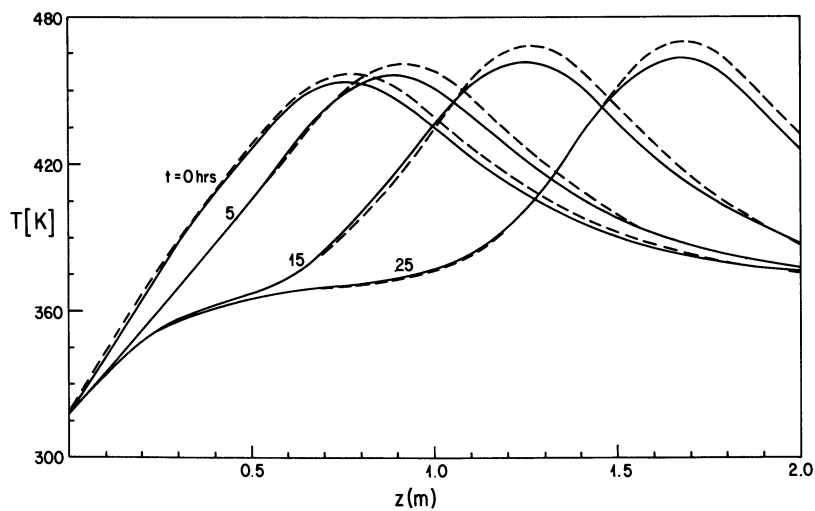
Figure 1. Axial Temperature profiles $E_D/R=545[K]$, $k_d^o=1.0$
_____ one-dimensional model   ----- two-dimensional model.
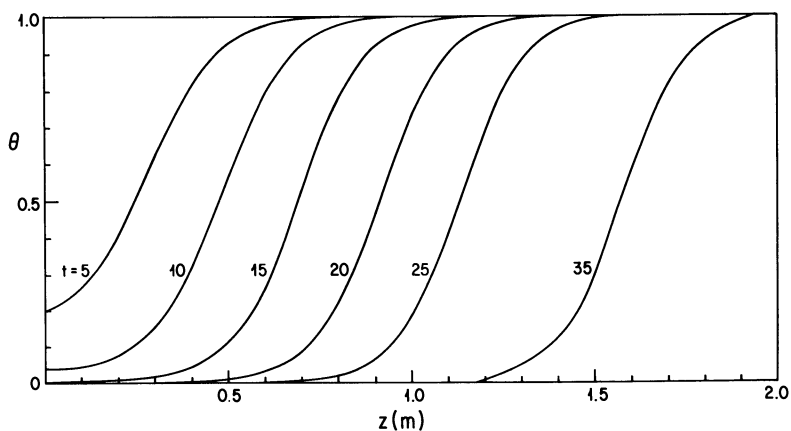
Figure 2. Axial profiles of activity, $E_D/R=545[K]$, $k_d^o=1.0$
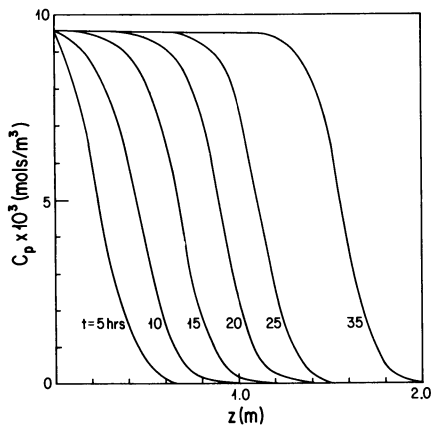
Figure 3. Axial profiles of poison concentration, $E_D/R=545$ [K], $k_d^{\circ}=1.0$.
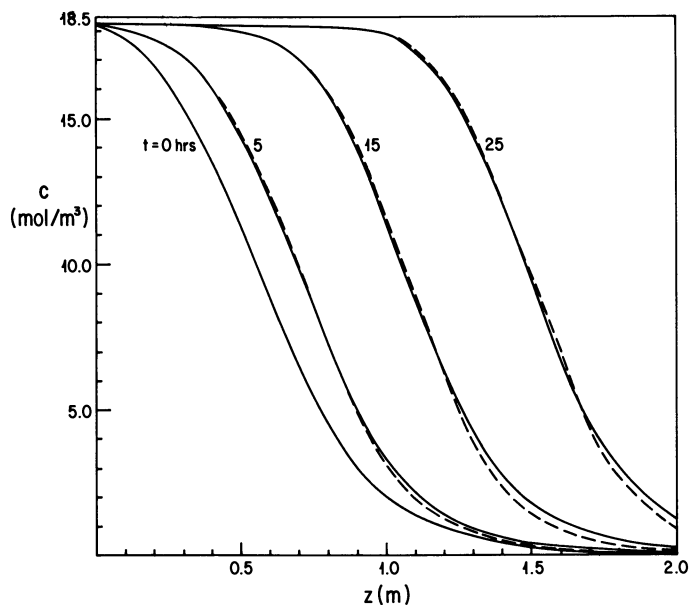
Figure 4. Axial profiles of benzene concentration $E_D/R=545$ [K], $k_d^{\circ}=1.0$. _____ one-dimensional model -----two-dimensional model.

The radial activity profile is a simple parabola-like function
with a minimum in the center of the tube. As a result, for a 2.54
cm tube, the deactivation process can be simulated very accurately
from the one-dimensional approximation. We can also notice that
both the one-and two-dimensional models predict correctly the
growing transient hot spot temperature. This effect was predicted
by Blaum (3) for extreme reaction conditions and was experimen-
tally observed by Mikus et al. (7). in a quasiadiabatic labora-
tory reaction. Evidently, this phenomenon can be observed also for
a rather mild condition in a deactivating bed of full size. After
25 hours of deactivation, the hot spot moved from z=0.75m to
z=1.65m and the temperature increased by 15°C.

   Frequently, for higher values of E_D or R_o, the one-dimensional
model can qualitatively predict a rather complex interaction
between the temperature and concentration fields. Such a situa-
tion is presented in Figures 5-7. For high values of E_D, the
activity θ is very sensitive to temperature fields and the activi-
ty calculated from one- and two-dimensional models can be diffe-
rent. For higher values of R_o (e.g. $R_o = 1"$), the activity profile
can be affected by both the temperature and concentration fields.
With higher temperatures, the consumption of benzene and poison
and the rate of deactivation is higher; however, the concentra-
tion of poison is lower. This complex interaction may result in
radial profiles of activity with minima outside the reactor axis
(c.f., Figure 8). Of course, the one-dimensional model cannot
correctly describe such a behavior.

   Deactivation Process and Waves in the Reactor. The complex
interaction between the reaction rate processes and irreversible
adsorption of the poison depends on a number of transport,
kinetic, and operational parameters. Nevertheless, certain
general properties of the deactivating bed can be found. Let us
return to Figures 1-4. We can easily note that after elapsing a
certain time the shape of the concentration profiles doesn't change
and the profiles propagate in the bed with constant speed. Such
profiles are frequently called "constant pattern profiles" or
"travelling waves." Evidently, the situation of constant pattern
profiles results if the rate of reaction and deactivation is
different. Consider for a moment consider the case where $r_p >> r_c$.
For $r_p \to \infty$, because of Eq. 2, a piston-like front results and the
poison will not penetrate in the reactor bed. The reaction will
occur in the fresh part of the bed. Obviously, for these considera-
tions, deactivation and reaction processes have strongly different
rates and both processes occur in different parts of the bed.
The deactivation takes place in the front part while reaction
occurs in the rear section. Evidently, the speed of the travelling
wave is given by the rate of deactivation. From Figure 9, we
can infer that an envelope of temperature profiles exist. This
envelope is determined by a completely deactivated bed. In the
part of the reactor specified by the envelope, the fresh feed is
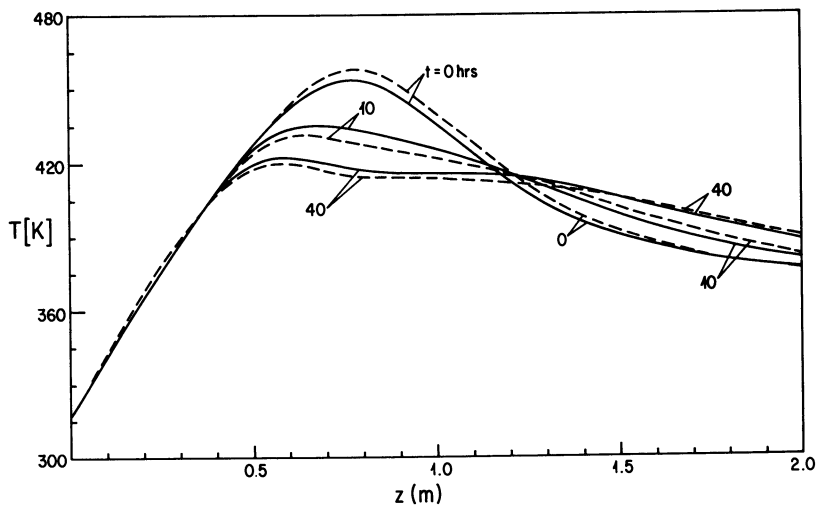
Figure 5. Axial temperature profiles, $E_D/R=15,000[K], k_d^o=10^{13}$ _____ one-dimensional model ----- two- dimensional model.
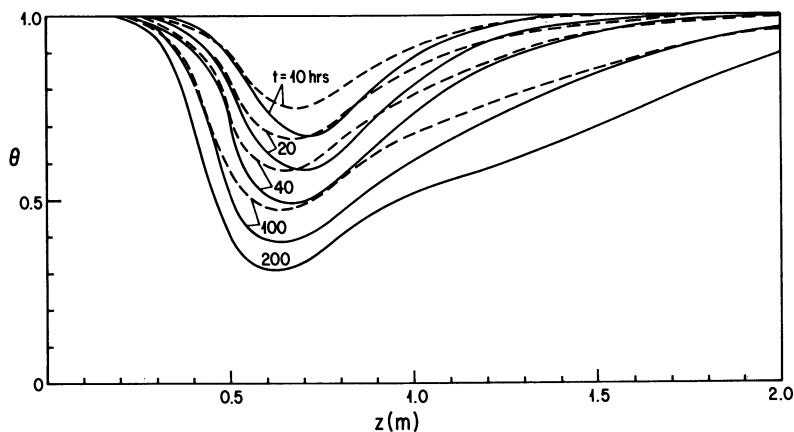
Figure 6. Axial profiles of activity, $E_D/R=15,000[K], k_d^o= 10^{13}$. _____ one-dimensional model   ----- two-dimensional model.
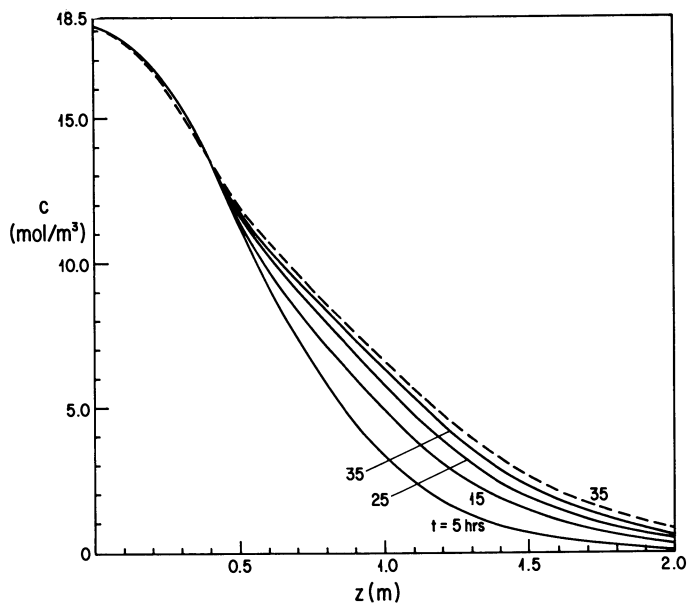
Figure 7. Axial profiles of benzene concentration $E_D/R=$ 15,000[K], $k_d^\circ = 10^{13}$. _____ one-dimensional model ------ two dimensional model.
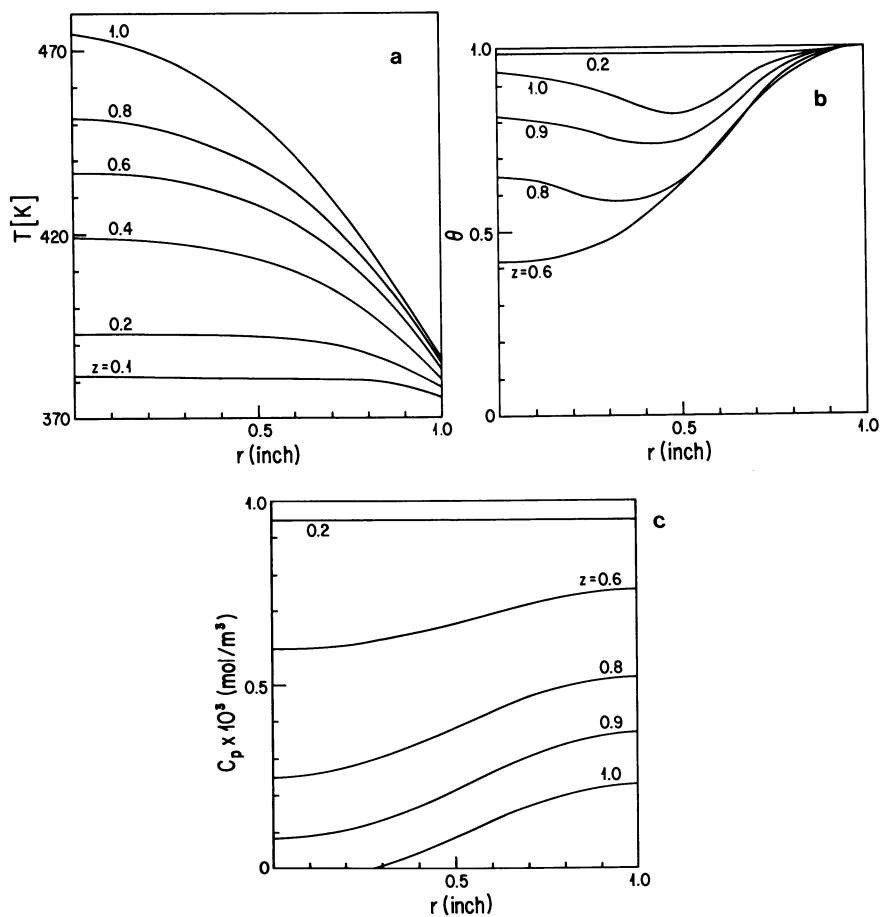
Figure 8. Radial profiles of (a) temperature (b) activity (c) concentration of poison. $E_D/R=15,000[K]$, $k_d^o=1.5\times10^{14}$ $R_o = 1.0"$, time of deactivation=2.5 hrs.
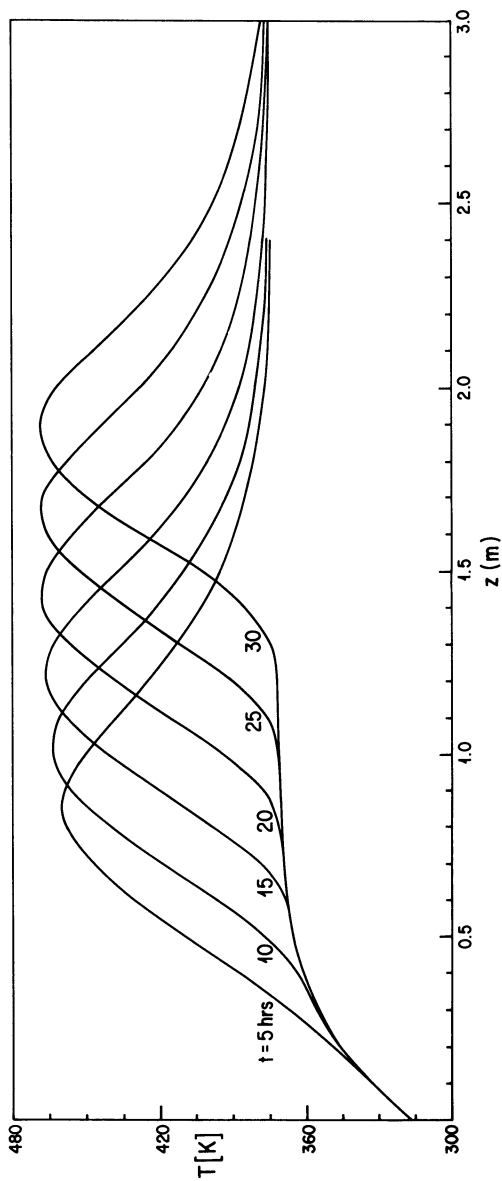
Figure 9. Axial temperature profiles. One-dimensional model. $E_D=0$, $k_d^o=0.5$.

heated up to the temperature of the cooling medium, and the reaction can start after the reacting gas leaves the completely deactivated part of the catalyst.

We can easily show that there exists asimilarity between temperature and concentration fields in a deactivating bed if $r_p \gg r_c$. Differentiating Eq. 1 with respect to t gives:

$$\frac{u}{\rho}\frac{\partial^2 C}{\partial z \partial t} = -\frac{\partial \theta}{\partial t} r_c + \theta \left[\frac{\partial r_c}{\partial C}\frac{\partial C}{\partial t} + \frac{\partial r_c}{\partial T}\frac{\partial T}{\partial t} \right] \qquad (17)$$

Substitution of Eq. 4 for $\frac{\partial \theta}{\partial t}$ and putting zero for quantities in the bracket (because $\frac{\partial C}{\partial t} \to 0$ and $\frac{\partial T}{\partial t} \to 0$) we get

$$\frac{u}{\rho}\frac{\partial^2 C}{\partial z \partial t} = -r_D r_c \qquad (18)$$

Differentiation of Eq. 3 gives

$$u \langle \rho C_{pf} \rangle \frac{\partial^2 T}{\partial z \partial t} = r_c r_D \rho (-\Delta H) \qquad (19)$$

After comparing Eq. 18 and 19 and denoting

$$\psi = C + \frac{\langle \rho C_{pf} \rangle}{(-\Delta H)} T \qquad (20)$$

we have

$$\frac{\partial^2 \psi}{\partial z \partial t} = 0 \qquad (21)$$

Evidently the value ψ is conserved in the reaction front and the temperature and concentration fields in the deactivating bed ($r_p \gg r_c$) are similar, c.f., Figures 1 and 4.

For the case $r_p \cong r_c$ or $r_p < r_c$, the situation is more complicated. In this case, the deactivation and reaction fronts are not separated but overlapped. Let us follow the physical situation drawn in Figures 5-7. The rate of deactivation for the inlet temperature is very low and no poison is deposited at the inlet part of the bed. Since the activation energy of the deactivation is high, with increasing temperature the role of the deactivation process becomes important. The poison penetrates and is adsorbed inside the bed. A standing wave of activity in the reactor results which propagates slowly toward the inlet as well as exit of the reactor (c.f. Figure 6). The temperature profile is also represented by a standing wave. The position of the hot spot is not very sensitive to the degree of deactivation. For this type of deactivation, the hot spot temperature will decrease with increasing time (c.f. Figure 5).

Effect of Operational Variables. There are three important operational variables which can affect the operation of a deactivating nonadiabatic reactor: (1) inlet temperature; (2) inlet poison concentration; and (3) tube diameter.

Effect of Inlet Temperature.   The effect of inlet tempera-
ture T_o depends on the type of the deactivation front in the
reactor.   For a travelling deactivation wave (see Figures 10 and
11),the effect of the inlet temperature is only of marginal im-
portance at the reactor inlet.   For higher times of deactivation,
the propagating temperature front is independent of inlet tempera-
ture.   This observation can be explained easily.   For this type of
deactivation the poison deactivates the inlet part of the reactor.
For higher times of deactivation this portion of the bed serves
as a heat exchanger.   For $T_o < T_c$ the fresh gas is heated up to
the temperature of the cooling medium T_c, while for $T_o > T_c$,the
feed is cooled down to T_c.   As a result, for this type of deac-
tivation, the unreacted feed enters the fresh part of the catalyst
bed at the same temperature.   For a standing wave type of deac-
tivation,the situation is completely different.   The inlet tempe-
rature dictates the depth of penetration of the poison (cf. Fig-
ures 12 and 13).   For increasing time of deactivation the hot
spot temperature moves slowly toward the reactor inlet, see Fig-
ure 12.

Effect of Poison Concentration.   The effect of poison con-
centration can be anticipated according to the type of deactiva-
tion.   For the travelling wave deactivation,the higher concentra-
tion of the poison in the feed will increase the speed of the
front.   Evidently, the velocity of the travelling wave is given
by the rate of deactivation.   For the case of low E_D and $r_D >> r_{pc}$,
the speed of the wave is proportional to the poison concentration
in the feed, as shown in Figure 14.
     For the standing wave deactivation,the higher poison concen-
tration will result in a higher amplitude of the standing wave,
cf.,Figure 15.

Effect of Tube Diameter.   For 1" tubes,the radial profiles
of activity are parabola –like functions with minimum value at
the center of the tube.   For tubes with higher values of the dia-
meter, e.g., 2" tubes, the picture can be rather different.   High
radial temperature gradients result also in large gradients of
benzene and poison.   For a deactivation process with high E_D,a
minimum on the activity profile can occur between the reactor
axis and wall, see Figure 8. Blaum (3) observed radial hot spots
of temperature between the reactor axis and wall for a very rapid
deactivation.   For slow deactivation,these hot spots are not
likely.

Effect of Kinetic Parameters.   The deactivation process is
affected by two important kinetic parameters: (a) Activation
energy of the deactivation step, E_D; (b) Value of the pre-
exponential factor of the deactivation, k_d^o.
     The effect of E_D was extensively discussed above. Here,
only the effect of k_d^o will be investigated.
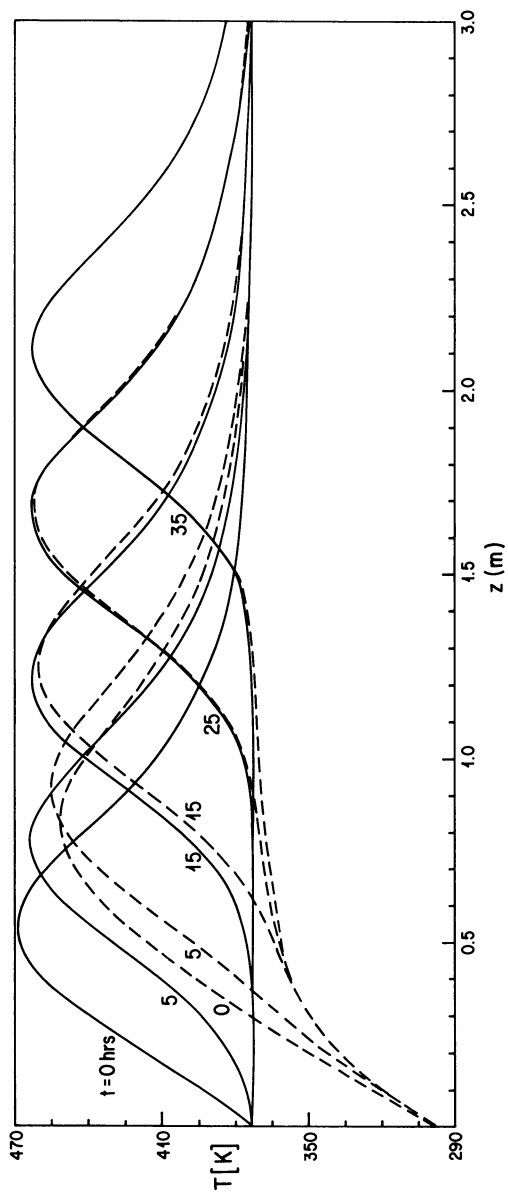
Figure 10. Axial temperature profiles, one-dimensional model. Constant pattern fronts. Effect of inlet temperature. ——— $T_o = 373°K$ ----- $T_o = 298°K$ $\frac{E_D}{R} = 545[K], k_d^o = 1.0.$
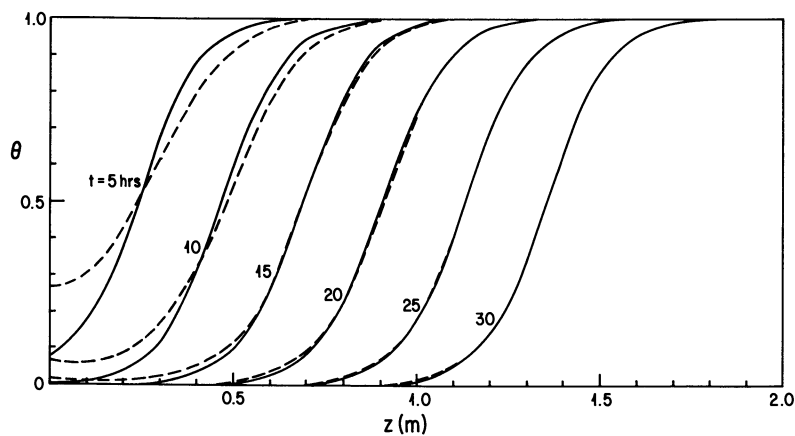
Figure 11. Axial activity profiles, one-dimensional model. Constant pattern fronts. Effect of inlet temperature $\frac{E_D}{R}$= 545[K], k_d°=1.0. _____T_o=373   ----T_o =298°K
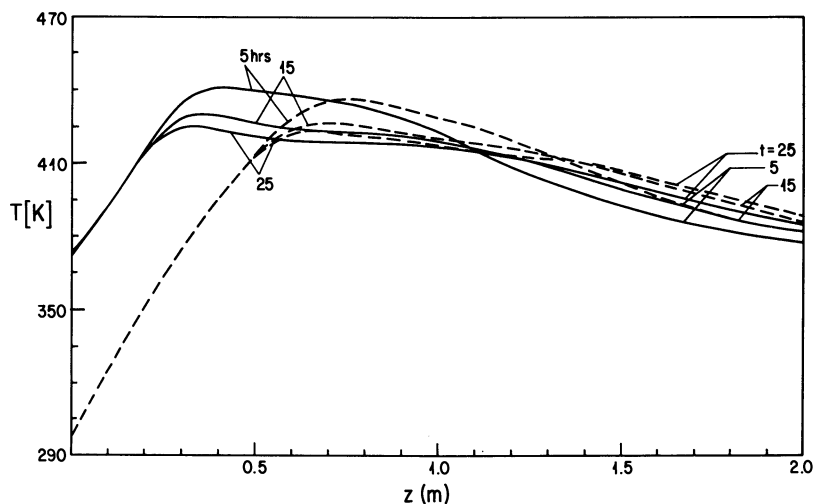
Figure 12. Axial temperature profiles, one-dimensional model. Standing wave situation. $\frac{E_D}{R}$= 15,000[K], k_d°=10^{13}
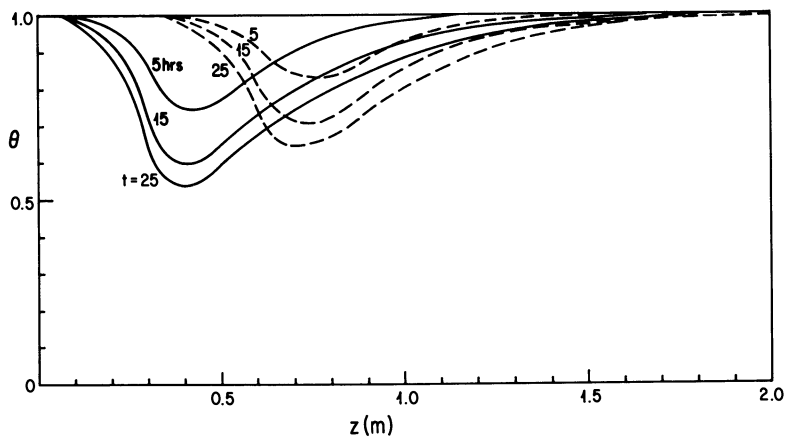
_____T_o = 373°K   ----- T_o=298°K.

Figure 13. Axial activity profiles, one-dimensional model. Standing wave situation.
———T_o =373°K ----T_o = 298°K. $\frac{E_D}{R}$= 15,000[K], k_d^o= 10^{13}
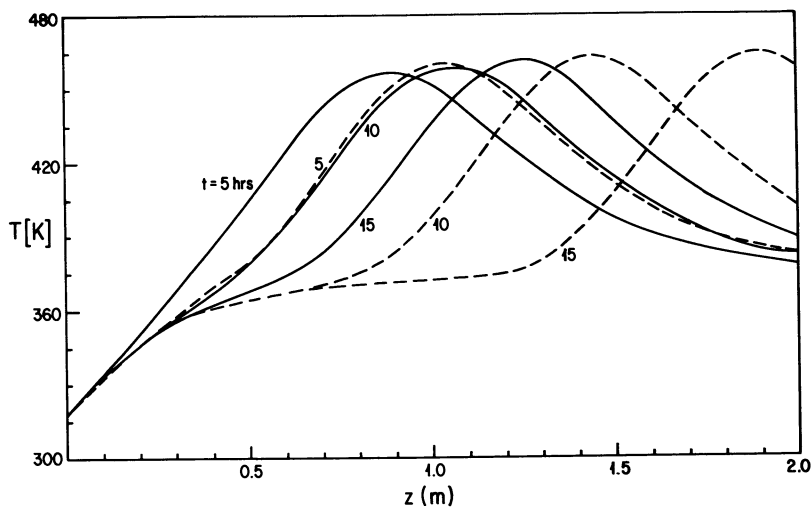
Figure 14. Axial temperature profiles. Constant pattern front. One-dimensional model. Effect of the inlet poison concentration. E_D/R = 545[K], k_d^o = 1.0. ——— C_{po} = 0.00958 [mol/m^3]. _ _ _ _ _ C_{po} =0.0196[mol/m^3].
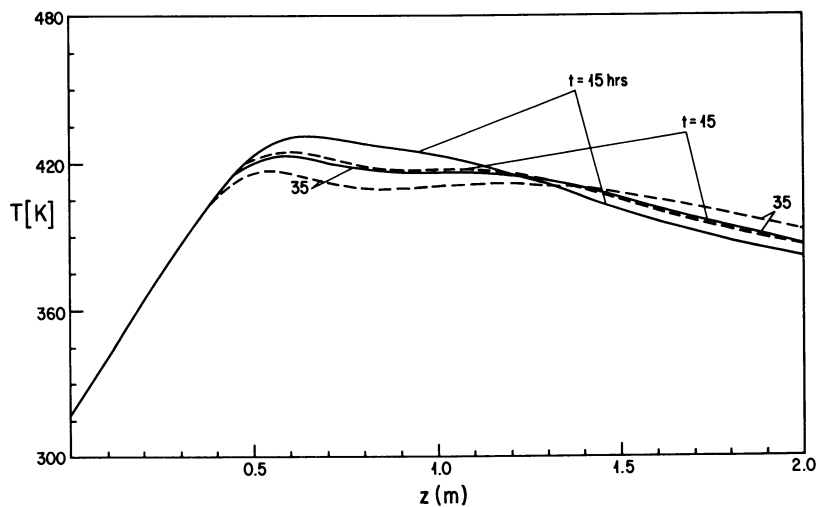
Figure 15. Axial temperature profiles. Standing wave situation. One-dimensional model. Effect of the inlet poison concentration. $E_D/R=15,000[K]$, $k_d^\circ=10^{13}$. _____ $C_{po}=0.00958[mol/m^3]$ _ _ _ _ _ $C_{po} = 0.0196[mol/m^3]$.

Effect of k_d^o. For a very low value of k_d^o and E_D, the axial profile of activity θ does not depend strongly on the axial co-ordinate z. The lower is k_d^o the more uniform is θ. Evidently, for low values of k_d^o, a standing wave type of deactivation occurs. Here, during the slow deactivation process, the temperature in the hot spot decreases. For k_d^o=20.0 (fast deactivation), a constant pattern profile exist and the temperature increases during the deactivation process.

Discussion and Conclusions

The models of catalyst deactivation in tubular nonadiabatic reactors proposed here include convection in axial direction and effective diffusion and conduction in the radial direction. For a   majority of industrially operated nonadiabatic reactors, the axial temperature gradients are not extremely steep and the axial dispersion process can be neglected. This conclusion is true for all types of full-size nonadiabatic hydrogenation reactors. Frequently, the activation energy of the deactivation process is very low and the reactor may be simulated using a one-dimensional description. Depending on the rate of deactivation (i.e. on the value k_d^o), two different deactivation processes can occur. For a low value of standing wave deactivation process occurs. The temperature in the hot spot will decrease during deactivation. For a fast deactivation, (i.e. higher values of k_d^o), a porpagating wave deactivation occurs. For this type of deactivation the hot spot temperature will increase and constant pattern profiles of temperature and concentration can be observed.

For high values of E_D, the poison will penetrate in the catalyst bed and a standing wave of deactivation occurs inside the reactor. For this type of deactivation, the radial profiles of activity can exhibit a complicated shape and a two-dimensional model is necessary for calculation.

The quasistationary model without dispersion can satisfactorily describe the majority of deactivation processes taking place in industrial packed bed reactors and can be used safely for calculations.

Legend of Symbols

C, C_p Concentration of benzene and poison, respectively.

C_{pf} Heat capacity of the gas

D_r, D_{pr} Radial dispersion coefficient of benzene and poison respectively.

E_D Activation energy for poisoning.

h_w Wall heat transfer coefficient

$(-\Delta H)$ Heat of reaction.

k_d°	Pre-exponential factor for poisoning.
L	Length of the reactor tube
M_T	Catalyst adsorption capacity for poison.
p_i	Partial pressure
P	Total pressure
r_c, r_p, r_D	Reaction rate, rate of poison chemisorption, rate of activity decay respectively.
r	radial coordinate
R_o	Reactor radius
t	time
T, T_c, T_w	Temperature, temperature of cooling medium and wall temperature, respectively.
u	Interstitial velocity.
U	Overall heat transfer coefficient.
x_p	Mole fraction of poison
z	Length variable.

Greek Symbols

ε	Bed void fraction.
λ_{er}	Bed effective thermal conductivity in the radial direction.
θ	Activity of the bed.
ρ, ρ_f	Catalyst and gas density

Subscript

o	Initial conditions

Literature Cited

1. Butt, J. B., Adv. Chem. 1972, 109, 259.
2. Butt, J. B.; Billimoria, R. M., Am. Chem. Soc. Symp. 1978, 72, 323.
3. Blaum, E., Chem. Eng. Sci. 1974, 29, 2263.
4. Weng, H. S.; Eigenberger, G.; Butt, J. B., Chem. Eng. Sci. 1975. 30, 1341.
5. Price, T. H.; Butt, J. B., Chem. Eng. Sci. 1977, 32, 393.
6. Billimoria, R. M.; Butt, J. B., Chem. Eng. J. 1981, 22, 71.
7. Mikus, O.; Pour, V.; Hlavacek, V.; J. Catal. 1977, 48, 98.
8. Mikus, O.; Pour, V.; Hlavacek, V.; J. Catal. 1981, 69, 140.
9. Franks, R. G. E., paper presented at the 3rd Iranian International Chemical Engineering Meeting (Shiraz, Iran 1977).
10. Puszynski, J.; Snita, D.; Hlavacek V., Hofmann, H., Chem. Eng. Sci. 1981, 36, 1605.

11.   Pexider, V.; Cerny, V.; Pasek, J., "A Contribution to Kinetic
      Studies Performed on a Nonisothermal Pilot-Plant Reactor,"
      in Chem. React. Engng., (Brussel, Sept. 1968), p. 239
      (Perganum Press, Oxford 1971).
12.   Hlavacek, V.; Votruba, J., Chapter 6 in "Chemical Reaction
      Theory. A Review", L. Lapidus, and N. R. Amundson (Editors),
      Prentice Hall, Englewood Cliffs, N.J. 1977.
13.   Bhatia, Q.S., M.S. Thesis, State University of New York at
      Buffalo, 1983.

Author Index

Subject Index

417

Author Index

Subject Index

417

Pressure
  equations, plant-scale catalytic
    reactor, 260
  influence on flow transition, 5
Pressure drop, related to gas and
    liquid flow rates, 5,8f
Pressure profiles, in large-scale
    reactors, 5
Progressive deactivation of plant-
    scale catalytic reactor, 263
Pseudohomogeneous one-dimensional
    cooled tubular reactor model, 326
Pseudohomogeneous one-dimensional
    plug-flow reactor model, catalyst
    poisoning, 379
Pseudohomogeneous parameters, two-
    dimensional, fixed-bed catalytic
    reactor, 242
Pseudohomogeneous temperature, fixed-
    bed catalytic reactor, 241

R

Radial mean conversion, fixed-bed
    catalytic reactor, 242
Rate-limiting step
  catalytic reaction rate data, 365
  plant-scale catalytic reactor, 259
Reaction factor, gas-liquid CSTRs, 96
Reaction kinetics, plant-scale
    catalytic reactor, 257
Reaction order, and stability of
    trickle-bed reactors, 77
Reaction parameters, and stability of
    trickle-bed reactors, 39,73
Reaction rate
  apparent, 26-30
  fixed-bed catalytic reactors, 245
  mathematical definition, 364
  stability of adiabatic reactors, 339
  trickle-bed reactor, 22,23f
Reaction system
  optimization of plant-scale
    catalytic reactor, 265-67
  safe design of cooled tubular
    reactors, 329
Reaction temperatures, equations,
    plant-scale catalytic reactor, 260
Reaction velocity constant, cooled
    tubular reactors, 327
Reactor dynamics and simulation,
    catalyst poisoning in
    fixed-bed reactors, 380-83
Reactor length, effect in
    countercurrent moving-bed
    catalytic reactor, 273,283
Reactor model, gas-liquid CSTRs, 98
Reactor performance, effect of solids-
    concentration profiles, 120
Reactor runaway, safe design of cooled
    tubular reactors, 323,325,330

Reactor schematic, countercurrent
    moving-bed catalytic reactor, 272f
Reactor simulation and optimization,
    plant-scale catalytic reactor, 259
Recycle reactor, catalytic reaction
    rate data, 367
Reforming, steam, methane over
    Ni/Al$_2$O$_3$ catalyst, 231-37
Residence-time parameter, critical,
    stability of adiabatic
    reactors, 355f
Residence-time predictions, in
    gas-liquid CSTRs, 101-103
Rotating disk reactor, CVD reactor, 202

S

Sauter mean bubble diameter, slurry
    bubble column reactor, 138
Second-order reaction, spline
    collocation, gas absorption
    with complex reaction, 90,91f
Series connection of unit batteries in
    cross-flow monolith fuel cell
    reactor, 183-84
Settling velocity, single particle
    in a stagnant liquid, 109
Shell temperatures, nonuniform, plant-
    scale catalytic reactor, 263
Shock plane, countercurrent moving-bed
    catalytic reactor, 275,276f
Silicon-derived electronic materials,
    CVD reactors, 197
Silicon film-thickness profiles,
    LPCVD model, 209,210f
Silicon growth-rate profiles,
    LPCVD model, 209,210f
Silicon oxide-isoparaffin system,
    solid dispersion
    coefficient, 117,120,121f
Silver catalyst, use in ethylene
    oxidation, 332
Single reactions, and diffusion
    in porous catalysts, 219
Sintering, and deactivation of non-
    adiabatic packed-bed reactor, 393
Site balance equation, catalytic
    reaction rate data, 365
Slurry bubble column, 125-146
Slurry velocity, effect on solid
    concentration profiles, 117,118f
Sodium hydroxide absorption of
    carbon dioxide, 158-60
Solid concentration profiles
  effect of particle size, 113-117
  effect of reactor performance, 120
  effect of slurry velocity, 117,118f
  three-phase bubble column, 109-110
Solid dispersion coefficient, three-
    phase bubble column
    reactors, 110,117,120,121f